automobile engine intake system. These steady flow tests, conducted over the full engine speed range,[3] show that the pressure loss depends on speed squared.

Equivalent flow-dependent pressure losses in the exhaust system result in the exhaust port and manifold having average pressure levels that are higher than atmospheric. Figure 6-6 shows the time-averaged exhaust manifold gauge pressure as a function of inlet manifold vacuum (which varies inversely to load) and

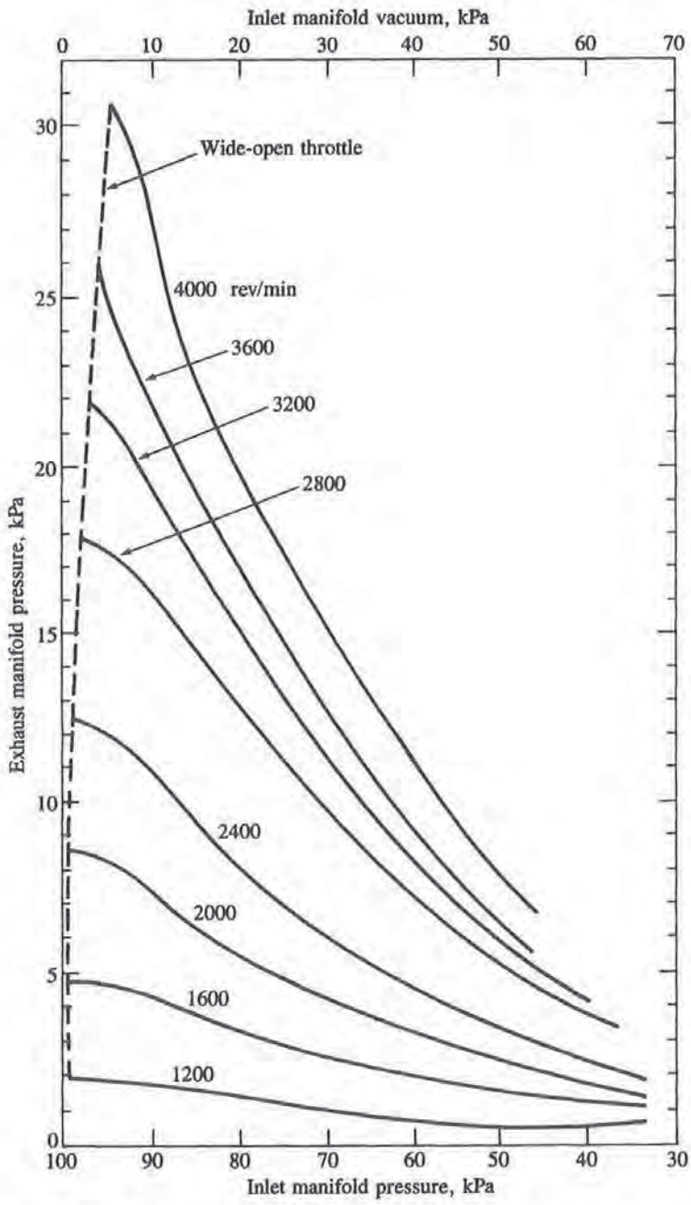


FIGURE 6-6
Exhaust manifold pressure as a function of load (defined by inlet manifold vacuum) and speed, four-stroke cycle four-cylinder spark-ignition engine.[4]

PETITIONER'S EXHIBIT 1002
US PATENT NO. 6,581,565

speed for a four-cylinder automobile spark-ignition engine.[4] At high speeds and loads the exhaust manifold operates at pressures substantially above atmospheric.

RAM EFFECT. The pressure in the inlet manifold varies during each cylinder's intake process due to the piston velocity variation, valve open area variation, and the unsteady gas-flow effects that result from these geometric variations. The mass of air inducted into the cylinder, and hence the volumetric efficiency, is almost entirely determined by the pressure level in the inlet port during the short period before the inlet valve is closed.[5] At higher engine speeds, the inertia of the gas in the intake system as the intake valve is closing increases the pressure in the port and continues the charging process as the piston slows down around BC and starts the compression stroke. This effect becomes progressively greater as engine speed is increased. The inlet valve is closed some 40 to 60° after BC, in part to take advantage of this ram phenomenon.

REVERSE FLOW INTO THE INTAKE. Because the inlet valve closes after the start of the compression stroke, a reverse flow of fresh charge from the cylinder back into the intake can occur as the cylinder pressure rises due to piston motion toward TC. This reverse flow is largest at the lowest engine speeds. It is an inevitable consequence of the inlet valve closing time chosen to take advantage of the ram effect at high speeds.

TUNING. The pulsating flow from each cylinder's exhaust process sets up pressure waves in the exhaust system. These pressure waves propagate at the local sound speed relative to the moving exhaust gas. The pressure waves interact with the pipe junctions and ends in the exhaust manifold and pipe. These interactions cause pressure waves to be reflected back toward the engine cylinder. In multicylinder engines, the pressure waves set up by each cylinder, transmitted through the exhaust and reflected from the end, can interact with each other. These pressure waves may aid or inhibit the gas exchange processes. When they aid the process by reducing the pressure in the exhaust port toward the end of the exhaust process, the exhaust system is said to be *tuned*.[6]

The time-varying inlet flow to the cylinder causes expansion waves to be propagated back into the inlet manifold. These expansion waves can be reflected at the open end of the manifold (at the plenum) causing positive pressure waves to be propagated toward the cylinder. If the timing of these waves is appropriately arranged, the positive pressure wave will cause the pressure at the inlet valve at the end of the intake process to be raised above the nominal inlet pressure. This will increase the inducted air mass. Such an intake system is described as *tuned*.[6]

Methods which predict the unsteady flows in the intake and exhaust systems of internal combustion engines with good accuracy have been developed. These methods are complicated, however, so more detailed discussion is deferred to Chap. 14.

PETITIONER'S EXHIBIT 1002
US PATENT NO. 6,581,565

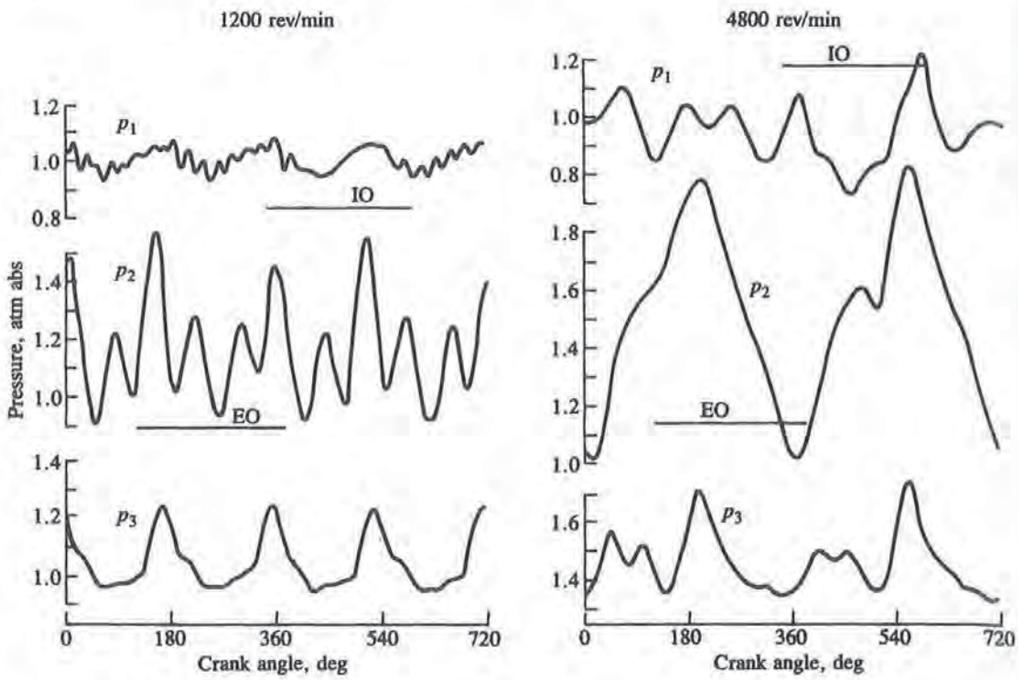


FIGURE 6-7
Instantaneous pressures in the intake and exhaust manifolds of a four-stroke cycle four-cylinder spark-ignition engine, at wide-open throttle. Locations: p_1, intake manifold runner 150 mm from cylinder 1; p_2, exhaust manifold runner 200 mm from cylinder 1; p_3, exhaust manifold runner 700 mm from cylinder 1. IO and EO, intake and exhaust valve open periods for that cylinder, respectively.[3] Stroke = 89 mm. Bore = 84 mm.

Examples of the pressure variations in the inlet and exhaust systems of a four-cylinder automobile spark-ignition engine at wide-open throttle are shown in Fig. 6-7. The complexity of the phenomena that occur is apparent. The amplitude of the pressure fluctuations increases substantially with increasing engine speed. The primary frequency in both the intake and exhaust corresponds to the frequency of the individual cylinder intake and exhaust processes. Higher harmonics that result from pressure waves in both the intake and exhaust are clearly important also.

6.2.3 Variation with Speed, and Valve Area, Lift, and Timing

Flow effects on volumetric efficiency depend on the velocity of the fresh mixture in the intake manifold, port, and valve. Local velocities for quasi-steady flow are equal to the volume flow rate divided by the local cross-sectional area. Since the intake system and valve dimensions scale approximately with the cylinder bore, mixture velocities in the intake system will scale with piston speed. Hence, volumetric efficiencies as a function of speed, for different engines, should be compared at the same mean piston speed.[7] Figure 6-8 shows typical curves of

PETITIONER'S EXHIBIT 1002
US PATENT NO. 6,581,565

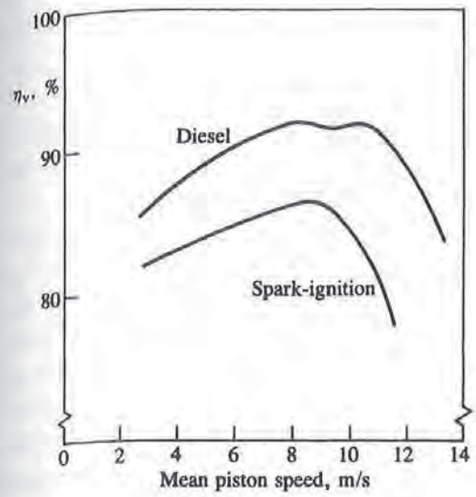


FIGURE 6-8
Volumetric efficiency versus mean piston speed for a four-cylinder automobile indirect-injection diesel[8] and a six-cylinder spark-ignition engine.[9]

volumetric efficiency versus mean piston speed for a four-cylinder automobile indirect-injection diesel engine[8] and a six-cylinder spark-ignition engine.[9] The volumetric efficiencies of spark-ignition engines are usually lower than diesel values due to flow losses in the carburetor and throttle, intake manifold heating, the presence of fuel vapor, and a higher residual gas fraction. The diesel curve with its double peak shows the effect of intake system tuning.

The shape of these volumetric efficiency versus mean piston speed curves can be explained with the aid of Fig. 6-9. This shows, in schematic form, how the

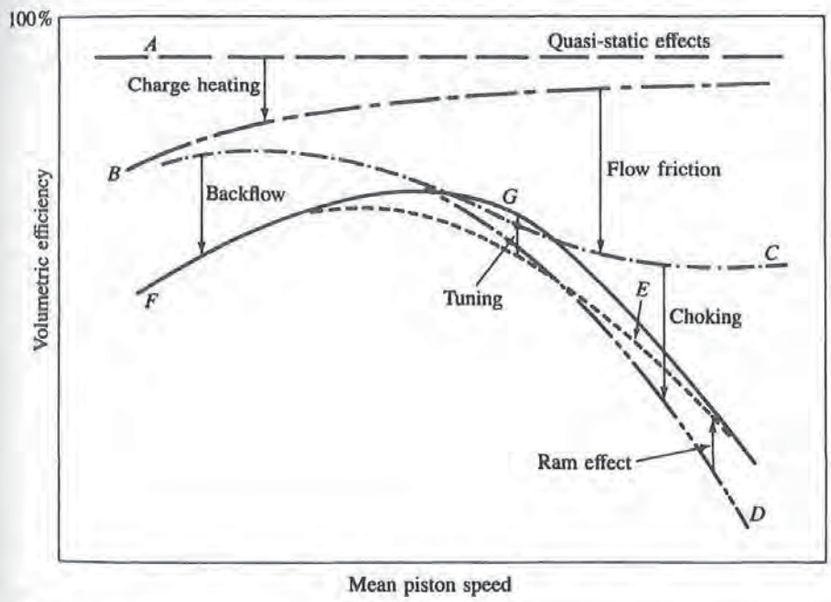


FIGURE 6-9
Effect on volumetric efficiency of different phenomena which affect the air flow rate as a function of speed. Solid line is final η_v versus speed curve.

PETITIONER'S EXHIBIT 1002
US PATENT NO. 6,581,565

effect on volumetric efficiency of each of the different phenomena described in this section varies with speed. Non-speed-dependent effects (such as fuel vapor pressure) drop η_v below 100 percent (curve *A*). Charge heating in the manifold and cylinder drops curve *A* to curve *B*. It has a greater effect at lower engine speeds due to longer gas residence times. Frictional flow losses increase as the square of engine speed, and drop curve *B* to curve *C*. At higher engine speeds, the flow into the engine during at least part of the intake process becomes choked (see Sec. 6.3.2). Once this occurs, further increases in speed do not increase the flow rate significantly so volumetric efficiency decreases sharply (curve *C* to *D*). The induction ram effect, at higher engine speeds, raises curve *D* to curve *E*. Late inlet valve closing, which allows advantage to be taken of increased charging at higher speeds, results in a decrease in η_v at low engine speeds due to backflow (curves *C* and *D* to *F*). Finally, intake and/or exhaust tuning can increase the volumetric efficiency (often by a substantial amount) over part of the engine speed range, curve *F* to *G*.

An example of the effect on volumetric efficiency of tuning the intake manifold runner is shown in Fig. 6-10. In an unsteady flow calculation of the gas exchange processes of a four-cylinder spark-ignition engine, the length of the intake manifold runners was increased successively by factors of 2. The 34-cm length produces a desirable "tuned" volumetric efficiency curve with increased low-speed air flow and flat mid-speed characteristics. While the longest runner further increases low-speed air flow, the loss in η_v at high speed would be unacceptable.[10] Further discussion of intake system tuning can be found in Sec. 7.6.2.

Figure 6-11 shows data from a four-cylinder spark-ignition engine[3] which illustrates the effect of varying valve timing and valve lift on the volumetric efficiency versus speed curve. Earlier-than-normal inlet valve closing reduces backflow losses at low speed and increases η_v. The penalty is reduced air flow at high speed. Later-than-normal inlet valve closing is only advantageous at very high

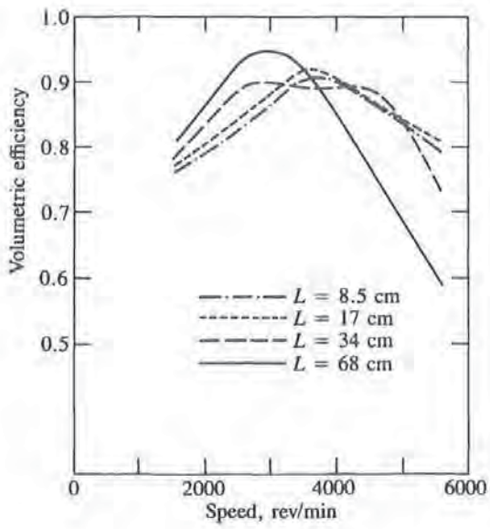


FIGURE 6-10
Effect of intake runner length on volumetric efficiency versus speed for 2.3-dm^3 four-cylinder spark-ignition engine.[10]

PETITIONER'S EXHIBIT 1002
US PATENT NO. 6,581,565

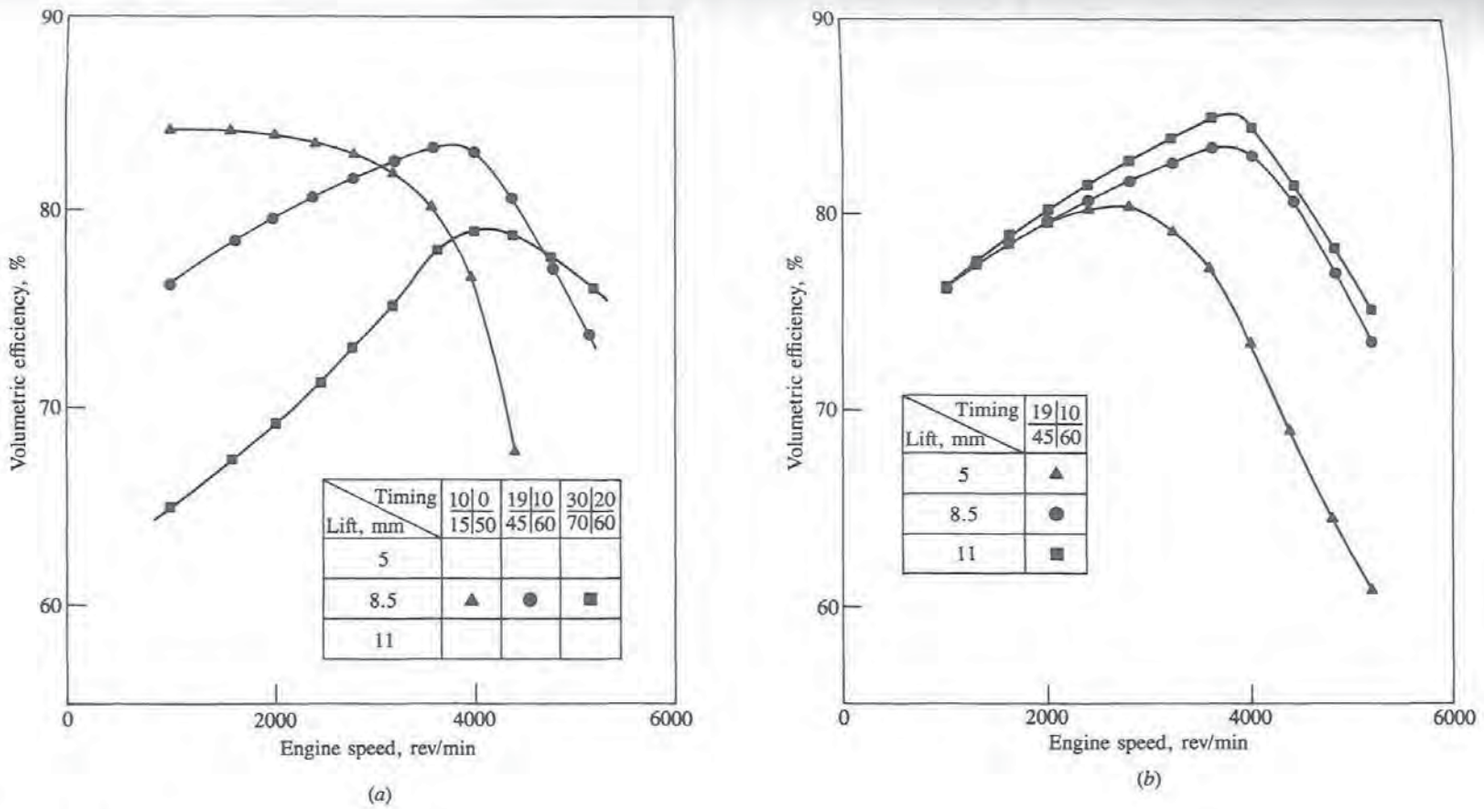


FIGURE 6-11
Effect of (*a*) valve timing and (*b*) valve lift on volumetric efficiency versus speed curves. Four-cylinder 1.6-dm^3 displacement spark-ignition engine at wide-open throttle, firing conditions, $(A/F) = 13$, MBT ignition timing. Timing numbers are: inlet valve opens (before TC) top left, closes (after BC) bottom left; exhaust valve opens (before BC) bottom right, closes (after TC) top right.[3] Stroke = 89 mm.

PETITIONER'S EXHIBIT 1002
US PATENT NO. 6,581,565

speeds. Low valve lifts significantly restrict engine breathing over the mid-speed and high-speed operating ranges. Above a critical valve lift, lift is no longer a major constraint on effective valve open area (see Sec. 6.3).

6.3 FLOW THROUGH VALVES

The valve, or valve and port together, is usually the most important flow restriction in the intake and the exhaust system of four-stroke cycle engines. The characteristics of flows through poppet valves will now be reviewed.

6.3.1 Poppet Valve Geometry and Timing

Figure 6-12 shows the main geometric parameters of a poppet valve head and seat. Figure 6-13 shows the proportions of typical inlet and exhaust valves and ports, relative to the valve inner seat diameter D. The inlet port is generally circular, or nearly so, and the cross-sectional area is no larger than is required to achieve the desired power output. For the exhaust port, the importance of good valve seat and guide cooling, with the shortest length of exposed valve stem, leads to a different design. Although a circular cross section is still desirable, a rectangular or oval shape is often essential around the guide boss area. Typical valve head sizes for different shaped combustion chambers in terms of cylinder bore B are given in Table 6.1.[11] Each of these chamber shapes (see Secs. 10.2 and 15.4 for a discussion of spark-ignition and diesel combustion chamber design) imposes different constraints on valve size. Larger valve sizes (or four valves compared with two) allow higher maximum air flows for a given cylinder displacement.

Typical valve timing, valve-lift profiles, and valve open areas for a four-stroke cycle spark-ignition engine are shown in Fig. 6-14. There is no universally accepted criterion for defining valve timing points. Some are based upon a spe-

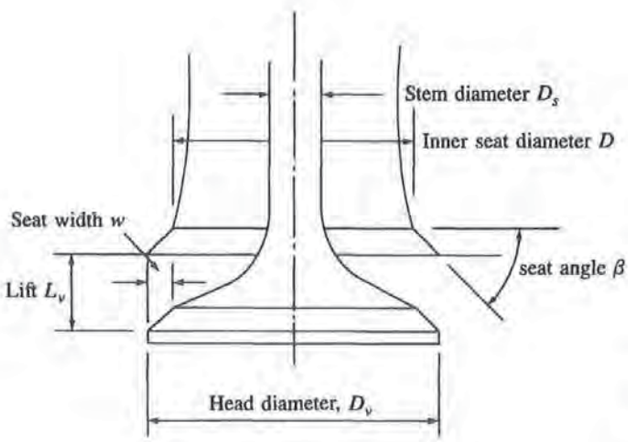
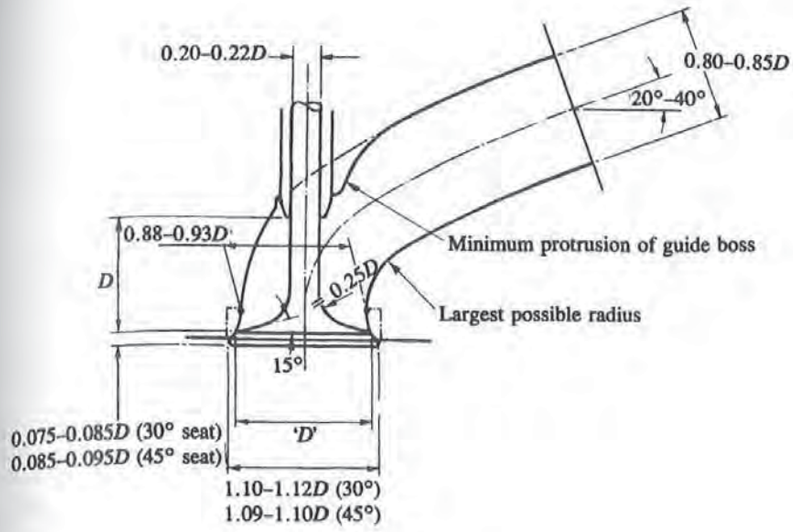
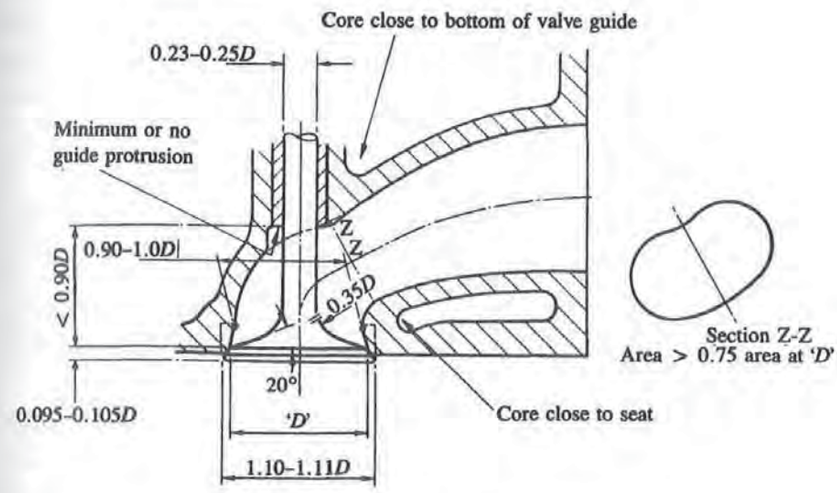


FIGURE 6-12
Parameters defining poppet valve geometry.

PETITIONER'S EXHIBIT 1002
US PATENT NO. 6,581,565



(a)



(b)

FIGURE 6-13
Shape, proportions, and critical design areas of typical inlet (top) and exhaust (bottom) valves and ports.[11]

cific lift criterion. For example, SAE defines valve timing events based on reference valve-lift points:[13]

1. Hydraulic lifters. Opening and closing positions are the 0.15-mm (0.006-in) valve-lift points.
2. Mechanical lifters. Valve opening and closing positions are the points of 0.15-mm (0.006-in) lift plus the specified lash.

PETITIONER'S EXHIBIT 1002
US PATENT NO. 6,581,565

TABLE 6.1
Valve head diameter in terms of cylinder bore B[11]

Combustion chamber shape†	Inlet	Exhaust	Approximate mean piston speed, max power, m/s
Wedge or bathtub	0.43–0.46B	0.35–0.37B	15
Bowl-in-piston	0.42–0.44B	0.34–0.37B	14
Hemispherical	0.48–0.5B	0.41–0.43B	18
Four-valve pent-roof	0.35–0.37B	0.28–0.32B	20

† See Fig. 15-15.

Alternatively, valve events can be defined based on angular criteria along the lift curve.[12] What is important is when significant gas flow through the valve-open area either starts or ceases.

The instantaneous valve flow area depends on valve lift and the geometric details of the valve head, seat, and stem. There are three separate stages to the flow area development as valve lift increases,[14] as shown in Fig. 6-14*b*. For low valve lifts, the minimum flow area corresponds to a frustrum of a right circular cone where the conical face between the valve and the seat, which is perpendicular to the seat, defines the flow area. For this stage:

$$\frac{w}{\sin \beta \cos \beta} > L_v > 0$$

and the minimum area is

$$A_m = \pi L_v \cos \beta \left(D_v - 2w + \frac{L_v}{2} \sin 2\beta \right) \tag{6.7}$$

where β is the valve seat angle, L_v is the valve lift, D_v is the valve head diameter (the outer diameter of the seat), and w is the seat width (difference between the inner and outer seat radii).

For the second stage, the minimum area is still the slant surface of a frustrum of a right circular cone, but this surface is no longer perpendicular to the valve seat. The base angle of the cone increases from $(90 - \beta)°$ toward that of a cylinder, 90°. For this stage:

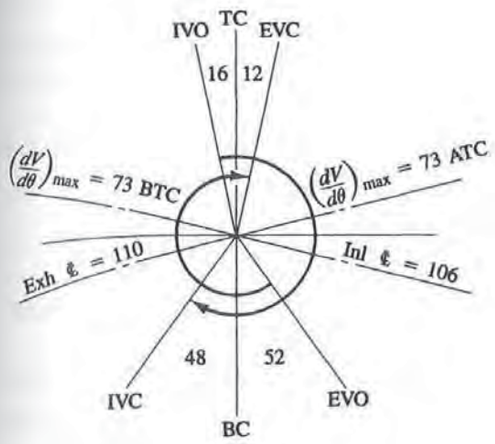
$$\left[\left(\frac{D_p^2 - D_s^2}{4D_m} \right) - w^2 \right]^{1/2} + w \tan \beta \geqslant L_v > \frac{w}{\sin \beta \cos \beta}$$

and

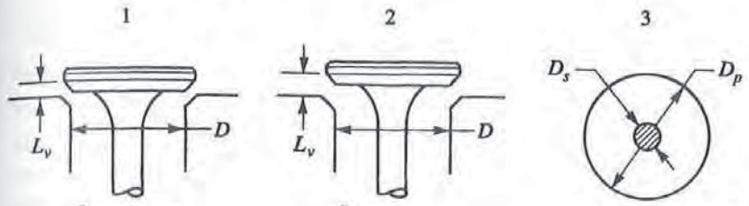
$$A_m = \pi D_m [(L_v - w \tan \beta)^2 + w^2]^{1/2} \tag{6.8}$$

where D_p is the port diameter, D_s is the valve stem diameter, and D_m is the mean seat diameter $(D_v - w)$.

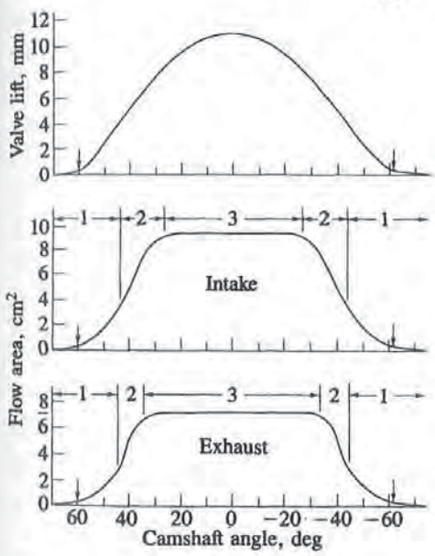
PETITIONER'S EXHIBIT 1002
US PATENT NO. 6,581,565



(*a*)



(*b*)



(*c*)

FIGURE 6-14
(*a*) Typical valve timing diagram for high-speed 2.2-dm^3 four-cylinder spark-ignition engine. (*b*) Schematic showing three stages of valve lift. (*c*) Valve-lift curve and corresponding minimum intake and exhaust valve open areas as a function of camshaft angle. Inlet and exhaust valve diameters are 3.6 and 3.1 cm, respectively.[12]

PETITIONER'S EXHIBIT 1002
US PATENT NO. 6,581,565

Finally, when the valve lift is sufficiently large, the minimum flow area is no longer between the valve head and seat; it is the port flow area minus the sectional area of the valve stem. Thus, for

$$L_v > \left[\left(\frac{D_p^2 - D_s^2}{4D_m}\right)^2 - w^2\right]^{1/2} + w \tan \beta$$

then

$$A_m = \frac{\pi}{4}(D_p^2 - D_s^2) \tag{6.9}$$

Intake and exhaust valve open areas corresponding to a typical valve-lift profile are plotted versus camshaft angle in Fig. 6-14*c*. These three different flow regimes are indicated. The maximum valve lift is normally about 12 percent of the cylinder bore.

Inlet valve opening (IVO) typically occurs 10 to 25° BTC. Engine performance is relatively insensitive to this timing point. It should occur sufficiently before TC so that cylinder pressure does not dip early in the intake stroke. Inlet valve closing (IVC) usually falls in the range 40 to 60° after BC, to provide more time for cylinder filling under conditions where cylinder pressure is below the intake manifold pressure at BC. IVC is one of the principal factors that determines high-speed volumetric efficiency; it also affects low-speed volumetric efficiency due to backflow into the intake (see Sec. 6.2.3). Exhaust valve opening (EVO) occurs 50 to 60° before BC, well before the end of the expansion stroke, so that blowdown can assist in expelling the exhaust gases. The goal here is to reduce cylinder pressure to close to the exhaust manifold pressure as soon as possible after BC over the full engine speed range. Note that the timing of EVO affects the cycle efficiency since it determines the effective expansion ratio. Exhaust valve closing (EVC) ends the exhaust process and determines the duration of the valve overlap period. EVC typically falls in the range 8 to 20° after TC. At idle and light load, in spark-ignition engines (which are throttled), it therefore regulates the quantity of exhaust gases that flow back into the combustion chamber through the exhaust valve under the influence of intake manifold vacuum. At high engine speeds and loads, it regulates how much of the cylinder burned gases are exhausted. EVC timing should occur sufficiently far after TC so that the cylinder pressure does not rise near the end of the exhaust stroke. Late EVC favors high power at the expense of low-speed torque and idle combustion quality. Note from the timing diagram (Fig. 6-14*a*) that the points of maximum valve lift and maximum piston velocity (Fig. 2-2) do not coincide.

The effect of valve geometry and timing on air flow can be illustrated conceptually by dividing the rate of change of cylinder volume by the instantaneous minimum valve flow area to obtain a *pseudo flow velocity* for each valve:[12]

$$v_{ps} = \frac{1}{A_m}\frac{dV}{d\theta} = \frac{\pi B^2}{4A_m}\frac{ds}{d\theta} \tag{6.10}$$

where V is the cylinder volume [Eq. (2.4)], B is the cylinder bore, s is the distance

PETITIONER'S EXHIBIT 1002
US PATENT NO. 6,581,565

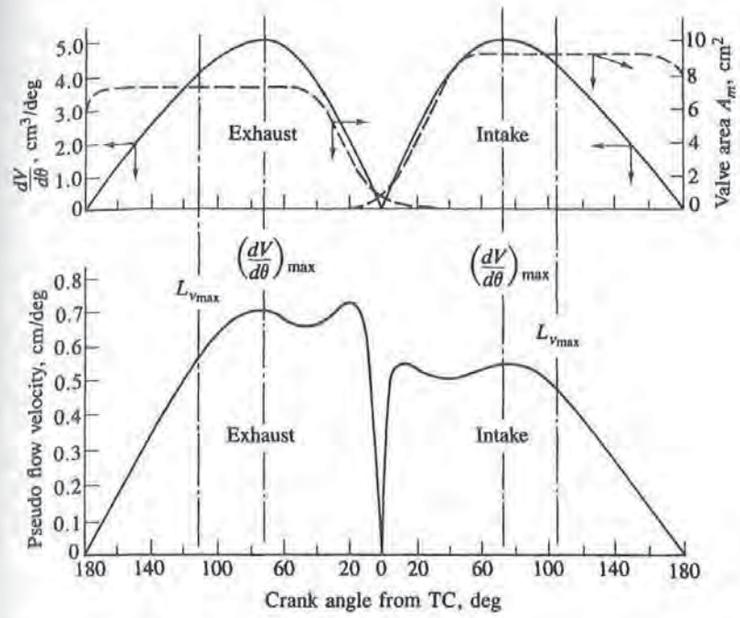


FIGURE 6-15
Rate of change of cylinder volume $dV/d\theta$, valve minimum flow area A_m, and pseudo flow velocity as function of crank angle for exhaust and inlet valves of Fig. 6-14.[12]

between the wrist pin and crank axis [see Fig. 2-1 and Eq. (2.5)] and A_m is the valve area given by Eqs. (6.7), (6.8), or (6.9). Instantaneous pseudo flow velocity profiles for the exhaust and intake strokes of a four-stroke four-cylinder engine are shown in Fig. 6-15. Note the appearance of two peaks in the pseudo flow velocity for both the exhaust and intake strokes. The broad peaks occurring at maximum piston velocity reflect the fact that valve flow area is constant at this point. The peaks close to TC result from the exhaust valve closing and intake valve opening profiles. The peak at the end of the exhaust stroke is important since it indicates a high pressure drop across the valve at this point, which will result in higher trapped residual mass. The magnitude of this exhaust stroke pseudo velocity peak depends strongly on the timing of exhaust valve closing. The pseudo velocity peak at the start of the intake stroke is much less important. That the pseudo velocities early in the exhaust stroke and late in the intake stroke are low indicates that phenomena other than quasi-steady flow govern the flow rate. These are the periods when exhaust blowdown and ram and tuning effects in the intake are most important.

6.3.2 Flow Rate and Discharge Coefficients

The mass flow rate through a poppet valve is usually described by the equation for compressible flow through a flow restriction [Eqs. (C.8) or (C.9) in App. C]. This equation is derived from a one-dimensional isentropic flow analysis, and

PETITIONER'S EXHIBIT 1002
US PATENT NO. 6,581,565

real gas flow effects are included by means of an experimentally determined discharge coefficient C_D. The air flow rate is related to the upstream stagnation pressure p_0 and stagnation temperature T_0, static pressure just downstream of the flow restriction (assumed equal to the pressure at the restriction, p_T), and a reference area A_R characteristic of the valve design:

$$\dot{m} = \frac{C_D A_R p_0}{(RT_0)^{1/2}} \left(\frac{p_T}{p_0}\right)^{1/\gamma} \left\{ \frac{2\gamma}{\gamma - 1} \left[1 - \left(\frac{p_T}{p_0}\right)^{(\gamma-1)/\gamma} \right] \right\}^{1/2} \tag{6.11}$$

When the flow is choked, i.e., $p_T/p_0 \leq [2/(\gamma + 1)]^{\gamma/(\gamma-1)}$, the appropriate equation is

$$\dot{m} = \frac{C_D A_R p_0}{(RT_0)^{1/2}} \gamma^{1/2} \left(\frac{2}{\gamma + 1}\right)^{(\gamma+1)/2(\gamma-1)} \tag{6.12}$$

For flow into the cylinder through an intake valve, p_0 is the intake system pressure p_i and p_T is the cylinder pressure. For flow out of the cylinder through an exhaust valve, p_0 is the cylinder pressure and p_T is the exhaust system pressure.

The value of C_D and the choice of reference area are linked together: their product, $C_D A_R$, is the effective flow area of the valve assembly A_E. Several different reference areas have been used. These include the valve head area $\pi D_v^2/4$,[7] the port area at the valve seat $\pi D_p^2/4$,[15] the geometric minimum flow area [Eqs. (6.7), (6.8), and (6.9)], and the curtain area $\pi D_v L_v$,[16] where L_v is the valve lift. The choice is arbitrary, though some of these choices allow easier interpretation than others. As has been shown above, the geometric minimum flow area is a complex function of valve and valve seat dimensions. The most convenient reference area in practice is the so-called valve curtain area:

$$A_C = \pi D_v L_v \tag{6.13}$$

since it varies linearly with valve lift and is simple to determine.

INLET VALVES. Figure 6-16 shows the results of steady flow tests on a typical inlet valve configuration with a sharp-cornered valve seat.[16] The discharge coefficient based on valve curtain area is a discontinuous function of the valve-lift/diameter ratio. The three segments shown correspond to different flow regimes as indicated. At very low lifts, the flow remains attached to the valve head and seat, giving high values for the discharge coefficient. At intermediate lifts, the flow separates from the valve head at the inner edge of the valve seat as shown. An abrupt decrease in discharge coefficient occurs at this point. The discharge coefficient then increases with increasing lift since the size of the separated region remains approximately constant while the minimum flow area is increasing. At high lifts, the flow separates from the inner edge of the valve seat as well.[14, 17] Typical maximum values of L_v/D_v are 0.25.

An important question is whether these steady flow data are representative of the dynamic flow behavior of the valve in an operating engine. There is some evidence that the "change points" between different flow regimes shown in Fig. 6-16 occur at slightly different valve lifts under dynamic operation than under

PETITIONER'S EXHIBIT 1002
US PATENT NO. 6,581,565

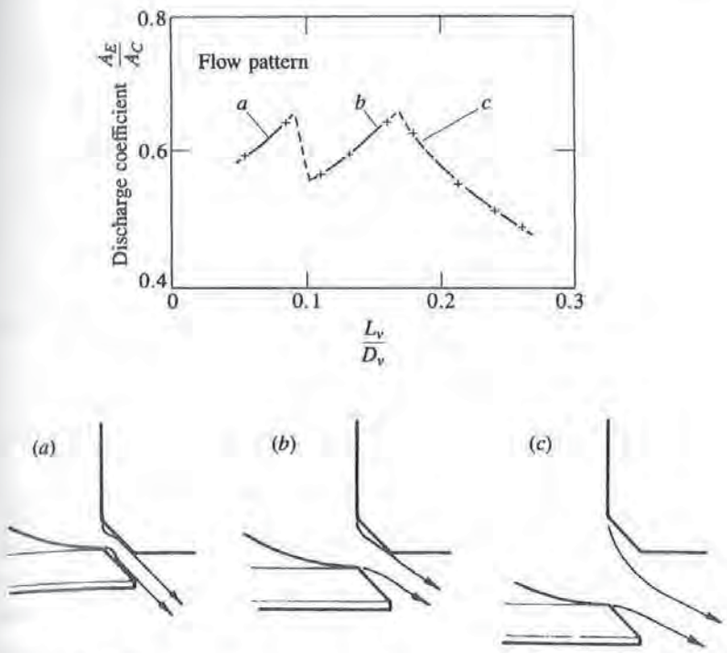


FIGURE 6-16
Discharge coefficient of typical inlet poppet valve (effective flow area/valve curtain area) as a function of valve lift. Different segments correspond to flow regimes indicated.[16]

steady flow operation. Also, as has been discussed in Sec. 6.2.2, the pressure upstream of the valve varies significantly during the intake process. However, it has been shown that over the normal engine speed range, steady flow discharge-coefficient results can be used to predict dynamic performance with reasonable precision.[14, 18]

In addition to valve lift, the performance of the inlet valve assembly is influenced by the following factors: valve seat width, valve seat angle, rounding of the seat corners, port design, cylinder head shape. In many engine designs the port and valve assembly are used to generate a rotational motion (swirl) inside the engine cylinder during the induction process, or the cylinder head can be shaped to restrict the flow through one side of the valve open area to generate swirl. Swirl production is discussed later, in Section 8.3. Swirl generation significantly reduces the valve (and port) flow coefficient. Changes in seat width affect the L_v/D_v at which the shifts in flow regimes illustrated in Fig. 6-16 occur. C_D increases as seat width decreases. The seat angle β affects the discharge coefficient in the low-lift regime in Fig. 6-16. Rounding the upstream corner of the valve seat reduces the tendency of the flow to break away, thus increasing C_D at higher lifts. At low valve lifts, when the flow remains attached, increasing the Reynolds number decreases the discharge coefficient. Once the flow breaks away from the wall, there is no Reynolds number dependence of C_D.[16]

For well-designed ports (e.g., Fig. 6-13) the discharge coefficient of the port and valve assembly need be no lower than that of the isolated valve (except when

PETITIONER'S EXHIBIT 1002
US PATENT NO. 6,581,565

the port is used to generate swirl). However, if the cross-sectional area of the port is not sufficient or the radius of the surface at the inside of the bend is too small, a significant reduction in C_D for the assembly can result.[16]

At high engine speeds, unless the inlet valve is of sufficient size, the inlet flow during part of the induction process can become choked (i.e., reach sonic velocity at the minimum valve flow area). Choking substantially reduces volumetric efficiency. Various definitions of inlet Mach number have been used to identify the onset of choking. Taylor and coworkers[7] correlated volumetric efficiencies measured on a range of engine and inlet valve designs with an *inlet Mach index Z* formed from an average gas velocity through the inlet valve:

$$Z = \frac{A_p \bar{S}_p}{C_i A_i a} \tag{6.14}$$

where A_i is the nominal inlet valve area ($\pi D_v^2/4$), C_i is a mean valve discharge coefficient based on the area A_i, and a is the sound speed. From the method used to determine C_i, it is apparent that $C_i A_i$ is the average effective open area of the valve (it is the average value of $C_D \pi D_v L_v$). Z corresponds closely, therefore, to the mean Mach number in the inlet valve throat. Taylor's correlations show that η_v decreases rapidly for $Z \geq 0.5$. An alternative equivalent approach to this problem has been developed, based on the average flow velocity through the valve during the period the valve is open.[19] A *mean inlet Mach number* was defined:

$$\bar{M}_i = \frac{\bar{v}_i}{a} \tag{6.15}$$

where $\bar{v}_i$ is the mean inlet flow velocity during the valve open period. $\bar{M}_i$ is related to Z via

$$\bar{M}_i = \frac{Z(\eta_v/100)180}{\theta_{\text{IVC}} - \theta_{\text{IVO}}} \tag{6.16}$$

This mean inlet Mach number correlates volumetric efficiency characteristics better than the Mach index. For a series of modern small four-cylinder engines, when $\bar{M}_i$ approaches 0.5 the volumetric efficiency decreases rapidly. This is due to the flow becoming choked during part of the intake process. This relationship can be used to size the inlet valve for the desired volumetric efficiency at maximum engine speed. Also, if the inlet valve is closed too early, volumetric efficiency will decrease gradually with increasing $\bar{M}_i$, for $\bar{M}_i < 0.5$, even if the valve open area is sufficiently large.[19]

EXHAUST VALVES. In studies of the flow from the cylinder through an exhaust poppet valve, different flow regimes at low and high lift occur, as shown in Fig. 6-17. Values of C_D based on the valve curtain area, for several different exhaust valve and port combinations, are given in Fig. 6-18. A sharp-cornered isolated poppet valve (i.e., straight pipe downstream, no port) gives the best performance.

PETITIONER'S EXHIBIT 1002
US PATENT NO. 6,581,565

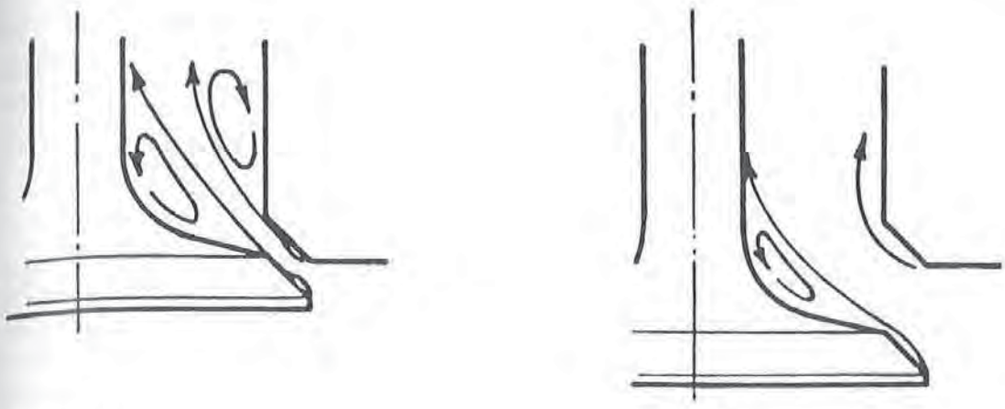


FIGURE 6-17
Flow pattern through exhaust valve at low and high lift.[16]

At high lifts, $L_v/D_v \geq 0.2$, the breakaway of the flow reduces the discharge coefficient. (At $L_v/D_v = 0.25$ the effective area is about 90 percent of the minimum geometric area. For $L_v/D_v < 0.2$ it is about 95 percent.[16]) The port design significantly affects C_D at higher valve lifts, as indicated by the data from four port designs in Fig. 6-18. Good designs can approach the performance of isolated

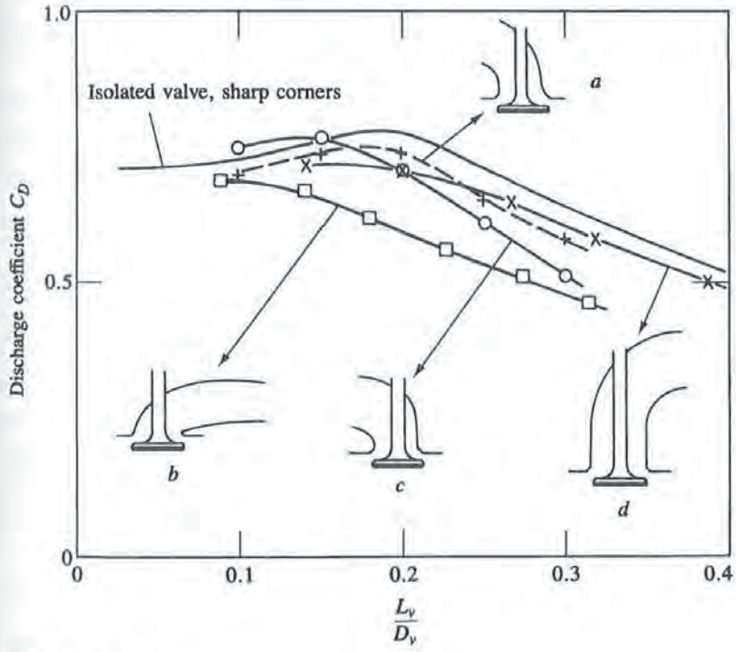


FIGURE 6-18
Discharge coefficient as function of valve lift for several exhaust valve and port designs.[16] *a*,[20] *b*,[15] *c*,[20] *d*.[21]

PETITIONER'S EXHIBIT 1002
US PATENT NO. 6,581,565

valves, however. Exhaust valves operate over a wide range of pressure ratios (1 to 5). For pressure ratios greater than about 2 the flow will be choked, but the effect of pressure ratio on discharge coefficient is small and confined to higher lifts (e.g., ± 5 percent at $L_v/D_v = 0.3$).[15]

6.4 RESIDUAL GAS FRACTION

The residual gas fraction in the cylinder during compression is determined by the exhaust and inlet processes. Its magnitude affects volumetric efficiency and engine performance directly, and efficiency and emissions through its effect on working-fluid thermodynamic properties. The residual gas fraction is primarily a function of inlet and exhaust pressures, speed, compression ratio, valve timing, and exhaust system dynamics.

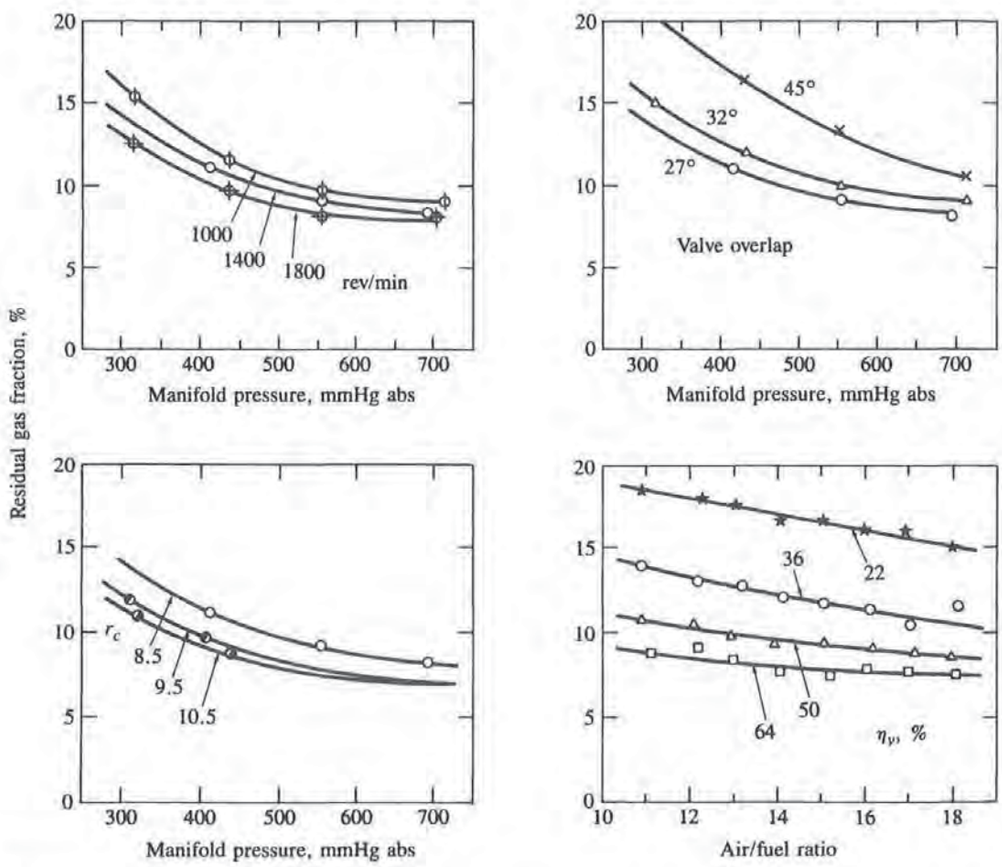


FIGURE 6-19
Residual gas fraction for 2-dm^3 four-cylinder spark-ignition engine as a function of intake manifold pressure for a range of speeds, compression ratios, and valve overlaps: also as a function of air/fuel ratio for a range of volumetric efficiencies. Operating conditions, unless noted: speed = 1400 rev/min, $A/F = 14.5$, spark timing set to give 0.95 maximum torque, compression ratio = 8.5.[22]

PETITIONER'S EXHIBIT 1002
US PATENT NO. 6,581,565

The residual gas mass fraction x_r (or burned gas fraction if EGR is used) is usually determined by measuring the CO_2 concentration in a sample of gas extracted from the cylinder during the compression stroke. Then

$$x_r = \frac{(\tilde{x}_{CO_2})_C}{(\tilde{x}_{CO_2})_e} \tag{6.17}$$

where the subscripts C and e denote compression and exhaust, and $\tilde{x}_{CO_2}$ are mole fractions in the wet gas. Usually CO_2 volume or mole fractions are measured in dry gas streams (see Sec. 4.9). A correction factor K,

$$K = \frac{(\tilde{x}_i)_{wet}}{(\tilde{x}_i)_{dry}} = \frac{1}{1 + 0.5[\, y(\tilde{x}^*_{CO_2} + x^*_{CO}) - 0.74\tilde{x}^*_{CO}]} \tag{6.18}$$

where y is the molar hydrogen/carbon ratio of the fuel and $\tilde{x}^*_{CO_2}$, $\tilde{x}^*_{CO}$ are dry mole fractions, can be used to convert the dry mole fraction measurements.

Residual gas measurements in a spark-ignition engine are given in Fig. 6-19, which shows the effect of changes in speed, valve overlap, compression ratio, and air/fuel ratio for a range of inlet manifold pressures for a 2-dm^3, 88.5-mm bore, four-cylinder engine.[22] The effect of variations in spark timing was negligible. Inlet pressure, speed, and valve overlap are the most important variables, though the exhaust pressure also affects the residual fraction.[23] Normal settings for inlet valve opening (about 15° before TC) and exhaust valve closing (about 12° after TC) provide sufficient overlap for good scavenging, but avoid excessive backflow from the exhaust port into the cylinder.

Residual gas fractions in diesel engines are substantially lower than in SI engines because inlet and exhaust pressures are comparable in magnitude and the compression ratio is 2 to 3 times as large. Also, a substantial fraction of the residual gas is air.

6.5 EXHAUST GAS FLOW RATE AND TEMPERATURE VARIATION

The exhaust gas mass flow rate and the properties of the exhaust gas vary significantly during the exhaust process. The origin of this variation for an ideal exhaust process is evident from Fig. 5-3. The thermodynamic state (pressure, temperature, etc.) of the gas in the cylinder varies continually during the exhaust blowdown phase, until the cylinder pressure closely approaches the exhaust manifold pressure. In the real exhaust process, the exhaust valve restricts the flow out of the cylinder, the valve lift varies with time, and the cylinder volume changes during the blowdown process, but the principles remain the same.

Measurements have been made of the variation in mass flow rate through the exhaust valve and gas temperature at the exhaust port exit during the exhaust process of a spark-ignition engine.[24] Figure 6-20 shows the instantaneous mass flow rate data at three different engine speeds. The blowdown and displacement

PETITIONER'S EXHIBIT 1002
US PATENT NO. 6,581,565

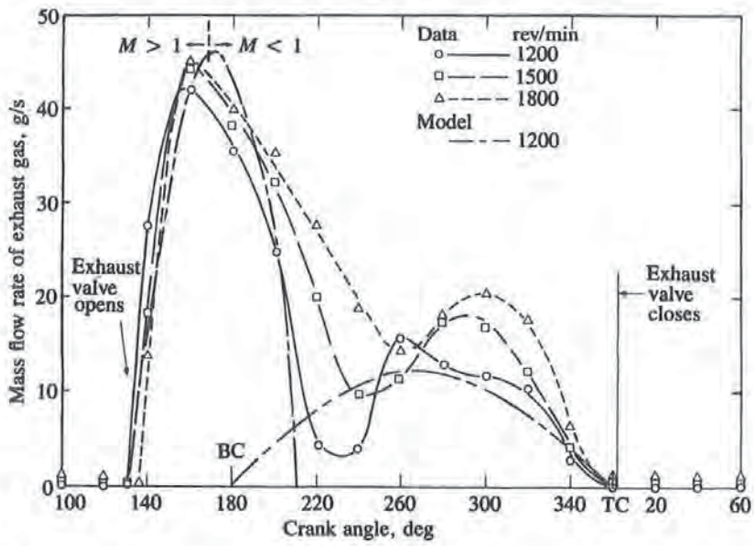


FIGURE 6-20
Instantaneous mass flow rate of exhaust gas through the valve versus crank angle: equivalence ratio = 1.2, wide-open throttle, compression ratio = 7. Dash-dot line is one-dimensional compressible flow model for blowdown and incompressible displacement model for exhaust stroke.[24]

phases of the exhaust process are evident. Simple quasi-steady models of these phases give good agreement with the data at lower engine speeds. The blowdown model shown applies orifice flow equations to the flow across the exhaust valve using the measured cylinder pressure and estimated gas temperature for upstream stagnation conditions. Equation (C.9) is used when the pressure ratio across the valve exceeds the critical value. Equation (C.8) is used when the pressure ratio is less than the critical value. The displacement model assumes the gas in the cylinder is incompressible as the piston moves through the exhaust stroke. As engine speed increases, the crank angle duration of the blowdown phase increases. There is evidence of dynamic effects occurring at the transition between the two phases. The peak mass flow rate during blowdown does not vary substantially with speed since the flow is choked. The mass flow rate at the time of maximum piston speed during displacement scales approximately with piston speed. As the inlet manifold pressure is reduced below the wide-open throttle value, the proportion of the charge which exits the cylinder during the blowdown phase decreases but the mass flow rate during displacement remains essentially constant.

The exhaust gas temperature varies substantially through the exhaust process, and decreases due to heat loss as the gas flows past the exhaust valve and through the exhaust system.

Figure 6-21 shows the measured cylinder pressure, calculated cylinder gas temperature and exhaust mass flow rate, and measured gas temperature at the exhaust port exit for a single-cylinder spark-ignition engine at mid-load and low speed.[25] The average cylinder-gas temperature falls rapidly during blowdown, and continues to fall during the exhaust stroke due to heat transfer to the cylin-

PETITIONER'S EXHIBIT 1002
US PATENT NO. 6,581,565

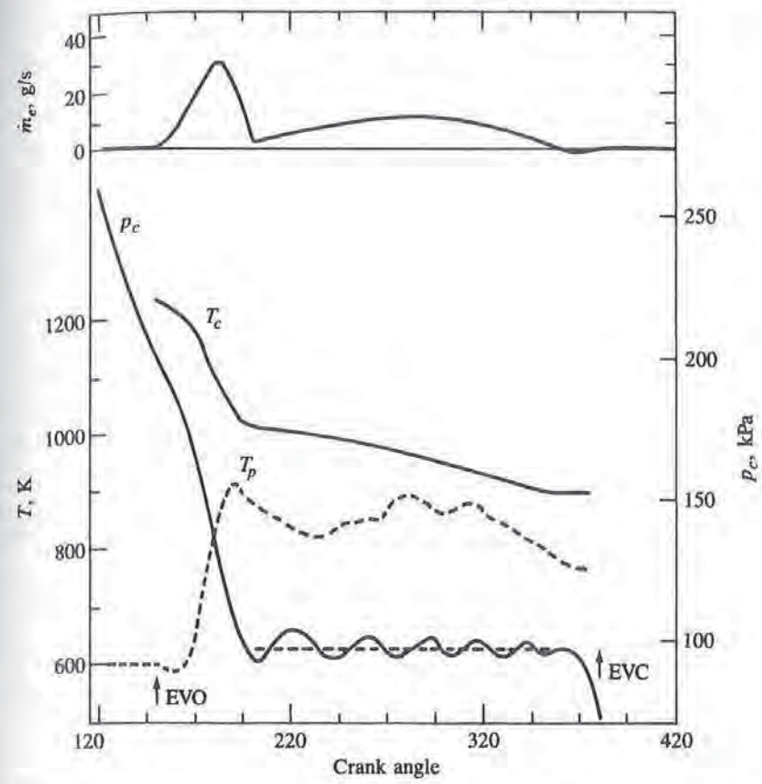


FIGURE 6-21
Measured cylinder pressure p_c, calculated cylinder-gas temperature T_c, exhaust mass flow rate $\dot{m}_e$, and measured gas temperature at exhaust port exit T_p, for single-cylinder spark-ignition engine. Speed = 1000 rev/min, imep = 414 kPa, equivalence ratio = 1.2, spark timing = 10° BTC, r_c = 7.2.[25]

der walls. The gas temperature at the port exit at the start of the exhaust flow pulse is a mixture of hotter gas which has just left the cylinder and cooler gas which left the cylinder at the end of the previous exhaust process and has been stationary in the exhaust port while the valve has been closed. The port exit temperature has a minimum where the transition from blowdown flow to displacement occurs, and the gas comes momentarily to rest and loses a substantial fraction of its thermal energy to the exhaust port walls.

Figure 6-22 shows the effect of varying load and speed on exhaust port exit temperatures. Increasing load ($A \rightarrow B \rightarrow C$) increases the mass and temperature in the blowdown pulse. Increasing speed ($B \rightarrow D$) raises the gas temperature throughout the exhaust process. These effects are the result of variations in the relative importance of heat transfer in the cylinder and heat transfer to the exhaust valve and port. The time available for heat transfer, which depends on engine speed and exhaust gas flow rate, is the most critical factor. The exhaust temperature variation with equivalence ratio follows from the variation in expansion stroke temperatures, with maximum values at $\phi = 1.0$ and lower values for leaner and richer mixtures.[24] Diesel engine exhaust temperatures are significantly

PETITIONER'S EXHIBIT 1002
US PATENT NO. 6,581,565

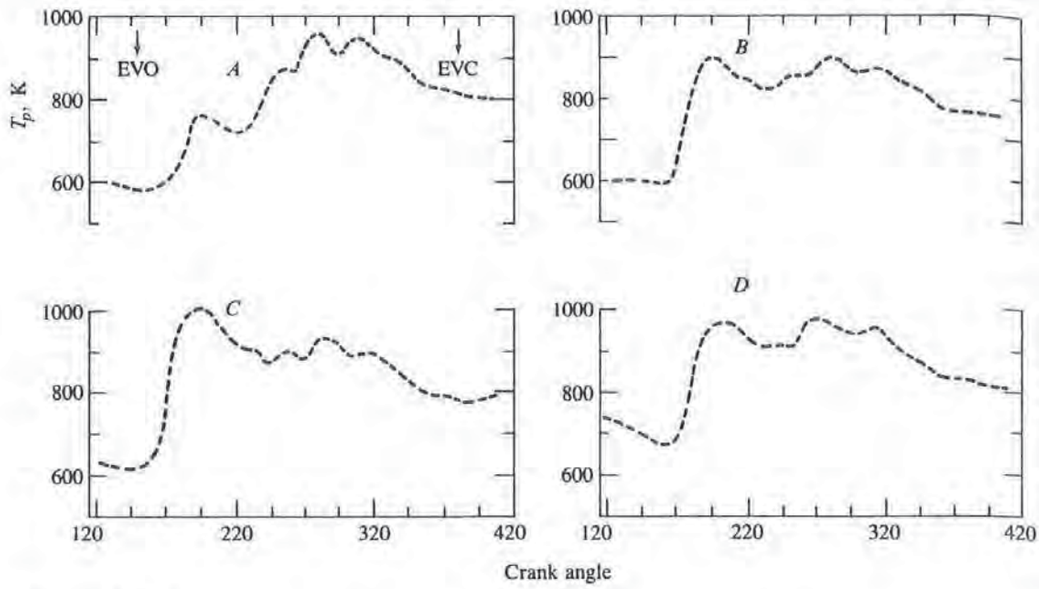


FIGURE 6-22
Measured gas temperature at exhaust port exit as a function of crank angle, single-cylinder spark-ignition engine, for different loads and speeds. Curve A: imep = 267 kPa, 1000 rev/min; curve B: imep = 414 kPa, 1000 rev/min; curve C: imep = 621 kPa, 1000 rev/min; curve D: imep = 414 kPa, 1600 rev/min. Equivalence ratio = 1.2, spark timing = 10° BTC, compression ratio = 7.2.[25]

lower than spark-ignition engine exhaust temperatures because of the lean operating equivalence ratio and their higher expansion ratio during the power stroke.

The average exhaust gas temperature is an important quantity for determining the performance of turbochargers, catalytic converters, and particulate traps. The time-averaged exhaust temperature does not correspond to the average energy of the exhaust gas because the flow rate varies substantially. An enthalpy-averaged temperature

$$\bar{T}_h = \left(\int_{\text{EVO}}^{\text{EVC}} \dot{m} c_p T_g \, d\theta \right) \Big/ \left(\int_{\text{EVO}}^{\text{EVC}} \dot{m} c_p \, d\theta \right) \tag{6.19}$$

is the best indicator of exhaust thermal energy. Average exhaust gas temperatures are usually measured with a thermocouple. Thermocouple-averaged temperatures are close to time-averaged temperatures. Mass-averaged exhaust temperatures (which are close to $\bar{T}_h$ if c_p variations are small) for a spark-ignition engine at the exhaust port exit are about 100 K higher than time-averaged or thermocouple-determined temperatures. Mass-average temperatures in the cylinder during the exhaust process are about 200 to 300 K higher than mass-averaged port temperatures. All these temperatures increase with increasing speed, load, and spark retard, with speed being the variable with the largest impact.[26]

PETITIONER'S EXHIBIT 1002
US PATENT NO. 6,581,565

6.6 SCAVENGING IN TWO-STROKE CYCLE ENGINES

6.6.1 Two-Stroke Engine Configurations

In two-stroke cycle engines, each outward stroke of the piston is a power stroke. To achieve this operating cycle, the fresh charge must be supplied to the engine cylinder at a high-enough pressure to displace the burned gases from the previous cycle. Raising the pressure of the intake mixture is done in a separate pump or blower or compressor. The operation of clearing the cylinder of burned gases and filling it with fresh mixture (or air)—the combined intake and exhaust process—is called *scavenging*. However, air capacity is just as important as in the four-stroke cycle; usually, a greater air mass flow rate must be achieved to obtain the same output power. Figures 1-12, and 1-5 and 1-24 show sectioned drawings of a two-stroke spark-ignition engine and two two-stroke diesels.

The different categories of two-stroke cycle scavenging flows and the port (and valve) arrangements that produce them are illustrated in Figs. 6-23 and 6-24. Scavenging arrangements are classified into: (*a*) *cross-scavenged*, (*b*) *loop-scavenged*, and (*c*) *uniflow-scavenged configurations*. The location and orientation of the scavenging ports control the scavenging process, and the most common arrangements are indicated. Cross- and loop-scavenging systems use exhaust and inlet ports in the cylinder wall, uncovered by the piston as it approaches BC.[27] The uniflow system may use inlet ports with exhaust valves in the cylinder head,

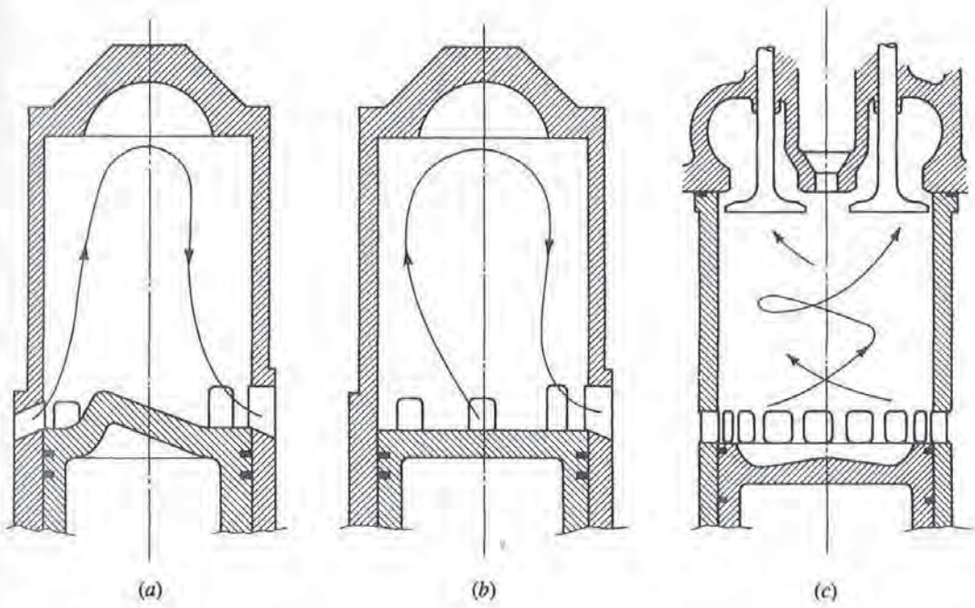


FIGURE 6-23
(*a*) Cross-scavenged, (*b*) loop-scavenged, and (*c*) uniflow-scavenged two-stroke cycle flow configurations.

PETITIONER'S EXHIBIT 1002
US PATENT NO. 6,581,565

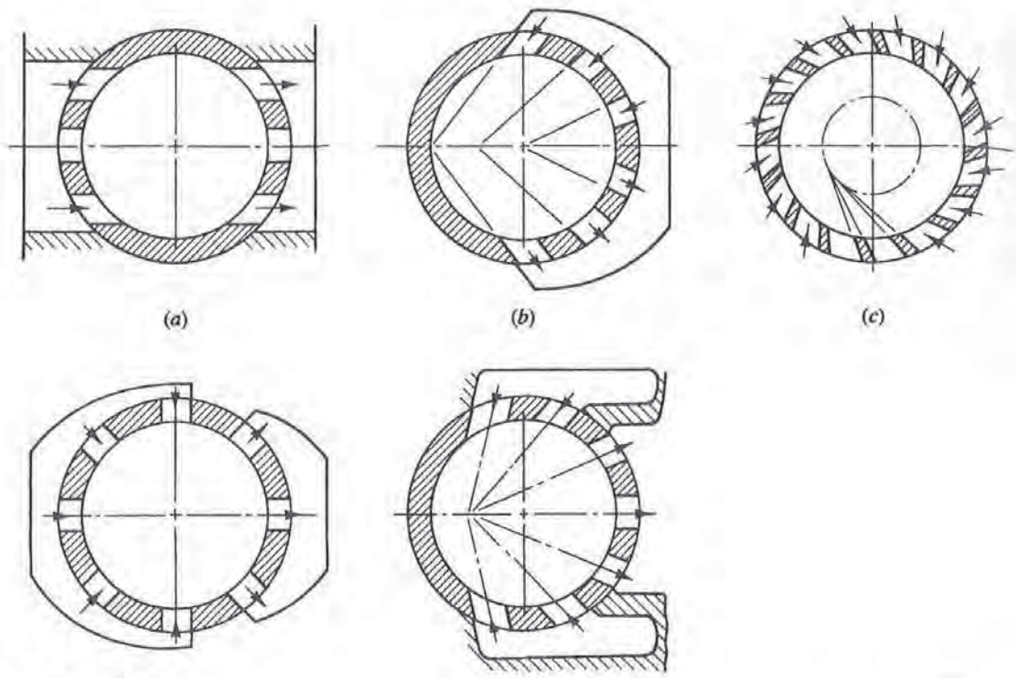


FIGURE 6-24
Common porting arrangements that go with (*a*) cross-scavenged, (*b*) loop-scavenged, and (*c*) uniflow-scavenged configurations.

or inlet and exhaust ports with opposed pistons. Despite the different flow patterns obtained with each cylinder geometry, the general operating principles are similar. Air in a diesel, or fuel-air mixture in a spark-ignition engine, must be supplied to the inlet ports at a pressure higher than the exhaust system pressure.

Figure 6-25 illustrates the principles of the scavenging process for a uniflow engine design. Between 100 and 110° after TC, the exhaust valve opens and a blowdown discharge process commences. Initially, the pressure ratio across the exhaust valve exceeds the critical value (see App. C) and the flow at the valve will be sonic: as the cylinder pressure decreases, the pressure ratio drops below the critical value. The discharge period up to the time of the scavenging port opening is called the blowdown (or free exhaust) period. The scavenging ports open between 60 and 40° before BC when the cylinder pressure slightly exceeds the scavenging pump pressure. Because the burned gas flow is toward the exhaust valves, which now have a large open area, the exhaust flow continues and no backflow occurs. When the cylinder pressure falls below the inlet pressure, air enters the cylinder and the scavenging process starts. This flow continues as long as the inlet ports are open and the inlet total pressure exceeds the pressure in the cylinder. As the cylinder pressure rises above the exhaust pressure, the fresh charge flowing into the cylinder displaces the burned gases: a part of the fresh charge mixes with the burned gases and is expelled with them. The exhaust valves usually close after the inlet ports close. Since the flow in the cylinder is toward the exhaust valve, additional scavenging is obtained. Figure 1-16 illustrates the

PETITIONER'S EXHIBIT 1002
US PATENT NO. 6,581,565

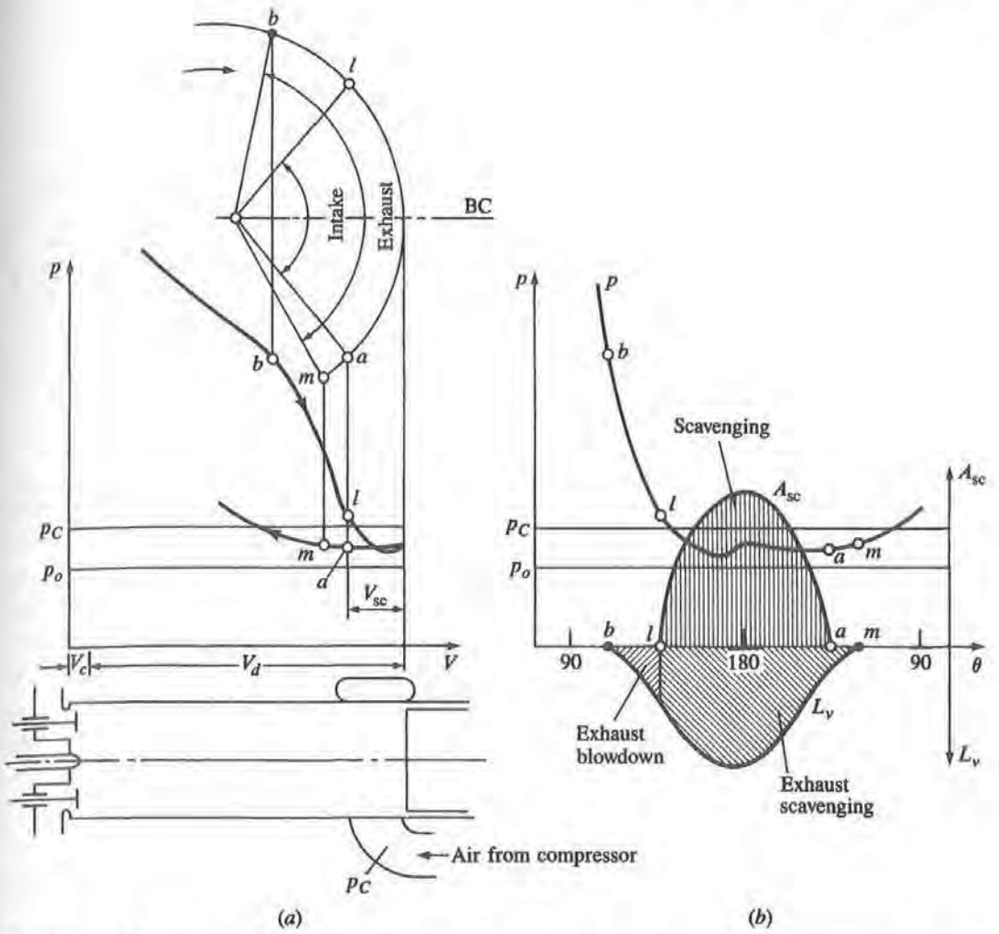


FIGURE 6-25
Gas exchange process in two-stroke cycle uniflow-scavenged diesel engine: (*a*) valve and port timing and pressure-volume diagram; (*b*) pressure, scavenging port open area A_{sc}, and exhaust valve lift L_v as functions of crank angle.[1]

similar sequence of events for a loop-scavenged engine. Proper flow patterns for the fresh charge are extremely important for good scavenging and charging of the cylinder.

Common methods for supercharging or pressurizing the fresh charge are shown in Fig. 6-26. In large two-stroke cycle engines, more complex combinations of these approaches are often used, as shown in Fig. 1-24.

6.6.2 Scavenging Parameters and Models

The following overall parameters are used to describe the scavenging process.[13]

The *delivery ratio* Λ:

$$\Lambda = \frac{\text{mass of delivered air (or mixture) per cycle}}{\text{reference mass}} \tag{6.20}$$

PETITIONER'S EXHIBIT 1002
US PATENT NO. 6,581,565

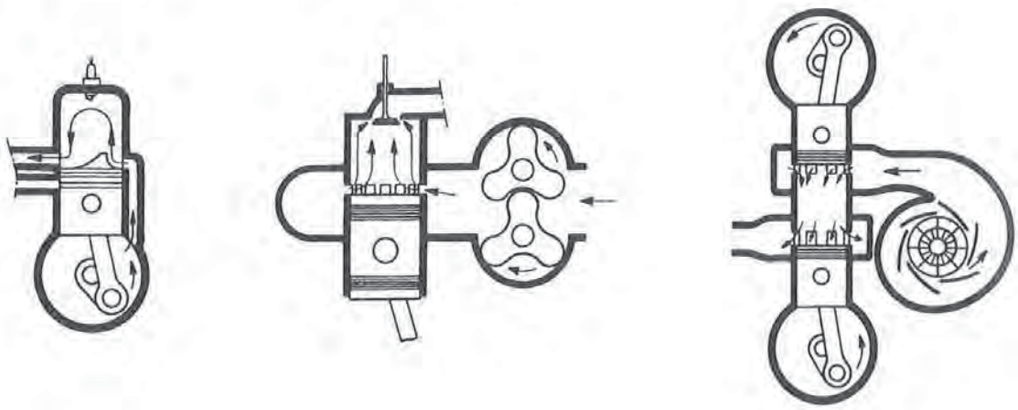


FIGURE 6-26
Common methods of pressurizing the fresh charge in two-stroke cycle engines: left, crankcase compression; center, roots blower; right, centrifugal compressor.[7]

compares the actual scavenging air mass (or mixture mass) to that required in an ideal charging process.† The reference mass is defined as displaced volume × ambient air (or mixture) density. Ambient air (or mixture) density is determined at atmospheric conditions or at intake conditions. This definition is useful for experimental purposes. For analytical work, it is often convenient to use the trapped cylinder mass m_{tr} as the reference mass.

The *trapping efficiency* η_{tr}:

$$\eta_{tr} = \frac{\text{mass of delivered air (or mixture) retained}}{\text{mass of delivered air (or mixture)}} \tag{6.21}$$

indicates what fraction of the air (or mixture) supplied to the cylinder is retained in the cylinder.

The *scavenging efficiency* η_{sc}:

$$\eta_{sc} = \frac{\text{mass of delivered air (or mixture) retained}}{\text{mass of trapped cylinder charge}} \tag{6.22}$$

indicates to what extent the residual gases in the cylinder have been replaced with fresh air.

The *purity* of the charge:

$$\text{Purity} = \frac{\text{mass of air in trapped cylinder charge}}{\text{mass of trapped cylinder charge}} \tag{6.23}$$

indicates the degree of dilution, with burned gases, of the unburned mixture in the cylinder.

† If scavenging is done with fuel-air mixture, as in spark-ignition engines, then mixture mass is used instead of air mass.

PETITIONER'S EXHIBIT 1002
US PATENT NO. 6,581,565

The *charging efficiency* η_{ch}:

$$\eta_{ch} = \frac{\text{mass of delivered air (or mixture) retained}}{\text{displaced volume} \times \text{ambient density}} \tag{6.24}$$

indicates how effectively the cylinder volume has been filled with fresh air (or mixture). Charging efficiency, trapping efficiency, and delivery ratio are related by

$$\eta_{ch} = \Lambda \eta_{tr} \tag{6.25}$$

When the reference mass in the definition of delivery ratio is the trapped cylinder mass m_{tr} (or closely approximated by it) then

$$\eta_{sc} = \Lambda \eta_{tr} \tag{6.26}$$

In real scavenging processes, mixing occurs as the fresh charge displaces the burned gases and some of the fresh charge may be expelled. Two limiting ideal models of this process are: (1) perfect displacement and (2) complete mixing. Perfect displacement or scavenging would occur if the burned gases were pushed out by the fresh gases without any mixing. Complete mixing occurs if entering fresh mixture mixes instantaneously and uniformly with the cylinder contents.

For *perfect displacement* (with m_{tr} as the reference mass in the delivery ratio),

$$\begin{aligned} \eta_{sc} &= \Lambda \quad \text{and} \quad \eta_{tr} = 1 \quad \text{for } \Lambda \leqslant 1 \\ \eta_{sc} &= 1 \quad \text{and} \quad \eta_{tr} = \Lambda^{-1} \quad \text{for } \Lambda > 1 \end{aligned} \tag{6.27}$$

For the *complete mixing* limit, consider the scavenging process as a quasi-steady flow process. Between time t and $t + dt$, a mass element dm_{ad} of air is delivered to the cylinder and is uniformly mixed throughout the cylinder volume. An equal amount of fluid, with the same proportions of air and burned gas as the cylinder contents at time t, leaves the cylinder during this time interval. Thus the mass of air delivered between t and $t + dt$ which is retained, dm_{ar}, is given by

$$dm_{ar} = dm_{ad}\left(1 - \frac{m_{ar}}{m_{tr}}\right)$$

Assuming m_{tr} is constant, this integrates over the duration of the scavenging process to give

$$\frac{m_{ar}}{m_{tr}} = 1 - \exp\left(\frac{m_{ad}}{m_{tr}}\right) \tag{6.28}$$

Thus, for *complete mixing*, with the above definitions,

$$\begin{aligned} \eta_{sc} &= 1 - e^{-\Lambda} \\ \eta_{tr} &= \frac{1}{\Lambda}(1 - e^{-\Lambda}) \end{aligned} \tag{6.29}$$

Figure 6-27 shows η_{sc} and η_{tr} for the perfect displacement and complete mixing assumptions as a function of Λ, the delivery ratio.

PETITIONER'S EXHIBIT 1002
US PATENT NO. 6,581,565

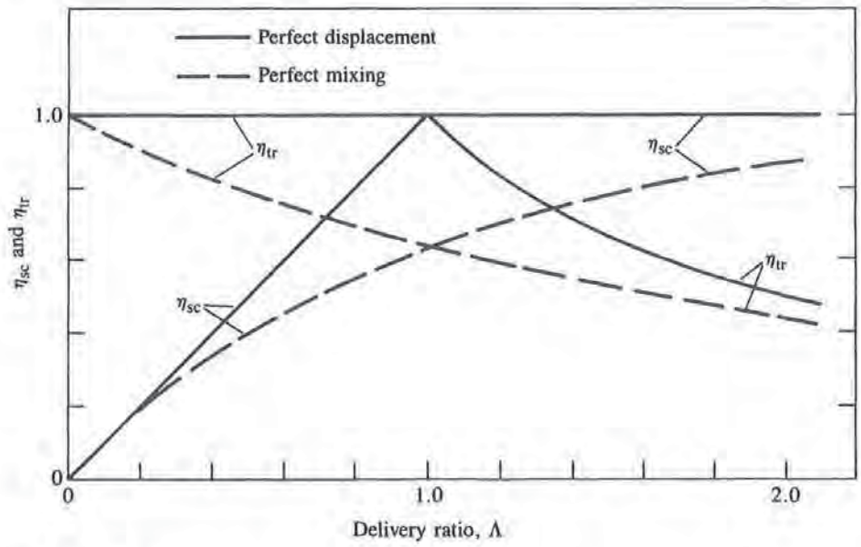


FIGURE 6-27
Scavenging efficiency η_{sc} and trapping efficiency η_{tr} versus delivery ratio Λ for perfect displacement and complete mixing models.

An additional possibility is the direct flow of fresh mixture through the cylinder into the exhaust without entraining burned gases. This is called *short-circuiting*; it is obviously undesirable since some fresh air or mixture is wasted. There is no simple model for this process. When short-circuiting occurs, lower scavenging efficiencies result even though the volume occupied by the short-circuiting flow through the cylinder does displace an equal volume of the burned gases. Another phenomenon which reduces scavenging efficiency is the formation of *pockets* or *dead zones* in the cylinder volume where burned gases can become trapped and escape displacement or entrainment by the fresh scavenging flow. These unscavenged zones are most likely to occur in regions of the cylinder that remain secluded from the main fresh mixture flow path.

6.6.3 Actual Scavenging Processes

Several methods have been developed for determining what occurs in actual cylinder scavenging processes.[27] Accurate measurement of scavenging efficiency is difficult due to the problem of measuring the trapped air mass. Estimation of η_{sc} from indicated mean effective pressure and from gas sampling are the most reliable methods.[7] Flow visualization experiments[28–30] in liquid analogs of the cylinder and flow velocity mapping techniques[31] have proved useful in providing a qualitative picture of the scavenging flow field and identifying problems such as short-circuiting and dead volumes.

Flow visualization studies indicate the key features of the scavenging process. Figure 6-28 shows a sequence of frames from a movie of one liquid scavenging another in a model of a large two-stroke cycle loop-scavenged

PETITIONER'S EXHIBIT 1002
US PATENT NO. 6,581,565

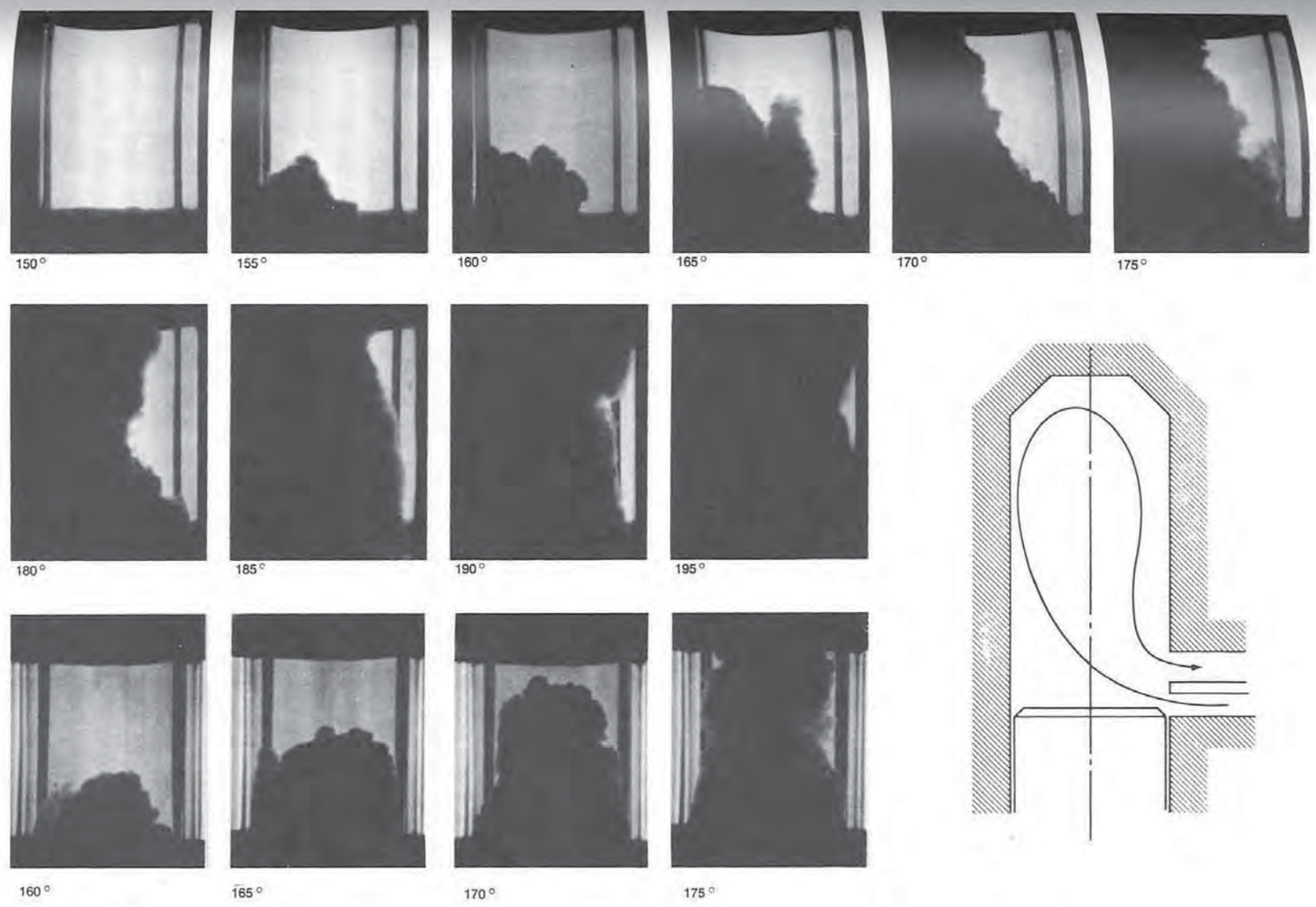


FIGURE 6-28
Photos of one fluid scavenging another in liquid analog experiments in model loop-scavenged engine cylinder. Top two rows: View perpendicular to scavenging loop. Bottom row: Orthogonal views. Dark denser fluid displacing light less dense fluid.[29]

PETITIONER'S EXHIBIT 1002
US PATENT NO. 6,581,565

diesel.[29] The physical variables were scaled to maintain the same values of the appropriate dimensionless numbers for the liquid analog flow and the real engine flow. The density of the liquid representing air (which is dark) was twice the density of the liquid representing burned gas (which is clear). Early in the scavenging process, the fresh air jets penetrate into the burned gas and displace it first toward the cylinder head and then toward the exhaust ports (the schematic gives the location of the ports). During this initial phase, the outflowing gas contains no air; pure displacement of the burned gas from the cylinder is being achieved. Then short-circuiting losses start to occur, due to the damming-up or buildup of fresh air on the cylinder wall opposite the exhaust ports. The short-circuiting fluid flows directly between the scavenge ports and the exhaust ports above them. Since this damming-up of the inflowing fresh air back toward the exhaust ports continues, short-circuiting losses will also continue. While the scavenging front remains distinct as it traverses the cylinder, its turbulent character indicates that mixing between burned gas and air across the front is taking place. For both these reasons (short-circuiting and short-range mixing), the outflowing gas, once the "displacement" phase is over, contains an increasing amount of fresh air.

Outflowing fluid composition measurements from this model study of a Sulzer two-stroke loop-scavenged diesel engine confirm this sequence of events. At 24 crank angle degrees after the onset of scavenging, fresh air due to short-circuiting was detected in the exhaust. At the time the displacement front reached the exhaust port (65° after the onset of scavenging), loss of fresh air due to scavenging amounted to 13 percent of the scavenge air flow. The actual plot of degree of purity (or η_{sc}) versus delivery ratio (Λ) closely followed the perfect displacement line for $\Lambda < 0.4$. For $\Lambda > 0.4$, the shape of the actual curve was similar in shape to the complete mixing curve.

Engine tests confirm these results from model studies. Initially, the exhausted gas contains no fresh air or mixture; only burned gas is being displaced from the cylinder. However, within the cylinder both displacement *and* mixing at the interface between burned gas and fresh gas are occurring. The departure from perfect scavenging behavior is evident when fresh mixture first appears in the exhaust. For loop-scavenged engines this is typically when $\Lambda \approx 0.4$. For uniflow scavenging this perfect scavenging phase lasts somewhat longer; for cross-scavenging it is over sooner (because the short-circuiting path is shorter).

The mixing that occurs is short-range mixing, not mixing throughout the cylinder volume. The jets of scavenging mixture, on entering the cylinder, mix readily with gases in the immediate neighborhood of the jet efflux. More efficient scavenging—i.e., less mixing—is obtained by reducing the size of the inlet ports while increasing their number.[32] It is important that the jets from the inlet ports slow down significantly once they enter the cylinder. Otherwise the scavenging front will reach the exhaust ports or valves too early. The jets are frequently directed to impinge on each other or against the cylinder wall. Swirl in uniflow-scavenged systems may be used to obtain an equivalent result.

The most desirable loop-scavenging flow is illustrated in Fig. 6-29. The

PETITIONER'S EXHIBIT 1002
US PATENT NO. 6,581,565

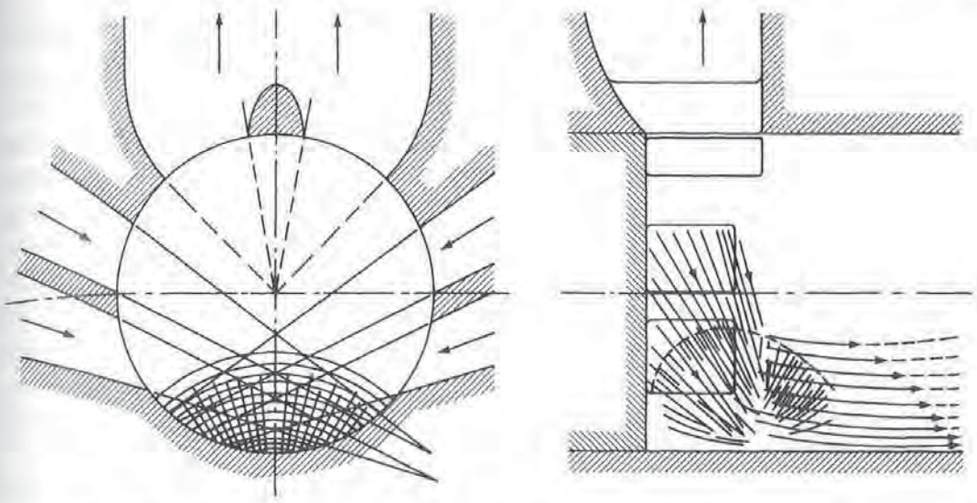


FIGURE 6-29
Desirable air flow in loop-scavenged engine: air from the entering jets impinges on far cylinder wall and flows toward the cylinder head.[31]

scavenging jets enter symmetrically with sufficient velocity to fill up about half the cylinder cross section, and thereafter flow at lower velocity along the cylinder wall toward the cylinder head. By proper direction of the scavenging jets it is possible to achieve almost no outflow in the direction of the exhaust from the cross-hatched stagnation zone on the opposite cylinder wall. In fact, measurement of the velocity profile in this region is a good indicator of the effectiveness of the scavenging flow. If the flow along the cylinder wall toward the head is stable, i.e., if its maximum velocity occurs near the wall and the velocity is near zero on the plane perpendicular to the axis of symmetry of the ports (which passes through the cylinder axis), the scavenging flow will follow the desired path. If there are "tongues" of scavenging flow toward the exhaust port, either in the center of the cylinder or along the walls, then significant short-circuiting will occur.[31]

In uniflow-scavenged configurations, the inlet ports are evenly spaced around the full circumference of the cylinder and are usually directed so that the scavenging jets create a swirling flow within the cylinder (see Fig. 6-24). Results of measurements of scavenging front location in rig flow tests of a valved uniflow two-stroke diesel cylinder, as the inlet port angle was varied to give a wide range of swirl, showed that inlet jets directed tangentially to a circle of half the cylinder radius gave the most stable scavenging front profile over a wide range of conditions.[33]

Though the scavenging processes in spark-ignition and diesel two-stroke engines are similar, these two types of engine operate with quite different delivery ratios. In mixture-scavenged spark-ignition engines, any significant expulsion of fresh fluid with the burned gas results in a significant loss of fuel and causes high hydrocarbon emissions as well as loss of the energy expended in pumping the

PETITIONER'S EXHIBIT 1002
US PATENT NO. 6,581,565

flow which passes straight through the cylinder. In diesels the scavenging medium is air, so only the pumping work is lost. One consequence of this is that two-stroke spark-ignition engines are usually crankcase pumped. This approach provides the maximum pressure and thus also the maximum velocity in the scavenging medium at the start of the scavenging process just after the cylinder pressure has blown down; as the crankcase pressure falls during the scavenging process, the motion of the scavenging front within the cylinder also slows down. Figure 6-30 shows the delivery ratio and trapping, charging, and scavenging efficiencies of two crankcase-scavenged spark-ignition engines as a function of engine speed. These quantities depend significantly on intake and exhaust port design and open period and the exhaust system configuration.[34–36] For two-stroke cycle spark-ignition engines, which use crankcase pumping, delivery ratios vary between about 0.5 and 0.8.

Figure 6-31 shows scavenging data typical of large two-stroke diesels.[37] The purity (mass of air in trapped cylinder charge/mass of trapped cylinder charge) is shown as a function of the delivery ratio. The different scavenging configurations have different degrees of effectiveness, with uniflow scavenging being the most efficient. These diesel engines normally operate with delivery ratios in the range 1.2 to 1.4.

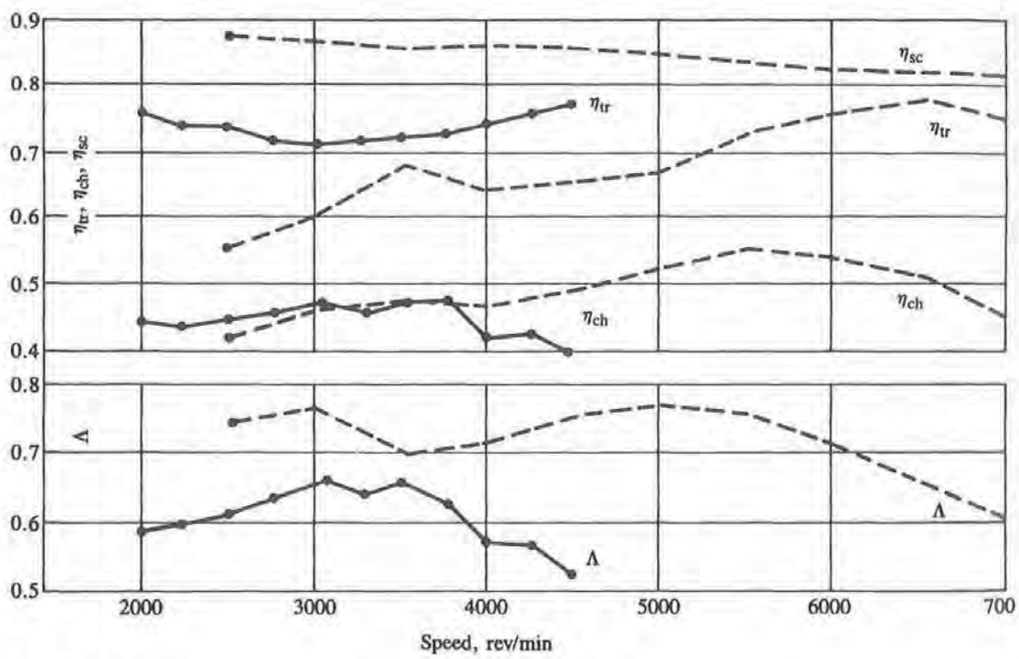


FIGURE 6-30
Delivery ratio Λ, trapping efficiency η_{tr}, charging efficiency η_{ch}, and scavenging efficiency η_{sc}, at full load, as functions of speed for two single-cylinder two-stroke cycle spark-ignition engines. Solid line is 147 cm^3 displacement engine.[34] Dashed line is loop-scavenged 246 cm^3 displacement engine.[35]

PETITIONER'S EXHIBIT 1002
US PATENT NO. 6,581,565

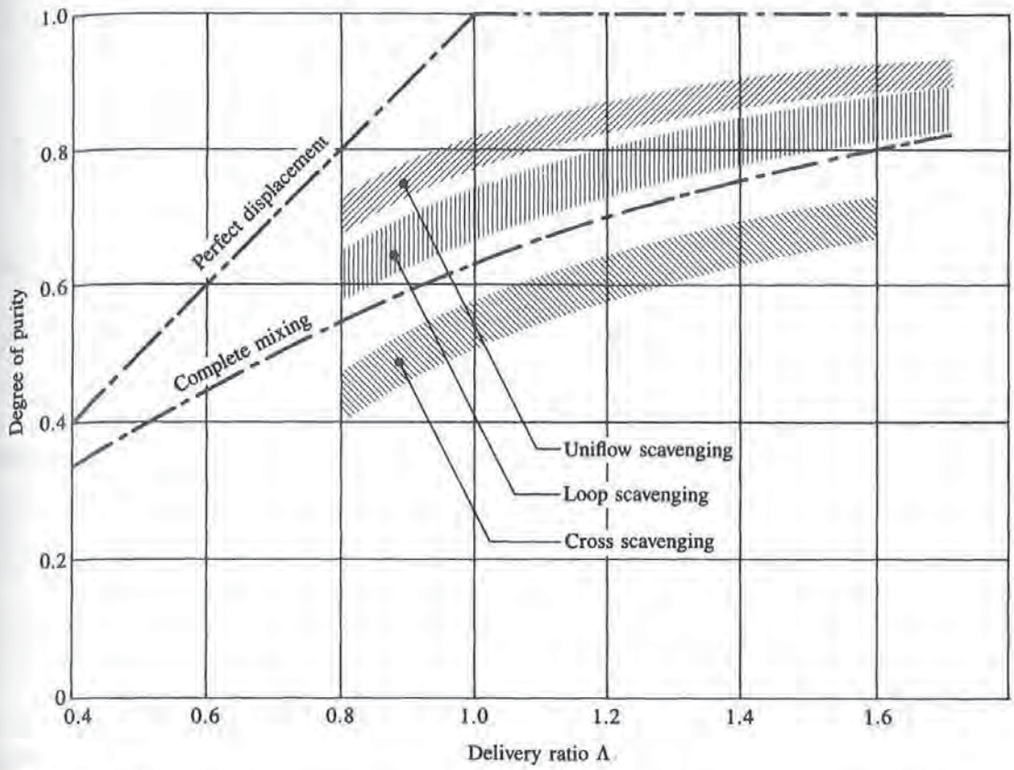


FIGURE 6-31
Purity as a function of delivery ratio Λ for different types of large marine two-stroke diesel engines.[37]

6.7 FLOW THROUGH PORTS

The importance of the intake and exhaust ports to the proper functioning of the two-stroke cycle scavenging process is clear from the discussion in Sec. 6.6. The crank angle at which the ports open, the size, number, geometry, and location of the ports around the cylinder circumference, and the direction and velocity of the jets issuing from the ports into the cylinder all affect the scavenging flow. A summary of the information available on flow through piston-controlled ports can be found in Annand and Roe.[16] Both the flow resistance of the inlet and exhaust port configurations, as well as the details of the flow pattern produced by the port system inside the cylinder during scavenging, are important. Figure 6-32 defines the essential geometrical characteristics of inlet ports. Rectangular ports make best use of the cylinder wall area and give precise timing control. Ports can be tapered, and may have axial and tangential inclination as shown.

Figure 6-33 illustrates the flow patterns expected downstream of piston-controlled inlet ports. For small openings, the flow remains attached to the port walls. For fully open ports with sharp corners the flow detaches at the upstream corners. Both a rounded entry and converging taper to the port help prevent flow detachment within the port. Discharge coefficients for ports have been measured as a function of the open fraction of the port, the pressure ratio across the port,

PETITIONER'S EXHIBIT 1002
US PATENT NO. 6,581,565

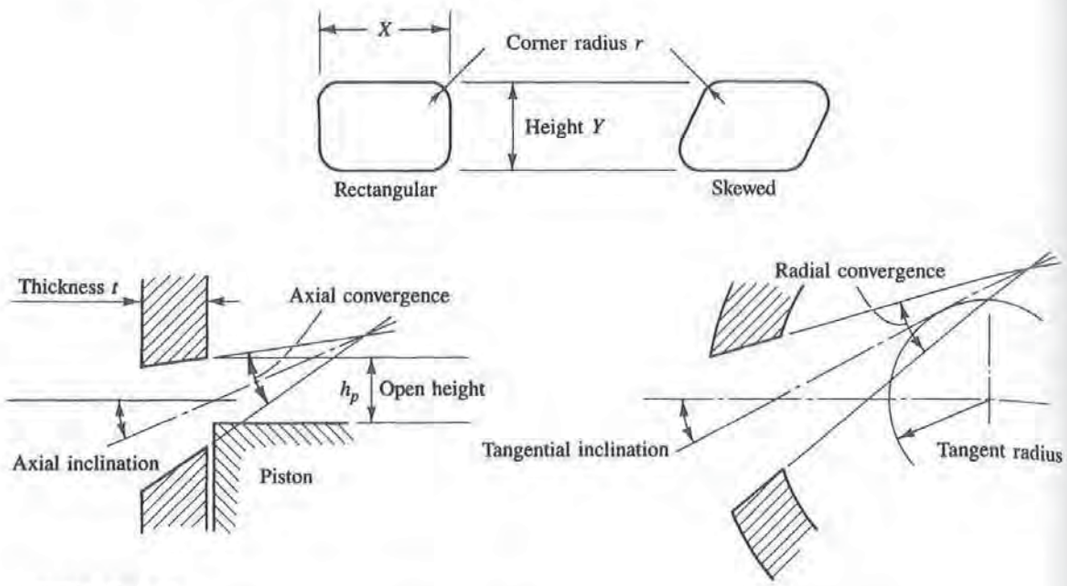


FIGURE 6-32
Parameters which define geometry of inlet ports.[16]

and port geometry and inclination (see Ref. 16 for a detailed summary). The most appropriate reference area for evaluating the discharge coefficient is the open area of the port (see Fig. 6-32). For the open height h_p less than $(Y - r)$ but greater than r this is

$$A_R = Xh_p - 0.43r^2 \tag{6.30}$$

where Y is the port height, X the port width, and r the corner radius. For $h_p = Y$, the reference area is

$$A_R = XY - 0.86r^2 \tag{6.31}$$

The effect of variations in geometry and operating conditions on the discharge coefficient C_D can usually be interpreted by reference to the flow patterns illustrated in Fig. 6-33. The effects of inlet port open fraction and port geometry on C_D are shown in Fig. 6-34: geometry effects are most significant at small and large open fractions.[20] C_D varies with pressure ratio, increasing as the pressure

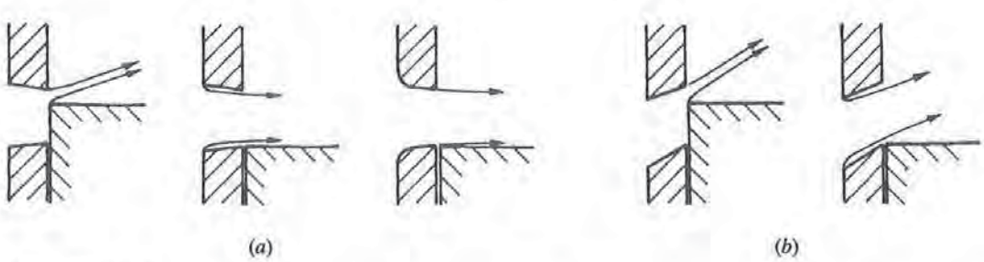


FIGURE 6-33
Flow pattern through piston-controlled inlet ports: (*a*) port axis perpendicular to wall; small opening and large opening with sharp and rounded entry; (*b*) port axis inclined.[16]

PETITIONER'S EXHIBIT 1002
US PATENT NO. 6,581,565

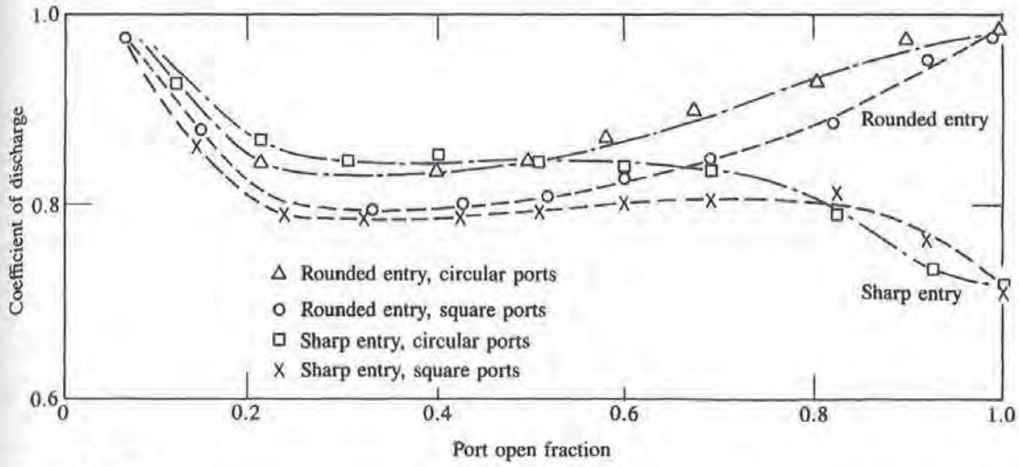


FIGURE 6-34
Discharge coefficients as a function of port open fraction (uncovered height/port height) for different inlet port designs. Pressure ratio across port = 2.35.[20]

ratio increases. Empirical relations that predict this variation with pressure ratio have been developed.[38]

Tangentially inclined inlet ports are used when swirl is desired to improve scavenging or when jet focusing or impingement within the cylinder off the cylinder axis is required (see Sec. 6.6.3). The discharge coefficient decreases as the jet tangential inclination increases. The jet angle and the port angle can deviate significantly from each other depending on the details of the port design and the open fraction.[31]

In piston-controlled exhaust ports, the angle of the jet from a thin-walled exhaust port increases as indicated in Fig. 6-35.[31] In thick ports, the walls are

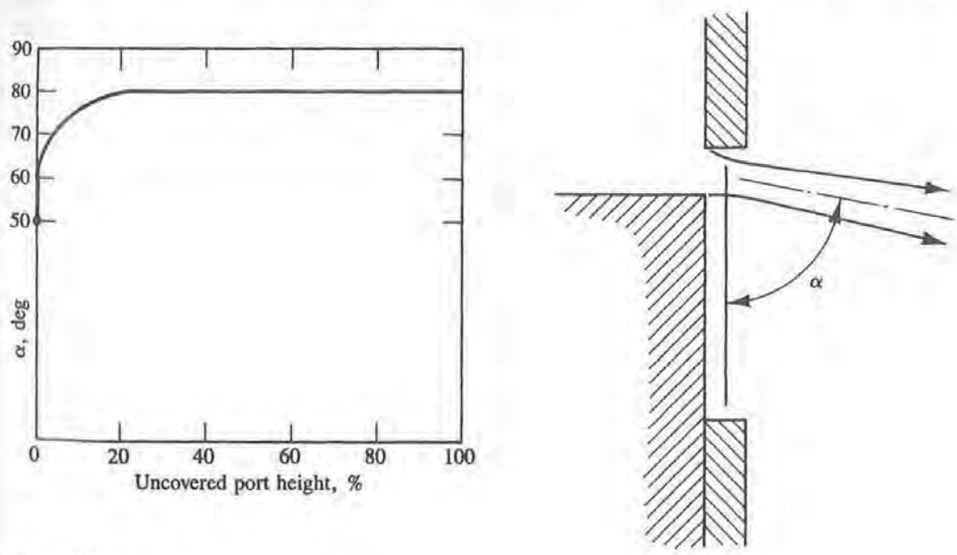


FIGURE 6-35
Angle of jet exiting exhaust port as a function of open port height.[31]

PETITIONER'S EXHIBIT 1002
US PATENT NO. 6,581,565

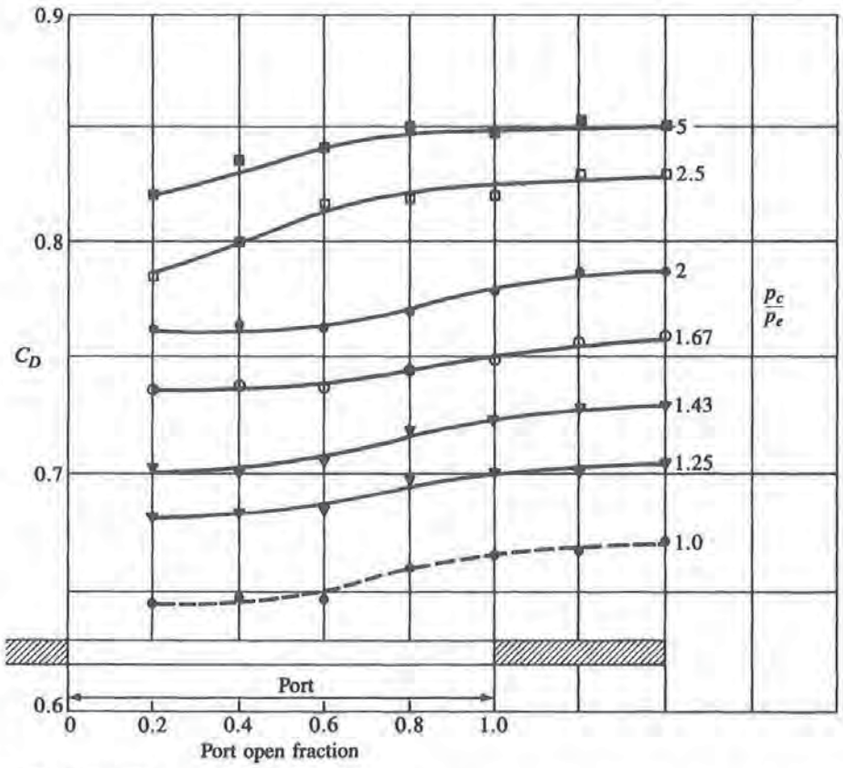


FIGURE 6-36
Discharge coefficient of a single rectangular exhaust port (7.6 mm wide × 12.7 mm high) in the wall of a 51-mm bore cylinder as a function of open fraction and pressure ratio. Steady-flow rig tests at 21°C. p_c = cylinder pressure, p_e = exhaust system pressure.[39]

usually tapered to allow the outward flow to diffuse. The pressure ratio across the exhaust ports varies substantially during the exhaust process. The pressure ratio has a significant effect on the exhaust port discharge coefficient, as shown in Fig. 6-36. The changes in exit jet angle and separation point explain the effects of increasing open fraction and pressure ratio. The discharge coefficient also increases modestly with increasing gas temperature.[39]

6.8 SUPERCHARGING AND TURBOCHARGING

6.8.1 Methods of Power Boosting

The maximum power a given engine can deliver is limited by the amount of fuel that can be burned efficiently inside the engine cylinder. This is limited by the amount of air that is introduced into each cylinder each cycle. If the inducted air is compressed to a higher density than ambient, prior to entry into the cylinder, the maximum power an engine of fixed dimensions can deliver will be increased. This is the primary purpose of supercharging; Eqs. (2.39) to (2.41) show how power, torque, and mean effective pressure are proportional to inlet air density.

PETITIONER'S EXHIBIT 1002
US PATENT NO. 6,581,565

The term *supercharging* refers to increasing the air (or mixture) density by increasing its pressure prior to entering the engine cylinder. Three basic methods are used to accomplish this. The first is *mechanical supercharging* where a separate pump or blower or compressor, usually driven by power taken from the engine, provides the compressed air. The second method is *turbocharging*, where a turbocharger—a compressor and turbine on a single shaft—is used to boost the inlet air (or mixture) density. Energy available in the engine's exhaust stream is used to drive the turbocharger turbine which drives the turbocharger compressor which raises the inlet fluid density prior to entry to each engine cylinder. The third method—*pressure wave supercharging*—uses wave action in the intake and exhaust systems to compress the intake mixture. The use of intake and exhaust manifold tuning to increase volumetric efficiency (see Sec. 6.2.2) is one example of this method of increasing air density. An example of a pressure wave supercharging device is the Comprex, which uses the pressure available in the exhaust gas stream to compress the inlet mixture stream by direct contact of the fluids in narrow flow channels (see Sec. 6.8.5). Figure 6-37 shows typical arrangements of the different supercharging and turbocharging systems. The most common arrangements use a mechanical supercharger (Fig. 6-37*a*) or turbocharger (Fig. 6-37*b*). Combinations of an engine-driven compressor and a turbocharger (Fig. 6-37*c*) are used (e.g., in large marine engines; Fig. 1-24). Two-stage turbocharging (Fig. 6-37*d*) is one viable approach for providing very high boost pressures (4 to 7 atm) to obtain higher engine brake mean effective pressures. Turbocompounding, i.e., use of a second turbine in the exhaust directly geared to the engine drive shaft (Fig. 6-37*e*), is an alternative method of increasing engine power (and efficiency). Charge cooling with a heat exchanger (often called an aftercooler or intercooler) after compression, prior to entry to the cylinder, can be used to increase further the air or mixture density as shown in Fig. 6-37*f*.

Supercharging is used in four-stroke cycle engines to boost the power per unit displaced volume. Some form of supercharging is necessary in two-stroke cycle engines to raise the fresh air (or mixture) pressure above the exhaust pressure so that the cylinder can be scavenged effectively. With additional boost in two-stroke cycle engines, the power density is also raised. This section reviews the operating characteristics of the blowers, compressors, turbines, and wave-compression devices used to increase inlet air or mixture density or convert exhaust-gas availability to work. The operating characteristics of supercharged and turbocharged engine systems are discussed in Chap. 15.

6.8.2 Basic Relationships

Expressions for the work required to drive a blower or compressor and the work produced by a turbine are obtained from the first and second laws of thermodynamics. The first law, in the form of the steady flow energy equation, applied to a control volume around the turbomachinery component is

$$\dot{Q} - \dot{W} = \dot{m}\left[\left(h + \frac{C^2}{2} + gz\right)_{\text{out}} - \left(h + \frac{C^2}{2} + gz\right)_{\text{in}}\right] \tag{6.32}$$

VW EX1014 (Part 2 of 4)
U.S. Patent No. 6,581,565

PETITIONER'S EXHIBIT 1002
US PATENT NO. 6,581,565

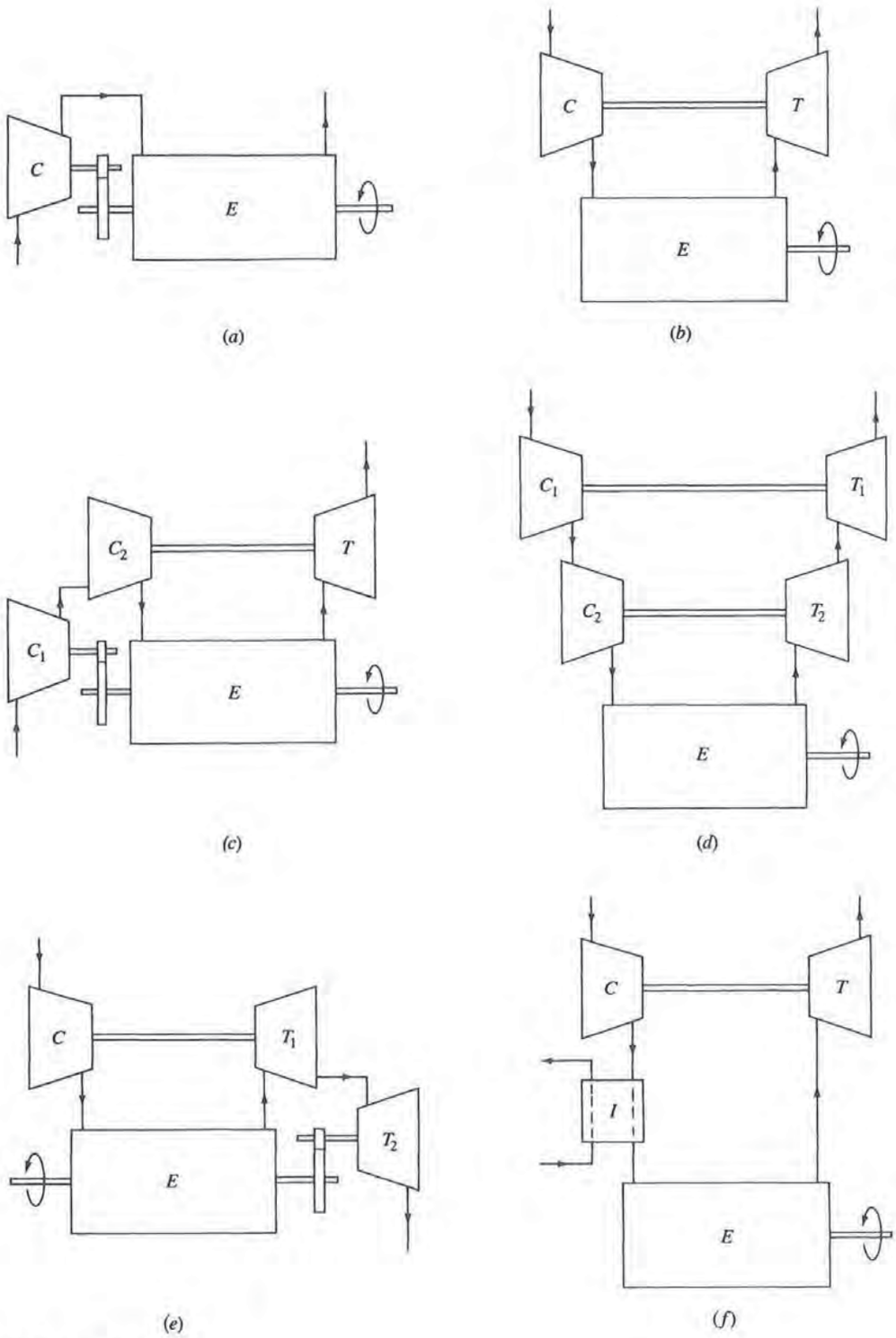


FIGURE 6-37
Supercharging and turbocharging configurations: (*a*) mechanical supercharging; (*b*) turbocharging; (*c*) engine-driven compressor and turbocharger; (*d*) two-stage turbocharging; (*e*) turbocharging with turbocompounding; (*f*) turbocharger with intercooler. *C* Compressor, *E* Engine, *I* Inter-cooler, *T* Turbine.

PETITIONER'S EXHIBIT 1002
US PATENT NO. 6,581,565

where $\dot{Q}$ is the heat-transfer rate into the control volume, $\dot{W}$ is the shaft work-transfer rate out of the control volume, $\dot{m}$ is the mass flow, h is the specific enthalpy, $C^2/2$ is the specific kinetic energy, and gz is the specific potential energy (which is not important and can be omitted).

A *stagnation* or *total enthalpy*, h_0, can be defined as

$$h_0 = h + \frac{C^2}{2} \tag{6.33}$$

For an ideal gas, with constant specific heats, a *stagnation* or *total temperature* follows from Eq. (6.33):

$$T_0 = T + \frac{C^2}{2c_p} \tag{6.34}$$

A *stagnation* or *total pressure* is also defined: it is the pressure attained if the gas is isentropically brought to rest:

$$p_0 = p\left(\frac{T_0}{T}\right)^{\gamma/(\gamma-1)} \tag{6.35}$$

$\dot{Q}$ in Eq. (6.32) for pumps, blowers, compressors, and turbines is usually small enough to be neglected. Equation (6.32) then gives the work-transfer rate as

$$-\dot{W} = \dot{m}(h_{0,\,\text{out}} - h_{0,\,\text{in}}) \tag{6.36}$$

A component efficiency is used to relate the actual work-transfer rate to the work-transfer rate required (or produced) by an equivalent reversible adiabatic device operating between the same pressures. The second law is then used to determine this reversible adiabatic work-transfer rate, which is that occurring in an isentropic process.

For a compressor, the *compressor isentropic efficiency* η_C is

$$\eta_C = \frac{\text{reversible power requirement}}{\text{actual power requirement}} \tag{6.37}$$

Figure 6-38 shows the end states of the gas passing through a compressor on an h-s diagram. Both static (p_1, p_2) and stagnation (p_{01}, p_{02}) constant-pressure lines are shown. The total-to-total isentropic efficiency is, from Eq. (6.37),

$$\eta_{\text{CTT}} = \frac{h_{02s} - h_{01}}{h_{02} - h_{01}} \tag{6.38}$$

which, since c_p is essentially constant for air, or fuel-air mixture, becomes

$$\eta_{\text{CTT}} = \frac{T_{02s} - T_{01}}{T_{02} - T_{01}} \tag{6.39}$$

Since the process 01 to 02s is isentropic,

$$T_{02s} = T_{01}\left(\frac{p_{02}}{p_{01}}\right)^{(\gamma-1)/\gamma}$$

PETITIONER'S EXHIBIT 1002
US PATENT NO. 6,581,565

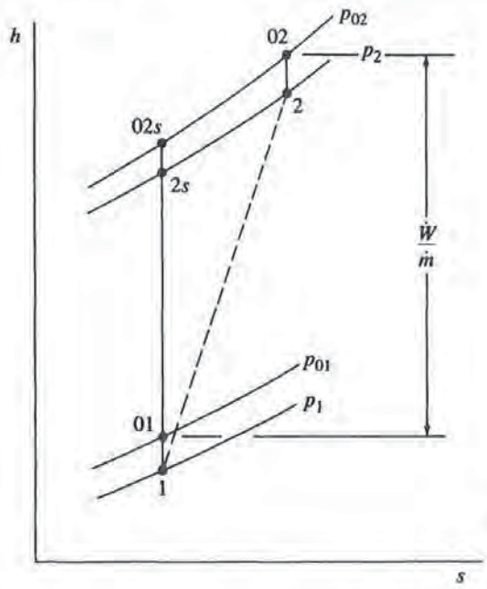


FIGURE 6-38
Enthalpy-entropy diagram for compressor. Inlet state 01, exit state 2; equivalent isentropic compressor exit state 2*s*.

Equation (6.39) becomes

$$\eta_{CTT} = \frac{(p_{02}/p_{01})^{(\gamma-1)/\gamma} - 1}{(T_{02}/T_{01}) - 1} \tag{6.40}$$

In deriving Eq. (6.40) it has been tacitly assumed that the kinetic energy pressure head $(p_{02} - p_2)$ can be recovered. In internal combustion engine applications the compressor feeds the engine via a large manifold, and much of this kinetic energy will be dissipated. The blower or compressor should be designed for effective recovery of this kinetic energy before the exit duct. Since the kinetic energy of the gas leaving the compressor is not usually recovered, a more realistic definition of efficiency is based on exit static conditions:[40]

$$\eta_{CTS} = \frac{T_{2s} - T_{01}}{T_{02} - T_{01}} = \frac{(p_2/p_{01})^{(\gamma-1)/\gamma} - 1}{(T_{02}/T_{01}) - 1} \tag{6.41}$$

This is termed the total-to-static efficiency. The basis on which the efficiency is calculated should always be clearly stated.

The work-transfer rate or power required to drive the compressor is obtained by combining Eq. (6.36), the ideal gas model, and Eq. (6.40):

$$-\dot{W}_C = \dot{m}_i c_{p,i}(T_{02} - T_{01}) = \frac{\dot{m}_i c_{p,i} T_{01}}{\eta_{CTT}} \left[\left(\frac{p_{02}}{p_{01}} \right)^{(\gamma-1)/\gamma} - 1 \right] \tag{6.42}$$

where the subscript i denotes inlet mixture properties. If η_{CTS} is used to define the compressor performance, then p_2 replaces p_{02} in Eq. (6.42). Equation (6.42) gives the thermodynamic power requirement. There will also be mechanical losses in

PETITIONER'S EXHIBIT 1002
US PATENT NO. 6,581,565

the blower or compressor. Thus the power required to drive the device, $-\dot{W}_{C,D}$, will be

$$-\dot{W}_{C,D} = -\frac{\dot{W}_C}{\eta_m} \tag{6.43}$$

where η_m is the blower or compressor mechanical efficiency.

Figure 6-39 shows the gas states at inlet and exit to a turbine on an h-s diagram. State 03 is the inlet stagnation state; 4 and 04 are the exit static and stagnation states, respectively. States 4s and 04s define the static and stagnation exit states of the equivalent reversible adiabatic turbine. The *turbine isentropic efficiency* is defined as

$$\eta_T = \frac{\text{actual power output}}{\text{reversible power output}} \tag{6.44}$$

Thus, the total-to-total turbine efficiency is

$$\eta_{TTT} = \frac{h_{03} - h_{04}}{h_{03} - h_{04s}} \tag{6.45}$$

If the exhaust gas is modeled as an ideal gas with constant specific heats, then Eq. (6.45) can be written

$$\eta_{TTT} = \frac{T_{03} - T_{04}}{T_{03} - T_{04s}} = \frac{1 - (T_{04}/T_{03})}{1 - (p_{04}/p_{03})^{(\gamma-1)/\gamma}} \tag{6.46}$$

Note that for exhaust gas over the temperature range of interest, c_p may vary significantly with temperature (see Figs. 4-10 and 4-17).

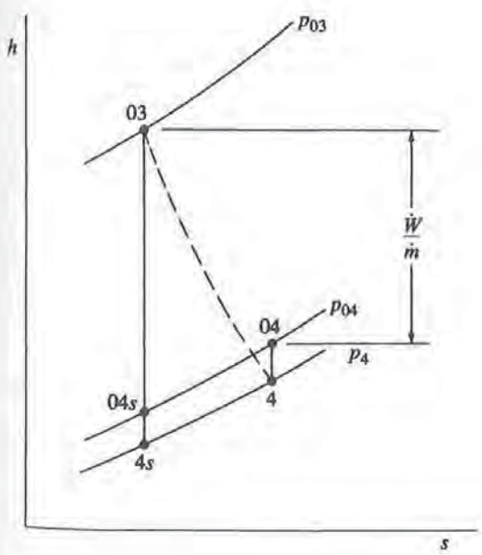


FIGURE 6-39
Enthalpy-entropy diagram for a turbine. Inlet state 03, exit state 4; equivalent isentropic turbine exit state 4s.

PETITIONER'S EXHIBIT 1002
US PATENT NO. 6,581,565

Since the kinetic energy at the exit of a turbocharger turbine is usually wasted, a total-to-static turbine isentropic efficiency, where the reversible adiabatic power output is that obtained between inlet stagnation conditions and the exit static pressure, is more realistic:[40]

$$\eta_{TTS} = \frac{h_{03} - h_{04}}{h_{03} - h_{4s}} = \frac{T_{03} - T_{04}}{T_{03} - T_{4s}} = \frac{1 - (T_{04}/T_{03})}{1 - (p_4/p_{03})^{(\gamma-1)/\gamma}} \tag{6.47}$$

The power delivered by the turbine is given by [Eqs. (6.36) and (6.46)]

$$\dot{W}_T = \dot{m}_e(h_{03} - h_{04}) = \dot{m}_e c_{p,e}(T_{03} - T_{04}) = \dot{m}_e c_{p,e} \eta_{TTT} T_{03}\left[1 - \left(\frac{p_{04}}{p_{03}}\right)^{(\gamma_e-1)/\gamma_e}\right] \tag{6.48}$$

where the subscript e denotes exhaust gas properties. If the total-to-static turbine efficiency (η_{TTS}) is used in the relation for $\dot{W}_T$, then p_4 replaces p_{04} in Eq. (6.48). With a turbocharger, the turbine is mechanically linked to the compressor. Hence, at constant turbocharger speed,

$$-\dot{W}_C = \eta_m \dot{W}_T \tag{6.49}$$

where η_m is the mechanical efficiency of the turbocharger. The mechanical losses are mainly bearing friction losses. The mechanical efficiency is usually combined with the turbine efficiency since these losses are difficult to separate out.

It is advantageous if the operating characteristics of blowers, compressors, and turbines can be expressed in a manner that allows easy comparison between different designs and sizes of devices. This can be done by describing the performance characteristics in terms of dimensionless numbers.[40] The most important dependent variables are: mass flow rate $\dot{m}$, component isentropic efficiency η, and temperature difference across the device ΔT_0. Each of these are a function of the independent variables: $p_{0,\text{in}}$, $p_{0,\text{out}}$ (or p_{out}), $T_{0,\text{in}}$, N(speed), D(characteristic dimension), R(gas constant), γ (c_p/c_v),and μ(viscosity); i.e.,

$$\dot{m},\ \eta,\ \Delta T_0 = f(p_{0,\text{in}},\ p_{0,\text{out}},\ T_{0,\text{in}},\ N,\ D,\ R,\ \gamma,\ \mu) \tag{6.50}$$

By dimensional analysis, these eight independent variables can be reduced to four dimensionless groups:

$$\frac{\dot{m}\sqrt{RT_{0,\text{in}}}}{p_{0,\text{in}}D^2},\ \eta,\ \frac{\Delta T_0}{T_{0,\text{in}}} = f\left(\frac{ND}{\sqrt{RT_{0,\text{in}}}},\ \frac{p_{0,\text{out}}}{p_{0,\text{in}}},\ \frac{\dot{m}}{\mu D},\ \gamma\right) \tag{6.51}$$

The Reynolds number, $\dot{m}/(\mu D)$, has little effect on performance and γ is fixed by the gas. Therefore these variables can be omitted and Eq. (6.51) becomes

$$\frac{\dot{m}\sqrt{RT_{0,\text{in}}}}{p_{0,\text{in}}D^2},\ \eta,\ \frac{\Delta T_0}{T_{0,\text{in}}} = f\left(\frac{ND}{\sqrt{RT_{0,\text{in}}}},\ \frac{p_{0,\text{out}}}{p_{0,\text{in}}}\right) \tag{6.52}$$

PETITIONER'S EXHIBIT 1002
US PATENT NO. 6,581,565

For a particular device, the dimensions are fixed and the value of R is fixed. So it has become the convention to plot

$$\frac{\dot{m}\sqrt{T_{0,\text{in}}}}{p_{0,\text{in}}},\ \eta,\ \frac{\Delta T_0}{T_{0,\text{in}}} = f\left(\frac{N}{\sqrt{T_{0,\text{in}}}},\ \frac{p_{0,\text{out}}}{p_{0,\text{in}}}\right) \tag{6.53}$$

$\dot{m}\sqrt{T_{0,\text{in}}}/p_{0,\text{in}}$ is referred to as the corrected mass flow; $N/\sqrt{T_{0,\text{in}}}$ is referred to as the corrected speed. The disadvantage of this convention of removing D and R is that the groups of variables are no longer dimensionless, and performance plots or maps relate to a specific machine.

Compressor characteristics are usually plotted in terms of the pressure ratio (p_{02}/p_{01}) or (p_2/p_{01}) against the corrected mass flow $(\dot{m}\sqrt{T_{01}}/p_{01})$ along lines of constant corrected speed $(N/\sqrt{T_{01}})$. Contours of constant efficiency are superposed. Similar plots are used for turbines: p_{03}/p_4 against $\dot{m}\sqrt{T_{03}}/p_{03}$ along lines of constant $N/\sqrt{T_{03}}$. Since these occupy a narrow region of the turbine performance map, other plots are often used (see Sec. 6.8.4).

6.8.3 Compressors

Practical mechanical supercharging devices can be classified into: (1) sliding vane compressors, (2) rotary compressors, and (3) centrifugal compressors. The first two types are positive displacement compressors; the last type is an aerodynamic compressor. Four different types of positive displacement compressors are illustrated in Fig. 6-40.

In the sliding vane compressor (Fig. 6-40*a*), deep slots are cut into the rotor to accommodate thin vanes which are free to move radially. The rotor is mounted eccentrically in the housing. As the rotor rotates, the centrifugal forces acting on the vanes force them outward against the housing, thereby dividing the crescent-shaped space into several compartments. Ambient air is drawn through the intake port into each compartment as its volume increases to a maximum. The trapped air is compressed as the compartment volume decreases, and is then discharged through the outlet port. The flow capacity of the sliding vane compressor depends on the maximum induction volume which is determined by the housing cylinder bore, rotor diameter and length, eccentricity, number of vanes, dimensions of the inlet and outlet ports. The actual flow rate and pressure rise at constant speed will be reduced by leakage. Also, heat transfer from the moving vanes and rotor and stator surfaces will reduce compression efficiency unless cooling is used to remove the thermal energy generated by friction between the vanes, and the rotor and stator. The volumetric efficiency can vary between 0.6 and 0.9 depending on the size of the machine, the quality of the design, and the method of lubrication and cooling employed. The displaced volume V_D is given by

$$V_D = \pi\varepsilon l(2r + \varepsilon) \tag{6.54}$$

PETITIONER'S EXHIBIT 1002
US PATENT NO. 6,581,565

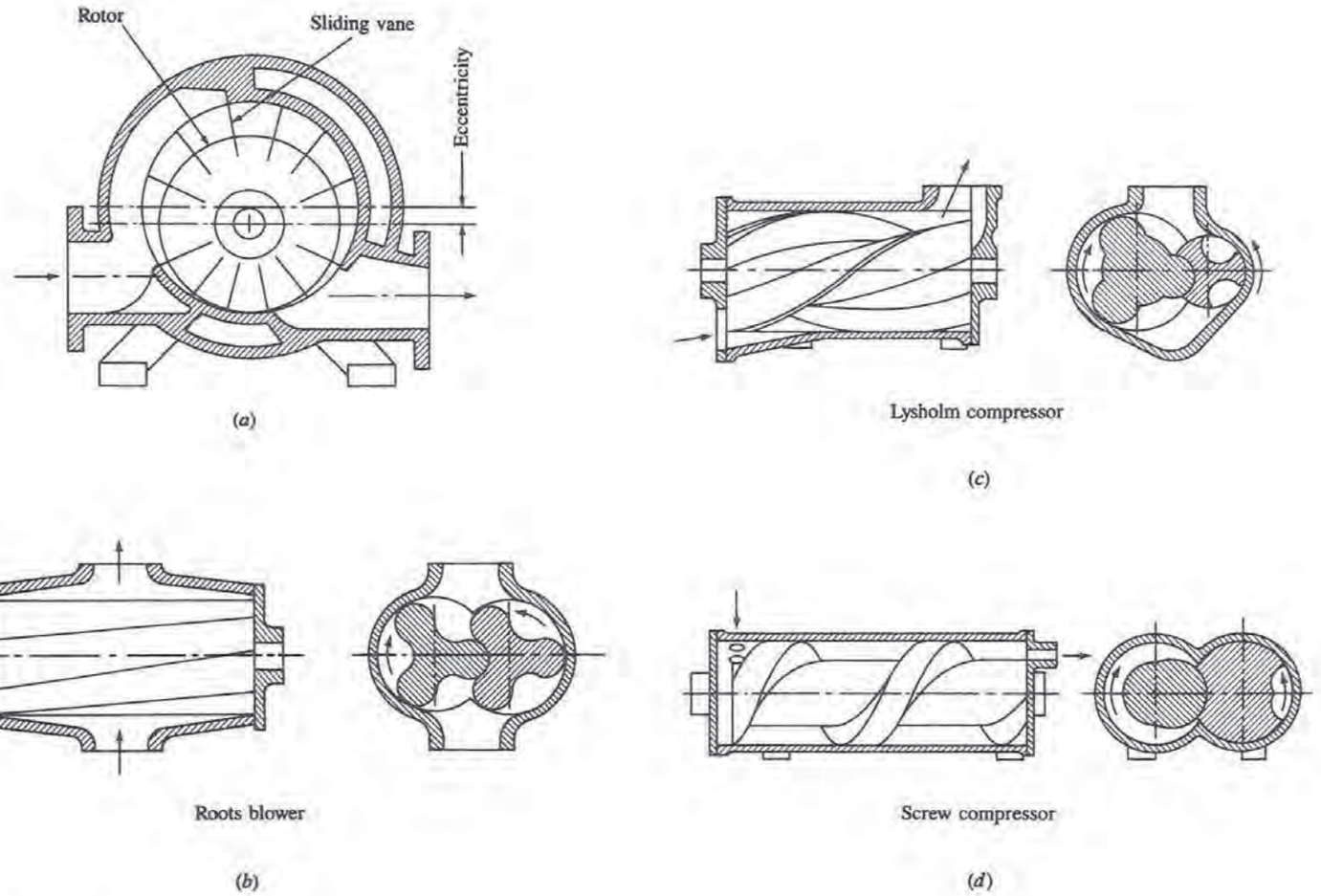


FIGURE 6-40
Positive displacement compressors: (*a*) sliding vane compressor; (*b*) roots blower; (*c*) Lysholm compressor; (*d*) screw compressor.[41]

PETITIONER'S EXHIBIT 1002
US PATENT NO. 6,581,565

where r is the rotor radius, ε the eccentricity, and l the axial length of the compressor. The mass flow rate parameter is

$$\frac{\dot{m}\sqrt{T_0/T_{\text{std}}}}{p_0/p_{\text{std}}} = \text{constant} \times \rho_i \eta_v N \varepsilon l(2r + \varepsilon) \tag{6.55}$$

where η_v is the device volumetric efficiency, N its speed, and the subscripts i, 0 and std refer to inlet, inlet stagnation, and standard atmospheric conditions, respectively. Figure 6-41 shows the performance characteristics of a typical sliding vane compressor. The mass flow rate at constant speed depends on the pressure ratio only through its (weak) effect on volumetric efficiency. The isentropic efficiency is relatively low.[41]

An alternative positive displacement supercharger is the roots blower (Fig. 6-40*b*). The two rotors are connected by gears. The working principles are as follows. Air trapped in the recesses between the rotor lobes and the housing is carried toward the delivery port without significant change in volume. As these recesses open to the delivery line, since the suction side is closed, the trapped air is suddenly compressed by the backflow from the higher-pressure delivery line. This intermittent delivery produces nonuniform torque on the rotor and pressure pulses in the delivery line. Roots blowers are most suitable for small pressure ratios (about 1.2). The volumetric efficiency depends on the running clearances, rotor length, rotational speed, and pressure ratio. In the three-lobe machines shown (two lobes are sometimes used) the volume of each recess V_R is

$$V_R = 0.546R^2 l$$

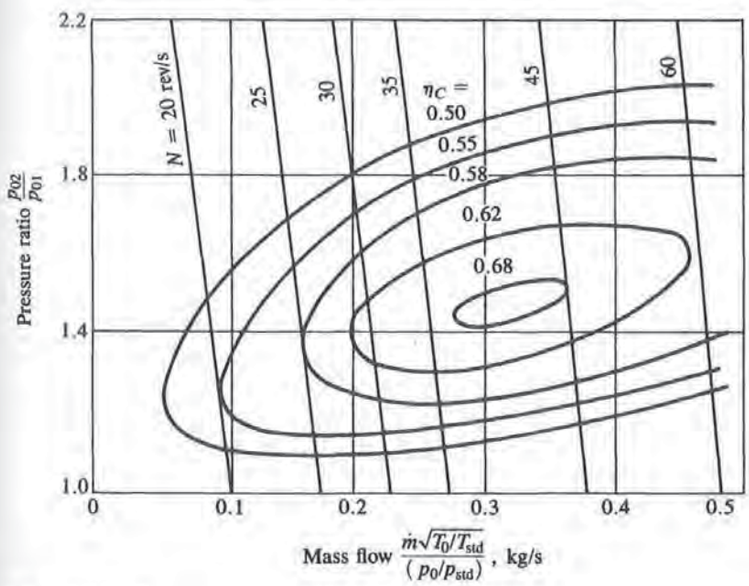


FIGURE 6-41
Performance map for sliding vane compressor.[41]

PETITIONER'S EXHIBIT 1002
US PATENT NO. 6,581,565

where R is the rotor radius and l the blower length. The mass flow parameter is

$$\frac{\dot{m}\sqrt{T_0/T_{std}}}{p_0/p_{std}} = \text{constant} \times \rho_i \eta_v N R^2 l \tag{6.56}$$

A performance map of a typical small roots blower is shown in Fig. 6-42. It is similar in character to that of the sliding vane compressor. At constant speed, the flow rate depends on increasing pressure ratio only through the resulting decrease in volumetric efficiency (Eq. 6.56).[41] The advantage of the roots blower is that its performance range is not limited by surge and choking as is the centrifugal compressor (see below). Its disadvantages are its high noise level, poor efficiency, and large size.[42]

Screw compressors (Fig. 6-40*c* and *d*) must be precision machined to achieve close tolerances between rotating and stationary elements for satisfactory operation. They run at speeds between 3000 and 30,000 rev/min. It is usually necessary to cool the rotors internally. High values of volumetric and isentropic efficiency are claimed.[41]

A *centrifugal compressor* is primarily used to boost inlet air or mixture density coupled with an exhaust-driven turbine in a turbocharger. It is a single-stage radial flow device, well suited to the high mass flow rates at the relatively low pressure ratios (up to about 3.5) required by the engine. To operate efficiently it must rotate at high angular speed. It is therefore much better suited to direct coupling with the exhaust-driven turbine of the turbocharger than to mechanical coupling through a gearbox to the engine for mechanical supercharging.

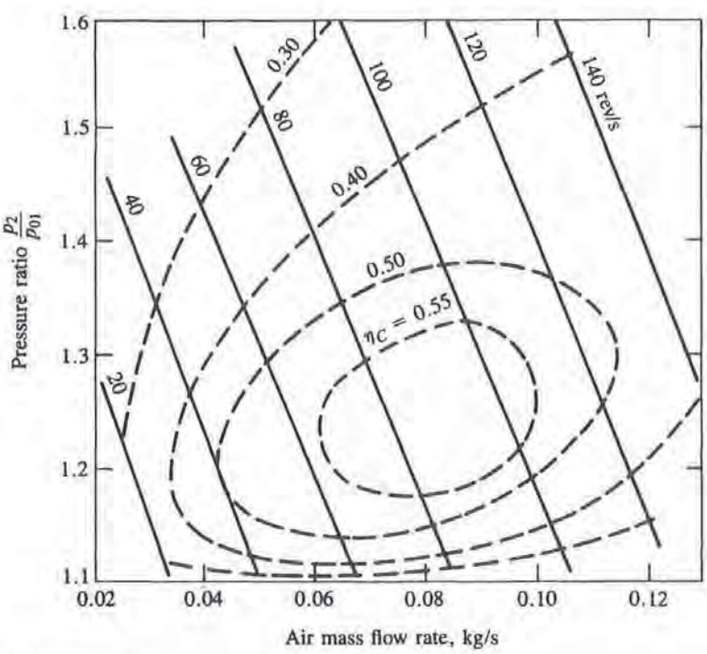


FIGURE 6-42
Performance map at standard inlet conditions for roots blower.[42]

PETITIONER'S EXHIBIT 1002
US PATENT NO. 6,581,565

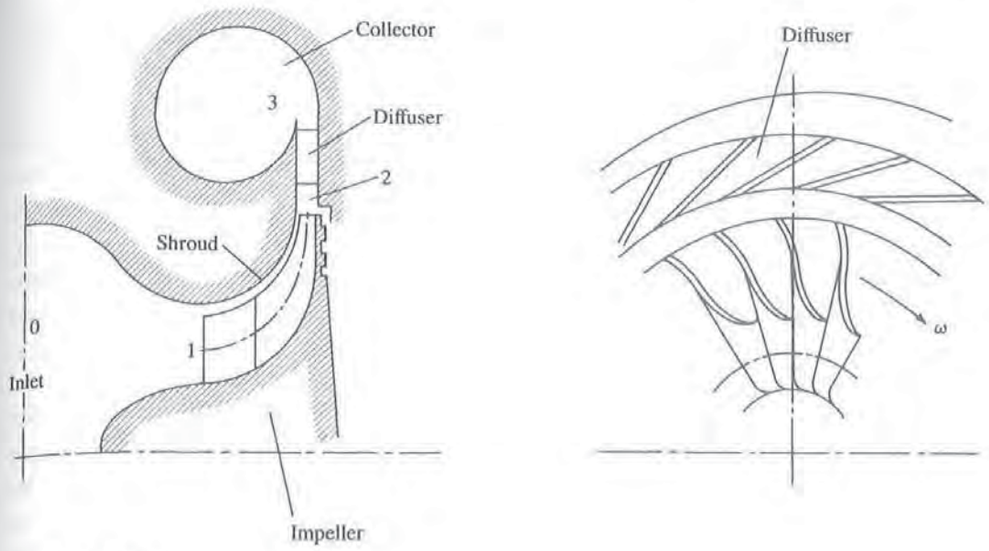


FIGURE 6-43
Schematic of centrifugal compressor.[40]

The centrifugal compressor consists of a stationary inlet casing, a rotating bladed impellor, a stationary diffuser (with or without vanes), and a collector or volute to bring the compressed air leaving the diffuser to the engine intake system (see Fig. 6-43). Figure 6-44 indicates, on an *h-s* diagram, how each component contributes to the overall pressure rise across the compressor. Air at stagnation

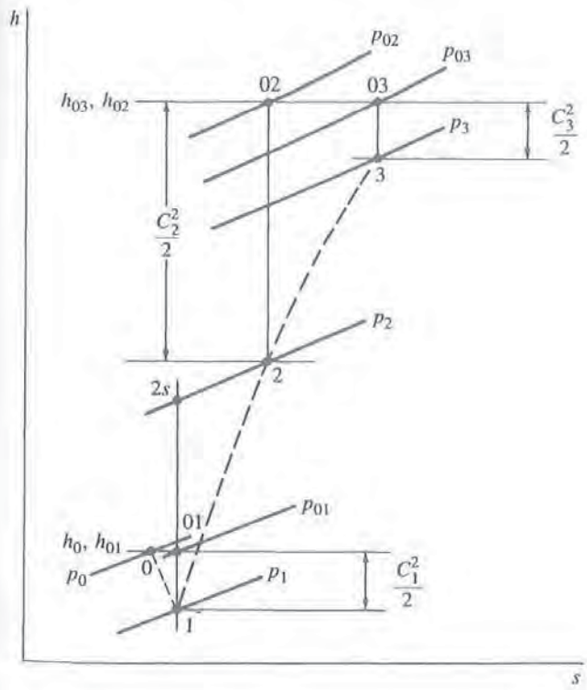


FIGURE 6-44
Enthalpy-entropy diagram for flow through centrifugal compressor.

PETITIONER'S EXHIBIT 1002
US PATENT NO. 6,581,565

state 0 is accelerated in the inlet to pressure p_1 and velocity C_1. The enthalpy change 01 to 1 is $C_1^2/2$. Compression in the impeller flow passages increases the pressure to p_2 and velocity to C_2, corresponding to a stagnation state 02 if all the exit kinetic energy were recovered. The isentropic equivalent compression process has an exit static state 2*s*. The diffuser, 2 to 3, converts as much as practical of the air kinetic energy at exit to the impeller ($C_2^2/2$) to a pressure rise ($p_3 - p_2$) by slowing down the gas in carefully shaped expanding passages. The final state, in the collector, has static pressure p_3, low kinetic energy $C_3^2/2$, and a stagnation pressure p_{03} which is less than p_{02} since the diffusion process is incomplete as well as irreversible.[40]

The work transfer to the gas occurs in the impeller. It can be related to the change in gas angular momentum via the velocity components at the impeller entry and exit, which are shown in Fig. 6-45. Here C_1 and C_2 are the absolute gas velocities, U_1 and U_2 are the tangential blade velocities, and w_1 and w_2 are the gas velocities relative to the impeller all at inlet (1) and exit (2), respectively. The torque T exerted on the gas by the impeller equals the rate of change of angular momentum:

$$T = \dot{m}(r_2 C_{\theta_2} - r_1 C_{\theta_1}) \tag{6.57}$$

The rate of work transfer to the gas is given by

$$-\dot{W}_C = T\omega = \dot{m}\omega(r_2 C_{\theta_2} - r_1 C_{\theta_1}) = \dot{m}(U_2 C_{\theta_2} - U_1 C_{\theta_1}) \tag{6.58}$$

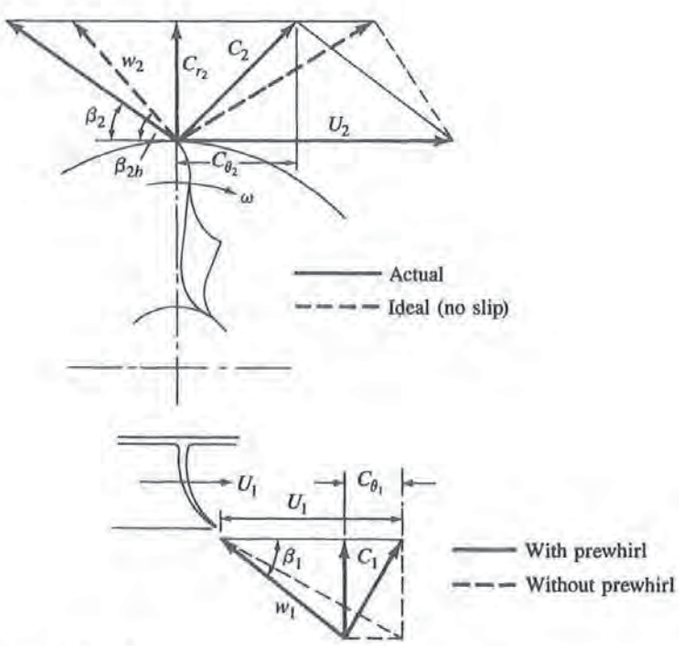


FIGURE 6-45
Velocity diagrams at inlet (1) and exit (2) to centrifugal compressor rotor or impeller.[40]

PETITIONER'S EXHIBIT 1002
US PATENT NO. 6,581,565

This is often called the Euler equation. Normally in compressors the inlet flow is axial so $C_{\theta_1} = 0$. Thus Eq. (6.58) can be written:

$$-\frac{\dot{W}_C}{\dot{m}} = U_2 C_{\theta_2} = U_2\left(1 - \frac{C_{r2}}{U_2}\cot\beta_2\right) \tag{6.59}$$

where β_2 is the backsweep angle. In the ideal case with no slip, β_2 is the blade angle, β_{2b}. In practice, there is slip and β_2 is less than β_{2b}. Many compressors have radial vanes (i.e., $\beta_{2b} = 90°$). A recent trend is backswept vanes ($\beta_{2b} < 90°$) which give higher efficiency. Since work transfer to the gas occurs only in the impeller, the work-transfer rate given by Eq. (6.59) equals the change in stagnation enthalpy ($h_{03} - h_{01}$) in Fig. 6-44 [see Eq. (6.36)].

The operating characteristics of the centrifugal compressor are usually described by a *performance map*. This shows lines of constant compressor efficiency η_C, and constant corrected speed $N/\sqrt{T_{0,\text{in}}}$, on a plot of pressure ratio $p_{0,\text{out}}/p_{0,\text{in}}$ against corrected mass flow $\dot{m}\sqrt{T_{0,\text{in}}}/p_{0,\text{in}}$ [see Eq. (6.53)]. Figure 6-46 indicates the form of such a map. The stable operating range in the center of the map is separated from an unstable region on the left by the *surge line*. When the mass flow is reduced at a constant pressure ratio, local flow reversal eventually occurs in the boundary layer. Further reductions in mass flow cause the flow to reverse completely, causing a drop in pressure. This relieves the adverse pressure gradient. The flow reestablishes itself, builds up again, and the process repeats. Compressors should not be operated in this unstable regime. The

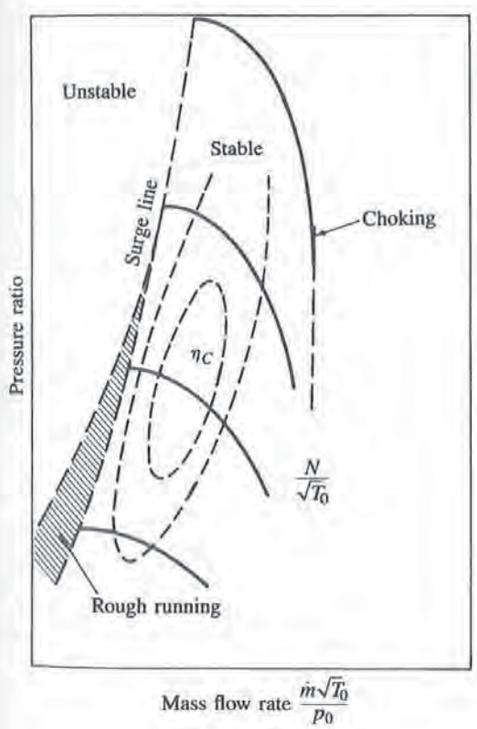


FIGURE 6-46
Schematic of compressor operating map showing stable operating range.[40]

PETITIONER'S EXHIBIT 1002
US PATENT NO. 6,581,565

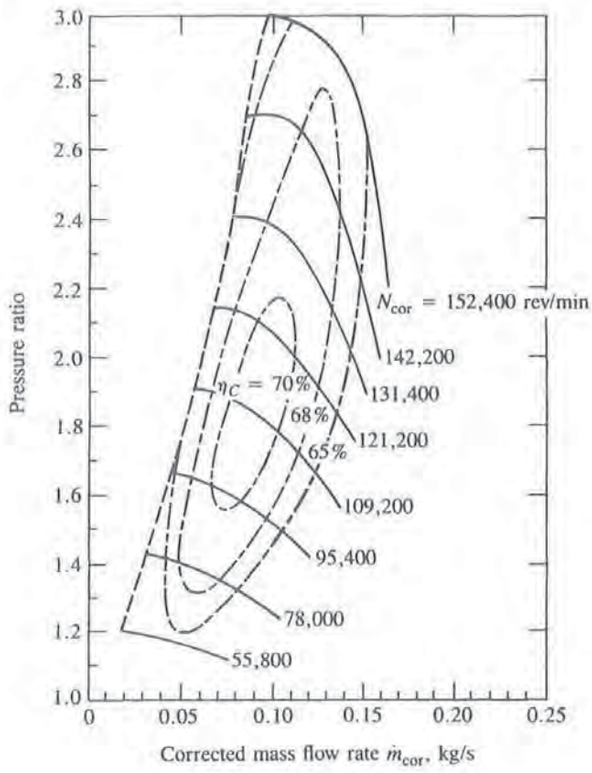


FIGURE 6-47
Centrifugal compressor operating map. Lines of constant corrected speed and compressor efficiency are plotted on a graph of pressure ratio against corrected mass flow.[43]

stable operating regime is limited on the right by choking. The velocities increase as $\dot{m}$ increases, and eventually the flow becomes sonic in the limiting area of the machine. Extra mass flow through the compressor can only be obtained by higher speed. When the diffuser is choked, compressor speed may rise substantially with only a limited increase in the mass flow rate.[40]

Figure 6-47 shows an actual turbocharger compressor performance map. In practice, the map variables corrected speed and mass flow rate are usually defined as[44]

$$N_{cor} = N\left(\frac{T_{ref}}{T_{0,\,in}}\right)^{1/2}$$
$$\dot{m}_{cor} = \dot{m}\left(\frac{T_{0,\,in}}{T_{ref}}\right)^{1/2}\left(\frac{p_{ref}}{p_{0,\,in}}\right) \tag{6.60}$$

where T_{ref} and p_{ref} are standard atmospheric temperature and pressure, respectively. Though the details of different compressor maps vary, their general characteristics are similar. The high efficiency region runs parallel to the surge line (and close to it for vaneless diffusers). A wide flow *range* for the compressor (see Fig. 6-46) is important in turbochargers used for transportation applications.

PETITIONER'S EXHIBIT 1002
US PATENT NO. 6,581,565

6.8.4 Turbines

The turbocharger turbine is driven by the energy available in the engine exhaust. The ideal energy available is shown in Fig. 6-48. It consists of the blowdown work transfer produced by expanding the gas in the cylinder at exhaust valve opening to atmospheric pressure (area *abc*) and (for the four-stroke cycle engine) the work done by the piston displacing the gases remaining in the cylinder after blowdown (area *cdef*).

The reciprocating internal combustion engine is inherently an unsteady pulsating flow device. Turbines can be designed to accept such an unsteady flow, but they operate more efficiently under steady flow conditions. In practice, two approaches for recovering a fraction of the available exhaust energy are commonly used: constant-pressure turbocharging and pulse turbocharging. In *constant-pressure turbocharging*, an exhaust manifold of sufficiently large volume to damp out the mass flow and pressure pulses is used so that the flow to the turbine is essentially steady. The disadvantage of this approach is that it does not make full use of the high kinetic energy of the gases leaving the exhaust port; the losses inherent in the mixing of this high-velocity gas with a large volume of low-velocity gas cannot be recovered. With *pulse turbocharging*, short small-cross-section pipes connect each exhaust port to the turbine so that much of the kinetic energy associated with the exhaust blowdown can be utilized. By suitably grouping the different cylinder exhaust ports so that the exhaust pulses are sequential and have minimum overlap, the flow unsteadiness can be held to an acceptable level. The turbine must be specifically designed for this pulsating flow to achieve adequate efficiencies. The combination of increased energy available at the turbine, with reasonable turbine efficiencies, results in the pulse system being more commonly used for larger diesels.[40] For automotive engines, constant-pressure turbocharging is used.

Two types of turbines are used in turbochargers: radial and axial flow turbines. The radial flow turbine is similar in appearance to the centrifugal compressor; however, the flow is radially inward not outward. Radial flow turbines are

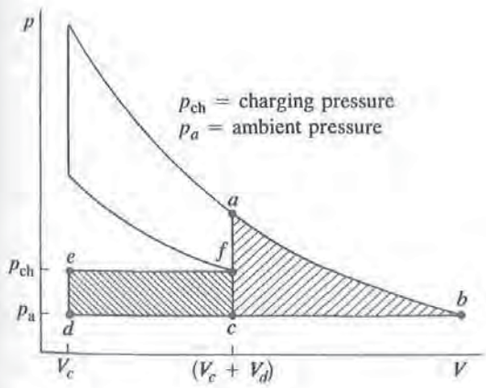


FIGURE 6-48
Constant-volume cycle *p-V* diagram showing available exhaust energy.

PETITIONER'S EXHIBIT 1002
US PATENT NO. 6,581,565

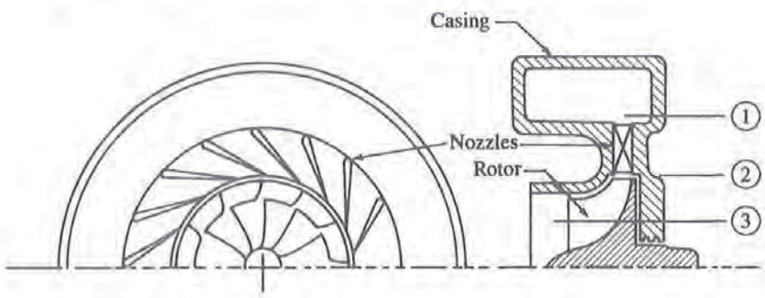


FIGURE 6-49
Schematic of radial flow turbine.

normally used in automotive or truck applications. Larger engines—locomotive, stationary, or marine—use axial flow turbines.

A drawing of a radial flow turbine is shown in Fig. 6-49. It consists of an inlet casing or scroll, a set of inlet nozzles (often omitted with small turbines), and the turbine rotor or wheel. The function of each component is evident from the *h-s* diagram and velocity triangles in Fig. 6-50. The nozzles (01-2) accelerate the flow, with modest loss in stagnation pressure. The drop in stagnation enthalpy, and hence the work transfer, occurs solely in the rotor passages, 2-3: hence, the rotor is designed for minimum kinetic energy $C_3^2/2$ at exit. The velocity triangles at inlet and exit relate the work transfer to the change in angular momentum via the Euler equation:

$$\dot{W}_T = T\omega = \dot{m}\omega(r_2 C_{\theta_2} - r_3 C_{\theta_3}) = \dot{m}(U_2 C_{\theta_2} - U_3 C_{\theta_3}) \tag{6.61}$$

where T is the torque and ω the rotor angular speed. For maximum work transfer the exit velocity should be axial. The work-transfer rate relates to the change in stagnation enthalpy via

$$\dot{W}_T = \dot{m}(h_{02} - h_{03}) = \dot{m}(h_{01} - h_{03}) \tag{6.62}$$

The turbine isentropic efficiency is given by Eqs. (6.44) to (6.47).

Many different types of plots have been used to define radial flow turbine characteristics. Figure 6-51 shows lines of constant corrected speed and efficiency on a plot of pressure ratio versus corrected mass flow rate. As flow rate increases at a given speed, it asymptotically approaches a limit corresponding to the flow becoming choked in the stator nozzle blades or the rotor. For turbines, efficiency is usually presented on a different diagram because the operating regime in Fig. 6-51 is narrow. Figure 6-52 shows an alternative plot for a radial turbine: corrected mass flow rate against corrected rotor speed. On this map, the operating regime appears broader.

A schematic of a turbocharger axial flow turbine is shown in Fig. 6-53. Usually a single stage is sufficient to expand the exhaust gas efficiently through the pressure ratios associated with engine turbocharging. This turbine consists of an annular flow passage, a single row of nozzles or stator blades, and a rotating blade ring. The changes in gas state across each component are similar to those

PETITIONER'S EXHIBIT 1002
US PATENT NO. 6,581,565

of the radial turbine shown in the h-s diagram of Fig. 6-50. The velocity triangles at entry and exit to the rotor, shown in Fig. 6-54, relate the work transfer from the gas to the rotor to the change in angular momentum:

$$\dot{W}_T = \omega T = \dot{m}\omega(r_2 C_{\theta_2} + r_3 C_{\theta_3})$$

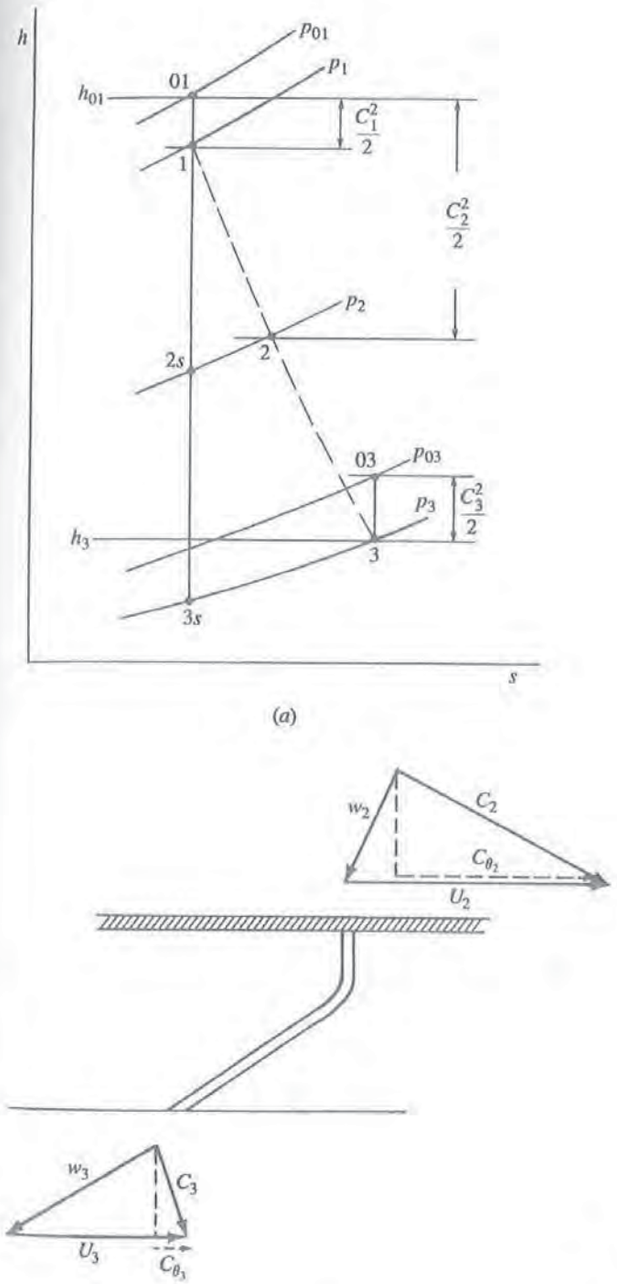


FIGURE 6-50
(*a*) Enthalpy-entropy diagram for radial turbine. (*b*) Velocity diagrams at turbine rotor inlet (2) and exit (3).

PETITIONER'S EXHIBIT 1002
US PATENT NO. 6,581,565

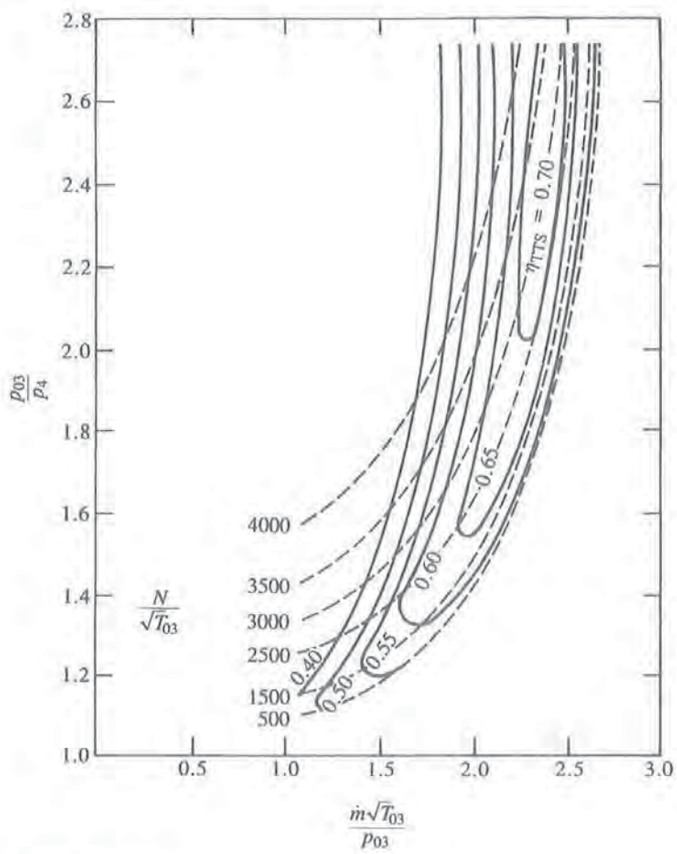


FIGURE 6-51
Radial turbine performance map showing lines of constant corrected speed and efficiency on a plot of pressure ratio versus corrected mass flow rate. T_{03} = turbine inlet temperature (K), p_{03} = turbine inlet pressure (bar), p_4 = turbine exit pressure (bar), $\dot{m}$ = mass flow rate (kg/s), N = speed (rev/min).[40]

Since the mid-radius r_2 usually equals the mid-radius r_3,

$$\dot{W}_T = \dot{m}U(C_{\theta_2} + C_{\theta_3}) = \dot{m}U(C_2 \sin \alpha_2 + C_3 \sin \alpha_3)$$
$$= \dot{m}U(C_{z_2} \tan \beta_2 + C_{z_3} \tan \beta_3) \qquad (6.63)$$

Equation (6.62) relates the work-transfer rate to the stagnation enthalpy change as in the radial turbine.

Figure 6-55 shows axial turbine performance characteristics on the standard dimensionless plot of pressure ratio versus corrected mass flow rate. Here the constant speed lines converge to a single choked flow limit as the mass flow is increased. In the radial turbine, the variation in centrifugal effects with speed cause a noticeable spread in the constant speed lines (Fig. 6-51).

An alternative performance plot for turbines is efficiency versus *blade speed ratio*. This ratio is the blade speed U (at its mean height) for an axial flow turbine

PETITIONER'S EXHIBIT 1002
US PATENT NO. 6,581,565

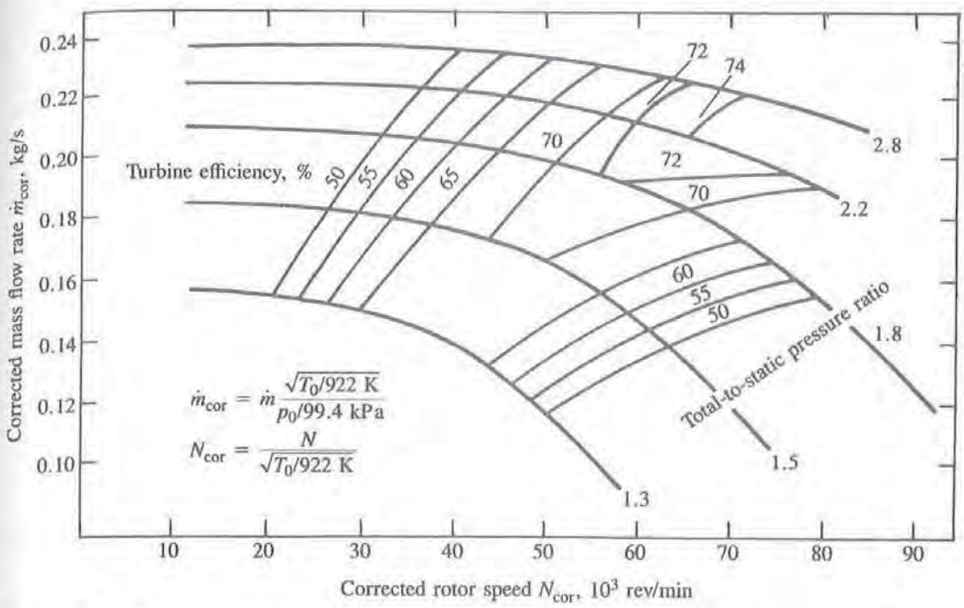


FIGURE 6-52
Alternative radial turbine performance map: corrected mass flow rate is plotted against corrected rotor speed.[45]

or the wheel tip speed for a radial flow turbine, divided by the velocity equivalent of the isentropic enthalpy drop across the turbine stage, C_s; i.e.,

$$\text{Blade speed ratio} = \frac{U}{C_s}$$

where

$$C_s = [2(h_{03} - h_{4s})]^{1/2} \tag{6.64}$$

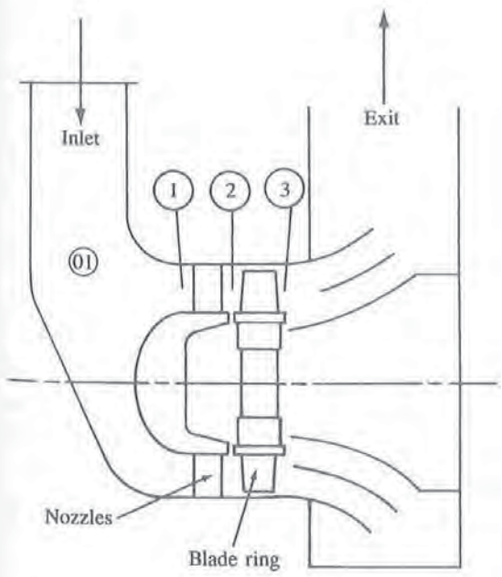


FIGURE 6-53
Schematic of single-stage axial flow turbine.

PETITIONER'S EXHIBIT 1002
US PATENT NO. 6,581,565

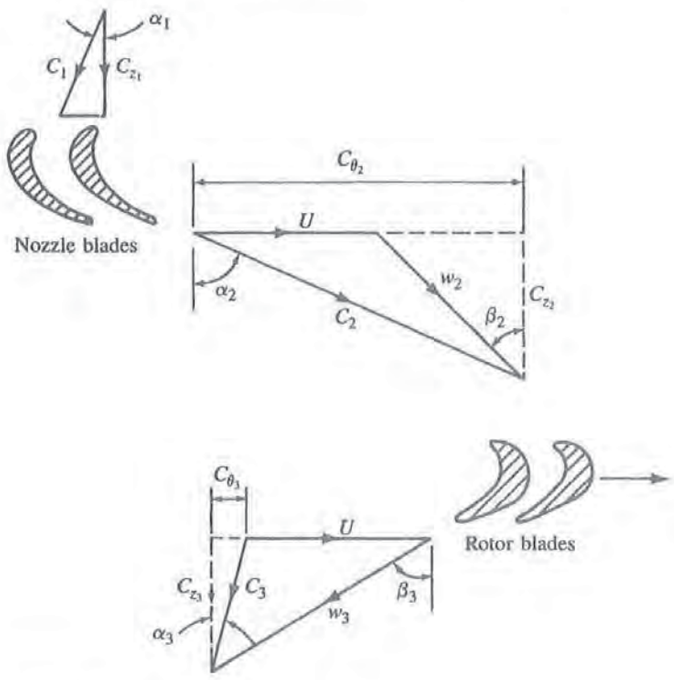


FIGURE 6-54
Velocity diagrams at entry (2) and exit (3) to axial flow turbine blade ring.[40]

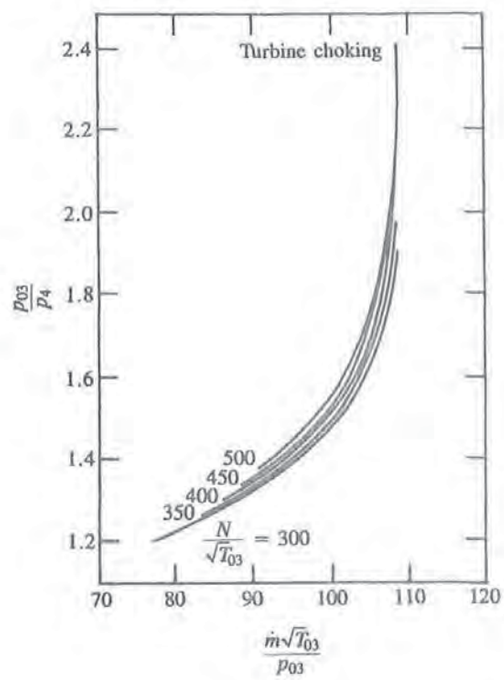


FIGURE 6-55
Axial flow turbine performance map: pressure ratio is plotted against corrected mass flow rate. T_{03} = turbine inlet temperature (K), p_{03} = turbine inlet pressure (bar), p_4 = turbine exit pressure (bar), $\dot{m}$ = mass flow rate (kg/s), N = speed (rev/min).[40]

PETITIONER'S EXHIBIT 1002
US PATENT NO. 6,581,565

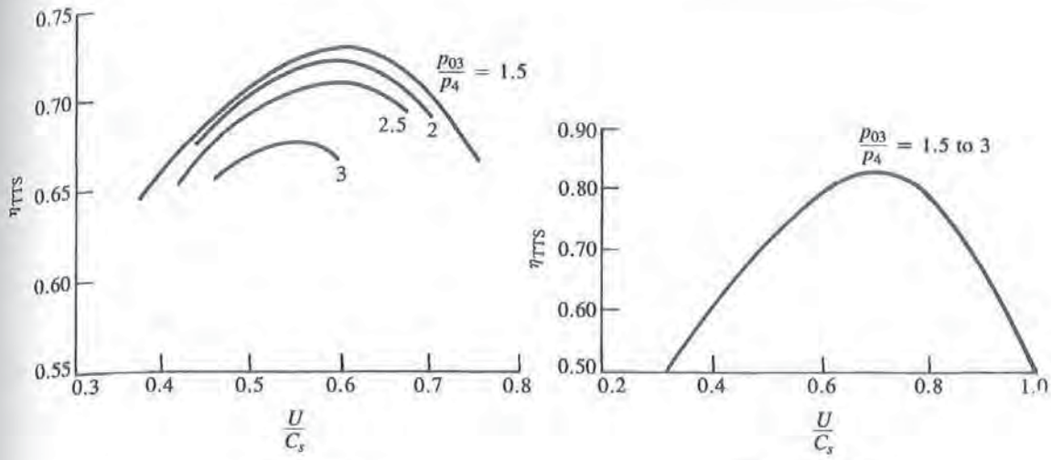


FIGURE 6-56
Plot of turbine total-to-static efficiency versus blade speed ratio U/C_s for (*a*) axial flow and (*b*) radial flow turbines.[40]

This method of displaying performance is useful for matching compressor and turbine wheel size for operation of the turbine at optimum efficiency. Figure 6-56 shows such plots for an axial and radial flow turbine. The peak efficiency can occur for $0.4 < U/C_s < 0.8$, depending on turbine design and application.[40]

For a given turbocharger, the compressor and turbine characteristics are linked. Since the compressor and turbine are on a common shaft with speed N:

$$\frac{N}{\sqrt{T_{01}}} = \frac{N}{\sqrt{T_{03}}} \left(\frac{T_{03}}{T_{01}}\right)^{1/2} \tag{6.65}$$

For $\dot{m}_C = \dot{m}_T = \dot{m}$ (if $\dot{m}_C[1 + (F/A)] = \dot{m}_T$, the equation is easily modified):

$$\frac{\dot{m}\sqrt{T_{01}}}{p_{01}} = \frac{\dot{m}\sqrt{T_{03}}}{p_{03}} \left(\frac{p_{03}}{p_{01}}\right)\left(\frac{T_{01}}{T_{03}}\right)^{1/2} \tag{6.66}$$

Since the compressor and turbine powers are equal in magnitude:

$$h_{02} - h_{01} = \eta_m(h_{03} - h_{04}) \tag{6.67}$$

or, with an ideal gas model,

$$c_{p,C}(T_{02} - T_{01}) = \eta_m c_{p,T}(T_{03} - T_{04}) \tag{6.68}$$

Equation (6.68), with Eqs. (6.40) and (6.46), gives

$$\left(\frac{p_{02}}{p_{01}}\right)^{(\gamma C - 1)/\gamma C} - 1 = \eta_C \eta_T \eta_m \frac{c_{p,T}}{c_{p,C}} \left[1 - \left(\frac{p_4}{p_{03}}\right)^{(\gamma T - 1)/\gamma T}\right] \frac{T_{03}}{T_{01}} \tag{6.69}$$

Assuming that the turbine exit pressure p_4 equals atmospheric pressure p_{01}, the equilibrium or steady-state running lines for constant values of T_{03}/T_{01} can be

PETITIONER'S EXHIBIT 1002
US PATENT NO. 6,581,565

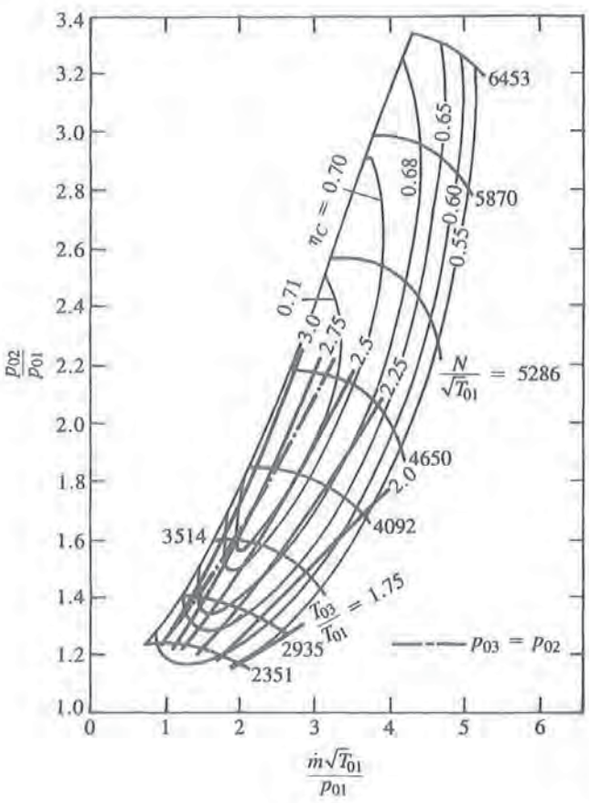


FIGURE 6-57
Steady-state turbocharger operating lines plotted as constant T_{03}/T_{01} lines on compressor map. Turbine characteristics defined by Fig. 6-51. p_{01} = compressor inlet pressure (bar), p_{02} = compressor exit pressure (bar), T_{01} = compressor inlet temperature (K), T_{03} = turbine inlet temperature (K), $\dot{m}$ = mass flow rate (kg/s), N = speed (rev/min).[40]

determined. Figure 6-57 shows an example of such a set of turbocharger characteristics, plotted on a turbocharger compressor map for a radial turbine with characteristics similar to Fig. 6-51. The dash-dot-dash line is for $p_{02} = p_{03}$. To the right of this line, $p_{03} > p_{02}$; to the left of this line $p_{02} > p_{03}$.[40]

The problem of overspeeding the turbocharger and generating very high cylinder pressures often requires that some of the exhaust be bypassed around the turbine. The bypass valve or *wastegate* is usually built into the turbocharger casing. It consists of a spring-loaded valve acting in response to the inlet manifold pressure on a controlling diaphragm. When the wastegate is open, only a portion of the exhaust gases will flow through the turbine and generate power; the remainder passes directly into the exhaust system downstream of the turbine.

6.8.5 Wave-Compression Devices

Pressure wave superchargers make use of the fact that if two fluids having different pressures are brought into direct contact in long narrow channels, equilization of pressure occurs faster than mixing. One such device, the Comprex, has been developed for internal combustion engine supercharging which operates using this principle.[46] It is shown schematically in Fig. 6-58. The working channels of the Comprex are arranged on a rotor or cell wheel (*b*) which is rotated

PETITIONER'S EXHIBIT 1002
US PATENT NO. 6,581,565

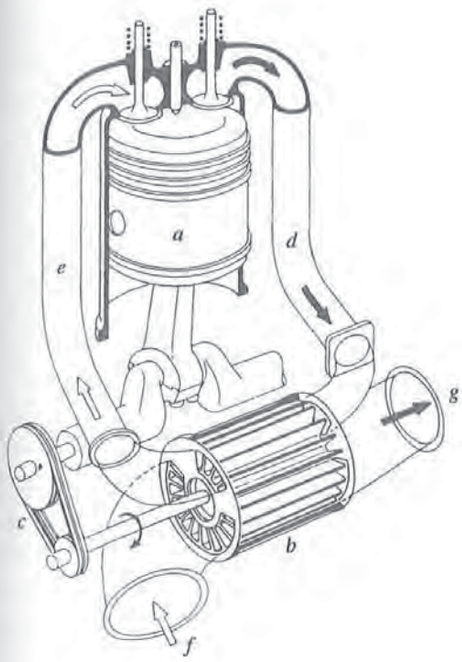


FIGURE 6-58
Schematic of Comprex supercharger.[47] *a* Engine, *b* Cell wheel or rotor, *c* Belt drive, *d* High-pressure exhaust gas (G-HP), *e* High-pressure air (A-HP), *f* Low-pressure air (A-LP), *g* Low-pressure exhaust gas (G-LP)

between two castings by a belt driven from the crankshaft (*c*). There is no contact between the rotor and the casing, but the gaps are kept small to minimize leakage. The belt drive merely overcomes friction and maintains the rotor at a speed proportional to engine speed (usually 4 or 5 times faster): it provides no compression work. One casing (the air casing) contains the passage which brings low-pressure air (*f*) to one set of ports and high-pressure air (*e*) from another set of ports in the rotor-side inner casing. The other casing (the gas casing) connects the high-pressure engine exhaust gas (*d*) to one set of ports at the other end of the rotor, and connects a second set of ports to the exhaust system (*g*). Fluid can flow into and out of the rotor channels through these ports. The exhaust gas inlet port is made small enough to cause a significant pressure rise in the exhaust manifold (e.g., 2 atm) when the engine is operated at its rated power. The pressure wave process does not depend on the pressure and flow fluctuations within the manifold caused by individual cylinder exhaust events: its operation can be explained assuming constant pressure at each set of ports. As the rotor makes one revolution, the ends of each channel are alternatively closed, or are open to a flow passage. By appropriate arrangement of these passages and selection of the geometry and location of the ports, an efficient energy transfer between the engine exhaust gases and the fresh charge can be realized.[46]

The wave-compression process in the Comprex can be explained in more detail with the aid of Fig. 6-59, where the rotational motion of the channels has been unrolled. Consider the channel starting at the top; it is closed at both ends and contains air at atmospheric pressure. As it opens at the upper edge of the high-pressure gas (G-HP) duct, a compression or shock wave (1) propagates from

PETITIONER'S EXHIBIT 1002
US PATENT NO. 6,581,565

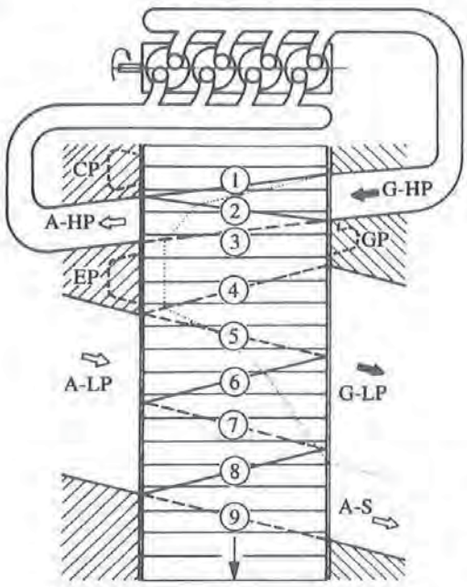


FIGURE 6-59
Unrolled view of the Comprex pressure-wave process.[47] A Air, G Gas, S Scavenging, HP High pressure, LP Low pressure; CP, EP, GP are pockets.

the right end of the channel toward the left, compressing the air through which it passes. The compressed air behind the wave occupies less space so the high-pressure exhaust gas moves into the channel as indicated by the dotted line. This line is the boundary between the two fluids. As this wave (1) reaches the left end, the channel is opened and compressed air flows into the engine inlet duct (A-HP). The inlet duct is shaped to provide the same mass flow at lower velocity: this deceleration of the air produces a second compression wave (2) which propagates back into the channel. As a result the compressed air leaving the cell on the left has a higher pressure than the driving gas on the right. As this wave (2) arrives at the right-hand side, the high-pressure gas (G-HP) channel closes. An expansion wave (3) then propagates back to the left, separating the now motionless and partly expanded fluid on the right from still-moving fluid on the left. When this wave (3) reaches the left-hand end, A-HP is closed and all the gases in the channel are at rest. Note that the first gas particles (dotted line) have not quite reached the air end of the channel: a cushion of air remains to prevent break-through.

The cell's contents are still at a higher pressure than the low pressure in the exhaust gas duct. When the right-hand end of the cell reaches this duct, the cell's contents expand into the exhaust. This motion is transferred through the channel by an expansion wave (4) which propagates to the left at sonic speed. When this wave reaches the left-hand end, the cell opens to the low-pressure air duct (A-LP) and fresh air is drawn into the cell. The flow to the right continues, but with decreasing speed due to wave action (5, 6, 7, 8) and pressure losses at each end of the cell. When the dotted line—the interface between air and the exhaust gas—reaches the right end of the cell, all the driving gas has left. The cell is then

PETITIONER'S EXHIBIT 1002
US PATENT NO. 6,581,565

purged by the scavenging air flow (A-S) and filled with fresh air at atmospheric pressure. At wave (9), the cell is closed at both ends, restoring it to its initial state.[47]

The speed of these pressure waves is the local sound speed and is a function of local gas temperature only. Thus, the above process will only work properly for a given exhaust gas temperature at a particular cell speed. The operating range is extended by the use of "pockets" as shown in Fig. 6-59. The pockets prevent the reflection of sound waves from a closed channel end which would cause a substantial change in flow velocity in the channel. These pockets, marked CP and EP on the air side and GP on the exhaust gas side, allow flow from one channel to adjacent channels via the pocket if the wave action requires it. Thus the device can be tuned for full-load medium-speed operation and still give acceptable performance at other loads and speeds because the pockets allow the particle paths to change without major losses.[46]

Figure 6-60 shows the apparent compressor performance map of a Comprex when connected to a small three-cylinder diesel engine. Note that the map depends on the engine to which the device is coupled because the exhaust gas expansion process and fresh air compression process occur within the same rotor. The volume flow rate is the net air: it is the total air flow into the device less the scavenging air flow. The values of isentropic efficiency [defined by Eq. (6.39)] are comparable to those of mechanical and aerodynamic compressors.

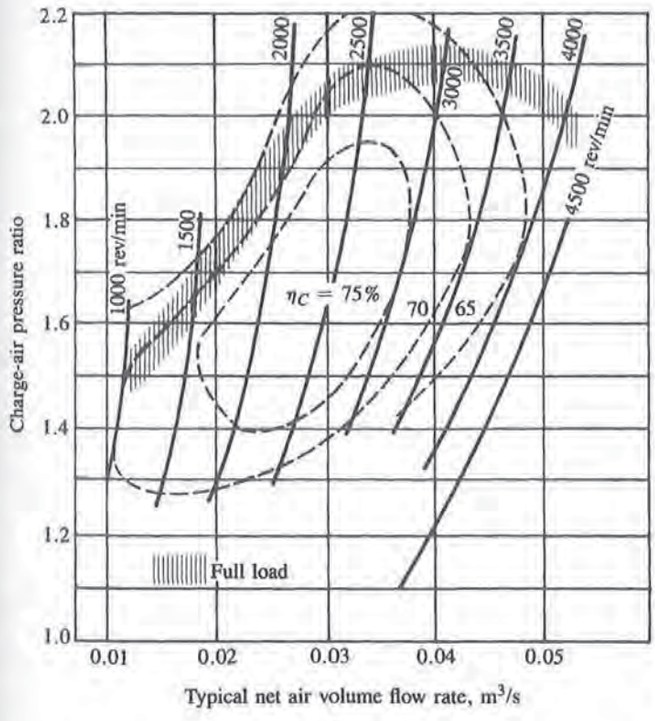


FIGURE 6-60
Apparent compressor map of Comprex connected to a 1.2-dm³ diesel engine: charge-air pressure ratio plotted versus net air volume flow rate (total air flow less scavenging air flow).[46]

PETITIONER'S EXHIBIT 1002
US PATENT NO. 6,581,565

PROBLEMS

6.1. A conventional spark-ignition engine operating with gasoline will not run smoothly (due to incomplete combustion) with an equivalence ratio leaner than about $\phi = 0.8$. It is desirable to extend the smooth operating limit of the engine to leaner equivalence ratios so that at part-throttle operation (with intake pressure less than 1 atmosphere) the pumping work is reduced. Leaner than normal operation can be achieved by adding hydrogen gas (H_2) to the mixture in the intake system. The addition of H_2 makes the fuel-air mixture easier to burn.

(*a*) The fuel composition with "mixed" fuel operation is $H_2 + C_8H_{18}$—one mole of hydrogen to every mole of gasoline, which is assumed the same as isooctane. What is the stoichiometric air/fuel ratio for the "mixed" fuel?

(*b*) The lower heating value of H_2 is 120 MJ/kg and for isooctane is 44.4 MJ/kg. What is the heating value per kilogram of fuel mixture?

(*c*) Engine operation with isooctane and the mixed ($H_2 + C_8H_{18}$) fuel is compared in a particular engine at a part-load condition (brake mean effective pressure of 275 kPa and 1400 rev/min). You are given the following information about the engine operation:

Fuel	C_8H_{18}	$H_2 + C_8H_{18}$
Equivalence ratio	0.8	0.5
Gross indicated fuel conversion efficiency	0.35	0.4
Mechanical rubbing friction mep	138 kPa	138 kPa
Inlet manifold pressure	46 kPa	?
Pumping mep	55 kPa	?

Estimate approximately the inlet manifold pressure and the pumping mean effective pressure with ($H_2 + C_8H_{18}$) fuel. Explain your method and assumptions clearly. Note that mechanical efficiency η_m is defined as

$$\eta_m = \frac{\text{bmep}}{\text{imep}_g} = \frac{\text{bmep}}{\text{bmep} + \text{rfmep} + \text{pmep}}$$

6.2. Hydrogen is a possible future fuel for spark-ignition engines. The lower heating value of hydrogen is 120 MJ/kg and for gasoline (C_8H_{14}) is 44 MJ/kg. The stoichiometric air/fuel ratio for hydrogen is 34.3 and for gasoline is 14.4. A disadvantage of hydrogen fuel in the SI engine is that the partial pressure of hydrogen in the H_2-air mixture reduces the engine's volumetric efficiency, which is proportional to the partial pressure of air. Find the partial pressure of air in the intake manifold downstream of the hydrogen fuel-injection location at wide-open throttle when the total intake manifold pressure is 1 atmosphere; the equivalence ratio is 1.0. Then estimate the ratio of the fuel energy per unit time entering a hydrogen-fueled engine operating with a stoichiometric mixture to the fuel energy per unit time entering an identical gasoline-fueled engine operating at the same speed with a stoichiometric mixture. (Note that the "fuel energy" per unit mass of *fuel* is the fuel's heating value.)

6.3. Sketch (*a*) shows an ideal cycle p-V diagram for a conventional throttled spark-ignition engine, 1-2-3-4-5-6-7-1. The gas properties c_v, c_p, γ, R throughout the cycle are constant. The mass of gas in the cylinder is m. The exhaust pressure is p_e.

Sketch (*b*) shows an ideal cycle p-V diagram 1-2-3-4-5-6-8-1 for a spark-ignition engine with novel inlet valve timing. The inlet manifold is unthrottled; it has essentially the same pressure as the exhaust. To reduce the mass inducted at part

PETITIONER'S EXHIBIT 1002
US PATENT NO. 6,581,565

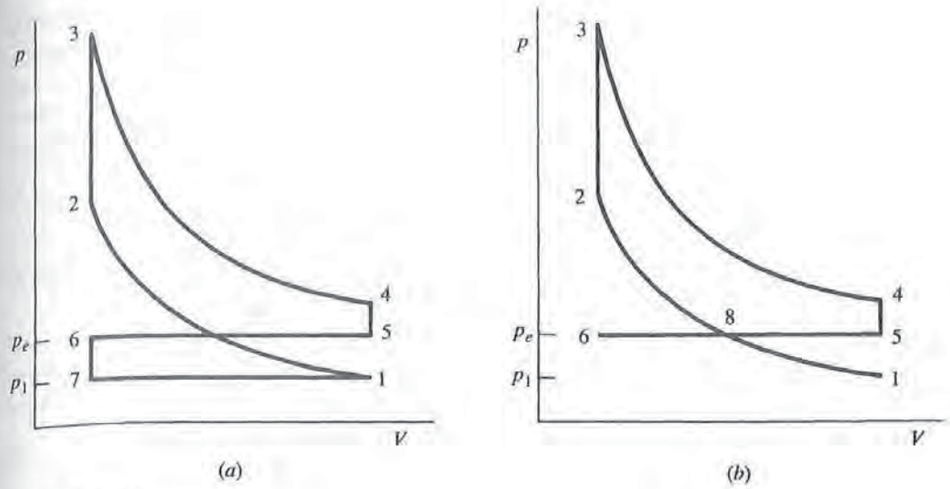


FIGURE P6-3

load, the inlet valve is closed rapidly *partway through the intake stroke* at point 8. The gas in the cylinder at inlet valve closing at 8 is then expanded isentropically to 1 with the inlet valve closed. The pressure p_1 at the start of compression is the same for both cycles.

(*a*) Indicate on p-V diagrams the area that corresponds to the pumping work per cycle for cycles (*a*) and (*b*). Which area is greater?

(*b*) Derive expressions for the pumping work per cycle W_p in terms of m, c_v, γ, T_1, (p_e/p_1), and the compression ratio r_c for cycles (*a*) and (*b*). Be consistent about the signs of the work transfers to and from the gas.

(*c*) For $\gamma = 1.3$, $r_c = 8$, and $(p_e/p_1) = 2$ find the ratio $W_p(b)/W_p(a)$, assuming the values of T_1 and m are the same in both cases.

6.4. For four-stroke cycle engines, the inlet and exhaust valve opening and closing crank angles are typically: IVO 15° BTC; IVC 50° ABC; EVO 55° BBC; EVC 10° ATC. Explain why these valve timings improve engine breathing relative to valve opening and closing at the beginnings and ends of the intake and exhaust strokes. Are there additional design issues that are important?

6.5. Estimate approximately the pressure drop across the inlet valve about halfway through the intake stroke and across the exhaust valve halfway through the exhaust stroke, when the piston speed is at its maximum for a typical four-stroke cycle spark-ignition engine with $B = L = 85$ mm at 2500 and 5000 rev/min at WOT. Assume appropriate values for any valve and port geometric details required, and for the gas composition and state.

6.6. Using the data in Fig. 6-21, estimate the fraction of the original mass left in the cylinder: (*a*) at the end of the blowdown process and (*b*) at the end of the exhaust stroke.

6.7. Compare the engine residual gas fraction data in Fig. 6-19 with ideal cycle estimates of residual gas fraction as follows. Using Eq. (5.47) plot the fuel-air cycle residual mass fraction x_r against p_i/p_e for $r_c = 8.5$ on the same graph as the engine data in Fig. 6-19 at 1400 rev/min and 27° valve overlap. Assume $T_r = 1400$ K and $(\gamma - 1)/\gamma = 0.24$ in Eq. (5.47). Suggest an explanation for any significant difference.

PETITIONER'S EXHIBIT 1002
US PATENT NO. 6,581,565

6.8. One concept that would increase SI engine efficiency is early intake valve closing (EIVC) where the intake valve closes *before* the piston reaches BC on the intake stroke, thus limiting the amount of charge inducted into the cylinder.
(*a*) Explain why EIVC improves engine efficiency at part load. (*Hint:* consider what must happen to the inlet manifold pressure in order to maintain constant mass in the cylinder as the intake valve is closed sooner.)
(*b*) This part load reduction in charge could be achieved by using late intake valve closing where the intake valve is not closed until the compression stroke has pushed some of the cylinder gases back out into the intake manifold. Based on a comparison of p-V diagrams, is this method inferior to EIVC?

6.9. An eight-cylinder turbocharged aftercooled four-stroke cycle diesel engine operates with an inlet pressure of 1.8 atmospheres at its maximum rated power at 2000 rev/min. $B = 128$ mm, $L = 140$ mm, η_v (based on inlet manifold conditions of 1.8 atm and 325 K after the aftercooler) = 0.9. The compressor isentropic efficiency is 0.7.
(*a*) Calculate the power required to drive the turbocharger compressor.
(*b*) If the exhaust gas temperature is 650°C and the turbocharger isentropic efficiency is 0.65, estimate the pressure at turbine inlet. The turbine exhausts to the atmosphere.

6.10. The charging efficiency of two-stroke cycle diesel engines can be estimated from measurement of the concentration of O_2 and CO_2 in the burned gases within the cylinder, or in the exhaust blowdown pulse prior to any mixing with fresh air. The engine bore = 125 mm, stroke = 150 mm, compression ratio = 15. The fuel flow rate at 1800 rev/min is 1.6 g/s per cylinder. The conditions used to evaluate the air density for the reference mass are 300 K and 1 atm. The molar concentrations (dry) of CO_2 and O_2 in the in-cylinder burned gases are 7.2 and 10.4 percent (see Fig. 4-22). The scavenging air flow rate is 80 g/s. Evaluate (*a*) the charging efficiency, (*b*) the delivery ratio, and (*c*) the trapping efficiency (assuming the trapped mass equals the reference mass).

REFERENCES

1. Khovakh, M.: *Motor Vehicle Engines*, English Translation, Mir Publishers, Moscow, 1976.
2. Matsuoka, S., Tasaka, H., and Tsuruta, J.: "The Evaporation of Fuel and Its Effect on Volumetric Efficiency," JARI technical memorandum no. 2, pp. 17–22, 1971.
3. Takizawa, M., Uno, T., Oue, T., and Yura, T.: "A Study of Gas Exchange Process Simulation of an Automotive Multi-Cylinder Internal Combustion Engine," SAE paper 820410, *SAE Trans.*, vol. 91, 1982.
4. Kay, I. W.: "Manifold Fuel Film Effects in an SI Engine," SAE paper 780944, 1978.
5. Ohata, A., and Ishida, Y.: "Dynamic Inlet Pressure and Volumetric Efficiency of Four Cycle Four Cylinder Engine," SAE paper 820407, *SAE Trans.*, vol. 91, 1982.
6. Benson, R. S., and Whitehouse, N. D.: *Internal Combustion Engines*, vol. 2, Pergamon Press, 1979.
7. Taylor, C. F.: *The Internal-Combustion Engine in Theory and Practice*, vol. 1, 2d ed., revised, MIT Press, Cambridge, Mass., 1985.
8. Hofbauer, P., and Sator, K.: "Advanced Automotive Power Systems, Part 2: A Diesel for a Subcompact Car," SAE paper 770113, *SAE Trans.*, vol. 86, 1977.
9. Armstrong, D. L., and Stirrat, G. F.: "Ford's 1982 3.8L V6 Engine," SAE paper 820112, *SAE Trans.*, vol. 91, 1982.
10. Chapman, M., Novak, J. M., and Stein, R. A.: "Numerical Modeling of Inlet and Exhaust Flows in Multi-Cylinder Internal Combustion Engines," in *Flows in Internal Combustion Engines*, Winter Annual Meeting, ASME, New York, 1982.

PETITIONER'S EXHIBIT 1002
US PATENT NO. 6,581,565

11. Barnes-Moss, H. W.: "A Designers Viewpoint," in *Passenger Car Engines, Conference Proceedings*, pp. 133–147, Institution of Mechanical Engineers, London, 1975.
12. Asmus, T. W.: "Valve Events and Engine Operation," SAE paper 820749, *SAE Trans.*, Vol. 91, 1982.
13. SAE Recommended Practice, "Engine Terminology and Nomenclature—General," in *SAE Handbook*, J604d.
14. Kastner, L. J., Williams, T. J., and White, J. B.: "Poppet Inlet Valve Characteristics and Their Influence on the Induction Process," *Proc. Instn Mech. Engrs*, vol. 178, pt. 1, no. 36, pp. 955–978, 1963–1964.
15. Woods, W. A., and Khan, S. R.: "An Experimental Study of Flow through Poppet Valves," *Proc. Instn Mech. Engrs*, vol. 180, pt. 3N, pp. 32–41, 1965–1966.
16. Annand, W. J. D., and Roe, G. E.: *Gas Flow in the Internal Combustion Engine*, Haessner Publishing, Newfoundland, N.J., 1974.
17. Tanaka, K.: "Air Flow through Exhaust Valve of Conical Seat," *Int. Congr. Appl. Mech.*, vol. 1, pp. 287–295, 1931.
18. Bicen, A. F., and Whitelaw, J. H.: "Steady and Unsteady Air Flow through an Intake Valve of a Reciprocating Engine," in *Flows in Internal Combustion Engines—II*, FED-vol. 20, Winter Annual Meeting, ASME, 1984.
19. Fukutani, I., and Watanabe, E.: "An Analysis of the Volumetric Efficiency Characteristics of 4-Stroke Cycle Engines Using the Mean Inlet Mach Number Mim," SAE paper 790484, *SAE Trans.*, vol. 88, 1979.
20. Wallace, W. B.: "High-Output Medium-Speed Diesel Engine Air and Exhaust System Flow Losses," *Proc. Instn Mech. Engrs*, vol. 182, pt. 3D, pp. 134–144, 1967–1968.
21. Cole, B. N., and Mills, B.: "The Theory of Sudden Enlargements Applied to Poppet Exhaust-Valve, with Special Reference to Exhaust-Pulse Scavenging," *Proc. Instn Mech. Engrs*, pt. 1B, pp. 364–378, 1953.
22. Toda, T., Nohira, H., and Kobashi, K.: "Evaluation of Burned Gas Ratio (BGR) as a Predominant Factor to NO_x," SAE paper 760765, *SAE Trans.*, vol. 85, 1976.
23. Benson, J. D., and Stebar, R. F.: "Effects of Charge Diluation on Nitric Oxide Emission from a Single-Cylinder Engine," SAE paper 710008, *SAE Trans.*, vol. 80, 1971.
24. Tabaczynski, R. J., Heywood, J. B., and Keck, J. C.: "Time-Resolved Measurements of Hydrocarbon Mass Flow Rate in the Exhaust of a Spark-Ignition Engine," SAE paper 720112, *SAE Trans.*, vol. 81, 1972.
25. Caton, J. A., and Heywood, J. B.: "An Experimental and Analytical Study of Heat Transfer in an Engine Exhaust Port," *Int. J. Heat Mass Transfer*, vol. 24, no. 4, pp. 581–595, 1981.
26. Caton, J. A.: "Comparisons of Thermocouple, Time-Averaged and Mass-Averaged Exhaust Gas Temperatures for a Spark-Ignited Engine," SAE paper 820050, 1982.
27. Phatak, R. G.: "A New Method of Analyzing Two-Stroke Cycle Engine Gas Flow Patterns," SAE paper 790487, *SAE Trans.*, vol. 88, 1979.
28. Rizk, W.: "Experimental Studies of the Mixing Processes and Flow Configurations in Two-Cycle Engine Scavenging," *Proc. Instn Mech. Engrs*, vol. 172, pp. 417–437, 1958.
29. Dedeoglu, N.: "Scavenging Model Solves Problems in Gas Burning Engine," SAE paper 710579, *SAE Trans.*, vol. 80, 1971.
30. Sher, E.: "Investigating the Gas Exchange Process of a Two-Stroke Cycle Engine with a Flow Visualization Rig," *Israel J. Technol.*, vol. 20, pp. 127–136, 1982.
31. Jante, A.: "Scavenging and Other Problems of Two-Stroke Cycle Spark-Ignition Engines," SAE paper 680468, *SAE Trans.*, vol. 77, 1968.
32. Kannappan, A.: "Cumulative Sampling Technique for Investigating the Scavenging Process in Two-Stroke Engine," ASME paper 74-DGP-11, 1974.
33. Ohigashi, S., Kashiwada, Y., and Achiwa, J.: "Scavenging the 2-Stroke Diesel Engine," *Bull. JSME*, vol. 3, no. 9, pp. 130–136, 1960.
34. Huber, E. W.: "Measuring the Trapping Efficiency of Internal Combustion Engines through Continuous Exhaust Gas Analysis," SAE paper 710144, *SAE Trans.*, vol. 80, 1971.
35. Blair, G. P., and Kenny, R. G.: "Further Developments in Scavenging Analysis for Two-Cycle Engines," SAE paper 800038, *SAE Trans.*, vol. 89, 1980.

PETITIONER'S EXHIBIT 1002
US PATENT NO. 6,581,565

36. Baudequin, F., and Rochelle, P.: "Some Scavenging Models for Two-Stroke Engines," *Proc. Instn Mech. Engrs, Automobile Division*, vol. 194, no. 22, pp. 203–210, 1980.
37. Gyssler, G.: "Problems Associated with Turbocharging Large Two-Stroke Diesel Engines," *Proc. CIMAC*, paper B.16, 1965.
38. Annand, W. J. D.: "Compressible Flow through Square-Edged Orifices: An Empirical Approximation for Computer Calculations," *J. Mech. Engng Sci.*, vol. 8, p. 448, 1966.
39. Benson, R. S.: "Experiments on a Piston Controlled Port," *The Engineer*, vol. 210, pp. 875–880, 1960.
40. Watson, N., and Janota, M. S.: *Turbocharging the Internal Combustion Engine*, Wiley-Interscience Publications, John Wiley, New York, 1982.
41. Bhinder, F. S.: "Supercharging Compressors—Problems and Potential of the Various Alternatives," SAE paper 840243, 1984.
42. Bhinder, F. S.: "Some Fundamental Considerations Concerning the Pressure Charging of Small Diesel Engines," SAE paper 830145, 1983.
43. Brandstetter, W., and Dziggel, R.: "The 4- and 5-Cylinder Turbocharged Diesel Engines for Volkswagen and Audi," SAE paper 820441, *SAE Trans.*, vol. 91, 1982.
44. SAE Recommended Practice, "Turbocharger Nomenclature and Terminology," in *SAE Handbook*, J922.
45. Flynn, P. F.: "Turbocharging Four-Cycle Diesel Engines," SAE paper 790314, *SAE Trans.*, vol. 88, 1979.
46. Gyarmathy, G.: "How Does the Comprex Pressure-Wave Supercharger Work?" SAE paper 830234, 1983.
47. Kollbrunner, T. A.: "Comprex Supercharging for Passenger Diesel Car Engines," SAE paper 800884, *SAE Trans.*, vol. 89, 1980.

PETITIONER'S EXHIBIT 1002
US PATENT NO. 6,581,565

CHAPTER 7

SI ENGINE FUEL METERING AND MANIFOLD PHENOMENA

7.1 SPARK-IGNITION ENGINE MIXTURE REQUIREMENTS

The task of the engine induction and fuel systems is to prepare from ambient air and fuel in the tank an air-fuel mixture that satisfies the requirements of the engine over its entire operating regime. In principle, the optimum air/fuel ratio for a spark-ignition engine is that which gives the required power output with the lowest fuel consumption, consistent with smooth and reliable operation. In practice, the constraints of emissions control may dictate a different air/fuel ratio, and may also require the recycling of a fraction of the exhaust gases (EGR) into the intake system. The relative proportions of fuel and air that provide the lowest fuel consumption, smooth reliable operation, and satisfy the emissions requirements, at the required power level, depend on engine speed and load. Mixture requirements and preparation are usually discussed in terms of the air/fuel ratio or fuel/air ratio (see Sec. 2.9) and percent EGR [see Eq. (4.2)]. While the fuel metering system is designed to provide the appropriate fuel flow for the *actual* air flow at each speed and load, the relative proportions of fuel and air can be stated more generally in terms of the fuel/air equivalence ratio ϕ, which is the actual fuel/air ratio normalized by dividing by the stoichiometric fuel/air ratio [Eq.

PETITIONER'S EXHIBIT 1002
US PATENT NO. 6,581,565

(3.8)]. The combustion characteristics of fuel-air mixtures and the properties of combustion products, which govern engine performance, efficiency, and emissions, correlate best for a wide range of fuels relative to the stoichiometric mixture proportions. Where appropriate, therefore, the equivalence ratio will be used as the defining parameter. A typical value for the stoichiometric air/fuel ratio of gasoline is 14.6.† Thus, for gasoline,

$$\phi \approx \frac{14.6}{A/F} \tag{7.1}$$

The effects of equivalence ratio variations on engine combustion, emissions, and performance are discussed more fully in Chaps. 9, 11, and 15. A brief summary is sufficient here. Mixture requirements are different for full-load (wide-open throttle) and for part-load operation. At the former operating condition, complete utilization of the *inducted air* to obtain maximum power for a given displaced volume is the critical issue. Where less than the maximum power at a given speed is required, efficient utilization of the *fuel* is the critical issue. At wide-open throttle, maximum power for a given volumetric efficiency is obtained with rich-of-stoichiometric mixtures, $\phi \approx 1.1$ (see the discussion of the fuel-air cycle results in Sec. 5.5.3). Mixtures that are richer still are sometimes used to increase volumetric efficiency by increasing the amount of charge cooling that accompanies fuel vaporization [see Eq. (6.5)], thereby increasing the inducted air density.

At part-load (or part-throttle) operating conditions, it is advantageous to dilute the fuel-air mixture, either with excess air or with recycled exhaust gas. This dilution improves the fuel conversion efficiency for three reasons:[1] (1) the expansion stroke work for a given expansion ratio is increased as a result of the change in thermodynamic properties of the burned gases—see Secs. 5.5.3 and 5.7.4; (2) for a given mean effective pressure, the intake pressure increases with increasing dilution, so pumping work decreases—see Fig. 5-10; (3) the heat losses to the walls are reduced because the burned gas temperatures are lower. In the absence of strict engine NO_x emission requirements, excess air is the obvious diluent, and at part throttle engines have traditionally operated lean. When tight control of NO_x, HC, and CO emissions is required, operation of the engine with a stoichiometric mixture is advantageous so that a three-way catalyst‡ can be used to clean up the exhaust. The appropriate diluent is then recycled exhaust gases which significantly reduces NO_x emissions from the engine itself. The amount of diluent that the engine will tolerate at any given speed and load depends on the details of the engine's combustion process. Increasing excess air

† Typical value only. Most gasolines have $(A/F)_s$ in the range 14.4 to 14.7. $(A/F)_s$ could lie between 14.1 and 15.2.

‡ A three-way catalyst system, when operated with a close-to-stoichiometric mixture, achieves substantial reductions in NO_x, CO, and HC emissions simultaneously; see Sec. 11.6.2.

PETITIONER'S EXHIBIT 1002
US PATENT NO. 6,581,565

or the amount of recycled exhaust slows down the combustion process and increases its variability from cycle to cycle. A certain minimum combustion repeatability or stability level is required to maintain smooth engine operation. Deterioration in combustion stability therefore limits the amount of dilution an engine can tolerate. As load decreases, less dilution of the *fresh* mixture can be tolerated because the internal dilution of the mixture with residual gas increases (see Sec. 6.4). At idle conditions, the fresh mixture will not usually tolerate any EGR and may need to be stoichiometric or fuel-rich to obtain adequate combustion stability.

Mixture composition requirements over the engine load and speed range are illustrated schematically for the two approaches outlined above in Fig. 7-1. If stoichiometric operation and EGR are not required for emissions control, as load increases the mixture is leaned out from a fuel-rich or close-to-stoichiometric composition at very light load. As wide-open throttle operation is approached at each engine speed, the mixture is steadily enriched to rich-of-stoichiometric at the maximum bmep point. With the stoichiometric operating conditions required for three-way-catalyst-equipped engines, when EGR is used, the percentage of recycled exhaust increases from zero at light load to a maximum at mid-load, and then decreases to zero as wide-open throttle conditions are approached so maximum bmep can be obtained. Combinations of these strategies are possible. For example, lean operation at light load can be used for best efficiency, and

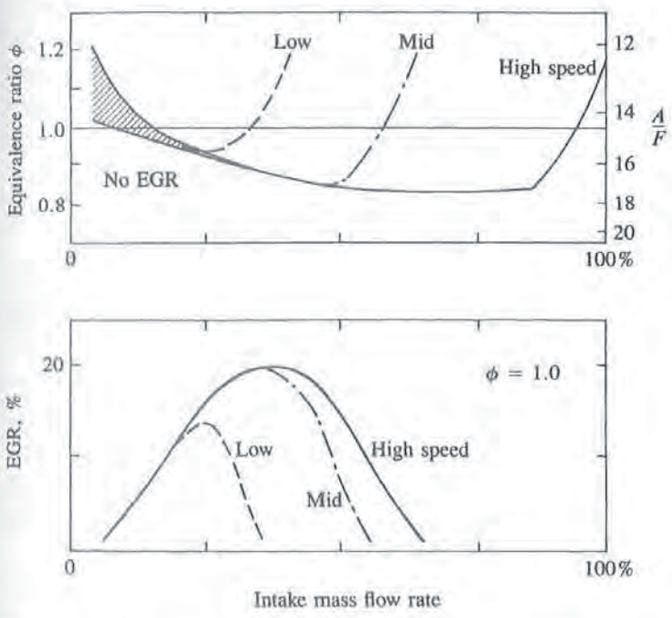


FIGURE 7-1
Typical mixture requirements for two common operating strategies. Top diagram shows equivalence ratio variation with intake mass flow rate (percent of maximum flow at rated speed) at constant low, mid, and high engine speeds. Bottom diagram shows recycled exhaust (EGR) schedule as a function of intake flow rate, for low, mid, and high speeds for stoichiometric operation.

PETITIONER'S EXHIBIT 1002
US PATENT NO. 6,581,565

stoichiometric mixtures (with a three-way catalyst) and/or EGR can be used at mid loads to control NO_x emissions.

In practical spark-ignition engine induction systems, the fuel and air distribution between engine cylinders is not uniform (and also varies in each individual cylinder on a cycle-by-cycle basis). A spread of one or more air/fuel ratios between the leanest and richest cylinders over the engine's load and speed range is not uncommon in engines with conventional carburetors. The average mixture composition must be chosen to avoid excessive combustion variability in the leanest operating cylinder. Thus, as the spread in mixture nonuniformity increases, the mean equivalence ratio must be moved toward stoichiometric and away from the equivalence ratio which gives minimum fuel consumption.

7.2 CARBURETORS

7.2.1 Carburetor Fundamentals

A carburetor has been the most common device used to control the fuel flow into the intake manifold and distribute the fuel across the air stream. In a carburetor, the air flows through a converging-diverging nozzle called a venturi. The pressure difference set up between the carburetor inlet and the throat of the nozzle (which depends on the air flow rate) is used to meter the appropriate fuel flow for that air flow. The fuel enters the air stream through the fuel discharge tube or ports in the carburetor body and is atomized and convected by the air stream past the throttle plate and into the intake manifold. Fuel evaporation starts within the carburetor and continues in the manifold as fuel droplets move with the air flow and as liquid fuel flows over the throttle and along the manifold walls. A modern carburetor which meters the appropriate fuel flow into the air stream over the complete engine operating range is a highly developed and complex device. There are many types of carburetors; they share the same basic concepts which we will now examine.

Figure 7-2 shows the essential components of an elementary carburetor. The air enters the intake section of the carburetor (1) from the air cleaner which removes suspended dust particles. The air then flows into the carburetor venturi (a converging-diverging nozzle) (2) where the air velocity increases and the pressure decreases. The fuel level is maintained at a constant height in the float chamber (3) which is connected via an air duct (4) to the carburetor intake section (1). The fuel flows through the main jet (a calibrated orifice) (5) as a result of the pressure difference between the float chamber and the venturi throat and through the fuel discharge nozzle (6) into the venturi throat where the air stream atomizes the liquid fuel. The fuel-air mixture flows through the diverging section of the venturi where the flow decelerates and some pressure recovery occurs. The flow then passes the throttle valve (7) and enters the intake manifold.

Note that the flow may be unsteady even when engine load and speed are constant, due to the periodic filling of each of the engine cylinders which draws air through the carburetor venturi. The induction time, 1/(2N) (20 ms at 1500

PETITIONER'S EXHIBIT 1002
US PATENT NO. 6,581,565

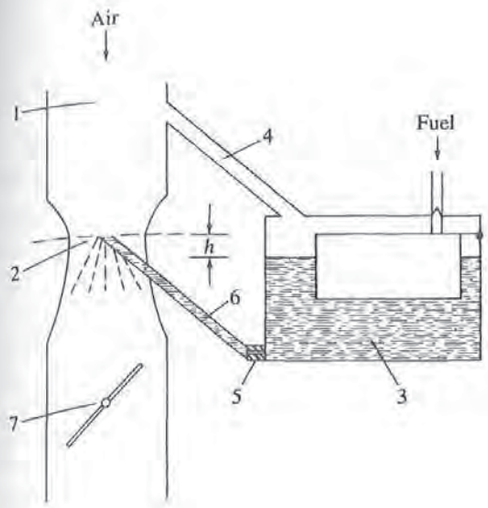


FIGURE 7-2
Schematic of elementary carburetor.
1 Inlet section
2 Venturi throat
3 Float chamber
4 Pressure equalizing passage
5 Calibrated orifice
6 Fuel discharge tube
7 Throttle plate

rev/min), is the characteristic time of this periodic cylinder filling process. Generally, the characteristic times of changes in throttle setting are longer; it takes several engine operating cycles to reestablish steady-state engine operation after a sudden change in throttle position.[2] It is usually assumed that the flow processes in the carburetor can be modeled as quasi steady.

FLOW THROUGH THE VENTURI. Equation (C.8) in App. C relates the mass flow rate of a gas through a flow restriction to the upstream stagnation pressure and temperature, and the pressure at the throat. For the carburetor venturi:

$$\dot{m}_a = \frac{C_{D_T} A_T p_0}{\sqrt{RT_0}} \left(\frac{p_T}{p_0}\right)^{1/\gamma} \left\{ \frac{2\gamma}{\gamma - 1} \left[1 - \left(\frac{p_T}{p_0}\right)^{(\gamma-1)/\gamma} \right] \right\}^{1/2} \tag{7.2}$$

where C_{D_T} and A_T are the discharge coefficient and area of the venturi throat, respectively. If we assume the velocity at the carburetor inlet can be neglected, Eq. (7.2) can be rearranged in terms of the pressure drop from upstream conditions to the venturi throat for the air stream, $\Delta p_a = p_0 - p_T$, as

$$\dot{m}_a = C_{D_T} A_T (2\rho_{a_0} \Delta p_a)^{1/2} \Phi \tag{7.3}$$

where

$$\Phi = \left[\left(\frac{\gamma}{\gamma - 1} \right) \frac{(p_T/p_0)^{2/\gamma} - (p_T/p_0)^{(\gamma+1)/\gamma}}{1 - (p_T/p_0)} \right]^{1/2} \tag{7.4}$$

and accounts for the effects of compressibility. Figure C-3 shows the value of Φ as a function of pressure drop. For the normal carburetor operating range, where $\Delta p_a/p_0 \leq 0.1$, the effects of compressibility which reduce Φ below 1.0 are small.

FLOW THROUGH THE FUEL ORIFICE. Since the fuel is a liquid and therefore essentially incompressible, the fuel flow rate through the main fuel jet is given by

PETITIONER'S EXHIBIT 1002
US PATENT NO. 6,581,565

Eq. (C.2) in App. C as

$$\dot{m}_f = C_{D_o} A_o (2\rho_f \Delta p_f)^{1/2} \tag{7.5}$$

where C_{D_o} and A_o are the discharge coefficient and area of the orifice, respectively, Δp_f is the pressure difference across the orifice, and the orifice area is assumed much less than the passage area. Usually, the fuel level in the float chamber is held below the fuel discharge nozzle, as shown in Fig. 7-2, to prevent fuel spillage when the engine is inclined to the horizontal (e.g., in a vehicle on a slope). Thus,

$$\Delta p_f = \Delta p_a - \rho_f g h$$

where h is typically of order 10 mm.

The discharge coefficient C_{D_o} in Eq. (7.5) represents the effect of all deviations from the ideal one-dimensional isentropic flow. It is influenced by many factors of which the most important are the following: (1) fluid mass flow rate; (2) orifice length/diameter ratio; (3) orifice/approach-area ratio; (4) orifice surface area; (5) orifice surface roughness; (6) orifice inlet and exit chamfers; (7) fluid specific gravity; (8) fluid viscosity; and (9) fluid surface tension. The use of the orifice Reynolds number, $\mathrm{Re}_o = \rho V D_o/\mu$, as a correlating parameter for the discharge coefficient accounts for effects of mass flow rate, fluid density and viscosity, and length scale to a good first approximation. The discharge coefficient of a typical carburetor main fuel-metering system orifice increases smoothly with increasing Re_o.[3]

CARBURETOR PERFORMANCE. The air/fuel ratio delivered by this carburetor is given by

$$\left(\frac{A}{F}\right) = \frac{\dot{m}_a}{\dot{m}_f} = \left(\frac{C_{D_T}}{C_{D_o}}\right)\left(\frac{A_T}{A_o}\right)\left(\frac{\rho_{a_0}}{\rho_f}\right)^{1/2}\left(\frac{\Delta p_a}{\Delta p_a - \rho_f g h}\right)^{1/2} \Phi \tag{7.6}$$

and the equivalence ratio ϕ $[=(A/F)_s/(A/F)]$ by

$$\phi = \frac{(A/F)_s}{\Phi}\left(\frac{C_{D_o}}{C_{D_T}}\right)\left(\frac{A_o}{A_T}\right)\left(\frac{\rho_f}{\rho_{a_0}}\right)^{1/2}\left(1 - \frac{\rho_f g h}{\Delta p_a}\right)^{1/2} \tag{7.7}$$

where $(A/F)_s$ is the stoichiometric air/fuel ratio. The terms A_o, A_T, ρ_f, and ρ_{a_0} are all constant for a given carburetor, fuel, and ambient conditions. Also, except for very low flows, $\rho_f g h \ll \Delta p_a$. The discharge coefficients, C_{D_o} and C_{D_T}, and Φ vary with flow rates, however. Hence, the equivalence ratio of the mixture delivered by an elementary carburetor is not constant.

Figure 7-3 illustrates the performance of the elementary carburetor. The top set of curves shows how Φ, C_{D_T}, and C_{D_o} typically vary with the venturi pressure drop.[4] Note that for $\Delta p_a \leq \rho_f g h$ there is no fuel flow. Once fuel starts to flow, as a consequence of these variations the fuel flow rate increases more rapidly than the air flow rate. The carburetor delivers a mixture of increasing fuel/air equivalence ratio as the flow rate increases. Suppose the venturi and orifice are sized to

PETITIONER'S EXHIBIT 1002
US PATENT NO. 6,581,565

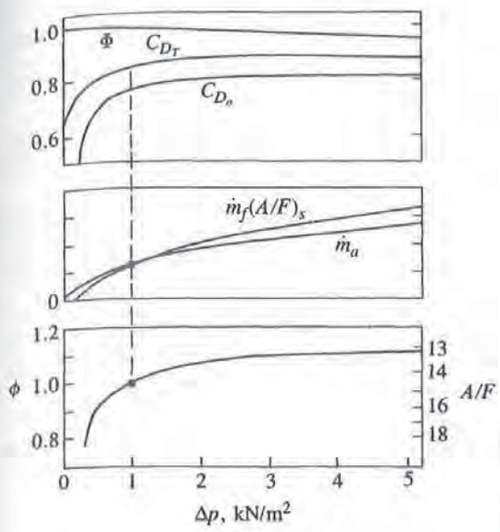


FIGURE 7-3
Performance of elementary carburetor: variation of C_{D_T}, C_{D_o}, Φ, $\dot{m}_f\,(A/F)_s$, $\dot{m}_a$, and equivalence ratio ϕ with venturi pressure drop.

give a stoichiometric mixture at an air flow rate corresponding to 1 kN/m^2 venturi pressure drop (middle graph in Fig. 7-3). At higher air flow rates, the carburetor will deliver a fuel-rich mixture; at very high flow rates it will eventually deliver an essentially constant equivalence ratio. At lower air flow rates, the mixture delivered leans out rapidly. Thus, the elementary carburetor cannot provide the variation in mixture ratio which the engine requires over the complete load range at any given speed (see Fig. 7-1).

The deficiencies of the elementary carburetor can be summarized as follows:

1. At low loads the mixture becomes leaner; the engine requires the mixture to be enriched at low loads.
2. At intermediate loads, the mixture equivalence ratio increases slightly as the air flow increases. The engine requires an almost constant equivalence ratio.
3. As the air flow approaches the maximum wide-open throttle value, the equivalence ratio remains essentially constant. However, the mixture equivalence ratio should increase to 1.1 or greater to provide maximum engine power.
4. The elementary carburetor cannot compensate for transient phenomena in the intake manifold. Nor can it enrich the mixture during engine starting and warm-up.
5. The elementary carburetor cannot adjust to changes in ambient air density (due primarily to changes in altitude).

7.2.2 Modern Carburetor Design

The changes required in the elementary carburetor so that it provides the equivalence ratio versus air flow distribution shown in Fig. 7-1 are:

PETITIONER'S EXHIBIT 1002
US PATENT NO. 6,581,565

1. The *main metering system* must be compensated to provide essentially constant lean or stoichiometric mixtures over the 20 to 80 percent air flow range.
2. An *idle system* must be added to meter the fuel flow at idle and light loads.
3. An *enrichment system* must be added so the engine can provide its maximum power as wide-open throttle is approached.
4. An *accelerator pump* which injects additional fuel when the throttle is opened rapidly is required to maintain constant the equivalence ratio delivered to the engine cylinder.
5. A *choke* must be added to enrich the mixture during engine starting and warm-up to ensure a combustible mixture within each cylinder at the time of ignition.
6. *Altitude compensation* is required to adjust the fuel flow to changes in air density.

In addition, it is necessary to increase the magnitude of the pressure drop available for controlling the fuel flow. Two common methods used to achieve this are the following.

BOOST VENTURIS. The carburetor venturi should give as large a vacuum at the throat as possible at maximum air flow, within the constraints of a low pressure loss across the complete venturi and diffuser. In a single venturi, as the diameter of the throat is decreased at a given air flow to increase the flow velocity and hence the metering signal at the throat, the pressure loss increases. A higher vacuum signal at the venturi throat and higher velocities for improved atomization can be obtained without increasing the overall pressure loss through the use of multiple venturis. Figure 7-4 shows the geometry and the pressure distribution in a typical double-venturi system. A boost venturi is positioned upstream of the throat of the larger main venturi, with its discharge at the location of maximum velocity in the main venturi. Only a fraction of the air flows through the boost venturi. Since the pressure at the boost venturi *exit* equals the pressure

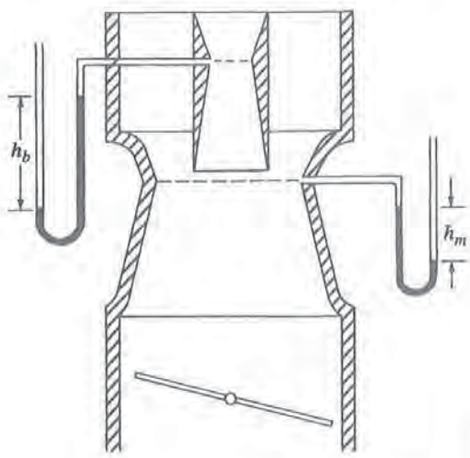


FIGURE 7-4
Schematic of carburetor double-venturi system.

PETITIONER'S EXHIBIT 1002
US PATENT NO. 6,581,565

at the main venturi *throat*, a higher vacuum $\Delta p_b = \rho_m g h_b$ is obtained at the boost venturi throat which can be used to obtain more precise metering of the fuel (ρ_m is the manometer fluid density). Best results are obtained with the boost venturi exit slightly upstream (≈ 5 mm) of the main venturi throat. Because only a fraction of the total air flow goes through the boost venturi, the use of multiple venturis makes it possible to obtain a high velocity air stream (up to 200 m/s) where the fuel is introduced at the boost venturi throat, and adequate vacuum, and to reduce the pressure loss across the total venturi system, without increasing the height of the carburetor. The fuel is better atomized in the smaller boost venturi with its higher air velocity, and since this air and fuel mixture is discharged centrally into the surrounding venturi, a more homogeneous mixture results. The vacuum developed at the venturi throat of a typical double-venturi system is about twice the theoretical vacuum of a single venturi of the same flow area.[5] A triple-venturi system can be used to give further increases in metering signal. The overall discharge coefficient of a multiple-venturi carburetor is lower than a single-venturi carburetor of equal cross-sectional area. The throat area of the main venturi in a multiple-venturi system is usually increased, therefore, above the single-venturi size to compensate for this. Some decrease in air stream velocity is tolerated to maintain a high discharge coefficient (and hence a high volumetric efficiency).[6]

MULTIPLE-BARREL CARBURETORS. Use of carburetors with venturi systems in parallel is a common way of maintaining an adequate part-load metering signal, high volumetric efficiency at wide-open throttle, and minimum carburetor height as engine size and maximum air flow increases. As venturi size in a single-barrel carburetor is increased to provide a higher engine air flow at maximum power, the venturi length increases and the metering signal generated at low flows decreases. Maximum wide-open throttle air flow is some 30 to 70 times the idle air flow (the value depending on engine displacement). Two-barrel carburetors usually consist of two single-barrel carburetors mounted in parallel. Four-barrel carburetors consist of a pair of two-barrel carburetors in parallel, with throttle plates compounded on two shafts. Air flows through the primary barrel(s) at low and intermediate engine loads. At higher loads, the throttle plate(s) on the secondary barrel(s) (usually of larger cross-sectional area) start to open when the air flow exceeds about 50 percent of the maximum engine air flow.

There are many different designs of complete carburetors. The operating principles of the methods most commonly used to achieve the above listed modifications will now be reviewed. Figure 7-5 shows a schematic of a conventional modern carburetor and the names of the various components and fuel passages.

COMPENSATION OF MAIN METERING SYSTEM. Figure 7-6 shows a main fuel-metering system with air-bleed compensation. As the pressure at the venturi throat decreases, air is bled through an orifice (or series of orifices) into the main fuel well. This flow reduces the pressure difference across the main fuel-metering orifice which no longer experiences the full venturi vacuum. The mixing of bleed

PETITIONER'S EXHIBIT 1002
US PATENT NO. 6,581,565

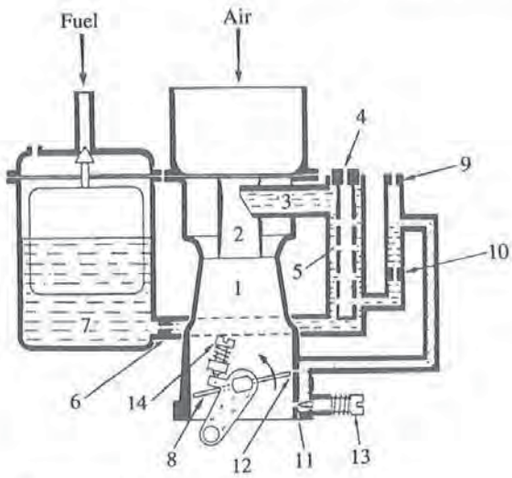


FIGURE 7-5
Schematic of modern carburetor.

1 Main venturi
2 Boost venturi
3 Main metering spray tube or nozzle
4 Air-bleed orifice
5 Emulsion tube or well
6 Main fuel-metering orifice
7 Float chamber
8 Throttle plate
9 Idle air-bleed orifice
10 Idle fuel orifice
11 Idle mixture orifice
12 Transition orifice
13 Idle mixture adjusting screw
14 Idle throttle setting adjusting screw

Fuel enters the air stream from the main metering system through (3). At idle, fuel enters air at (11). During transition, fuel enters at (11), (12), and (3). (*Courtesy S.p.A.E. Weber.*)

air with the fuel forms an emulsion which atomizes more uniformly to smaller drop sizes on injection at the venturi throat. The schematic in Fig. 7-6 illustrates the operating principle. When the engine is not running, the fuel is at the same level in the float bowl and in the main well. With the engine running, as the throttle plate is opened, the air flow and the vacuum in the venturi throat increase. For $\Delta p_v (= p_0 - p_v) < \rho_f g h_1$, there is no fuel flow from the main metering system. For $\rho_f g h_1 < \Delta p_v < \rho_f g h_2$, only fuel flows through the main well and nozzle, and the system operates just like an elementary carburetor. For $\Delta p_v > \rho_f g h_2$, air enters the main well together with fuel. The amount of air entering the well is controlled by the size of the main air-bleed orifice. The amount of air is

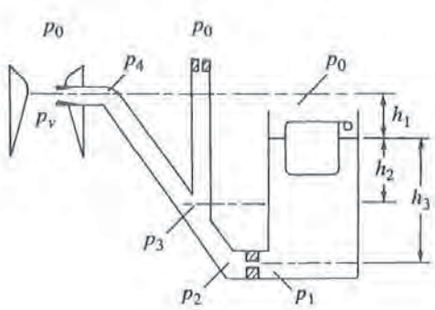


FIGURE 7-6
Schematic of main metering system with air-bleed compensation.

PETITIONER'S EXHIBIT 1002
US PATENT NO. 6,581,565

small and does not significantly affect the composition of the mixture. The air-bleed mass flow rate is given by

$$\dot{m}_{a_b} = C_{D_b} A_b [2(p_0 - p_3)\rho_a]^{1/2} \tag{7.8}$$

where C_{D_b} and A_b are the discharge coefficient and the area of the air-bleed orifice. The fuel mass flow rate through the fuel orifice is given by

$$\dot{m}_f = C_{D_o} A_o [2(p_1 - p_2)\rho_f]^{1/2} \tag{7.9}$$

where

$$p_1 = p_0 + \rho_f g h_3 \qquad \text{and} \qquad p_2 = p_3 + \rho_f g(h_3 - h_2)$$

The density of the emulsion ρ_{em} in the main well and nozzle is usually approximated by

$$\rho_{em} = \frac{\dot{m}_{a_b} + \dot{m}_f}{\dot{m}_{a_b}/\rho_a + \dot{m}_f/\rho_f} \tag{7.10}$$

Since typical values are $\rho_f = 730$ kg/m^3 and $\rho_a = 1.14$ kg/m^3, usually $\rho_f \gg \rho_{em} \gg \rho_a$. Thus, as the air-bleed flow rate increases, the height of the column of emulsion becomes less significant. However, the decrease in emulsion density due to increasing air bleed increases the flow velocity, which results in a significant pressure drop across the main nozzle. This pressure drop depends on nozzle length and diameter, fuel flow rate, bleed air flow rate, relative velocity between fuel and bleed air, and fuel properties. It is determined empirically, and has been found to correlate with ρ_{em} [as defined by Eq. (7.10)].[2, 6] The pressure loss at the main discharge nozzle with two-phase flow can be several times the pressure loss with single-phase flow.

Figure 7-7 illustrates the behavior of the system shown in Fig. 7-6: $\dot{m}_a$, $\dot{m}_f$, and the fuel/air equivalence ratio ϕ are plotted against Δp_v. Once the bleed system is operating ($\Delta p_v > \rho_f g h_2$) the fuel flow rate is reduced below its equivalent elementary carburetor value (the $A_b = 0$ line). As the bleed orifice area is increased, in the limit of large A_b and neglecting the pressure losses in the main nozzle, the fuel flow rate remains constant ($A_b \to \infty$). An appropriate choice of bleed orifice area A_b will provide the desired equivalence ratio versus pressure drop or air flow characteristic.

Additional control flexibility is obtained in practice through use of a second orifice, or of a series of holes in the main well or emulsion tube as shown in Fig. 7-5. Main metering systems with controlled air bleed provide reliable and stable control of mixture composition at part throttle engine operation. They are simple, have considerable design flexibility, and atomize the fuel effectively. In some carburetor designs, an additional compensation system consisting of a tapered rod or needle in the main metering orifice is used. The effective open area of the main metering orifice, and hence the fuel flow rate, can thus be directly related to throttle position (and manifold vacuum).

A wide range of two-phase flow patterns can be generated by bleeding an air flow into a liquid flow. Fundamental studies of the generation and flow of

PETITIONER'S EXHIBIT 1002
US PATENT NO. 6,581,565

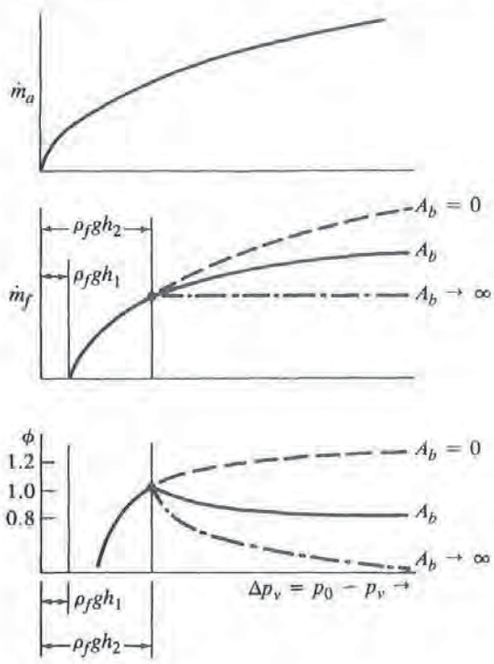


FIGURE 7-7
Metering characteristics of system with air-bleed compensation: mass flow rate of air $\dot{m}_a$, mass flow rate of fuel $\dot{m}_f$, and equivalence ratio ϕ as functions of venturi pressure drop for different air-bleed orifice areas A_b.

two-phase mixtures in small diameter tubes with bleed holes similar to those used in carburetors have been carried out.[7] For a given pipe and bleed hole size, the type of flow pattern set up depends on the flow rates of the two phases.

IDLE SYSTEM. The idle system is required because at low air flows through the carburetor insufficient vacuum is created at the venturi throat to draw fuel into the air stream. However, at idle and light loads, the manifold vacuum is high, with the pressure drop occurring across the almost-closed throttle plate. This low manifold pressure at idle is exploited for the idle fuel system by connecting the main fuel well to an orifice in the throttle body downstream of the throttle plate. Figure 7-5 shows the essential features of an idle system. The main well (5) is connected through one or more orifices (10), past one or more idle air-bleed orifices (or holes) (9), past an idle mixture adjusting screw (13), to the idle discharge port (11) in the throttle body. Emulsifying air is admitted into the idle system [at (9) and (12)] to reduce the pressure drop across the idle port and permit larger-sized ports (which are easier to manufacture) to be used. Satisfactory engine operation at idle is obtained empirically by means of the idle throttle position stop adjustment (14) and the idle mixture adjustment (13). As the throttle is opened from its idle position, the idle metering system performs a transitional function. One or more holes (12) located above the idle discharge port (11) assist as air bleeds when the throttle is at or near its idle position. As the throttle plate opens and the air flow increases, these additional discharge holes are exposed to the manifold vacuum. Additional fuel is forced out of these holes into the air stream to provide the appropriate mixture ratio. As the throttle plate is opened further, the main fuel metering system starts to supply fuel also. Because the two

PETITIONER'S EXHIBIT 1002
US PATENT NO. 6,581,565

systems are coupled, they interact and the main system behavior in this *transition region* is modified by the fuel flow through the idle system. The total combined fuel flow provides a rich (or close-to-stoichiometric) mixture at idle, a progressive leaning of the mixture as air flow increases, and eventually (as the main system takes over full control of the fuel flow rate) an approximately constant mixture composition.

POWER ENRICHMENT SYSTEM. This system delivers additional fuel to enrich the mixture as wide-open throttle is approached so the engine can deliver its maximum power. The additional fuel is normally introduced via a submerged valve which communicates directly with the main discharge nozzle, bypassing the metering orifice. The valve, which is spring loaded, is operated either mechanically through a linkage with the throttle plate (opening as the throttle approaches its wide-open position) or pneumatically (using manifold vacuum).

ACCELERATOR PUMP. When the throttle plate is opened rapidly, the fuel-air mixture flowing into the engine cylinder leans out temporarily. The primary reason for this is the time lag between fuel flow into the air stream at the carburetor and the fuel flow past the inlet valve (see Sec. 7.6.3). While much of the fuel flow into the cylinder is fuel vapor or small fuel droplets carried by the air stream, a fraction of the fuel flows onto the manifold and port walls and forms a liquid film. The fuel which impacts on the walls evaporates more slowly than fuel carried by the air stream and introduces a lag between the air/fuel ratio produced at the carburetor and the air/fuel ratio delivered to the cylinder. An accelerator pump is used as the throttle plate is opened rapidly to supply additional fuel into the air stream at the carburetor to compensate for this leaning effect. Typically, fuel is supplied to the accelerator pump chamber from the float chamber via a small hole in the bottom of the fuel bowl, past a check valve. A pump diaphragm and stem is actuated by a rod attached to the throttle plate lever. When the throttle is opened to increase air flow, the rod-driven diaphragm will increase the fuel pressure which shuts the valve and discharges fuel past a discharge check valve or weight in the discharge passage, through the accelerator pump discharge nozzle(s), and into the air stream. A calibrated orifice controls the fuel flow. A spring connects the rod and diaphragm to extend the fuel discharge over the appropriate time period and to reduce the mechanical strain on the linkage.

CHOKE. When a cold engine is started, especially at low ambient temperatures, the following factors introduce additional special requirements for the complete carburetor:

1. Because the starter-cranked engine turns slowly (70 to 150 rev/min) the intake manifold vacuum developed during engine start-up is low.
2. This low manifold vacuum draws a lower-than-normal fuel flow from the carburetor idle system.

PETITIONER'S EXHIBIT 1002
US PATENT NO. 6,581,565

3. Because of the low manifold temperature and vacuum, fuel evaporation in the carburetor, manifold, and inlet port is much reduced.

Thus, during cranking, the mixture which reaches the engine cylinder would be too lean to ignite. Until normal manifold conditions are established, fuel distribution is also impaired. To overcome these deficiencies and ensure prompt starts and smooth operation during engine warm-up, the carburetor must supply a fuel-rich mixture. This is obtained with a choke. Once normal manifold conditions are established, the choke must be excluded. The primary element of a typical choke system is a plate, upstream of the carburetor, which can close off the intake system. At engine start-up, the choke plate is closed to restrict the air flow into the carburetor barrel. This causes almost full manifold vacuum within the venturi which draws a large fuel flow through the main orifice. When the engine starts, the choke is partly opened to admit the necessary air flow and reduce the vacuum in the venturi to avoid flooding the intake with fuel. As the engine warms up, the choke is opened either manually or automatically with a thermostatic control. For normal engine operation the choke plate is fully open and does not influence carburetor performance. A manifold vacuum control is often used to close the choke plate partially if the engine is accelerated during warm-up. During engine warm-up the idle speed is increased to prevent engine stalling. A fast idle cam is rotated into position by the automatic choke lever.

ALTITUDE COMPENSATION. An inherent characteristic of the conventional float type carburetor is that it meters fuel flow in proportion to the air *volume* flow rate. Air density changes with ambient pressure and temperature, with changes due to changes in pressure with altitude being most significant. For example, at 1500 m above sea level, mean atmospheric pressure is 634 mmHg or 83.4 percent of the mean sea-level value. While ambient temperature variations, winter to summer, can produce changes of comparable magnitude, the temperature of the air entering the carburetor for warmed-up engine operation is controlled to within much closer tolerances by drawing an appropriate fraction of the air from around the exhaust manifold.

Equation (7.6) shows how the air/fuel ratio delivered by the main metering system will vary with inlet air conditions. The primary dependence is through the $\sqrt{\rho_{a_0}}$ term; depending on what is held constant (e.g., throttle setting or air mass flow rate) there may be an additional, much smaller dependence through Φ and Δp_a (see Ref. 5). To a good approximation, the enrichment E with increasing altitude z is given by

$$1 + E = \frac{(F/A)_z}{(F/A)_0} = \left(\frac{\rho_{a_0}}{\rho_{a_z}}\right)^{1/2} \tag{7.11}$$

For $z = 1500$ m, $E = 9.5$ percent; thus, a cruise equivalence ratio of 0.9 or $(A/F) = 16.2$ would be enriched to close to stoichiometric.

The effects of increase in altitude on the carburetor flow curve shown in Fig. 7-1 are: (1) to enrich the entire part-throttle portion of the curve and (2) to

PETITIONER'S EXHIBIT 1002
US PATENT NO. 6,581,565

bring in the power-enrichment system at a lower air flow rate due to decreased manifold vacuum. To reduce the impact to changes in altitude on engine emissions of CO and HC, modern carburetors are altitude compensated. A number of methods can be used to compensate for changes in ambient pressure with altitude:

1. *Venturi bypass method.* To keep the air volume flow rate through the venturi equal to what it was at sea-level atmospheric pressure (calibration condition), a bypass circuit around the venturi for the additional volume flow is provided.
2. *Auxiliary jet method.* An auxiliary fuel metering orifice with a pressure-controlled tapered metering rod connects the fuel bowl to the main well in parallel with the main metering orifice.
3. *Fuel bowl back-suction method.* As altitude increases, an aneroid bellows moves a tapered rod from an orifice near the venturi throat, admitting to the bowl an increasing amount of the vacuum signal developed at the throat.
4. *Compensated air-bleed method.* The orifices in the bleed circuits to each carburetor system are fitted with tapered metering pins actuated by a single aneroid bellows.[8]

TRANSIENT EFFECTS. The pulsating and transient nature of the flow through a carburetor during actual engine operation is illustrated by the data shown in Fig. 7-8.[2] The changes in pressure with time in the intake manifold and at the boost venturi throat of a standard two-barrel carburetor installed on a production V-8 engine are shown as the throttle is opened from light load (22°) to wide-open throttle at 1000 rev/min. Note the rapid increase in boost venturi suction as the throttle is suddenly opened. This results from the sudden large increase in the air flow rate and corresponding increase in air velocity within the boost venturi. Note also that the pressure fluctuations decay rapidly, and within a few engine revolutions have stabilized at the periodic values associated with the new throttle angle. At wide-open throttle, the pulsating nature of the flow as each

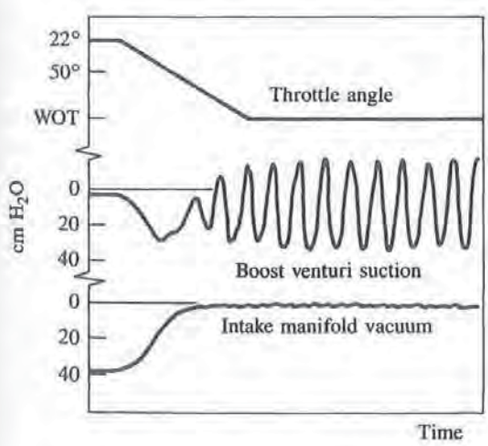


FIGURE 7-8
Throttle angle, boost venturi suction, and intake manifold vacuum variation with time as throttle is opened from light load (22°) to wide-open throttle at 1000 rev/min. Standard two-barrel carburetor and production V-8 engine.[2]

PETITIONER'S EXHIBIT 1002
US PATENT NO. 6,581,565

cylinder draws in its charge is evident. The pressure drop across the main metering jet also fluctuates. The pulsations in the venturi air flow (and hence fuel flow) due to the filling of each cylinder in turn are negligibly small at small throttle angles and increase to a maximum at wide-open throttle. At small throttle openings, the choked flow at the throttle plate prevents the manifold pressure fluctuations from propagating upstream into the venturi. The effective time-averaged boost venturi suction is greater for the pulsating flow case than for the steady flow case. If the ratio of the effective metering signal for a pulse cycle to that for steady air flow at the same average mass flow is denoted as $1 + \Omega$, where Ω is the pulsation factor, then Ω is related to the amplitude and frequency of pressure waves within the intake manifold as well as the damping effect of the throttle plate. An empirical equation for Ω is

$$\Omega = \frac{\text{constant} \times (1 - M)p_m n_R}{N n_{c/b}} \tag{7.12}$$

where M is the throttle plate Mach number, p_m the manifold pressure, n_R the number of revolutions per power stroke, N the crank speed, and $n_{c/b}$ the number of cylinders per barrel. The value of the constant depends on carburetor and engine geometry. For p_m in kilonewtons per square meter and N in revolutions per minute a typical value for the constant is 7.3.[2] Thus, at wide-open throttle at 1500 rev/min, Ω has a value of about 0.2. The transient behavior of the air and fuel flows in the manifold are discussed more fully in Sec. 7.6.

7.3 FUEL-INJECTION SYSTEMS

7.3.1 Multipoint Port Injection

The fuel-injection systems for conventional spark-ignition engines inject the fuel into the engine intake system. This section reviews systems where the fuel is injected into the intake port of each engine cylinder. Thus these systems require one injector per cylinder (plus, in some systems, one or more injectors to supplement the fuel flow during starting and warm-up). There are both mechanical injection systems and electronically controlled injection systems. The advantages of port fuel injection are increased power and torque through improved volumetric efficiency and more uniform fuel distribution, more rapid engine response to changes in throttle position, and more precise control of the equivalence ratio during cold-start and engine warm-up. Fuel injection allows the amount of fuel injected per cycle, for each cylinder, to be varied in response to inputs derived from sensors which define actual engine operating conditions. Two basic approaches have been developed; the major difference between the two is the method used to determine the air flow rate.

Figure 7-9 shows a schematic of a *speed-density* system, where engine speed and manifold pressure and air temperature are used to calculate the engine air flow. The electrically driven fuel pump delivers the fuel through a filter to the fuel line. A pressure regulator maintains the pressure in the line at a fixed value (e.g.,

PETITIONER'S EXHIBIT 1002
US PATENT NO. 6,581,565

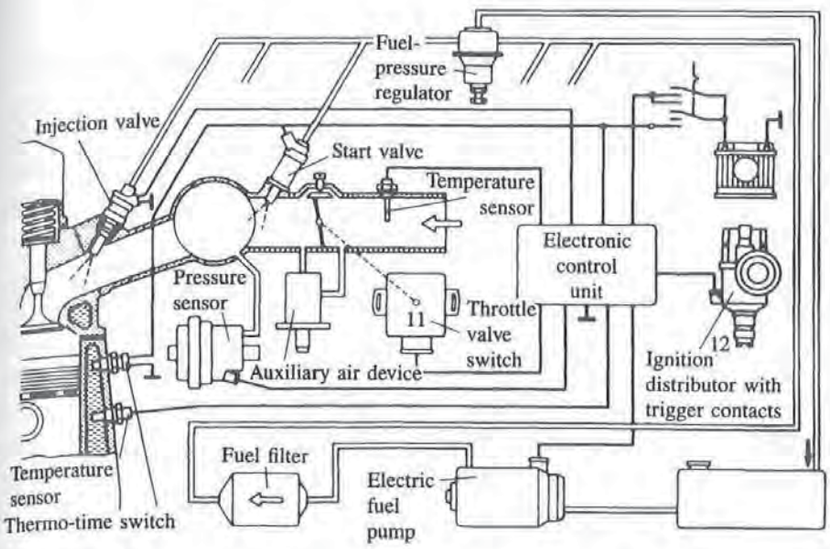


FIGURE 7-9
Speed-density electronic multipoint port fuel-injection system: Bosch D-Jetronic System.[9] (*Courtesy Robert Bosch GmbH and SAE.*)

270 kN/m^2, 39 lb/in^2, usually relative to manifold pressure to maintain a constant fuel pressure drop across the injectors). Branch lines lead to each injector; the excess fuel returns to the tank via a second line. The inducted air flows through the air filter, past the throttle plate to the intake manifold. Separate runners and branches lead to each inlet port and engine cylinder. An electromagnetically actuated fuel-injection valve (see Fig. 7-10) is located either in the intake manifold tube or the intake port of each cylinder. The major components of the injector are the valve housing, the injector spindle, the magnetic plunger to which the spindle is connected, the helical spring, and the solenoid coil. When the solenoid is not excited, the solenoid plunger of the magnetic circuit is forced, with its seal, against the valve seat by the helical spring and closes the fuel passage. When the solenoid coil is excited, the plunger is attracted and lifts the spindle about

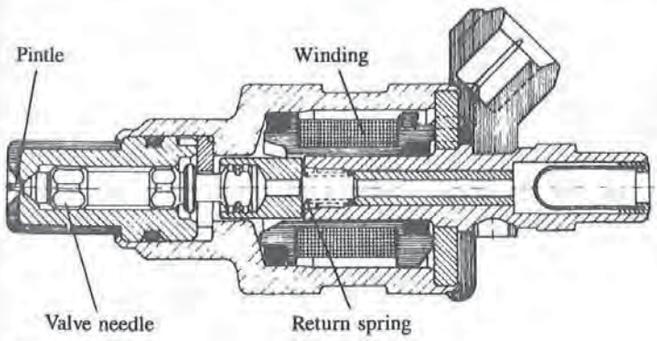


FIGURE 7-10
Cross section of fuel injector.[10]

PETITIONER'S EXHIBIT 1002
US PATENT NO. 6,581,565

0.15 mm so that fuel can flow through the calibrated annular passage around the valve stem. The front end of the injector spindle is shaped as an atomizing pintle with a ground top to atomize the injected fuel. The relatively narrow spray cone of the injector, shown in the photo in Fig. 7-11, minimizes the intake manifold wall wetting with liquid fuel. The mass of fuel injected per injection is controlled by varying the duration of the current pulse that excites the solenoid coil. Typical injection times for automobile applications range from about 1.5 to 10 ms.[11]

The appropriate coil excitation pulse duration or width is set by the electronic control unit (ECU). In the speed-density system, the primary inputs to the ECU are the outputs from the manifold pressure sensor, the engine speed sensor (usually integral with the distributor), and the temperature sensors installed in the intake manifold to monitor air temperature and engine block to monitor the water-jacket temperature—the latter being used to indicate fuel-enrichment requirements during cold-start and warm-up. For warm-engine operation, the mass of air per cylinder per cycle m_a is given by

$$m_a = \eta_v(N)\rho_a(T_i, p_i)V_d = \frac{\eta_v V_d p_i}{R_a T_i} \tag{7.13}$$

where η_v is the volumetric efficiency, N is engine speed, ρ_a is the inlet air density, and V_d is the displaced volume per cylinder. The electronic control unit forms the pulse which excites the injector solenoids. The pulse width depends primarily on the manifold pressure; it also depends on the variation in volumetric efficiency η_v with speed N and variations in air density due to variations in air temperature. The control unit also initiates mixture enrichment during cold-engine operation and during accelerations that are detected by the throttle sensor.

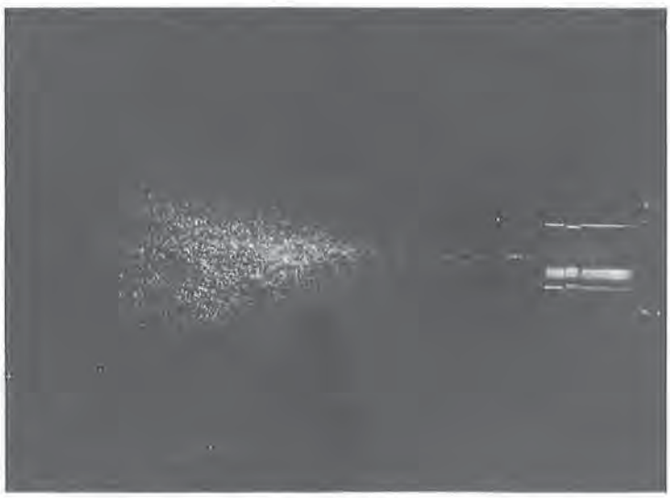


FIGURE 7-11
Short time-exposure photograph of liquid fuel spray from Bosch-type injector. (*Courtesy Robert Bosch GmbH.*)

PETITIONER'S EXHIBIT 1002
US PATENT NO. 6,581,565

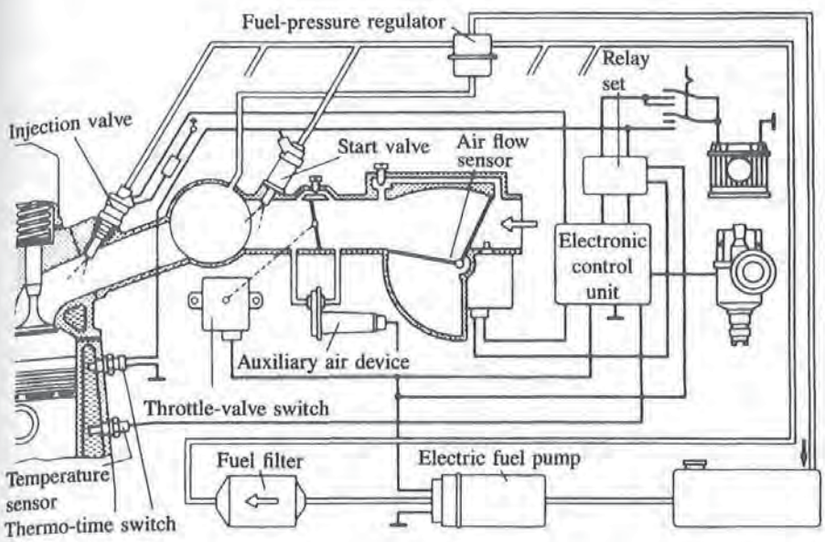


FIGURE 7-12
Electronic multipoint port fuel-injection system with air-flow meter: Bosch L-Jetronic system.[9] (*Courtesy Robert Bosch GmbH and SAE.*)

Figure 7-12 shows an alternative EFI system (the Bosch L-Jetronic) which uses an air-flow meter to measure air flow directly. The air-flow meter is placed upstream of the throttle. The meter shown measures the force exerted on a plate as it is displaced by the flowing air stream; it provides a voltage proportional to the air flow rate. An alternative air-flow measuring approach is to use a hot-wire air mass flow meter.[10] The advantages of direct air-flow measurement are:[12] (1) automatic compensation for tolerances, combustion chamber deposit buildup, wear and changes in valve adjustments; (2) the dependence of volumetric efficiency on speed and exhaust backpressure is automatically accounted for; (3) less acceleration enrichment is required because the air-flow signal precedes the filling of the cylinders; (4) improved idling stability; and (5) lack of sensitivity of the system to EGR since only the fresh air flow is measured.

The mass of air inducted per cycle to each cylinder, m_a, varies as

$$m_a \propto \frac{\dot{m}_a}{N} \tag{7.14}$$

Thus the primary signals for the electronic control unit are air flow and engine speed. The pulse width is inversely proportional to speed and directly proportional to air flow. The engine block temperature sensor, starter switch, and throttle valve switch provide input signals for the necessary adjustments for cold-start, warm-up, idling, and wide-open throttle enrichment.

For cold-start enrichment, one (or more) cold-start injector valve is used to inject additional fuel into the intake manifold (see Figs. 7-9 and 7-12). Since short opening and closing times are not important, this valve can be designed to

PETITIONER'S EXHIBIT 1002
US PATENT NO. 6,581,565

provide extremely fine atomization of the fuel to minimize the enrichment required.

Mechanical, air-flow-based metering, continuous injection systems are also used. Figure 7-13 shows a schematic of the Bosch K-Jetronic system.[9,10] Air is drawn through the air filter, flows past the air-flow sensor, past the throttle valve, into the intake manifold, and into the individual cylinders. The fuel is sucked out of the tank by a roller-cell pump and fed through the fuel accumulator and filter to the fuel distributor. A primary pressure regulator in the fuel distributor maintains the fuel pressure constant. Excess fuel not required by the engine flows back to the tank. The mixture-control unit consists of the air-flow sensor and fuel distributor. It is the most important part of the system, and provides the desired metering of fuel to the individual cylinders by controlling the cross section of the metering slits in the fuel distributor. Downstream of each of these metering slits is a differential pressure valve which for different flow rates maintains the pressure drop at the slits constant.

Fuel-injection systems offer several options regarding the timing and location of each injection relative to the intake event.[10] The K-Jetronic mechanical injection system injects fuel continuously in front of the intake valves with the spray directed toward the valves. Thus about three-quarters of the fuel required for any engine cycle is stored temporarily in front of the intake valve, and one-quarter enters the cylinder directly during the intake process.

With electronically controlled injection systems, the fuel is injected intermittently toward the intake valves. The fuel-injection pulse width to provide the appropriate mass of fuel for each cylinder air charge varies from about 1.5 to 10 ms over the engine load and speed range. In crank angle degrees this varies

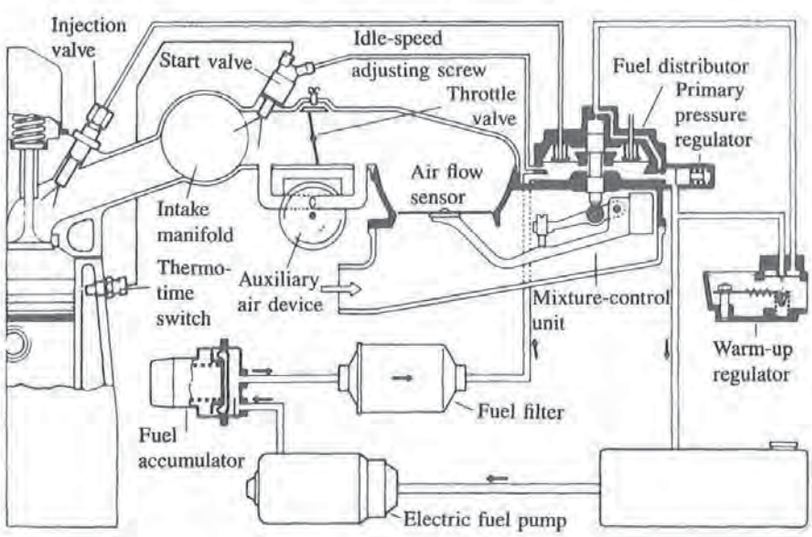


FIGURE 7-13
Mechanical multipoint port fuel-injection system: Bosch K-Jetronic system.[9] (*Courtesy Robert Bosch GmbH and SAE.*)

PETITIONER'S EXHIBIT 1002
US PATENT NO. 6,581,565

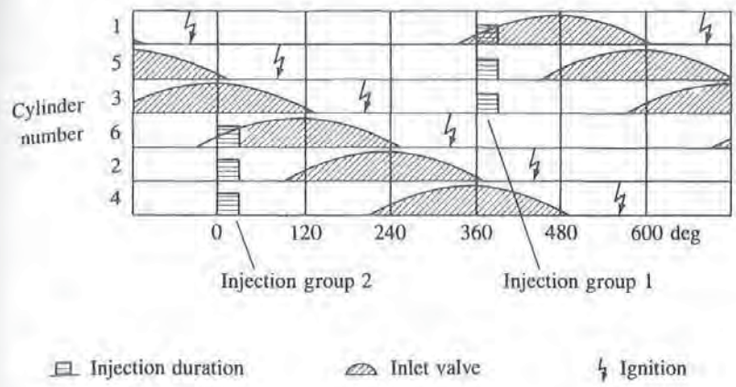


FIGURE 7-14
Injection pulse diagram for D-Jetronic system in six-cylinder engine.[10]

from about 10° at light load and low speed to about 300° at maximum speed and load. Thus the pulse width varies from being much less than to greater than the duration of the intake stroke. To reduce the complexity of the electronic control unit, groups of injectors are often operated simultaneously. In the Bosch L-Jetronic system, all injectors are operated simultaneously. To achieve adequate mixture uniformity, given the short pulse width relative to the intake process over much of the engine load-speed range, fuel is injected twice per cycle; each injection contributes half the fuel quantity required by each cylinder per cycle. (This approach is called simultaneous double-firing.) In the speed-density system, the injectors are usually divided into groups, each group being pulsed simultaneously. For example, for a six-cylinder engine, two groups of three injectors may be used. Injection for each group is timed to occur while the inlet valves are closed or just starting to open, as shown in Fig. 7-14. The other group of injectors inject one crank revolution later. Sequential injection timing, where the phasing of *each* injection pulse relative to its intake valve lift profile is the same, is another option. Engine performance and emissions do change as the timing of the start of injection relative to inlet valve opening is varied. Injection with valve lift at its maximum, or decreasing, is least desirable.[10]

7.3.2 Single-Point Throttle-Body Injection

Single-point fuel-injection systems, where one or two electronically controlled injectors meter the fuel into the air flow directly above the throttle body, are also used. They provide straightforward electronic control of fuel metering at lower cost than multipoint port injection systems. However, as with carburetor systems, the problems associated with slower transport of fuel than the air from upstream of the throttle plate to the cylinder must now be overcome (see Sec. 7.6). Figure 7-15 shows a cutaway of one such system.[13] Two injectors, each in a separate air-flow passage with its own throttle plate, meter the fuel in response to calibrations of air flow based on intake manifold pressure, air temperature, and

PETITIONER'S EXHIBIT 1002
US PATENT NO. 6,581,565

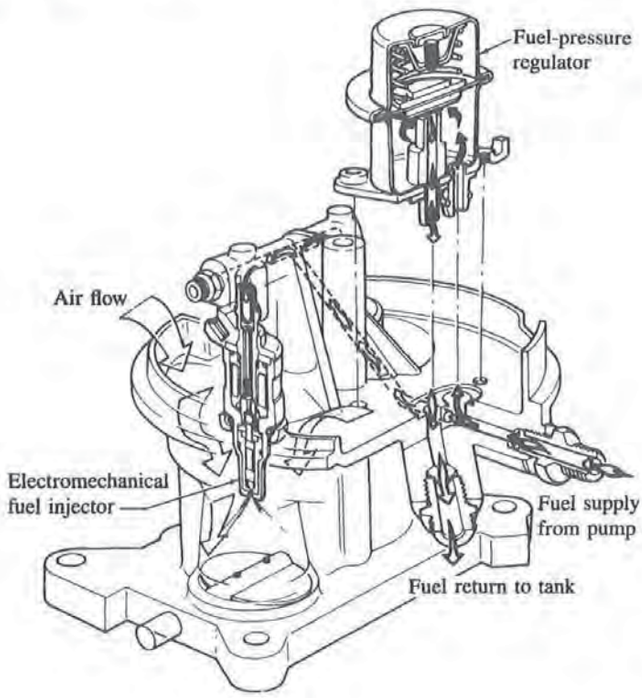


FIGURE 7-15
Cutaway drawing of a two-injector throttle-body electronic fuel-injection system.[13]

engine speed using the speed-density EFI logic described in the previous section. Injectors are fired alternatively or simultaneously, depending on load and speed and control logic used. Under alternative firing, each injection pulse corresponds to one cylinder filling. Smoothing of the fuel-injection pulses over time is achieved by proper placement of the fuel injector assembly above the throttle bore and plate. The walls and plate accumulate liquid fuel which flows in a sheet toward the annular throttle opening (see Sec. 7.6.3). The high air velocity created

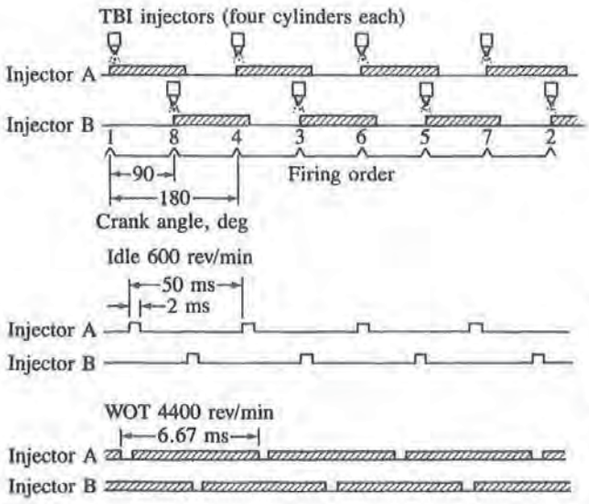


FIGURE 7-16
Injector fuel delivery schedule for two-injector throttle-body injection system for eight-cylinder engine with dual plane intake manifold. Each injection nozzle feeds one plane of the manifold and its four cylinders.[14]

PETITIONER'S EXHIBIT 1002
US PATENT NO. 6,581,565

by the pressure drop across the throttle shears and atomizes the liquid sheet. Vigorous mixing of fuel and air then occurs, especially at part throttle, and provides good mixture uniformity and distribution between cylinders. Injector fuel delivery scheduling is illustrated in Fig. 7-16 for an eight-cylinder engine for a throttle-body fuel-injection system.[14]

7.4 FEEDBACK SYSTEMS

It is possible to reduce engine emissions of the three pollutants—unburned hydrocarbons, carbon monoxide, and oxides of nitrogen—with a single catalyst in the exhaust system if the engine is operated very close to the stoichiometric air/fuel ratio. Such systems (called three-way catalyst systems) are described in more detail in Sec. 11.6.2. The engine operating air/fuel ratio is maintained close to stoichiometric through the use of a sensor in the exhaust system, which provides a voltage signal dependent on the oxygen concentration in the exhaust gas stream. This signal is the input to a feedback system which controls the fuel feed to the intake.

The sensor [called an oxygen sensor or lambda sensor—λ being the symbol used for the relative air/fuel ratio, Eq. (3.9)] is an oxygen concentration cell with a solid electrolyte through which the current is carried by oxygen ions. The electrolyte is yttria (Y_2O_3)-stabilized zirconia (ZrO_2) ceramic which separates two gas chambers (the exhaust manifold and the atmosphere) which have different oxygen partial pressures. The cell can be represented as a series of interfaces as follows:

Exhaust	Metal	Ceramic	Metal	Air
p'_{O_2}	M_e	ZrO_2, Y_2O_3	M_e	p''_{O_2}

p''_{O_2} is the oxygen partial pressure of the air (≈ 20 kN/m^2) and p'_{O_2} is the equilibrium oxygen partial pressure in the exhaust gases. An electrochemical reaction takes place at the metal electrodes:

$$O_2 + 4M_e \rightleftharpoons 2O^{2-}$$

and the oxygen ions transport the current across the cell. The open-circuit output voltage of the cell V_o can be related to the oxygen partial pressures p'_{O_2} and p''_{O_2} through the Nernst equation:

$$V_o = \frac{RT}{4F} \ln \left(\frac{p''_{O_2}}{p'_{O_2}} \right) \tag{7.15}$$

where F is the Faraday constant. Equilibrium is established in the exhaust gases by the catalytic activity of the platinum metal electrodes. The oxygen partial pressure in equilibrated exhaust gases decreases by many orders of magnitude as the equivalence ratio changes from 0.99 to 1.01, as shown in Fig. 7-17*a*. Thus the sensor output voltage increases rapidly in this transition from a lean to a rich

PETITIONER'S EXHIBIT 1002
US PATENT NO. 6,581,565

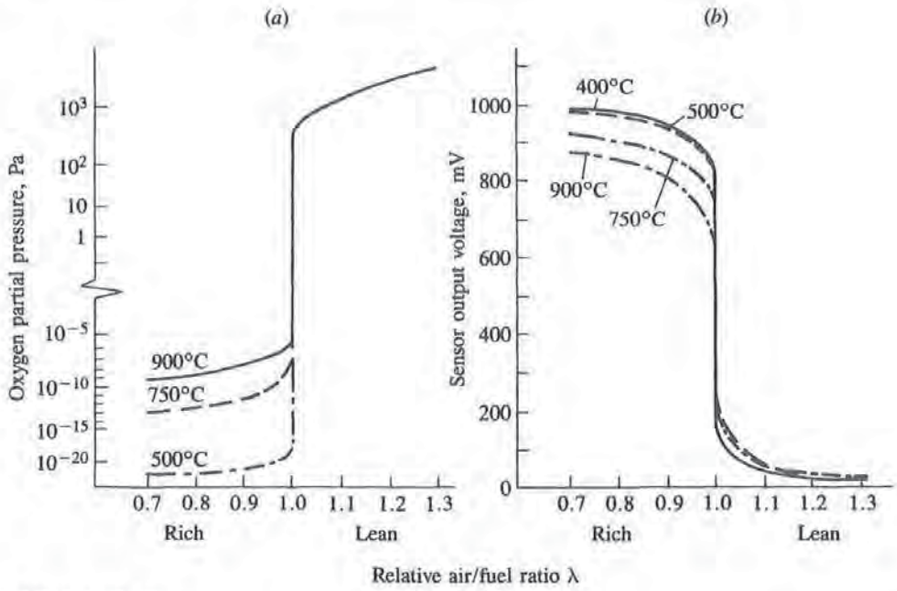


FIGURE 7-17
Oxygen-sensor characteristics. Variation as a function of relative air/fuel ratio and temperature of: (*a*) oxygen partial pressure in equilibrated combustion products; (*b*) sensor output voltage.[15]

mixture at the stoichiometric point, as shown in Fig. 7-17*b*. Since this transition is not temperature dependent, it is well suited as a sensor signal for a feedback system.[15]

Figure 7-18 shows a cross-section drawing of a lambda sensor, screwed into the wall of the exhaust manifold. This location provides rapid warm-up of the sensor following engine start-up. It also gives the shortest flow time from the fuel injector or carburetor location to the sensor—a delay time which is important in the operation of the feedback system. The sensor body is made of ZrO_2 ceramic stabilized with Y_2O_3 to give adequate low-temperature electrical conductivity. The inner and outer electrodes are 10-μm thick porous platinum layers to provide the required catalytic equilibration. The outer electrode which is exposed to the exhaust gases is protected against corrosion and erosion by a 100-μm spinal coat and a slotted shield. Air passes to the inner electrode through holes in the protective sleeve. The shield, protective sleeve, and housing are made from heat- and corrosion-resistant steel alloys. Such sensors were first developed for air/fuel ratio control at close to the stoichiometric value. Use of a similar sensor to control air/fuel ratios at lean-of-stoichiometric values during part-throttle engine operation is also feasible.

For closed-loop feedback control at close-to-stoichiometric, use is made of the sensor's low-voltage output for lean mixtures and a high-voltage output for rich mixtures. A control voltage reference level is chosen at about the mid-point of the steep transition in Fig. 7-17*b*. In the electronic control unit the sensor signal is compared to the reference voltage in the comparator as shown in Fig. 7-19*a*. The comparator output is then integrated in the integral controller whose

PETITIONER'S EXHIBIT 1002
US PATENT NO. 6,581,565

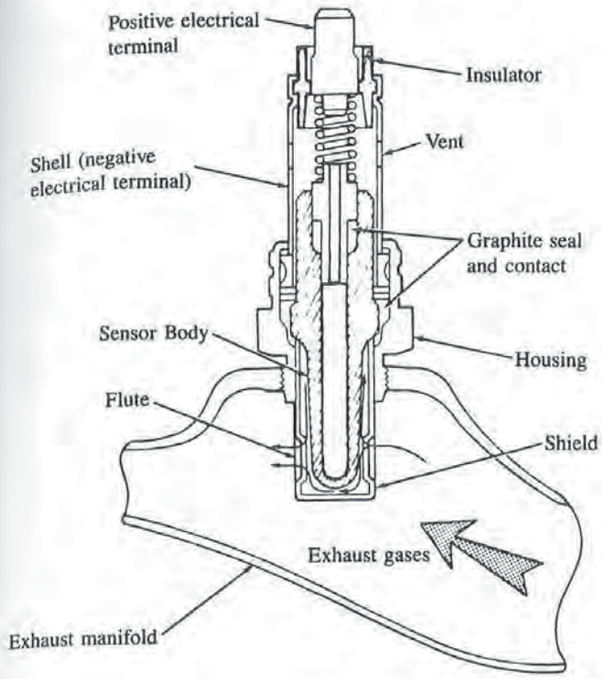


FIGURE 7-18
Cross-section drawing of exhaust oxygen sensor.[16]

output varies the fuel quantity linearly in the opposite direction to the sign of the comparator signal. There is a time lag τ_L in the loop composed of the transport time of fuel-air mixture from the point of fuel admission in the intake system to the sensor location in the exhaust, and the sensor and control system time delay. Because of this time lag, the controller continues to influence the fuel flow rate in the same direction, although the reference point $\phi = 1.0$ has been passed, as shown in Fig. 7-19*b*. Thus, oscillations in the equivalence ratio delivered to the engine exist even under steady-state conditions of closed-loop control. This behavior of the control system is called the *limit cycle*. The frequency f of this limit cycle is given by

$$f_{LC} = \frac{1}{4\tau_L} \tag{7.16}$$

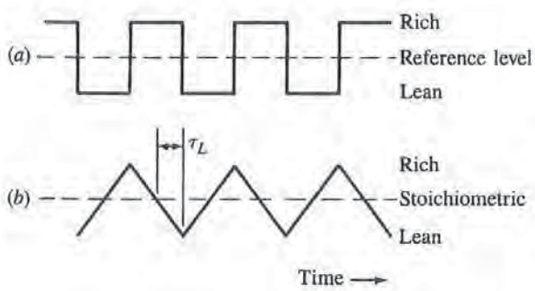


FIGURE 7-19
Operation of electronic control unit for closed-loop feedback: (*a*) sensor signal compared with reference level; (*b*) controller output voltage—the integrated comparator output.[12]

PETITIONER'S EXHIBIT 1002
US PATENT NO. 6,581,565

and the change in equivalence ratio peak-to-peak is

$$\Delta\phi = 2K\tau_L \tag{7.17}$$

where K is the integrator gain (in equivalence ratio units per unit time).

Depending on the details of the three-way catalyst used for cleanup of all three pollutants (CO, HC, and NO_x) in the exhaust, the optimum average equivalence ratio may not be precisely the stoichiometric value. Furthermore, the reference voltage for maximum sensor durability may not correspond exactly to the stoichiometric point or the desired catalyst mean operating point. While a small shift ($\sim \pm 1$ percent) in operating point from the stoichiometric can be obtained by varying the reference voltage level, larger shifts are obtained by modifying the control loop to provide a steady-state bias. One method of providing a bias—asymmetrical gain rate biasing[17]—uses two separate integrator circuits with different gain rates K^+ and K^- to integrate the comparator output, depending on whether the comparator output is positive (rich) or negative (lean). An alternative biasing technique incorporates an additional delay time τ_D so that the controller output continues decreasing (or increasing) even though the sensor signal has switched from the high to the low level (or vice versa). By introducing this additional delay only on the negative slope of the sensor signal, a net lean bias is produced. Introducing the additional delay on the positive slope of the sensor signal produces a net rich bias.[12]

Note that the sensor only operates at elevated temperatures. During engine start-up and warm-up, the feedback system does not operate and conventional controls are required to obtain the appropriate fuel-air mixture for satisfactory engine operation.

7.5 FLOW PAST THROTTLE PLATE

Except at or close to wide-open throttle, the throttle provides the minimum flow area in the entire intake system. Under typical road-load conditions, more than 90 percent of the total pressure loss occurs across the throttle plate. The minimum-to-maximum flow area ratio is large—typically of order 100. Throttle

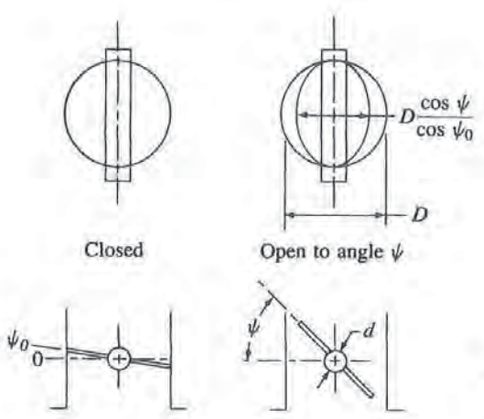
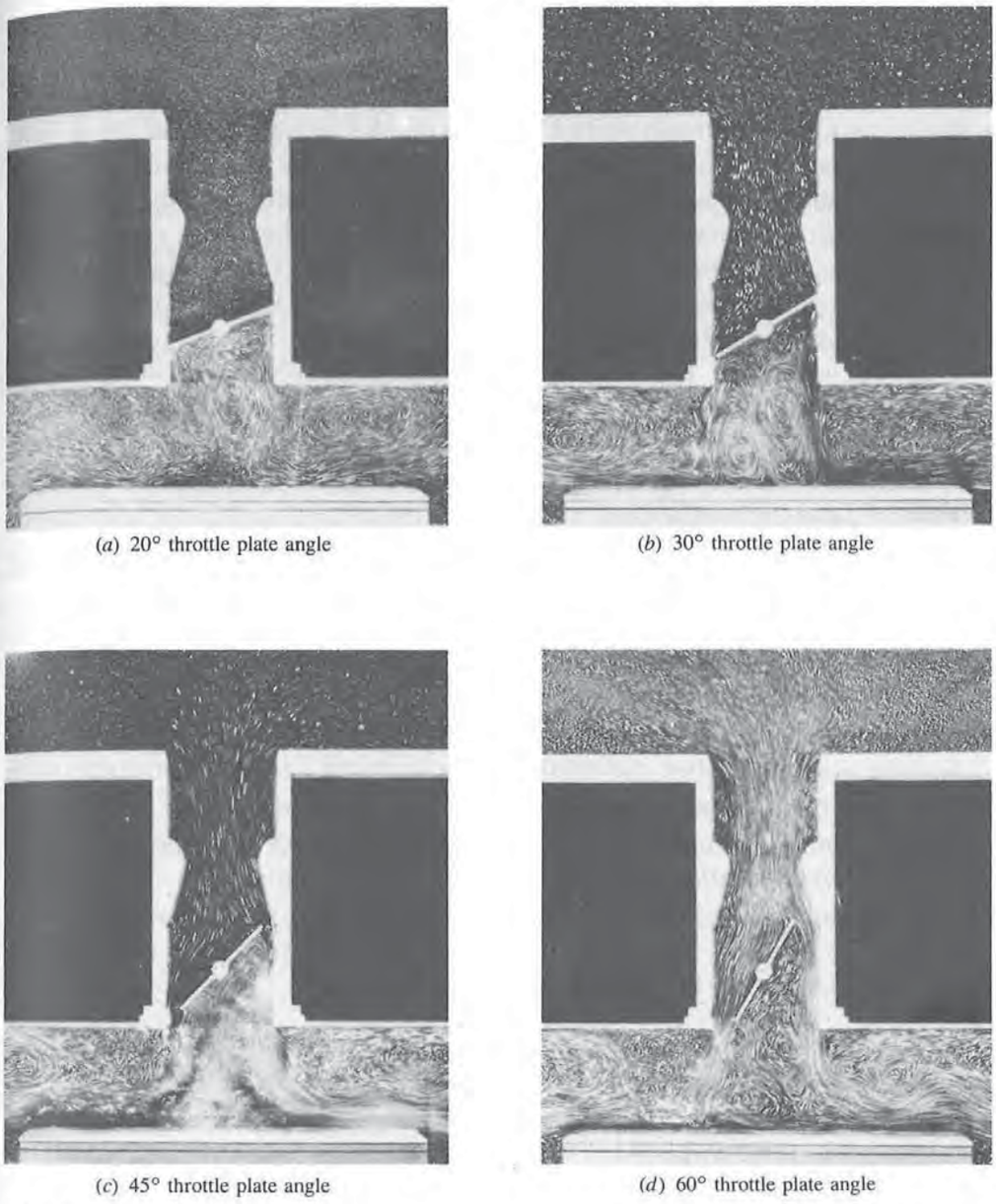


FIGURE 7-20
Throttle plate geometry.[2]

PETITIONER'S EXHIBIT 1002
US PATENT NO. 6,581,565



(*a*) 20° throttle plate angle

(*b*) 30° throttle plate angle

(*c*) 45° throttle plate angle

(*d*) 60° throttle plate angle

FIGURE 7-21
Photographs of flow in two-dimensional hydraulic analog of carburetor venturi, throttle plate, and manifold plenum floor at different throttle plate angles.[18]

plate geometry and parameters are illustrated in Fig. 7-20. A throttle plate of conventional design such as Fig. 7-20 creates a three-dimensional flow field. At part-throttle operating conditions the throttle plate angle is in the 20 to 45° range and jets issue from the "crescent moon"-shaped open areas on either side of the throttle plate. The jets are primarily two dimensional. Figure 7-21 shows photographs taken of a two-dimensional hydraulic analog of a typical carburetor

PETITIONER'S EXHIBIT 1002
US PATENT NO. 6,581,565

venturi and throttle plate in steady flow at different throttle angles. The path lines traced by the particles in the flow indicate the relative magnitude of the flow velocity.[18] The flow accelerates through the carburetor venturi (separation occurs at the corners of the entrance section); it then divides on either side of the throttle plate. There is a stagnation point on the upstream side of the throttle plate. The wake of the throttle plate contains two vortices which rotate in opposite directions. The jets on either side of the wake (at part throttle) are at or near sonic velocity. There is little or no mixing between the two jets. Thus, if maldistribution of the fuel-air mixture occurs above the throttle plate, it is not corrected immediately below the throttle plate.

In analyzing the flow through the throttle plate, the following factors should be considered:[2, 19, 20]

1. The throttle plate shaft is usually of sufficient size to affect the throttle open area.
2. To prevent binding in the throttle bore, the throttle plate is usually completely closed at some nonzero angle (5, 10, or 15°).
3. The discharge coefficient of the throttle plate is less than that of a smooth converging-diverging nozzle, and varies with throttle angle, pressure ratio, and throttle plate Reynolds number.
4. Due to the manufacturing tolerances involved, there is usually some minimum leakage area even when the throttle plate is closed against the throttle bore. This leakage area can be significant at small throttle openings.
5. The measured pressure drop across the throttle depends (± 10 percent) on the circumferential location of the downstream pressure tap.
6. The pressure loss across the throttle plate under the actual flow conditions (which are unsteady even when the engine speed and load are constant, see Fig. 7-8) may be less than under steady flow conditions.

The throttle plate open area A_{th}, as a function of angle ψ for the geometry in Fig. 7-20, is given by[2]

$$\frac{4A_{th}}{\pi D^2} = \left(1 - \frac{\cos\psi}{\cos\psi_0}\right) + \frac{2}{\pi}\left[\frac{a}{\cos\psi}(\cos^2\psi - a^2\cos^2\psi_0)^{1/2} - \frac{\cos\psi}{\cos\psi_0}\sin^{-1}\left(\frac{a\cos\psi_0}{\cos\psi}\right) - a(1-a^2)^{1/2} + \sin^{-1}a\right] \quad (7.18)$$

where $a = d/D$, d is the throttle shaft diameter, D is the throttle bore diameter, and ψ_0 is the throttle plate angle when tightly closed against the throttle bore. When $\psi = \cos^{-1}(a\cos\psi_0)$, the throttle open area reaches its maximum value ($\approx \pi D^2/4 - dD$). The throttle plate discharge coefficient (which varies with A_{th}), and minimum leakage area, must be determined experimentally.

The mass flow rate through the throttle valve can be calculated from standard orifice equations for compressible fluid flow [see App. C, Eqs. (C-8) and

PETITIONER'S EXHIBIT 1002
US PATENT NO. 6,581,565

(C-9)]. For pressure ratios across the throttle less than the critical value ($p_T/p_0 = 0.528$), the mass flow rate is given by

$$\dot{m}_{th} = \frac{C_D A_{th} p_0}{\sqrt{RT_0}} \left(\frac{p_T}{p_0}\right)^{1/\gamma} \left\{\frac{2\gamma}{\gamma - 1}\left[1 - \left(\frac{p_T}{p_0}\right)^{(\gamma-1)/\gamma}\right]\right\}^{1/2} \tag{7.19}$$

where A_{th} is the throttle plate open area [Eq. (7.18)], p_0 and T_0 are the upstream pressure and temperature, p_T is the pressure downstream of the throttle plate (assumed equal to the pressure at the minimum area: i.e., no pressure recovery occurs), and C_D is the discharge coefficient (determined experimentally). For pressure ratios greater than the critical ratio, when the flow at the throttle plate is choked,

$$\dot{m}_{th} = \frac{C_D A_{th} p_0}{\sqrt{RT_0}} \gamma^{1/2} \left(\frac{2}{\gamma + 1}\right)^{(\gamma+1)/2(\gamma-1)} \tag{7.20}$$

The relation between air flow rate, throttle angle, intake manifold pressure, and engine speed for a two-barrel carburetor and a 4.7-dm^3 (288-in^3) displacement eight-cylinder production engine is shown in Fig. 7-22. While the lines are predictions from a quasi-steady computer simulation, the agreement with data is excellent. The figure shows that for an intake manifold pressure below the critical

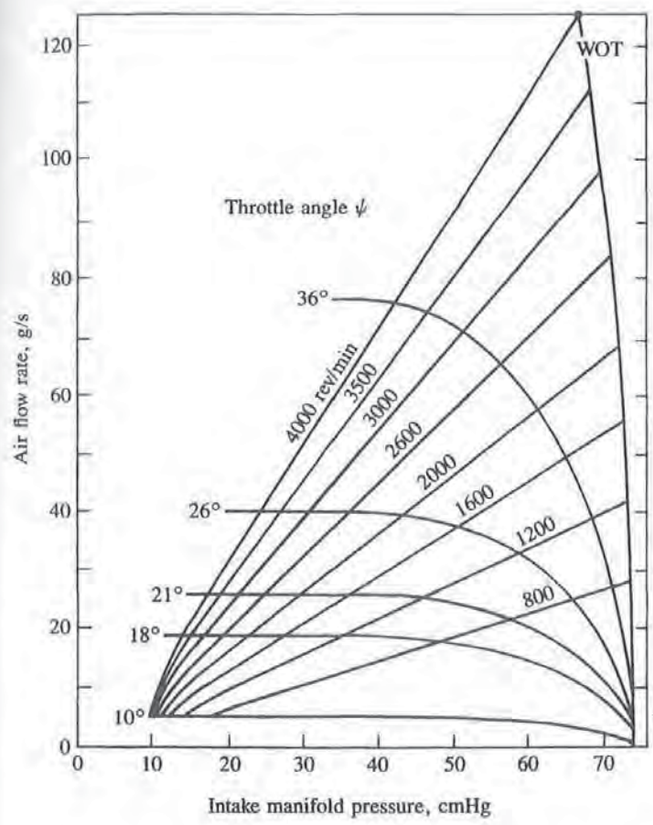


FIGURE 7-22
Variation in air flow rate past a throttle, with inlet manifold pressure, throttle angle, and engine speed. 4.7-dm^3 displacement eight-cylinder engine.[2]

PETITIONER'S EXHIBIT 1002
US PATENT NO. 6,581,565

value ($0.528 \times p_{atm} = 53.5$ kN/m^2 = 40.1 cmHg) the air flow rate at a given throttle position is independent of manifold pressure and engine speed because the flow at the throttle plate is choked.[2]

7.6 FLOW IN INTAKE MANIFOLDS

7.6.1 Design Requirements

The details of the air and fuel flow in intake manifolds are extremely complex. The combination of pulsating flow into each cylinder, different geometry flow paths from the plenum beneath the throttle through each runner and branch of the manifold to each inlet port, liquid fuel atomization, vaporization and transport phenomena, and the mixing of EGR with the fresh mixture under steady-state engine operating conditions are difficult enough areas to untangle. During engine transients, when the throttle position is changed, the fact that the processes which govern the air and the fuel flow to the cylinder are substantially different introduces additional problems. This section reviews our current understanding of these phenomena.

Intake manifolds consist typically of a plenum, to the inlet of which bolts the throttle body, with individual runners feeding branches which lead to each cylinder (or the plenum can feed the branches directly). Important design criteria are: low air flow resistance; good distribution of air and fuel between cylinders; runner and branch lengths that take advantage of ram and tuning effects; sufficient (but not excessive) heating to ensure adequate fuel vaporization with carbureted or throttle-body injected engines. Some compromises are necessary; e.g., runner and branch sizes must be large enough to permit adequate flow without allowing the air velocity to become too low to transport the fuel droplets. Some of these design choices are illustrated in Fig. 7-23 which shows an inlet manifold and carburetor arrangement for a modern four-cylinder 1.8-dm^3 engine. In this design the four branches that link the plenum beneath the carburetor and throttle with the inlet ports are similar in length and geometry, to provide closely comparable flow paths. This manifold is heated by engine coolant as shown and uses an electrically heated grid beneath the carburetor to promote rapid fuel evaporation.[21] Exhaust gas heated stoves at the floor of the plenum are also used in some intake manifolds to achieve adequate fuel vaporization and distribution. Note that with EGR, the intake manifold may contain passages to bring the exhaust gas to the plenum or throttle body.

With port fuel-injection systems, the task of the inlet manifold is to control the air (and EGR) flow. Fuel does not have to be transported from the throttle body through the entire manifold. Larger and longer runners and branches, with larger angle bends, can be used to provide equal runner lengths and take greater advantage of ram and tuning effects. With port fuel injection it is not normally necessary to heat the manifold.

A large number of different manifold arrangements are used in practice. Different cylinder arrangements (e.g., four, V-six, in-line-six, etc.) provide quite different air and fuel distribution problems. Air-flow phenomena in manifolds can

PETITIONER'S EXHIBIT 1002
US PATENT NO. 6,581,565

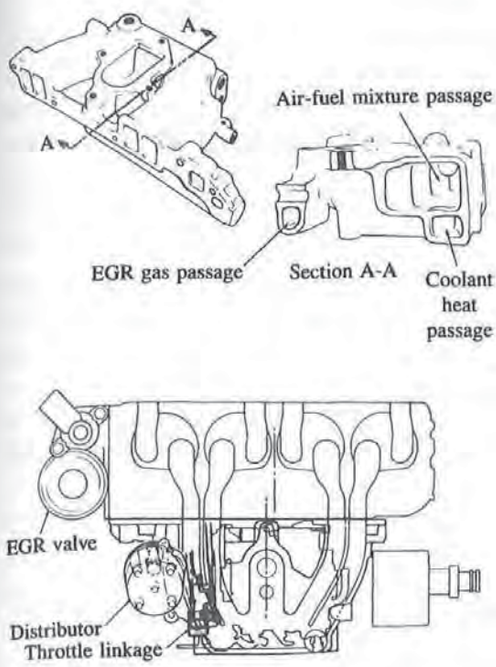


FIGURE 7-23
Inlet manifold for four-cylinder 1.8-dm^3 displacement spark-ignition engine.[21]

be considered as unaffected by the fuel flow. The reverse is definitely not the case: the fuel flow—liquid and vapor—depends strongly on the air flow. These two topics will therefore be reviewed in sequence.

7.6.2 Air-Flow Phenomena

The air flow out of the manifold occurs in a series of pulses, one going to each cylinder. Each pulse is approximately sinusoidal in shape. For four- and eight-cylinder engines, these flow pulses sequence such that the outflow is essentially zero between pulses. For six-cylinder arrangements the pulses will overlap. When the engine is throttled, backflow from the cylinder into the intake manifold occurs during the early part of the intake process until the cylinder pressure falls below the manifold pressure. Backflow can also occur early in the compression stroke before the inlet valve closes, due to rising cylinder pressure. The flow at the throttle will fluctuate as a consequence of the pulsed flow out of the manifold into the cylinders. At high intake vacuum, the flow will be continuously inward at the throttle and flow pulsations will be small. When the outflow to the cylinder which is undergoing its intake stroke is greater than the flow through the throttle, the cylinder will draw mixture from the rest of the intake manifold. During the portion of the intake stroke when the flow into the cylinder is lower than the flow through the throttle, mixture will flow back into the rest of the manifold. At wide-open throttle when the flow restriction at the throttle is a minimum, flow pulsations at the throttle location will be much more pronounced.[19]

The air flows to each cylinder of a multicylinder engine, even under steady operating conditions, are not identical. This is due to differences in runner and

PETITIONER'S EXHIBIT 1002
US PATENT NO. 6,581,565

branch length and other geometric details of the flow path to each cylinder. Also, as each cylinder's intake flow commences, air is drawn from the branch and runner leading to the cylinder, the plenum, and the other runners and branches feeding the plenum, as well as past the throttle. This "drawing down" of other parts of the intake manifold depends on the arrangement of the plenum, runners, and branches, and the firing order of the cylinders. Thus the air flow to each individual cylinder is affected by the details of its own branch, how that branch connects to the rest of the intake manifold, and the cylinder firing order.[22] The differences between the air flows to individual cylinders have been measured. Variations in the average air mass flow rate to each individual cylinder of up to about 5 percent above and below the average are quite common. Larger peak-to-peak variations (± 15 percent) have been measured. The extent of each cylinder's difference from the average flow varied significantly as engine speed and load were varied.[23, 24]

Typical quantities that characterize manifold air flow are given in Table 7.1 for a four- and an eight-cylinder spark-ignition engine. The volume of mixture pulled into each cylinder per cycle is about the same as the volume of one direct flow path between the throttle plate and inlet valve. Thus, one stroke loads the manifold, the next one pulls the charge into the cylinder.

An additional phenomenon becomes important when engine load is changed by opening or closing the throttle: the mass of air in the induction system volume takes a finite time to adjust to the new engine operating conditions. For example, as the throttle is opened the air flow into the manifold increases as the throttle open area increases. However, due to the finite volume of

TABLE 7.1
Parameters that characterize manifold air flow

Engine geometry	I-4†	V-8‡
Typical flow-path distance between throttle bore and intake valve, cm	33	30
Average intake-passage flow area, cm^2	9.4	16
Volume of one direct flow path from throttle bore to intake valve, cm^3	300	500
Range of speeds, etc.	**Maximum**	**Minimum**
Crankshaft, rev/min	5000	650
Peak air velocity in manifold branch, m/s	130†, 100‡	15
Peak Reynolds number in manifold branch	4×10^5	5×10^4
Duration of individual cylinder intake process, ms	6	46

† 1.8-dm^3 four-cylinder in-line SI engine.[21]
‡ 5.6-dm^3 V eight-cylinder SI engine.[25]

PETITIONER'S EXHIBIT 1002
US PATENT NO. 6,581,565

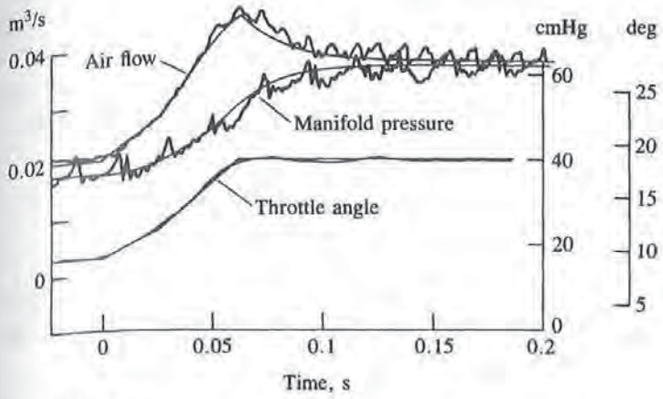


FIGURE 7-24
Throttle angle, intake manifold pressure, and air flow rate past the throttle versus time for 10° part-load throttle opening. 5-dm³ V-8 engine.[25]

the manifold, the pressure level in the manifold increases more slowly than would be the case if steady-state conditions prevailed at each throttle position. Thus, the pressure difference across the throttle is larger than it would be under steady flow conditions and the throttle air flow overshoots its steady-state value. The air flow into each cylinder depends on the pressure in the manifold, so this lags the throttle air flow. This transient air-flow phenomenon affects fuel metering. For throttle-body injection or a carburetor, fuel flow should be related to throttle air flow. For port fuel injection, fuel flow should be related to cylinder air flow. Actual results for the air flow rate and manifold pressure in response to an opening of the throttle (increase in throttle angle) are shown in Fig. 7-24. The overshoot in throttle air flow and lag in manifold pressure as the throttle angle is increased are evident. Opposite effects will occur for a decrease in throttle angle.

AIR-FLOW MODELS. Several models of the flow in an intake manifold have been proposed.[26, 27] One simple manifold model that describes many of the above phenomena is the *plenum* or *filling and emptying* model. It is based on the assumption that at any given time the manifold pressure is uniform. The continuity equation for air flow into and out of the intake manifold is

$$\frac{dm_{a,\,m}}{dt} = \dot{m}_{a,\,\mathrm{th}} - \sum \dot{m}_{a,\,\mathrm{cyl}} \tag{7.21}$$

where $m_{a,\,m}$ is the mass of air in the manifold, and $\dot{m}_{a,\,\mathrm{th}}$ and $\dot{m}_{a,\,\mathrm{cyl}}$ are the air mass flow rates past the throttle and into each cylinder, respectively. The flow rate past the throttle is given by Eq. (7.19) or (7.20). For manifold pressures sufficiently low to choke the flow past the throttle plate, the flow rate is independent of manifold pressure. The mass flow rate to the engine cylinders can be modeled at several levels of accuracy. The air flow through the valve to each cylinder can be computed from the valve area, discharge coefficient, and pressure

PETITIONER'S EXHIBIT 1002
US PATENT NO. 6,581,565

difference across the valve; or a sine wave function can be assumed. In the general case, Eq. (7.21) must be combined with the first law for an open system (see Sec. 14.2.2). For calculating the manifold response to a change in load or throttle setting, simplifying assumptions can be made. A quasi-steady approximation for the cylinder air flow:

$$\sum \dot{m}_{a,\,\mathrm{cyl}} = \frac{\eta_v \rho_{a,\,m} V_d N}{2}$$

is usually adequate, and the air temperature can be assumed constant.[25] Then, using the ideal gas law for the manifold, $p_m V_m = m_{a,\,m} R_a T_m$, Eq. (7.21) can be written as

$$\frac{dp_m}{dt} + \frac{\eta_v V_d N}{2V_m} p_m = \dot{m}_{a,\,\mathrm{th}} \frac{RT_m}{V_m} \tag{7.22}$$

Both η_v and $\dot{m}_{a,\,\mathrm{th}}$ have some dependence on p_m [e.g., see Eq. (6.2)]. In the absence of this weak dependence, Eq. (7.22) would be a first-order equation for p_m with a time constant $\tau = 2V_m/(\eta_v V_d N) \approx V_m/\dot{V}_{\mathrm{cyl}}$, which is 2 to 4 times the intake stroke duration. The smooth curves in Fig. 7-24 are predictions made with Eq. (7.22) and show good agreement with the data. The plenum model is useful for investigating manifold pressure variations that result from load changes. It provides no information concerning pressure variations associated with momentum effects.

Helmholtz resonator models for the intake system have been proposed. This type of model can predict the resonant frequencies of the combined intake and engine cylinder system, and hence the engine speeds at which increases in air flow due to intake tuning occur. It does not predict the magnitude of the increase in volumetric efficiency. The Helmholtz resonator theory analyzes what happens during one inlet stroke, as the air in the manifold pipe is acted on by a forcing function produced by the piston motion. As the piston moves downward during the intake stroke, a reduced pressure occurs at the inlet valve relative to the pressure at the open end of the inlet pipe. A rarefraction wave travels down the intake pipe to the open end and is reflected as a compression wave. A positive tuning effect occurs when the compression wave arrives at the inlet valve as the valve is closing.[27] A single-cylinder engine modeled as a Helmholtz resonator is shown in Fig. 7-25*a*. The effective resonator volume V_{eff} is chosen to be one-half of the displaced volume plus the clearance volume; the piston velocity is then close to its maximum and the pressure in the inlet system close to its minimum. The tuning peak occurs when the natural frequency of the cylinder volume coupled to the pipe is about twice the piston frequency. For a single-cylinder, fed by a single pipe open to the atmosphere, the resonant tuning speed N_t is given by

$$N_t(\mathrm{rev/min}) = \frac{955}{K}\, a\left(\frac{A}{lV_{\mathrm{eff}}}\right)^{1/2} \tag{7.23}$$

where a is the sound speed (m/s), A the effective cross-sectional area of the inlet system (cm^2), l the effective length of the inlet system (cm), K a constant equal to about 2 for most engines, and $V_{\mathrm{eff}} = V_d(r_c + 1)/[2(r_c - 1)]$ (cm^3).[28]

PETITIONER'S EXHIBIT 1002
US PATENT NO. 6,581,565

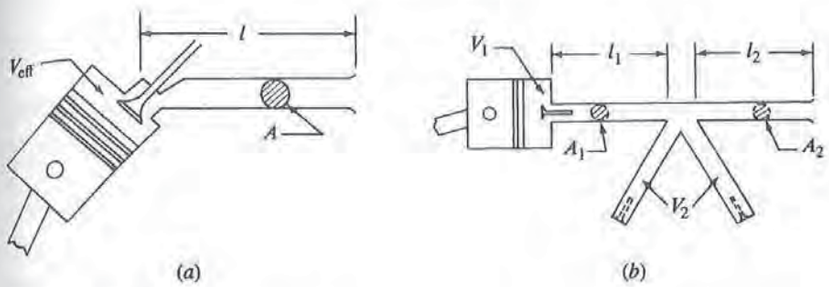


FIGURE 7-25
Helmholtz resonator models for (*a*) single-cylinder engine and (*b*) multicylinder engine.[27]

The Helmholtz theory for multicylinder engines treats the pipes of cylinders not undergoing induction as an additional volume. The two pipes, (l_1, A_1) and (l_2, A_2), and two volumes, V_1 and V_2, in Fig. 7-25*b* form a vibrating system with two degrees of freedom and two resonant frequencies. The following equation, based on an electrical analog (in which capacitors represent volumes and inductors pipes), gives the two frequencies at which the manifold shown in Fig. 7-25*b* would be tuned:[28]

$$f_{\mp} = \frac{1}{2\pi}\left\{\frac{(\alpha\beta + \alpha + 1) \mp [(\alpha\beta + \alpha + 1)^2 - 4\alpha\beta]^{1/2}}{2\alpha\beta L_1 C_1}\right\}^{1/2} \tag{7.24}$$

where $\alpha = L_2/L_1$, $\beta = C_2/C_1$, $C_1 = V_1$, $C_2 = V_2$, $L_1 = (l/A)_1$, $L_2 = (l/A)_2$, and $V_{eff} = V_1$. The Helmholtz theory predicts the engine speeds at which positive tuning resonances occur with reasonable accuracy.[27]

The dynamics of the flow in multicylinder intake (and exhaust) systems can be modeled most completely using one-dimensional unsteady compressible flow equations. The standard method of solution of the governing equations has been the method of characteristics (see Benson[29]). Recently, finite difference techniques which are more efficient have been used.[30] The assumptions usually made in this type of analysis are:

1. The intake (or exhaust) system can be modeled as a combination of pipes, junctions, and plenums.
2. Flow in the pipes is one dimensional and no axial heat conduction occurs.
3. States in the engine cylinders and plenums are uniform in space.
4. Boundary conditions are considered quasi steady.
5. Coefficients of discharge, heat transfer, pipe friction, and bend losses for steady flow are valid for unsteady flow.
6. The gases can be modeled as ideal gases.

This approach to intake and exhaust flow analysis is discussed more fully in Sec. 14.3.4.

PETITIONER'S EXHIBIT 1002
US PATENT NO. 6,581,565

7.6.3 Fuel-Flow Phenomena

TRANSPORT PROCESSES. With conventional spark-ignition engine liquid-fuel metering systems, the fuel enters the air stream as a liquid jet. The liquid jet atomizes into droplets. These mix with the air and also deposit on the walls of the intake system components. The droplets vaporize; vaporization of the liquid fuel on the walls occurs. The flow of liquid fuel along the walls can be significant. The transport of fuel as vapor, droplets, and liquid streams or films can all be important. The fuel transport processes in the intake system are obviously extremely complex.

The details of the fuel transport process are different for multipoint fuel-injection systems than for carburetor and throttle-body injection systems. For the latter systems, fuel must be transported past the throttle plate and through the complete intake manifold. For the former systems, the liquid fuel is injected in the inlet port, toward the back of the intake valve. For all these practical fuel metering systems, the quality of the mixture entering the engine is imperfect. The fuel, air, recycled exhaust, mixture is not homogeneous; the fuel may not be fully vaporized as it enters the engine. The charge going to each cylinder is not usually uniform in fuel/air ratio throughout its volume, and the distribution of fuel between the different engine cylinders is not exactly equal. During engine transients, when engine fuel and air requirements and manifold conditions change, it is obvious that the above fuel transport processes will not all vary with time in the same way. Thus, in addition to the transient non-quasi-steady air-flow phenomena described above, there are transient fuel-flow phenomena. These have to be compensated for in the fuel metering strategy.

Since gasoline, the standard spark-ignition engine fuel, is a mixture of a large number of individual hydrocarbons it has a boiling temperature range rather than a single boiling point. Typically, this range is 30 to 200°C. Individual hydrocarbons have the saturation pressure-temperature relationships of a pure substance. The lower the molecular weight, the higher will be the saturated vapor pressure at a given temperature. The boiling point of hydrocarbons depends primarily on their molecular weight: the vapor pressure also depends on molecular structure. The equilibrium state of a hydrocarbon-air mixture depends therefore on the vapor pressure of the hydrocarbon at the given temperature, the relative amounts of the hydrocarbon and air, and the total pressure of the mixture. The equilibrium fraction of fuel evaporated at a given temperature and pressure can be calculated from Bridgeman charts[31] and the distillation characteristics of the fuel (defined by the ASTM distillation curve[32]). Figure 7-26*a* shows the effect of mixture temperature on percent of indolene fuel (a specific gasoline) evaporated at equilibrium at atmospheric pressure. Figure 7-26*b* shows the effect of reduced manifold pressure on the amount evaporated.[18] While insufficient time is usually available in the manifold to establish equilibrium, the trends shown are indicative of what happens in practice: lower pressures increase the relative amount of fuel vaporized and charge heating is usually required to vaporize a substantial fraction of the fuel.

PETITIONER'S EXHIBIT 1002
US PATENT NO. 6,581,565

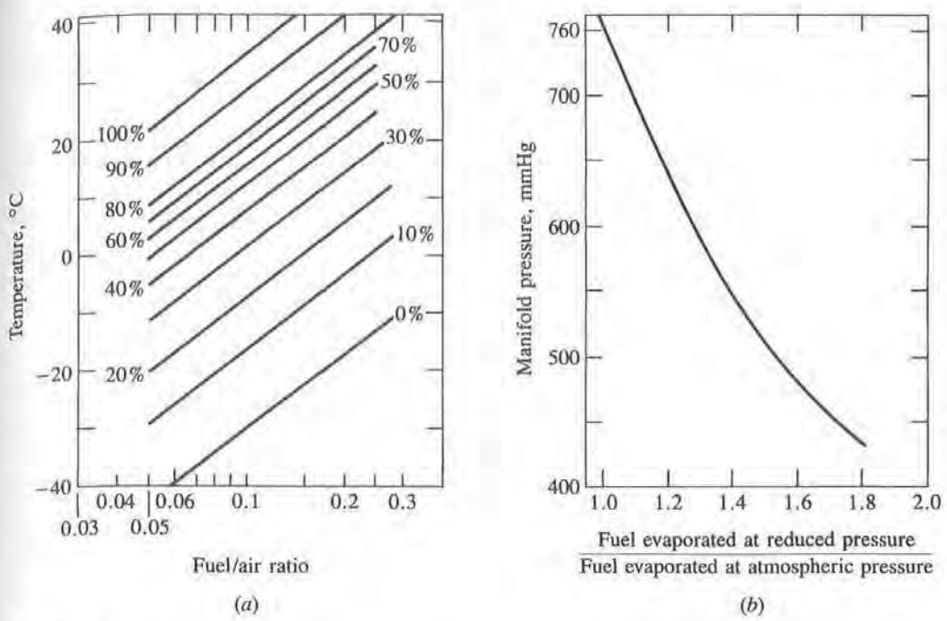


FIGURE 7-26
(*a*) Percentage of indolene fuel evaporated at equilibrium at 1 atmosphere pressure. (*b*) Effect of pressure on amount of indolene fuel evaporated.[18]

For carbureted and throttle-body injection systems, the fuel path is the following. Until the throttle plate is close to fully opened, most of the fuel metered into the air stream impacts on the throttle plate and throttle-body walls. Only a modest fraction of the fuel vaporizes upstream of the throttle. The liquid is reentrained as the air flows at high velocity past the throttle plate. The fuel does not usually divide equally on either side of the throttle plate axis. The air undergoes a 90° bend in the plenum beneath the throttle; much of the fuel which has not evaporated is impacted on the manifold floor. Observations of fuel behavior in intake manifolds with viewing ports or transparent sections show that there is substantial liquid fuel on the walls with carburetor fuel metering systems. Figure 7-27 shows the engine conditions under which liquid fuel was observed on the floor of the manifold plenum beneath the throttle plate and in the manifold runners, in a standard four-cylinder production engine.[23] This manifold was heated by engine coolant at 90°C. The greatest amount of liquid was present at high engine loads and low speeds. Heating the manifold to a higher temperature with steam at 115°C resulted in a substantial reduction in the amount of liquid: there was no extensive puddling on the plenum floor, liquid films or rivulets were observed in a zone bounded by 120 mmHg vacuum and 2500 rev/min, and there were no films or rivulets in the manifold runner. Depending on engine operating conditions, transport of fuel as a liquid film or rivulet in the manifold and vaporization from these liquid fuel films and rivulets and subsequent transport as vapor may occur.

Vaporized fuel and liquid droplets which remain suspended in the air

PETITIONER'S EXHIBIT 1002
US PATENT NO. 6,581,565

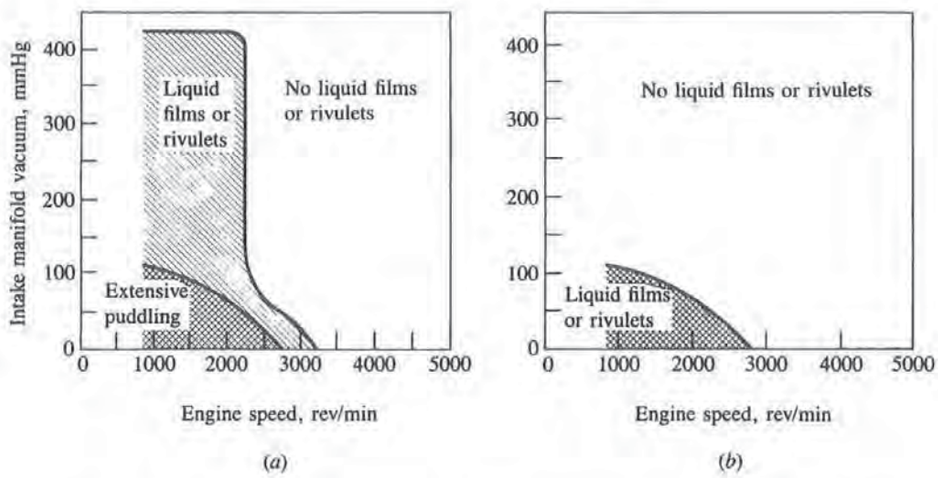


FIGURE 7-27
Regions of engine load and speed range where extensive pools or puddles, liquid films, or rivulets were observed: (*a*) on manifold plenum floor and (*b*) in manifold runner. Four-cylinder automobile engine. Manifold heated by coolant at 90°C.[23]

stream will be transported with the air stream. However, droplet deposition on the manifold walls may occur due to gravitational settling and to inertial effects as the flow goes round bends in the manifold.

The fuel transport processes for port fuel-injection systems are different and will depend significantly on the timing and duration of the injection pulse. Fuel is injected onto the back of the inlet valve (and surrounding port wall), usually while the valve is closed or only partly open. Vaporization of liquid fuel off the valve and walls occurs, enhanced by the backflow of hot residual gases from the cylinder (especially at part load). There is evidence that, even under fully warmed-up engine conditions, some fuel is carried as liquid drops into the cylinder.[33]

FUEL DROPLET BEHAVIOR. With carburetor and throttle-body injection systems, the liquid fuel atomizes as it enters the air stream. In the carburetor venturi this occurs as the fuel-air emulsion from the fuel jet(s) enters the high-velocity (>100 m/s) air stream. With an injector, the velocity of the liquid jet as it exits the nozzle is high enough to shatter the flowing liquid, and its interaction with the coaxial air flow further atomizes the fuel. Typical droplet-size distributions are not well defined; size would vary over the load and speed range. Droplet diameters in the 25 to 100 μm range are usually assumed to be representative: larger drops are also produced. The liquid fuel drops are accelerated by the surrounding air stream and start to vaporize. Vaporization rates have been calculated using established formulas for heat and mass transfer between a droplet and a surrounding flowing gas stream (see Ref. 34 for a review of methods of calculating droplet vaporization rates). Calculations of fuel vaporization in a carburetor venturi and upstream of the throttle plate show that the temperature

PETITIONER'S EXHIBIT 1002
US PATENT NO. 6,581,565

of the liquid fuel droplets decreases rapidly (by up to about 30°C[35]), and the fraction of the fuel vaporized is small (in the 2 to 15 percent range[35, 36]).

Liquid fuel drops, due to their density being many times that of the air, will not exactly follow the air flow. Droplet impaction on the walls may occur as the flow changes direction, and the greater inertia of the droplets causes them to move across the streamlines to the outer wall. Deposition on the manifold floor due to gravity may also occur. The equation of motion for an individual droplet in a flowing gas stream is

$$(\tfrac{1}{6}\pi D_d^3 \rho_f)\mathbf{a} = m_d \mathbf{g} - \tfrac{1}{2}(\mathbf{v}_d - \mathbf{v}_g)|\mathbf{v}_d - \mathbf{v}_g|\rho_g C_D \frac{\pi D_d^2}{4} \tag{7.25}$$

where D_d is the droplet diameter, ρ_f and ρ_g are liquid and gas densities, $\mathbf{v}_d$ and $\mathbf{v}_g$ are the droplet and gas velocities, $\mathbf{a}$ is the droplet acceleration, $\mathbf{g}$ acceleration due to gravity, and C_D is the drag coefficient. For $6 < \mathrm{Re} < 500$ the drag coefficient of an evaporating droplet is a strong function of the Reynolds number, Re: e.g.,

$$C_D = 27\ \mathrm{Re}^{-0.84} \tag{7.26}$$

where $\mathrm{Re} = (\rho_g D_d|\mathbf{v}_d - \mathbf{v}_g|/\mu_g)$.

Studies of droplet impaction and evaporation using the above equations and typical manifold conditions and geometries indicate the following.[26, 35, 37] For 90° bends, drops of less than 10 μm diameter are essentially carried by the gas stream (<10 percent impaction); almost all droplets larger than 25 μm impact on the walls. Droplet sizes produced first in the carburetor venturi or fuel injector spray and then by secondary atomization as liquid fuel is entrained from the throttle plate and throttle-body walls depend on the local gas velocity: higher local relative velocities between the gas and liquid produce smaller drop sizes. Approximate estimates which combine the two phenomena outlined above show that at low engine air flow rates, almost all of the fuel will impact first on the throttle plate and then on the manifold floor as the flow turns 90° into the manifold runners. At high air flows, because the drops are smaller, a substantial fraction of the drops may stay entrained in the air flow. Secondary atomization at the throttle at part-load operating conditions is important to the fuel transport process: the very high air velocities at the edge of the throttle plate produce droplets of order or less than 10 μm diameter. However, coalescence and deposition on the walls and subsequent reentrainment probably increase the mean droplet size. In the manifold, gravitational settling of large (>100 μm) droplets would occur at low air flow rates,[38] but these drops are also likely to impact the walls due to their inertia as the flow is turned.

Estimates of droplet evaporation rates in the manifold indicate the following. With a representative residence time in the manifold of about one crank revolution (10 ms at 6000 rev/min, 100 ms at 600 rev/min), only drops of size less than about 10 μm will evaporate at the maximum speed; 100 μm droplets will not vaporize fully at any speed. Most of these large droplets impact on the walls, anyway. Drops small enough to be carried by the air stream are likely to vaporize in the manifold.[26]

PETITIONER'S EXHIBIT 1002
US PATENT NO. 6,581,565

FUEL-FILM BEHAVIOR. The fuel which impacts on the wall will also vaporize and, depending on where in the manifold deposition occurs and the local manifold geometry, may be transported along the manifold as a liquid film or rivulet. If the vaporization rate off the wall is sufficiently high, then a liquid film will not build up. Any liquid film or pool on the manifold floor or walls is important because it introduces additional fuel transport processes—deposition, liquid transport, and evaporation—which together have a much longer time constant than the air transport process. Thus changes in the air and the fuel flow into each engine cylinder, during a change in engine load, will not occur in phase with each other unless compensation is made for the slower fuel transport.

Several models of the behavior of liquid-fuel wall-films have been developed. One approach analyzes a liquid puddle on the floor of the manifold plenum.[38] Metered fuel enters the puddle; fuel leaves primarily through vaporization. The equation for rate of change of mass of fuel in the puddle is

$$\dot{m}_{f,p} = \dot{m}_{f,\text{in}} - \dot{m}_{f,\text{out}} = x\dot{m}_{f,m} - \frac{m_{f,p}}{\tau} \tag{7.27}$$

where $m_{f,p}$ is the mass of fuel in the puddle, $\dot{m}_{f,m}$ is the metered fuel flow rate, and x is the fraction of the metered flow that enters the puddle. It is assumed that the reentrainment/evaporation rate is proportional to the mass of fuel in the puddle divided by the characteristic time τ of the reentrainment/evaporation process. The puddle behavior predicted by this model in response to a step increase in engine load is shown in Fig. 7-28*a*. Because only part $(1 - x)$ of the fuel flows directly with the air, as the throttle is opened rapidly a lean air/fuel ratio excursion is predicted. Figure 7-28*b* shows that this behavior (without any metering compensation) is observed in practice. Estimates of the volume of fuel in the puddle (for a 5-liter V-8 engine) are of order 1000 mm^3, and increase with

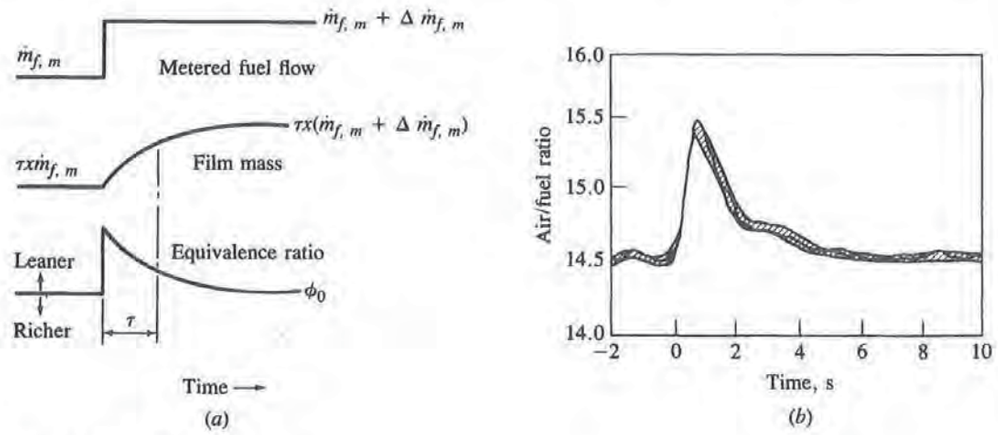


FIGURE 7-28
(*a*) Predicted behavior of the fuel film for an uncompensated step change in engine operating conditions. (*b*) Observed variation in air/fuel ratio for uncompensated throttle opening at 1600 rev/min which increased manifold pressure from 48 to 61 cmHg.[38]

PETITIONER'S EXHIBIT 1002
US PATENT NO. 6,581,565

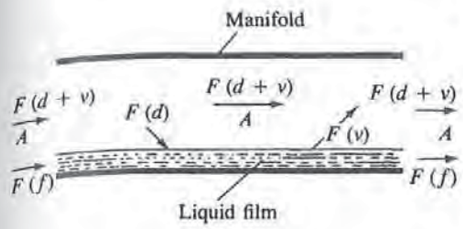


FIGURE 7-29
Schematic of fuel flow paths in the manifold when liquid film flows along the manifold runner floor.
A Air
F Fuel
f Liquid fuel film
d Liquid fuel droplets
v Fuel vapor

increasing load and speed. The time constant is of order 2 seconds for a fully warmed-up engine; it varies with engine operating conditions and is especially sensitive to intake manifold temperature. Such models have been used primarily to develop fuel metering strategies which compensate for the fuel transport lag.[38]

An alternative model, for liquid film flow in the manifold runner and branch, has been developed.[37] Fuel is deposited on the manifold walls and forms a film which flows toward the cylinder due to the shear force at the gas/liquid interface as shown in Fig. 7-29. Vaporization from the film also occurs. An analysis of the dynamics of the fuel film leads to expressions for steady-state film velocity and thickness. As air and metered fuel flows change due to a throttle position change, the characteristic time for reestablishing steady state is $l/(2u_f)$, where l is the manifold length and u_f the average film velocity. This characteristic response time is of order 1 second for typical manifold conditions, in approximate agreement with values obtained from transient engine experiments.

A more extensive analysis of both fuel droplet and film evaporation in a complete carburetor, throttle, manifold system,[35] with a multicomponent model for gasoline based on its distillation curve, indicates the following phenomena are important. Secondary atomization of the liquid fuel at the throttle, which produces the smallest droplet sizes when the throttle open angle is small, significantly increases the fraction of fuel evaporation in the manifold. Increasing inlet air temperature increases the fraction of fuel vaporized; this effect is larger at lower loads since secondary atomization under these conditions increases the liquid fuel surface area significantly. Heating the wall, which heats the liquid film on the wall directly, provides a greater increase in fraction evaporated than does equivalent heating of the air flow upstream of the carburetor. Due to the multicomponent nature of the fuel, the residual liquid fuel composition changes significantly as fuel is transported from the carburetor to the manifold exit. Of the full boiling range liquid composition at entry, all the light ends, most of the mid-range components, but only a modest amount of the high boiling point fraction have evaporated at the manifold exit. The predicted fuel fraction evaporated ranged from 40 to 60 percent for the conditions examined. One set of measurements of the fraction of fuel vaporized in the manifold of a warmed-up four-cylinder engine showed that 70 to 80 percent of the fuel had vaporized, confirming that under these operating conditions "most" but not necessarily "all" the fuel enters the cylinder in vapor form.[39]

The engine operating range where fuel puddling, fuel films, and rivulets are observed (see Fig. 7-27) can now be explained. At light load, secondary atom-

PETITIONER'S EXHIBIT 1002
US PATENT NO. 6,581,565

ization at the throttle and the lower manifold pressure would reduce the amount of liquid fuel impinging on the manifold plenum floor. Also, typical manifold heating at light load substantially exceeds the heat required to vaporize the fuel completely,[40] and manifold floor temperatures are of order 15°C higher than at full load. All the above is consistent with less liquid on the floor and none in the runners at light load, compared to what occurs at full load. At high speed, drop sizes produced in the carburetor are much smaller, so impingement on the walls is much reduced.

The fuel flow to each cylinder per cycle is not exactly the same. There is a *geometric variation* where fuel is not divided equally among individual cylinders. There is also a *time variation* under steady-state engine conditions where the air/fuel ratio in a given cylinder varies cycle-by-cycle.[41] Data on time-averaged air/fuel ratios in each cylinder of multicylinder engines show that the extent of the maldistribution varies from engine to engine, and for a particular engine varies over the load and speed range. Spreads in the equivalence ratio (maximum to minimum) of about 5 percent of the mean value are typical at light load for carbureted engines. Largest variations between cylinders usually occur at wide-open throttle. WOT spreads in the equivalence ratio of about 15 percent of the mean appear to be typical, again for carbureted engines, while spreads as high as 20 to 30 percent are not uncommon at particular speeds for some engines.[23, 40] Time variations are less well defined; the limited data available suggest they could be of comparable magnitude.[41]

With multipoint port fuel-injection systems, the fuel transport processes are substantially different and are not well understood. Air-flow phenomena are comparable to those with carbureted or throttle-body injection systems. However, manifold design can be optimized for air flow alone since fuel transport from the throttle through the manifold is no longer a design constraint. Because the manufacture and operation of individual fuel injectors are not identical, there is still some variation in fuel mass injected cylinder-to-cylinder and cycle-to-cycle. Since individual cylinder air flows depend on the design of the manifold, whereas the amount of fuel injected does not, uniform air distribution is especially important with port injection systems. The fuel vaporization and transport processes will depend on the duration of injection and the timing of injection pulse(s) relative to the intake valve-lift profile. Some of the injected fuel will impinge on the port walls, valve stem, and backside of the valve, especially when injection toward a closed valve occurs. Backflow of hot residual gases at part-load operation will have a substantial effect on fuel vaporization. Compensation for fuel lag during transient engine operation is still required; sudden throttle openings are accompanied by a "lean spike" in the mixture delivered to the engine, comparable to though smaller than that shown in Fig. 7-28 for a throttle-body fuel-injection system. Thus wall wetting, evaporation off the wall, and liquid flow along the wall are all likely to be important with port fuel-injection systems also.

With port fuel-injection systems, liquid fuel enters the cylinder and droplets are present during intake and compression. Limited measurements have been made of the distribution, size, and number density of these fuel droplets. During

PETITIONER'S EXHIBIT 1002
US PATENT NO. 6,581,565

intake, the droplet number density in the clearance volume increased to a maximum at the end of injection (the injection lasted from 45 to 153° ATC) and then decreased due to evaporation during compression to a very small value at the time of ignition. Average droplet size during intake was 10 to 20 μm in diameter; it increased during compression as the smaller drops in the distribution evaporated. At the conditions tested, some 10 to 20 percent of the fuel was in droplet form at the end of injection. At ignition, the surviving droplets contained a negligible fraction of the fuel. During injection, the distribution of droplets across the clearance volume was nonuniform. It became much more uniform with time, after injection ended.[33]

PROBLEMS

7.1. The equivalence ratio in a conventional spark-ignition engine varies from no load (idle) to full load, at a fixed engine speed, as shown at the top of Fig. P7-1. (By load is meant the percentage of the maximum brake torque at that speed.) Also shown is the variation in total friction (pumping plus mechanical rubbing plus accessory friction). Using formats similar to those shown, draw *carefully proportioned qualitative* graphs of the following parameters versus load (0 to 100 percent):

Combustion efficiency, η_c
Gross indicated fuel conversion efficiency, $\eta_{f,ig}$
Gross indicated mean effective pressure, imep_g
Brake mean effective pressure, bmep
Mechanical efficiency, η_m

Indicate clearly where the maximum occurs if there is one, and where the value is zero or unity or some other obvious value, if appropriate. Provide a *brief justification* for the shape of the curves you draw.

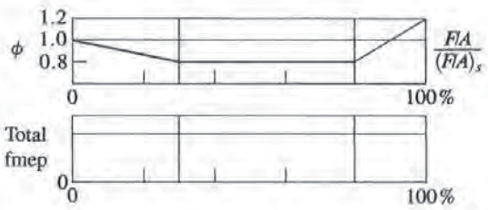


FIGURE P7-1

7.2. The four-cylinder spark-ignition engine shown in the figure uses an oxygen sensor in the exhaust system to determine whether the exhaust gas composition is lean or rich of the stoichiometric point, and a throttle-body injection system with feedback to maintain engine operation close to stoichiometric. However, since there is a time delay between a change in the fuel/air ratio at the injector location and the detection of that change by the sensor (corresponding to the flow time between the injector and the sensor), the control system shown results in oscillations in fuel/air ratio about the stoichiometric point.

(*a*) Estimate the average flow time between the injector and the sensor at an engine speed of 2000 rev/min.

PETITIONER'S EXHIBIT 1002
US PATENT NO. 6,581,565

(*b*) The sensor and control unit provide a voltage V of $+V_s$ volts when the fuel/air equivalence ratio ϕ is less than one and a voltage of $-V_s$ volts when ϕ is greater than one. The feedback injection system provides a fuel/air ratio (F/A) given by

$$\left(\frac{F}{A}\right) = \left(\frac{F}{A}\right)_{t=0} (1 + CVt)$$

where t is the time (in seconds) after the voltage signal last changed sign, $(F/A)_{t=0}$ is the fuel/air ratio at the injector at $t = 0$, and C is a constant. Develop carefully proportioned quantitative sketches of the variation in the fuel/air ratio at the injector and at the exhaust sensor, with time, showing the phase relation between the two curves. Explain briefly how you developed these graphs.

(*c*) Find the value of the constant C, in volts^{-1}-seconds^{-1} (the feedback system gain), such that (F/A) variations about the stoichiometric value do not exceed ± 10 percent for $V_s = 1$ V.

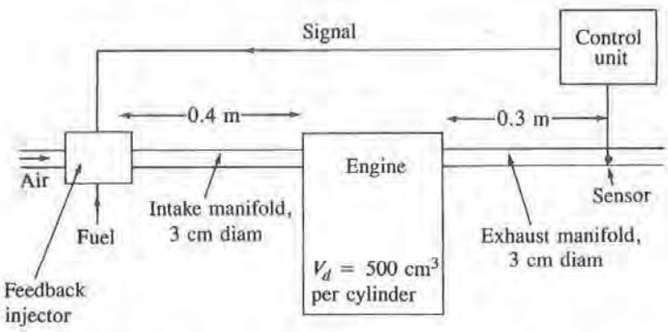


FIGURE P7-2

7.3. In many spark-ignition engines, liquid fuel is added to the inlet air upstream of the inlet manifold above the throttle. The inlet manifold is heated to ensure that under steady-state conditions the fuel is vaporized before the mixture enters the cylinder.

(*a*) At normal wide-open throttle operating conditions, in a four-stroke cycle 1.6-dm^3 displacement four-cylinder engine, at 2500 rev/min, the temperature of the air entering the carburetor is 40°C. The heat of vaporization of the fuel is 350 kJ/kg and the rate of heat transfer to the intake mixture is 1.4 kW. Estimate the temperature of the inlet mixture as it passes through the inlet valve, assuming that the fuel is fully vaporized. The volumetric efficiency is 0.85. The air density is 1.06 kg/m^3 and c_p for air is 1 kJ/kg · K. You may neglect the effects of the heat capacity of the liquid and vapor fuel.

(*b*) With port electronic fuel-injection systems, the fuel is injected directly into the intake port. The intake manifold is no longer heated. However, the fuel is only partly vaporized prior to entering the cylinder. Estimate the mixture temperature as it passes through the inlet valve with the EFI system, assuming that the air temperature entering the intake manifold is still 40°C and 50 percent of the fuel is vaporized.

(*c*) Estimate the ratio of the maximum indicated power obtained at these conditions with this engine with a carburetor, to the maximum power obtained with port fuel injection. Assume that the inlet valve is the dominant restriction in the flow into the engine and that the pressure ratio across the inlet valve is the same for both carbureted and port-injection fueled engines. The intake mixture pressure and equivalence ratio remain the same in both these cases.

PETITIONER'S EXHIBIT 1002
US PATENT NO. 6,581,565

7.4. Port fuel-injection systems are replacing carburetors in automobile spark-ignition engines. List the major advantages and any disadvantages of fuel metering with port fuel injection relative to carburetion.

7.5. With multipoint port fuel injection and single-point injection systems, the fuel flow rate is controlled by the injection pulse duration. If each injector operates continuously at the maximum rated power point (wide-open throttle, $A/F = 12$, 5500 rev/min) of an automobile spark-ignition engine, estimate approximately the injection pulse duration (in crank angle degrees) for the same engine at idle. Idle conditions are: 700 rev/min, 0.3 atm inlet manifold pressure, stoichiometric mixture.

7.6. The fuel-air cycle results indicate that the maximum imep is obtained with gasoline-air mixtures at equivalence ratios of about 1.0. In practice, the maximum wide-open throttle power of a spark-ignition engine at a given speed is obtained with an air/fuel ratio of about 12. The vaporization of the additional gasoline lowers the temperature of the inlet air and the richer mixture has a lower ratio of specific heats γ_u during compression. Estimate approximately the change in mixture temperature due to vaporization of the additional fuel used to decrease A/F from 14.6 (an equivalence ratio of 1.0) to 12.2 in the intake system, and the combined effect of vaporization and lower γ_u on the unburned mixture temperature at WOT when the cylinder pressure is at its peak of 40 atm. (The principal effect of the richer mixture is its impact on knock.)

7.7. (*a*) Plot dimensionless throttle plate open area $4A_{th}/(\pi D^2)$ as a function of throttle plate angle ψ. Assume $\psi_0 = 10°$, D (throttle bore diameter) = 57 mm, d (throttle shaft diameter) = 10.4 mm. What is the *throttle plate* area?

(*b*) Estimate the average velocity of the air flowing through the throttle plate open area for $\psi = 26°$ at 3000 rev/min and $\psi = 36°$ at 2000 rev/min. Use the relationship between ψ, engine speed, and inlet manifold pressure given in Fig. 7-22. Assume a discharge coefficient $C_D = 0.8$.

(*c*) For the throttle of part (*a*), estimate and plot the total force on the throttle plate and shaft, and the force parallel and perpendicular to the throttle bore axis (i.e., in the mean flow direction and normal to that direction) as a function of throttle angle at 2000 rev/min. Again use Fig. 7-22 for the relationship between ψ and inlet manifold pressure.

7.8. For the engine and intake manifold shown in Fig. 7-23, estimate the ratio of the intake manifold runner cross-sectional area to $(\pi B^2/4)$, the ratio of the length of the flow path from the intake manifold entrance to the inlet valve seat to the bore, the ratio of the volume of each inlet port to each cylinder's displaced volume, and the ratio of the volume of each intake manifold runner to each cylinder's displaced volume. The cylinder bore is 89 mm.

REFERENCES

1. Nakajima, Y., Sugihara, K., Takagi, Y., and Muranaka, S.: "Effects of Exhaust Gas Recirculation on Fuel Consumption," in *Proceedings of Institution of Mechanical Engineers, Automobile Division*, vol. 195, no. 30, pp. 369–376, 1981.
2. Harrington, D. L., and Bolt, J. A.: "Analysis and Digital Simulation of Carburetor Metering," SAE paper 700082, *SAE Trans.*, vol. 79, 1970.
3. Bolt, J. A., Derezinski, S. J., and Harrington, D. L.: "Influence of Fuel Properties on Metering in Carburetors," SAE paper 710207, *SAE Trans.*, vol. 80, 1971.

PETITIONER'S EXHIBIT 1002
US PATENT NO. 6,581,565

4. Khovakh, M.: *Motor Vehicle Engines* (English translation), Mir Publishers, Moscow, 1976.
5. Bolt, J. A., and Boerma, M. J.: "Influence of Air Pressure and Temperature on Carburetor Metering," SAE paper 660119, 1966.
6. Shinoda, K., Koide, H., and Yii, A.: "Analysis and Experiments on Carburetor Metering at the Transition Region to the Main System," SAE paper 710206, *SAE Trans.*, vol. 80, 1971.
7. Oya, T.: "Upward Liquid Flow in a Small Tube into which Air Streams," *Bull. JSME*, vol. 14, no. 78, pp. 1320–1329, 1971.
8. Wrausmann, R. C., and Smith, R. J.: "An Approach to Altitude Compensation of the Carburetor," SAE paper 760286, 1976.
9. Bosch, *Automotive Handbook*, 1st English ed., Robert Bosch GmbH, Stuttgart, 1978.
10. Glöckler, O., Knapp, H., and Manger, H.: "Present Status and Future Development of Gasoline Fuel Injection Systems for Passenger Cars," SAE paper 800467, 1980.
11. Greiner, M., Romann, P., and Steinbrenner, U.: "BOSCH Fuel Injectors—New Developments," SAE paper 870124, 1987.
12. Gorille, I., Rittmannsberger, N., and Werner, P.: "Bosch Electronic Fuel Injection with Closed Loop Control," SAE paper 750368, *SAE Trans.*, vol. 84, 1975.
13. Czadzeck, G. H.: "Ford's 1980 Central Fuel Injection System," SAE paper 790742, 1979.
14. Bowler, L. L.: "Throttle Body Fuel Injection (TBI)—An Integrated Engine Control System," SAE paper 800164, *SAE Trans.*, vol. 89, 1980.
15. Hamann, E., Manger, H., and Steinke, L.: "Lambda-Sensor with Y_2O_3-Stabilized ZrO_2-Ceramic for Application in Automotive Emission Control Systems," SAE paper 770401, *SAE Trans.*, vol. 86, 1977.
16. Seiter, R. E., and Clark, R. J.: "Ford Three-Way Catalyst and Feedback Fuel Control System," SAE paper 780203, *SAE Trans.*, vol. 87, 1978.
17. Camp, J., and Rachel, T.: "Closed-Loop Electronic Fuel and Air Control of Internal Combustion Engines," SAE paper 750369, 1975.
18. Liimatta, D. R., Hurt, R. F., Deller, R. W., and Hull, W. L.: "Effects of Mixture Distribution on Exhaust Emissions as Indicated by Engine Data and the Hydraulic Analogy," SAE paper 710618, *SAE Trans.*, vol. 80, 1971.
19. Benson, R. S., Baruah, P. C., and Sierens, I. R.: "Steady and Non-steady Flow in a Simple-Carburetor," in *Proceedings of Institution of Mechanical Engineers*, vol. 188, no. 53/74, pp. 537–548, 1974.
20. Woods, W. A., and Goh, G. K.: "Compressible Flow through a Butterfly Throttle Valve in a Pipe," in *Proceedings of Institution of Mechanical Engineers*, vol. 193, no. 10, pp. 237–244, 1979.
21. Walker, J. W.: "The GM 1.8 Liter L-4 Gasoline Engine Designed by Chevrolet," SAE paper 820111, *SAE Trans.*, vol. 91, 1982.
22. Chapman, M.: "Two Dimensional Numerical Simulation of Inlet Manifold Flow in a Four Cylinder Internal Combustion Engine," SAE paper 790244, 1979.
23. Kay, I. W.: "Manifold Fuel Film Effects in an SI Engine," SAE paper 780944, 1978.
24. Brandstetter, W. R., and Carr, M. J.: "Measurement of Air Distribution in a Multicylinder Engine by Means of a Mass Flow Probe," SAE paper 730494, 1973.
25. Aquino, C. F.: "Transient *A/F* Control Characteristics of the 5 Liter Central Fuel Injection Engine," SAE 810494, *SAE Trans.*, vol. 90, 1981.
26. Trayser, D. A., Creswick, F. A., Giesike, J. A., Hazard, H. R., Weller, A. E., and Locklin, D. W.: "A Study of the Influence of Fuel Atomization, Vaporization, and Mixing Processes on Pollutant Emissions from Motor-Vehicle Powerplants," Battelle Memorial Institute, Columbus, Ohio, 1969.
27. Tabaczysnki, R. J.: "Effects of Inlet and Exhaust System Design on Engine Performance," SAE paper 821577, 1982.
28. Engelman, H. W.: "Design of a Tuned Intake Manifold," ASME paper 73-WA/DGP-2, 1973.
29. Benson, R. S.: in J. H. Horlock and D. E. Winterbone (eds.), *The Thermodynamics and Gas Dynamics of Internal Combustion Engines*, vol. 1, Clarendon Press, Oxford, 1982.
30. Chapman, M., Novak, J. M., and Stein, R. A.: "Numerical Modeling of Inlet and Exhaust Flows in Multi-cylinder Internal Combustion Engines," in *Flows in Internal Combustion Engines*, ASME Winter Annual Meeting, Nov. 14–19, 1982, ASME, New York.

PETITIONER'S EXHIBIT 1002
US PATENT NO. 6,581,565

31. Bridgeman, O. C.: "Equilibrium Volatility of Motor Fuels from the Standpoint of Their Use in Internal Combustion Engines," National Bureau of Standards research paper 694, 1934.
32. ASTM Standard Method: "Distillation of Petroleum Products," ANSI/ASTM D86 (1P 123/68).
33. Peters, B. D.: "Laser-Video Imaging and Measurement of Fuel Droplets in a Spark-Ignition Engine," in *Proceedings of Conference on Combustion in Engineering*, Oxford, Apr. 11–14, 1983, Institution of Mechanical Engineers, 1983.
34. Sirignano, W. A.: "Fuel Droplet Vaporization and Spray Combustion Theory," *Prog. Energy and Combust. Sci.*, vol. 9, pp. 291–322, 1983.
35. Boam, D. J., and Finlay, I. C.: "A Computer Model of Fuel Evaporation in the Intake System of a Carbureted Petrol Engine," Conference on *Fuel Economy and Emissions of Lean Burn Engines*, London, June 12–14, 1979, paper C89/79, Institution of Mechanical Engineers, 1979.
36. Yun, H. J., and Lo, R. S.: "Theoretical Studies of Fuel Droplet Evaporation and Transportation in a Carburetor Venturi," SAE paper 760289, 1976.
37. Servati, H. B., and Yuen, W. W.: "Deposition of Fuel Droplets in Horizontal Intake Manifolds and the Behavior of Fuel Film Flow on Its Walls," SAE paper 840239, *SAE Trans.*, vol. 93, 1984.
38. Hires, S. D., and Overington, M. T.: "Transient Mixture Strength Excursions—An Investigation of Their Causes and the Development of a Constant Mixture Strength Fueling Strategy," SAE paper 810495, *SAE Trans.*, vol. 90, 1981.
39. Collins, M. H.: "A Technique to Characterize Quantitatively the Air/Fuel Mixture in the Inlet Manifold of a Gasoline Engine," SAE paper 690515, *SAE Trans.*, vol. 78, 1969.
40. Blackmore, D. R., and Thomas, A.: *Fuel Economy of the Gasoline Engine*, John Wiley, 1977.
41. Yu, H. T. C.: "Fuel Distribution Studies—A New Look at an Old Problem," *SAE Trans.*, vol. 71, pp. 596–613, 1963.

PETITIONER'S EXHIBIT 1002
US PATENT NO. 6,581,565

CHAPTER 8

CHARGE MOTION WITHIN THE CYLINDER

Gas motion within the engine cylinder is one of the major factors that controls the combustion process in spark-ignition engines and the fuel-air mixing and combustion processes in diesel engines. It also has a significant impact on heat transfer. Both the bulk gas motion and the turbulence characteristics of the flow are important. The initial in-cylinder flow pattern is set up by the intake process. It may then be substantially modified during compression. This chapter reviews the important features of gas motion within the cylinder set up by flows into and out of the cylinder through valves or ports, and by the motion of the piston.

8.1 INTAKE JET FLOW

The engine intake process governs many important aspects of the flow within the cylinder. In four-stroke cycle engines, the inlet valve is the minimum area for the flow (see Sec. 6.3) so gas velocities at the valve are the highest velocities set up during the intake process. The gas issues from the valve opening into the cylinder as a conical jet and the radial and axial velocities in the jet are about 10 times the mean piston speed. Figure 8-1 shows the radial and axial velocity components close to the valve exit, measured during the intake process, in a motored model engine with transparent walls and single valve located on the cylinder axis, using laser doppler anemometry (see next section).[1] The jet separates from the valve

PETITIONER'S EXHIBIT 1002
US PATENT NO. 6,581,565

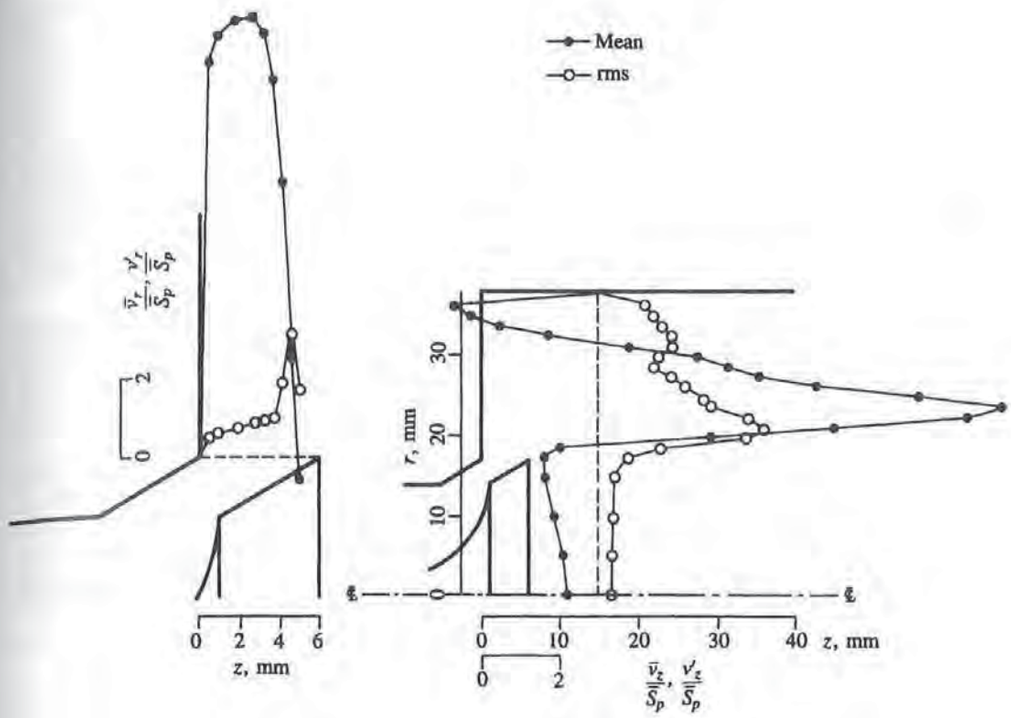


FIGURE 8-1
Radial mean velocity $\bar{v}_r$ and root mean square (rms) velocity fluctuations v'_r at the valve exit plane, and axial mean velocity $\bar{v}_z$ and rms velocity fluctuation v'_z 15 mm below the cylinder head, at 36° ATC in model engine operated at 200 rev/min. Valve lift = 6 mm. Velocities normalized by mean piston speed.[1]

seat and lip, producing shear layers with large velocity gradients which generate turbulence. This separation of the jet sets up recirculation regions beneath the valve head and in the corner between the cylinder wall and cylinder head.

The motion of the intake jet within the cylinder is shown in the schlieren photographs in Fig. 8-2 taken in a transparent engine. This engine had a square cross-section cylinder made up of two quartz walls and two steel walls, to permit easy optical access. The schlieren technique makes regions with density gradients in the flow show up as lighter or darker regions on the film.[2] The engine was throttled to one-half an atmosphere intake pressure, so the jet starts after the intake stroke has commenced, at 35° ATC, following backflow of residual into the intake manifold. The front of the intake jet can be seen propagating from the valve to the cylinder wall at several times the mean piston speed. Once the jet reaches the wall ($\theta > 41°$ ATC), the wall deflects the major portion of the jet downward toward the piston; however, a substantial fraction flows upward toward the cylinder head. The highly turbulent nature of the jet is evident.

The interaction of the intake jet with the wall produces large-scale rotating flow patterns within the cylinder volume. These are easiest to visualize where the engine geometry has been simplified so the flow is axisymmetric. The photograph

PETITIONER'S EXHIBIT 1002
US PATENT NO. 6,581,565

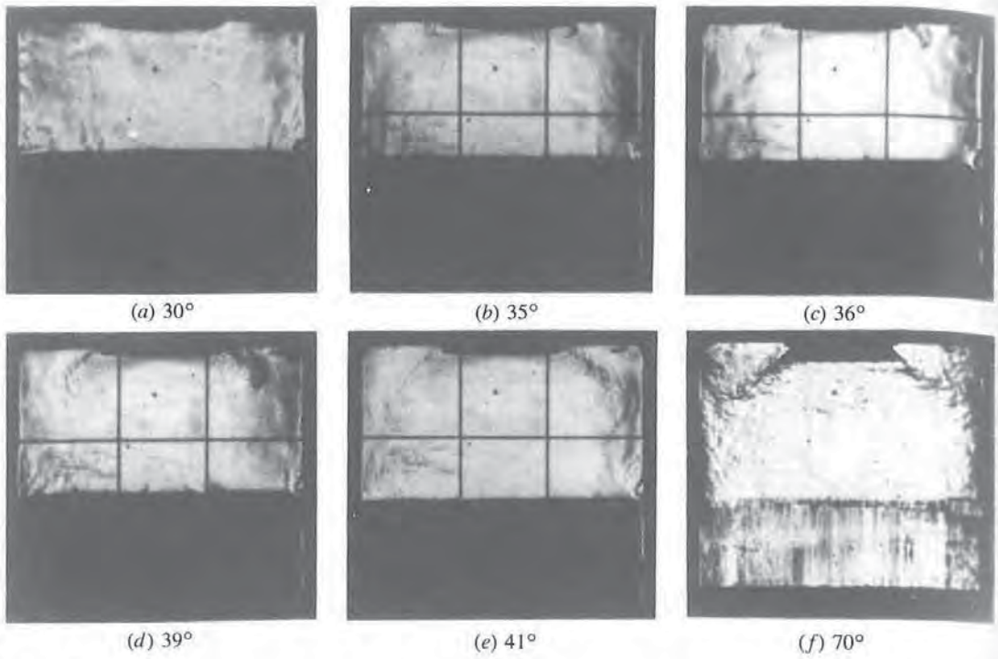


FIGURE 8-2
Sequence of schlieren photographs of intake jet as it develops during intake stroke. Numbers are crank angle degrees after TC.[2]

in Fig. 8-3 of a water analog of an engine intake flow was taken in a transparent model of an engine cylinder and piston. The valve is located in the center of the cylinder head, and the flow into the valve is along the cylinder axis. The experimental parameters have been scaled so that the appropriate dimensionless numbers which govern the flow, the Reynolds and Strouhal numbers, were maintained equal to typical engine values. The photograph shows the major features

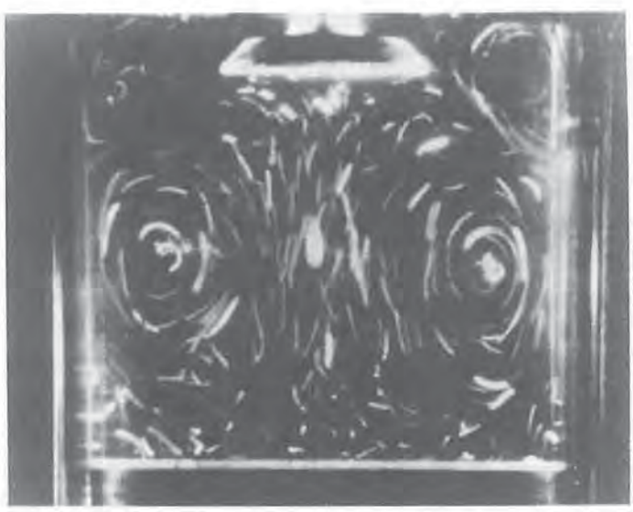
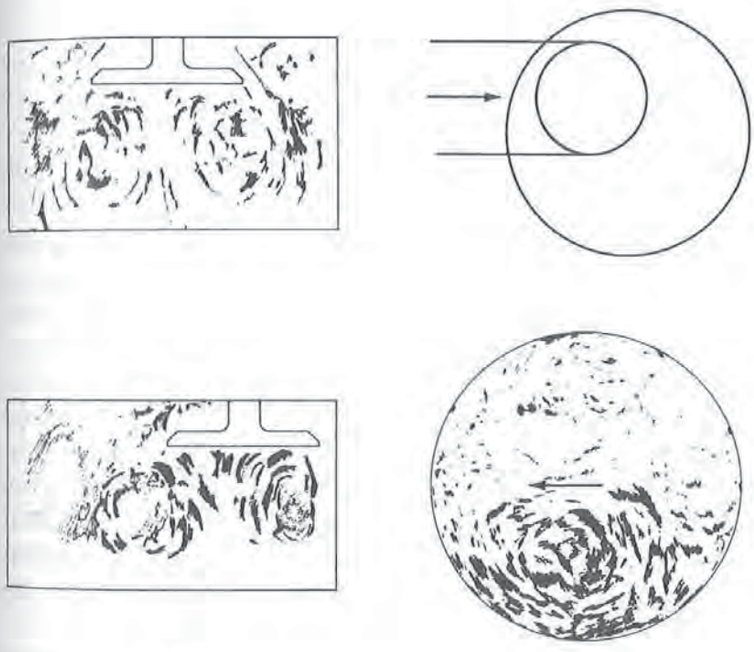


FIGURE 8-3
Large-scale rotating flow pattern set up within the cylinder by the intake jet. Photograph of streak lines in water flow into model engine with axisymmetric valve.[3]

PETITIONER'S EXHIBIT 1002
US PATENT NO. 6,581,565

of the intake generated flow in a thin illuminated plane through the cylinder axis. The streaks are records of the paths of tracer particles in the flow during the period the camera shutter is open. The bulk of the cylinder as the piston moves down is filled with a large ring vortex, whose center moves downward and remains about halfway between the piston and the head. The upper corner of the cylinder contains a smaller vortex, rotating in the opposite direction. These vortices persist until about the end of the intake stroke, when they became unstable and break up.[3]

With inlet valve location and inlet port geometry more typical of normal engine practice, the intake generated flow is more complex. However, the presence of large-scale rotating flow patterns can still be discerned. Figure 8-4*a* shows the effect of off-axis valve location (with the flow into the valve still parallel to the cylinder and valve axis). During the first half of the inlet stroke, at least, a flow pattern similar in character to that in Fig. 8-3 is evident. The vortices are now displaced to one side, however, and the planes of their axes of rotation are no longer perpendicular to the cylinder axis but are tipped at an angle to it. The vortices become unstable and break up earlier in the intake stroke than was the case with the axisymmetric flow.[3] With an offset valve and a normal inlet port configuration which turns the flow through 50 to 70° (see Fig. 6-13), photographs



(*a*) (*b*)

FIGURE 8-4
Sketches from: (*a*) streak photographs of in-cylinder intake generated flow in water analog of intake process in model engine with offset inlet valve, at 90° ATC;[3] (*b*) streak photographs of flow in diametral plane; 30 mm below cylinder head, with intake port and valve geometry shown, with steady water flow into cylinder. Valve lift = 4 mm.[4]

PETITIONER'S EXHIBIT 1002
US PATENT NO. 6,581,565

of the flow pattern in a diametral plane show an additional large-scale rotation. Figure 8-4*b* shows the flow pattern observed in a water-flow model of the cylinder in a plane 30 mm (one-third of the bore) from the cylinder head, with a standard inlet port design. The direction of flow with this vortex pair is toward the left across the center of the cylinder. This flow pattern occurs because the cylinder wall closest to the valve impedes the flow out of the valve and forces the flow on either side of the plane passing through the valve and cylinder axes to circulate around the cylinder in opposite directions. The upper vortex follows the flow direction of the port and becomes larger still as the valve lift increases. The details of this aspect of the intake flow depend on the port design, valve stem orientation, and the valve lift.[4] With suitable port and/or cylinder head design, it is possible to develop a single vortex flow within the bulk of the cylinder. The production and characteristics of such "swirling" flows are reviewed in Sec. 8.3.

In summary, the jet-like character of the intake flow, interacting with the cylinder walls and moving piston, creates large-scale rotating flow patterns within the cylinder. The details of these flows are strongly dependent on the inlet port, valve, and cylinder head geometry. These flows appear to become unstable, either during the intake or the compression process, and break down into three-dimensional turbulent motions. Recirculating flows of this type are usually sensitive to small variations in the flow: hence there are probably substantial cycle-by-cycle flow variations.[5]

8.2 MEAN VELOCITY AND TURBULENCE CHARACTERISTICS

8.2.1 Definitions

The flow processes in the engine cylinder are turbulent. In turbulent flows, the rates of transfer and mixing are several times greater than the rates due to molecular diffusion. This turbulent "diffusion" results from the local fluctuations in the flow field. It leads to increased rates of momentum and heat and mass transfer, and is essential to the satisfactory operation of spark-ignition and diesel engines. Turbulent flows are always dissipative. Viscous shear stresses perform deformation work on the fluid which increases its internal energy at the expense of its turbulence kinetic energy. So energy is required to generate turbulence: if no energy is supplied, turbulence decays. A common source of energy for turbulent velocity fluctuations is shear in the mean flow. Turbulence is rotational and is characterized by high fluctuating vorticity: these vorticity fluctuations can only persist if the velocity fluctuations are three dimensional.[6]

The character of a turbulent flow depends on its environment. In the engine cylinder, the flow involves a complicated combination of turbulent shear layers, recirculating regions, and boundary layers. The flow is unsteady and may exhibit substantial cycle-to-cycle fluctuations. Both large-scale and small-scale turbulent motions are important factors governing the overall behavior of the flow.[5]

An important characteristic of a turbulent flow is its irregularity or ran-

PETITIONER'S EXHIBIT 1002
US PATENT NO. 6,581,565

domness. Statistical methods are therefore used to define such a flow field. The quantities normally used are: the mean velocity, the fluctuating velocity about the mean, and several length and time scales. In a steady turbulent flow situation, the instantaneous local fluid velocity U (in a specific direction) is written:

$$U(t) = \bar{U} + u(t) \tag{8.1}$$

For steady flow, the mean velocity $\bar{U}$ is the time average of $U(t)$:

$$\bar{U} = \lim_{\tau \to \infty} \frac{1}{\tau} \int_{t_0}^{t_0+\tau} U(t)\, dt \tag{8.2}$$

The fluctuating velocity component u is defined by its root mean square value, the turbulence intensity, u':

$$u' = \lim_{\tau \to \infty} \left(\frac{1}{\tau} \int_{t_0}^{t_0+\tau} u^2\, dt \right)^{1/2} \tag{8.3a}$$

Alternatively,

$$u' = \lim_{\tau \to \infty} \left[\frac{1}{\tau} \int_{t_0}^{t_0+\tau} (U^2 - \bar{U}^2)\, dt \right]^{1/2} \tag{8.3b}$$

since the time average of $(u\bar{U})$ is zero.

In engines, the application of these turbulence concepts is complicated by the fact that the flow pattern changes during the engine cycle. Also, while the overall features of the flow repeat each cycle, the details do not because the mean flow can vary significantly from one engine cycle to the next. There are both cycle-to-cycle variations in the mean or bulk flow at any point in the cycle, as well as turbulent fluctuations about that specific cycle's mean flow.

One approach used in quasi-periodic flows such as that which occurs in the engine cylinder is *ensemble-averaging* or *phase-averaging*. Usually, velocity measurements are made over many engine cycles, and over a range of crank angles. The instantaneous velocity at a specific crank angle position θ in a particular cycle i can be written as

$$U(\theta, i) = \bar{U}(\theta, i) + u(\theta, i) \tag{8.4}$$

The ensemble- or phase-averaged velocity, $\bar{U}(\theta)$, is defined as the average of values at a specific phase or crank angle in the basic cycle. Figure 8-5 shows this approach applied schematically to the velocity variation during a two-stroke engine cycle, with small and large cycle-to-cycle variations. The ensemble-averaged velocity is the average over a large number of measurements taken at the same crank angle (two such points are indicated by dots):

$$\bar{U}_{\mathrm{EA}}(\theta) = \frac{1}{N_c} \sum_{i=1}^{N_c} U(\theta, i) \tag{8.5}$$

where N_c is the number of cycles for which data are available. By repeating this

PETITIONER'S EXHIBIT 1002
US PATENT NO. 6,581,565

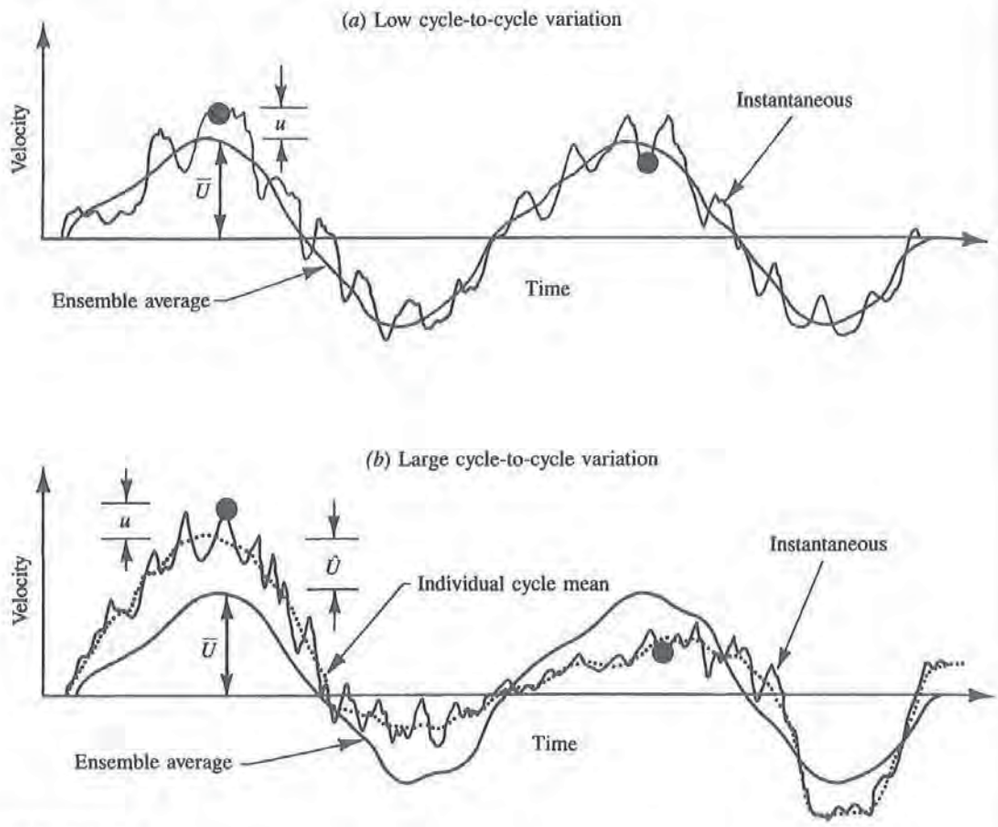


FIGURE 8-5
Schematic of velocity variation with crank angle at a fixed location in the cylinder during two consecutive cycles of an engine. Dots indicate measurements of instantaneous velocity at the same crank angle. Ensemble- or phase-averaged velocity obtained by averaging over a large number of such measurements shown as solid smooth line. Top graph: low cycle-to-cycle flow variations. Here the individual-cycle mean velocity and ensemble-averaged velocity are closely comparable. Bottom graph: large cycle-to-cycle variations. Here the individual-cycle mean velocity (dotted line) is different from the ensemble-averaged mean by $\hat{U}$. The turbulent fluctuation u is then defined in relation to the individual-cycle mean.[5]

process at many crank angle locations, the ensemble-averaged velocity profile over the complete cycle is obtained.

The ensemble-averaged mean velocity is only a function of crank angle since the cyclic variation has been averaged out. The difference between the mean velocity in a particular cycle and the ensemble-averaged mean velocity over many cycles is defined as the cycle-by-cycle variation in mean velocity:

$$\hat{U}(\theta, i) = \bar{U}(\theta, i) - \bar{U}_{EA}(\theta) \tag{8.6}$$

Thus the instantaneous velocity, given by Eq. (8.4), can be split into three components:[7]

$$U(\theta, i) = \bar{U}_{EA}(\theta) + \hat{U}(\theta, i) + u(\theta, i) \tag{8.7}$$

PETITIONER'S EXHIBIT 1002
US PATENT NO. 6,581,565

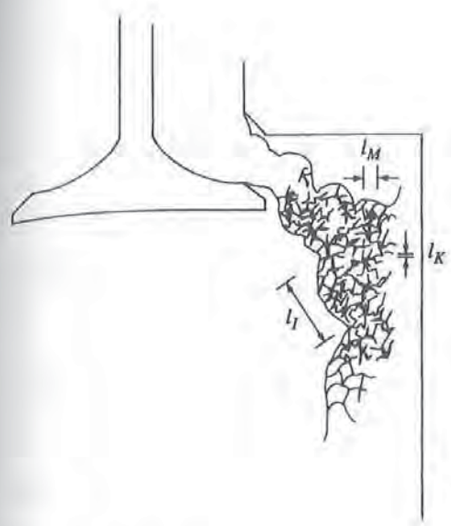


FIGURE 8-6
Schematic of jet created by flow through the intake valve indicating its turbulent structure.[5, 6]

Figure 8-5 illustrates this breakdown of the instantaneous velocity into an ensemble-averaged component, an individual-cycle mean velocity, and a component which randomly fluctuates in time at a particular point in space in a single cycle. This last component is the conventional definition of the turbulent velocity fluctuation. Whether this differs significantly from the fluctuations about the ensemble-averaged velocity depends on whether the cycle-to-cycle fluctuations are small or large. The figure indicates these two extremes.†

In turbulent flows, a number of length scales exist that characterize different aspects of the flow behavior. The largest eddies in the flow are limited in size by the system boundaries. The smallest scales of the turbulent motion are limited by molecular diffusion. The important length scales are illustrated by the schematic of the jet issuing into the cylinder from the intake valve in Fig. 8-6. The eddies responsible for most of the turbulence production during intake are the large eddies in the conical inlet jet flow. These are roughly equal in size to the local jet thickness. This scale is called the *integral scale*, l_I: it is a measure of the largest scale structure of the flow field. Velocity measurements made at two points separated by a distance x significantly less than l_I will correlate with each other; with $x \gg l_I$, no correlation will exist. The integral length scale is, therefore, defined as the integral of the autocorrelation coefficient of the fluctuating velocity at two adjacent points in the flow with respect to the variable distance between

† There is considerable debate as to whether the fluctuating components of the velocity $U(\theta, i)$ defined by Eq. (8.7) (cycle fluctuations in the mean velocity and fluctuations in time about the individual cycle mean) are physically distinct phenomena. The high-frequency fluctuations in velocity are often defined as "turbulence." The low-frequency fluctuations are generally attributed to the variations in the mean flow between individual cycles, a phenomenon that is well established. Whether this distinction is valid has yet to be resolved.

PETITIONER'S EXHIBIT 1002
US PATENT NO. 6,581,565

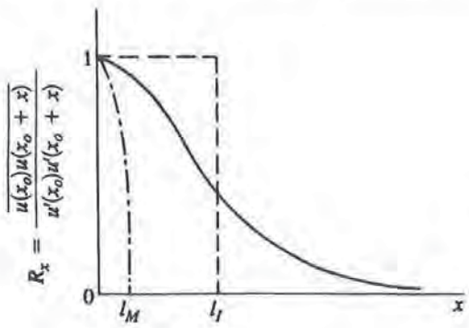


FIGURE 8-7
Spatial velocity autocorrelation R_x as a function of x, defining the integral length scale l_I and the micro length scale l_M.

the points, as shown in Fig. 8-7: i.e.,

$$l_I = \int_0^\infty R_x \, dx \tag{8.8a}$$

where

$$R_x = \frac{1}{N_m - 1} \sum_{i=1}^{N_m} \frac{u(x_0)u(x_0 + x)}{u'(x_0)u'(x_0 + x)} \tag{8.8b}$$

This technique for determining the integral scale requires simultaneous measurements at two points. Due to the difficulty of applying such a technique in engines, most efforts to determine length scales have first employed correlations to determine the *integral time scale*, τ_I. The integral time scale of turbulence is defined as a correlation between two velocities at a fixed point in space, but separated in time:

$$\tau_I = \int_0^\infty R_t \, dt \tag{8.9a}$$

where

$$R_t = \frac{1}{N_m - 1} \sum_{i=1}^{N_m} \frac{u(t_0)u(t_0 + t)}{u'(t_0)u'(t_0 + t)} \tag{8.9b}$$

and N_m is the number of measurements. Under conditions where the turbulence pattern is convected past the observation point without significant distortion and the turbulence is relatively weak, the integral length and time scales are related by

$$l_I = \bar{U}\tau_I \tag{8.10}$$

In flows where the large-scale structures are convected, τ_I is a measure of the time it takes a large eddy to pass a point. In flows without mean motion, the integral time scale is an indication of the lifetime of an eddy.[5, 8]

Superposed on this large-scale flow is a range of eddies of smaller and smaller size, fed by the continual breakdown of larger eddies. Since the smaller eddies respond more rapidly to changes in local flow pattern, they are more likely

PETITIONER'S EXHIBIT 1002
US PATENT NO. 6,581,565

to be isotropic (have no preferred direction) than are the large eddies, and have a structure like that of other turbulent flows. The dissipation of turbulence energy takes place in the smallest structures. At this smallest scale of the turbulent motion, called the *Kolmogorov scale*, molecular viscosity acts to dissipate small-scale kinetic energy into heat. If ε is the energy dissipation rate per unit mass and ν the kinematic viscosity, Kolmogorov length and time scales are defined by

$$l_K = \left(\frac{\nu^3}{\varepsilon}\right)^{1/4} \qquad \tau_K = \left(\frac{\nu}{\varepsilon}\right)^{1/2} \tag{8.11}$$

The Kolmogorov length scale indicates the size of the smallest eddies. The Kolmogorov time scale characterizes the momentum-diffusion of these smallest structures.

A third scale is useful in characterizing a turbulent flow. It is called the *microscale* (or Taylor microscale). The micro length scale l_M is defined by relating the fluctuating strain rate of the turbulent flow field to the turbulence intensity:

$$\frac{\partial u}{\partial x} \approx \frac{u'}{l_M} \tag{8.12}$$

It can be determined from the curvature of the spatial correlation curve at the origin, as shown in Fig. 8-7.[5, 6] More commonly, the micro time scale τ_M is determined from the temporal autocorrelation function of Eq. (8.9):

$$\tau_M^2 = -\frac{2}{(\partial^2 R_t/\partial t^2)_{t_0}}$$

For turbulence which is homogeneous (has no spatial gradients) and is isotropic (has no preferred direction), the microscales l_M and τ_M are related by

$$l_M = \bar{U}\tau_M \tag{8.13}$$

These different scales are related as follows. The turbulent kinetic energy per unit mass in the large-scale eddies is proportional to u'^2. Large eddies lose a substantial fraction of this energy in one "turnover" time l_I/u'. In an equilibrium situation the rate of energy supply equals the rate of dissipation:

$$\varepsilon \approx \frac{u'^3}{l_I}$$

Thus,

$$\frac{l_K}{l_I} \approx \left(\frac{u' l_I}{\nu}\right)^{-3/4} = \mathrm{Re}_T^{-3/4} \tag{8.14}$$

where Re_T is the turbulent Reynolds number, $u' l_I/\nu$.

Within the restrictions of homogeneous and isotropic turbulence, an energy budget can be used to relate l_I and l_M:[6]

$$\varepsilon = \frac{Au'^3}{l_I} = \frac{15\nu u'^2}{l_M^2}$$

PETITIONER'S EXHIBIT 1002
US PATENT NO. 6,581,565

where A is a constant of order 1. Thus,

$$\frac{l_M}{l_I} = \left(\frac{15}{A}\right)^{1/2} \mathrm{Re}_T^{-1/2} \tag{8.15}$$

These restrictions are not usually satisfied within the engine cylinder during intake. They are approximately satisfied at the end of compression.

8.2.2 Application to Engine Velocity Data

As has been explained above, it is necessary to analyze velocity data on an individual cycle basis as well as using ensemble-averaging techniques. The basic definitions for obtaining velocities which characterize the flow will now be developed. The ensemble-averaged velocity $\bar{U}_{\mathrm{EA}}$ has already been defined by Eq. (8.5). The ensemble-averaged fluctuation intensity $u'_{F,\,\mathrm{EA}}$ is given by

$$u'_{F,\,\mathrm{EA}}(\theta) = \left\{\frac{1}{N_c}\sum_{i=1}^{N_c}[u(\theta, i)]^2\right\}^{1/2} = \left\{\frac{1}{N_c}\sum_{i=1}^{N_c}[U(\theta, i)^2 - \bar{U}_{\mathrm{EA}}(\theta)^2]\right\}^{1/2} \tag{8.16}$$

It includes all fluctuations about the ensemble-averaged mean velocity.

Use of Eqs. (8.5) and (8.16) requires values for U and u at each specific crank angle under consideration. While some measurement techniques (e.g., hot-wire anemometry) provide this, the preferred velocity measurement method (laser doppler anemometry) provides an intermittent signal. With laser doppler anemometry (LDA), interference fringes are produced within the small volume created by the intersection of two laser beams within the flow field. When a small particle passes through this volume, it scatters light at a frequency proportional to the particle velocity. By seeding the flow with particles small enough to be carried without slip by the flow and collecting this scattered light, the flow velocity is determined.[9] A signal is only produced when a particle moves through the measurement volume; thus one collects data as velocity crank angle pairs. It is necessary, therefore, to perform the ensemble-averaging over a finite crank angle window $\Delta\theta$ around the specific crank angle of interest, $\bar{\theta}$. The ensemble-averaged velocity equation becomes

$$\bar{U}_{\mathrm{EA}}(\bar{\theta}) = \frac{1}{N_t}\sum_{i=1}^{N_c}\sum_{j=1}^{N_l} U_{i,j}\left(\bar{\theta} \pm \frac{\Delta\theta}{2}\right) \tag{8.17}$$

where N_i is the number of velocity measurements recorded in the window during the ith cycle, N_c is the number of cycles, and N_t is the total number of measurements.† The corresponding equation for the ensemble-averaged root mean square

† This need to ensemble-average over a finite crank angle window introduces an error called crank angle broadening, due to change in the mean velocity across the window. This error depends on the velocity gradient, and can be made negligibly small by suitable choice of window size.[9–11]

PETITIONER'S EXHIBIT 1002
US PATENT NO. 6,581,565

velocity fluctuation is

$$u'_{F,\,\mathrm{EA}}(\bar{\theta}) = \left\{ \frac{1}{N_t} \sum_{i=1}^{N_c} \sum_{j=1}^{N_i} \left[u_{i,j}\left(\bar{\theta} \pm \frac{\Delta\theta}{2} \right) \right]^2 \right\}^{1/2} \tag{8.18}$$

where

$$u_{i,j} = U_{i,j} - \bar{U}_{\mathrm{EA}} \tag{8.19}$$

As has already been explained, this definition of fluctuation intensity [the ensemble-averaged rms velocity fluctuation, Eq. (8.18)] includes cyclic variations in the mean flow as well as the turbulent fluctuations about each cycle's mean flow.[7] It is necessary to determine the mean and fluctuating velocities on an individual-cycle basis to characterize the flow field more completely. The critical part of this process is defining the mean velocity at a specific crank angle (or within a small window centered about that crank angle) in each cycle. Several methods have been used to determine this individual-cycle mean velocity (e.g., moving window, low-pass filtering, data smoothing, conditional sampling; see Ref. 7 for a summary). A high data rate is required.

In this individual-cycle velocity analysis the individual-cycle time-averaged or mean velocity $\bar{U}(\bar{\theta}, i)$ is first determined.[7, 12] The ensemble average of this mean velocity

$$\bar{U}_{\mathrm{EA}}(\bar{\theta}) = \frac{1}{N_c} \sum_{i=1}^{N_c} \bar{U}\left(\bar{\theta} \pm \frac{\Delta\theta}{2}, i \right) \tag{8.20}$$

is identical to the ensemble-averaged value given by Eq. (8.17). The root mean square fluctuation in individual-cycle mean velocity can then be determined from

$$U_{\mathrm{RMS}}(\bar{\theta}) = \left\{ \frac{1}{N_c} \sum_{i=1}^{N_c} \left[\bar{U}\left(\bar{\theta} \pm \frac{\Delta\theta}{2}, i \right) - \bar{U}_{\mathrm{EA}}(\bar{\theta}) \right]^2 \right\}^{1/2} \tag{8.21}$$

This indicates the magnitude of the cyclic fluctuations in the mean motion. The instantaneous velocity fluctuation from the mean velocity, within a specified window $\Delta\theta$ at a particular crank angle $\bar{\theta}$, is obtained from Eq. (8.4). This instantaneous velocity fluctuation is ensemble-averaged, because it varies substantially cycle-by-cycle and because the amount of data is usually insufficient to give reliable individual-cycle results:

$$u'_{T,\,\mathrm{EA}}(\bar{\theta}) = \left\{ \frac{1}{N_c} \sum_{i=1}^{N_c} \left[U\left(\bar{\theta} \pm \frac{\Delta\theta}{2}, i \right) - \bar{U}\left(\bar{\theta} \pm \frac{\Delta\theta}{2}, i \right) \right]^2 \right\}^{1/2} \tag{8.22}$$

This quantity is the ensemble-averaged turbulence intensity.

Several different techniques have been used to measure gas velocities within the engine cylinder (see Refs. 13 and 14 for brief reviews and references). The technique which provides most complete and accurate data is laser doppler anemometry.[9] Sample results obtained with this technique will now be reviewed to

PETITIONER'S EXHIBIT 1002
US PATENT NO. 6,581,565

illustrate the major features of the in-cylinder gas motion. The available results must be interpreted with caution since they have been obtained in special engines where the geometry and flow have been modified to make the experiments and their interpretation easier. Also, the flow within the cylinder is three dimensional in nature. It takes measurements at many points within the flow field and the use of a flow visualization technique to characterize the flow adequately.

Figure 8-8 shows ensemble-averaged velocities throughout the engine cycle at two measurement locations in a special L-head engine designed to generate a swirling flow within the cylinder. The engine was motored at 300 rev/min, giving a mean piston speed of 0.76 m/s. Figure 8-8*b* shows the mean velocity in the path of the swirling intake flow within the clearance volume, in the swirl direction. High velocities are generated during the intake process, rising to a maximum and then decreasing in response to the piston motion (see Fig. 2-2). During the compression stroke, the velocity continues to decrease but at a much slower rate. This is a motored engine cycle. A comparison of intake and compression velocities with an equivalent firing cycle showed close agreement.[15] The expansion and

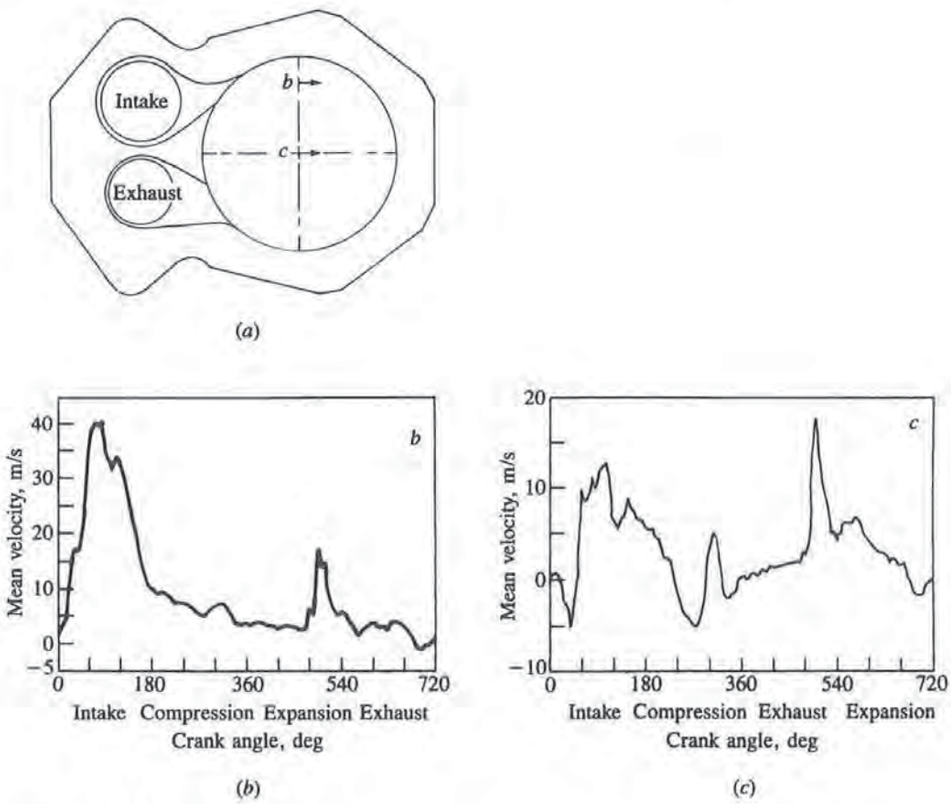


FIGURE 8-8
Ensemble-averaged velocities throughout the engine cycle in motored four-stroke L-head engine: 300 rev/min, mean piston speed 0.76 m/s. (*a*) Engine schematic showing measurement locations and velocity directions; (*b*) velocity at *b* in intake flow path; (*c*) velocity at *c* on cylinder axis.[11]

PETITIONER'S EXHIBIT 1002
US PATENT NO. 6,581,565

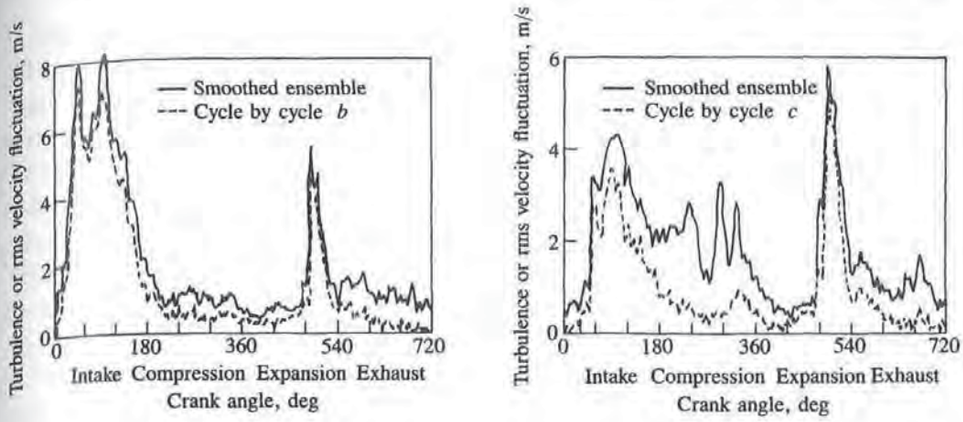


FIGURE 8-9
Ensemble-averaged rms velocity fluctuation and ensemble-averaged individual-cycle turbulence intensity as a function of crank angle: (*a*) at location *b* in Fig. 8-8*a*; (*b*) at location *c* in Fig. 8-8*a*.[11]

exhaust stroke velocities are not typical of firing engine behavior, however.† Figure 8-8*c* shows the mean velocity in the clearance volume in the same direction but on the cylinder axis. At this location, positive and negative flow velocities were measured. Since this location is out of the path of the intake generated flow, velocities during the intake stroke are much lower. The nonhomogeneous character of this particular ensemble-mean flow is evident.

Figure 8-9 shows the ensemble-averaged rms velocity fluctuation (which includes contributions from cycle-by-cycle variations in the mean flow and turbulence) and the ensemble-averaged individual-cycle turbulence intensity at these same two locations and directions. The difference between the two curves in each graph is an indication of the cycle-by-cycle variation in the mean flow [see Eq. (8.7)]. During the intake process, within the directed intake flow pattern, the cycle-by-cycle variation in the mean flow is small in comparison to the high turbulence levels created by the intake flow. Outside this directed flow region, again during intake, this cycle-by-cycle contribution is more significant relative to the turbulence. During compression, the cycle-by-cycle mean flow variation is comparable in magnitude to the ensemble-averaged turbulence intensity. It is therefore highly significant.

Two important questions regarding the turbulence in the engine cylinder are whether it is homogeneous (i.e., uniform) and whether it is isotropic (i.e., independent of direction). The data already presented in Figs. 8-8 and 8-9 show that during intake the flow is far from homogeneous. Nor is it isotropic.[11]

† The increase in velocity when the exhaust valve opens is due to the flow of gas *into* the cylinder because, due primarily to heat losses, the cylinder pressure is then below 1 atm.

PETITIONER'S EXHIBIT 1002
US PATENT NO. 6,581,565

However, it is the character of the turbulence at the end of the compression process that is most important: that is what controls the fuel-air mixing and burning rates. Only limited data are available which relate to these questions. With open disc-shaped combustion chambers, measurements at different locations in the clearance volume around TC at the end of compression show the turbulence intensity to be relatively homogeneous. In the absence of an intake generated swirling flow, the turbulence intensity was also essentially isotropic near TC.[16] These specific results support the more general conclusion that the inlet boundary conditions play the dominant role in the generation of the mean flow and turbulence fields during the intake stroke. However, in the absence of swirl, this intake generated flow structure has almost disappeared by the time the compression process commences. The turbulence levels follow this trend in the mean flow, with the rapid decay process lasting until intake valve closing. Later in the compression process the turbulence becomes essentially homogeneous.[17]

When a swirling flow is generated during intake, an almost solid-body rotating flow develops which remains stable for much longer than the inlet jet generated rotating flows illustrated in Fig. 8-3. With simple disc-shaped chambers, the turbulence still appears to become almost homogeneous at the end of compression. With swirl and bowl-in-piston geometry chambers, however, the flow is more complex (see Sec. 8.3).

The flow through the intake valve or port is responsible for many features of the in-cylinder motion. The flow velocity through the valve is proportional to the piston speed [see Eq. (6.10) for pseudo valve flow velocity, and Eq. 2.10)]. It would be expected therefore that in-cylinder flow velocities at different engine speeds would scale with mean piston speed [Eq. (2.11)]. Figure 8-10 shows ensemble-averaged mean and rms velocity fluctuations, normalized by the mean piston speed through the cycle at three different engine speeds. The measurement location is in the path of the intake generated swirling flow (point *b* in Fig. 8-8*a*). All the curves have approximately the same shape and magnitude, indicating the

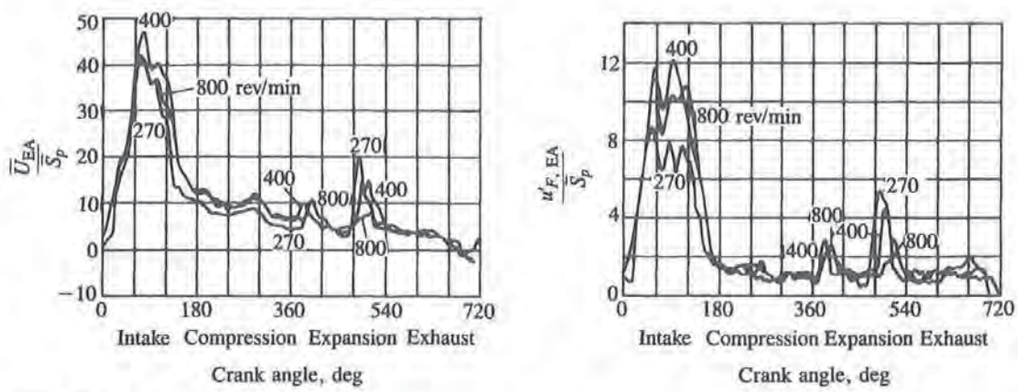


FIGURE 8-10
Ensemble-averaged mean and rms velocity fluctuations, normalized by mean piston speed, throughout the engine cycle for three engine speeds. Location *b* in Fig. 8-8*a*.[11]

PETITIONER'S EXHIBIT 1002
US PATENT NO. 6,581,565

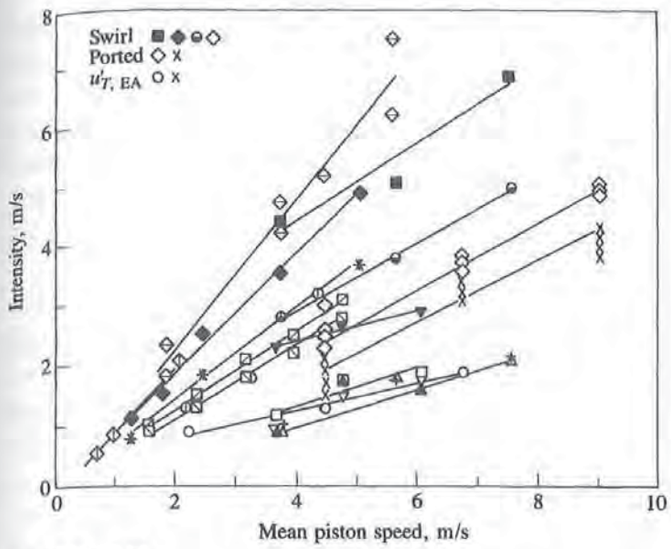


FIGURE 8-11
Individual-cycle turbulence intensity $u'_{T,\,EA}$ (OX) and ensemble-averaged rms fluctuation velocity (remaining symbols) at TC at the end of compression, for a number of different flow configurations and chamber geometries as a function of mean piston speed.[16] Two data sets for two-stroke ported engines. Four data sets with intake generated swirl.

appropriateness of this velocity scaling.† Other results support this conclusion, though in the absence of an ordered mean motion such as swirl when the ensemble-averaged mean velocities at the end of compression are low, this scaling for the mean velocity does not always hold.[16] Figure 8-11 shows a compilation of ensemble-averaged rms fluctuation velocity or ensemble-averaged individual-cycle turbulence intensity results at TC at the end of compression, from 13 different flow configurations and combustion chamber geometries. Two of these sets of results are from two-stroke cycle ported configurations. The measured fluctuating velocities or turbulence intensities are plotted against mean piston speed. The linear relationship holds well. There is a substantial variation in the proportionality constant, in part because in most of these studies (identified in the figure) the ensemble-averaged rms fluctuation velocity was the quantity measured. Since this includes the cycle-by-cycle fluctuation in the mean velocity, it is larger (by up to a factor of 2) than the average turbulence intensity $u'_{T,\,EA}$.

A consensus conclusion is emerging from these studies that the turbulence intensity at top-center, with open combustion chambers in the absence of swirl, has a maximum value equal to about half the mean piston speed:[16, 18]

$$u'_{T,\,EA}(TC) \approx 0.5\bar{S}_p \tag{8.23}$$

† Note that because of the valve and combustion chamber of this particular engine, the ratio of $\bar{U}$ to $\bar{S}_p$ is higher than is typical of normal engine geometries.

PETITIONER'S EXHIBIT 1002
US PATENT NO. 6,581,565

The available data show that the turbulence intensity at TC with swirl is usually higher than without swirl[16] (see the four data sets with swirl in Fig. 8-11). Some data, however, indicate that the rms fluctuation intensity with swirl may be lower.[18] The ensemble-averaged cyclic variation in individual-cycle mean velocity at the end of compression also scales with mean piston speed. This quantity can be comparable in magnitude to the turbulence intensity. It usually decreases when a swirling flow is generated within the cylinder during the intake process.[11, 16]

During the compression stroke, and also during combustion while the cylinder pressure continues to rise, the unburned mixture is compressed. Turbulent flow properties are changed significantly by the large and rapidly imposed distortions that result from this compression. Such distortions, in the absence of dissipation, would conserve the angular momentum of the flow: rapid compression would lead to an increase in vorticity and turbulence intensity. There is evidence that, with certain types of in-cylinder flow pattern, an increase in turbulence intensity resulting from piston motion and combustion does occur toward the end of the compression process. The compression of large-scale rotating flows can cause this increase due to the increasing angular velocity required to conserve angular momentum resulting in a growth in turbulence generation by shear.[19]

Limited results are available which characterize the turbulence time and length scales in automobile engine flows. During the intake process, the integral length scale is of the order of the intake jet diameter, which is of the order of the valve lift ($\lesssim$10 mm in automobile-size engines). During compression the flow relaxes to the shape of the combusion chamber. The integral time scale at the end of compression decreases with increasing engine speed. It is of order 1 ms at engine speeds of about 1000 rev/min. The integral length scale at the end of compression is believed to scale with the clearance height and varies little with engine speed. It decreases as the piston approaches TC to about 2 mm (0.2 $\times$ clearance height). The micro time scale at the end of compression is of order 0.1 ms at 1000 rev/min, and decreases as engine speed increases (again in automobile-size engine cylinders). Micro length scales are of order 1 mm at the end of compression and vary little with engine speed. Kolmogorov length scales at the end of compression are of order 10^{-2} mm.[8, 20, 21]

8.3 SWIRL

Swirl is usually defined as organized rotation of the charge about the cylinder axis. Swirl is created by bringing the intake flow into the cylinder with an initial angular momentum. While some decay in swirl due to friction occurs during the engine cycle, intake generated swirl usually persists through the compression, combustion, and expansion processes. In engine designs with bowl-in-piston combustion chambers, the rotational motion set up during intake is substantially modified during compression. Swirl is used in diesels and some stratified-charge engine concepts to promote more rapid mixing between the inducted air charge

PETITIONER'S EXHIBIT 1002
US PATENT NO. 6,581,565

and the injected fuel. Swirl is also used to speed up the combustion process in spark-ignition engines. In two-stroke engines it is used to improve scavenging. In some designs of prechamber engines, organized rotation about the prechamber axis is also called swirl. In prechamber engines where swirl within the precombustion chamber is important, the flow into the prechamber during the compression process creates the rotating flow. Prechamber flows are discussed in Sec. 8.5.

8.3.1 Swirl Measurement

The nature of the swirling flow in an actual operating engine is extremely difficult to determine. Accordingly, steady flow tests are often used to characterize the swirl. Air is blown steadily through the inlet port and valve assembly in the cylinder head into an appropriately located equivalent of the cylinder. A common technique for characterizing the swirl within the cylinder has been to use a light paddle wheel, pivoted on the cylinder centerline (with low friction bearings), mounted between 1 and 1.5 bore diameters down the cylinder. The paddle wheel diameter is close to the cylinder bore. The rotation rate of the paddle wheel is used as a measure of the air swirl. Since this rotation rate depends on the location of the wheel and its design, and the details of the swirling flow, this technique is being superseded by the impulse swirl meter shown in Fig. 8-12. A honeycomb flow straightener replaces the paddle wheel: it measures the total torque exerted by the swirling flow. This torque equals the flux of angular

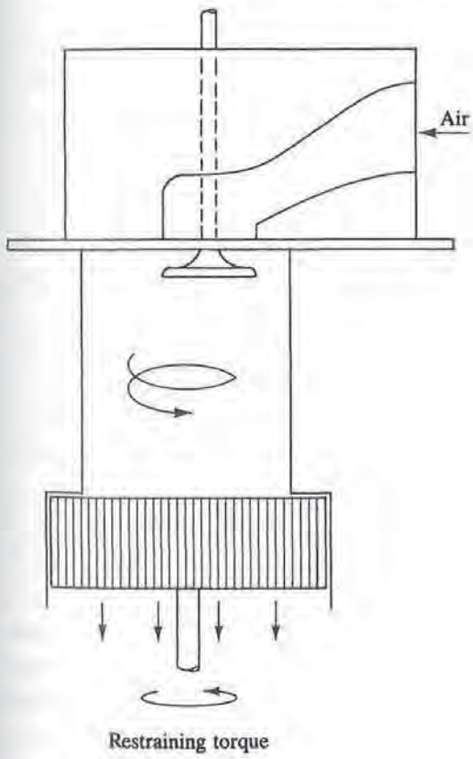


FIGURE 8-12
Schematic of steady-flow impulse torque swirl meter.[22]

PETITIONER'S EXHIBIT 1002
US PATENT NO. 6,581,565

momentum through the plane coinciding with the flow-straightener upstream face.

For each of these approaches, a *swirl coefficient* is defined which essentially compares the flow's angular momentum with its axial momentum. For the paddle wheel, the swirl coefficient C_s is defined by

$$C_s = \frac{\omega_p B}{v_0} \tag{8.24}$$

where ω_p is the paddle wheel angular velocity ($=2\pi N_p$, where N_p is the rotational speed) and the bore B has been used as the characteristic dimension. The characteristic velocity, v_0, is derived from the pressure drop across the valve using an incompressible flow equation:

$$v_0 = \left[\frac{2(p_0 - p_c)}{\rho}\right]^{1/2} \tag{8.25}$$

or a compressible flow equation:

$$v_0 = \left\{\frac{2\gamma}{(\gamma - 1)}\frac{p_0}{\rho_0}\left[1 - \left(\frac{p_c}{p_0}\right)^{(\gamma-1)/\gamma}\right]\right\}^{1/2} \tag{8.26}$$

where the subscripts 0 and c refer to upstream stagnation and cylinder values, respectively. The difference between Eqs. (8.25) and (8.26) is usually small. With the impulse torque meter, characteristic velocity and length scales must also be introduced. Several swirl parameters have been defined.[22, 23] The simplest is

$$C_s = \frac{8T}{\dot{m} v_0 B} \tag{8.27}$$

where T is the torque and $\dot{m}$ the air mass flow rate. The velocity v_0, defined by Eq. (8.25) or Eq. (8.26), and the bore have again been used to obtain a dimensionless coefficient. Note that for solid-body rotation of the fluid within the cylinder at the paddle wheel speed ω_p, Eqs. (8.24) and (8.27) give identical swirl coefficients. In practice, because the swirling flow is not solid-body rotation and because the paddle wheel usually lags the flow due to slip, the impulse torque meter gives higher swirl coefficients.[23] When swirl measurements are made in an operating engine, a *swirl ratio* is normally used to define the swirl. It is defined as the angular velocity of a solid-body rotating flow ω_s, which has equal angular momentum to the actual flow, divided by the crankshaft angular rotational speed:

$$R_s = \frac{\omega_s}{2\pi N} \tag{8.28}$$

During the induction stroke in an engine the flow and the valve open area, and consequently the angular momentum flux into the cylinder, vary with crank angle. Whereas in rig tests the flow and valve open area are fixed and the angular momentum passes down the cylinder continuously, in the engine intake process

PETITIONER'S EXHIBIT 1002
US PATENT NO. 6,581,565

the momentum produced under corresponding conditions of flow and valve lift remains in the cylinder. Steady-state impulse torque-meter flow rig data can be used to estimate engine swirl in the following manner.[23] Assuming that the port and valve retain the same characteristics under the transient conditions of the engine as on the steady-flow rig, the equivalent solid-body angular velocity ω_s at the end of the intake process is given by

$$\omega_s = \frac{8}{B^2}\left(\int_{\theta_1}^{\theta_2} T\, d\theta\right)\Big/\left(\int_{\theta_1}^{\theta_2} \dot{m}\, d\theta\right)$$

where θ_1 and θ_2 are crank angles at the start and end of the intake process and the torque T and mass flow rate $\dot{m}$ are evaluated at the valve lift corresponding to the local crank angle. Using Eq. (8.27) for T, Eq. (6.11) for $\dot{m}$, assuming v_0 and ρ are constant throughout the intake process, and introducing volumetric efficiency η_v based on intake manifold conditions via Eq. (2.27), it can be shown that

$$R_s = \frac{\omega_s}{2\pi N} = \pi \eta_v BL\left[\int_{\theta_1}^{\theta_2} (A_v C_D) C_s\, d\theta\right]\Big/\left[\int_{\theta_1}^{\theta_2} (A_v C_D)\, d\theta\right]^2 \qquad (8.29)$$

where $A_v C_D$ is the effective valve open area at each crank angle. Note that the crank angle in Eq. (8.29) should be in radians. Except for its (weak) dependence on η_v, Eq. (8.29) gives R_s independent of operating conditions directly from rig test results and engine geometry.

The relationship between steady-flow rig tests (which are extensively used because of their simplicity) and actual engine swirl patterns is not fully understood. Steady-flow tests adequately describe the swirl generating characteristics of the intake port and valve (at fixed valve lift) and are used extensively for this purpose. However, the swirling flow set up in the cylinder during intake can change significantly during compression.

8.3.2 Swirl Generation during Induction

Two general approaches are used to create swirl during the induction process. In one, the flow is discharged into the cylinder tangentially toward the cylinder wall, where it is deflected sideways and downward in a swirling motion. In the other, the swirl is largely generated within the inlet port: the flow is forced to rotate about the valve axis *before* it enters the cylinder. The former type of motion is achieved by forcing the flow distribution around the circumference of the inlet valve to be nonuniform, so that the inlet flow has a substantial net angular momentum about the cylinder axis. The directed port and deflector wall port in Fig. 8-13 are two common ways of achieving this result. The directed port brings the flow toward the valve opening in the desired tangential direction. Its passage is straight, which due to other cylinder head requirements restricts the flow area and results in a relatively low discharge coefficient. The deflector wall port uses the port inner side wall to force the flow preferentially through the outer periphery of the valve opening, in a tangential direction. Since only one wall is used to obtain a directional effect, the port areas are less restrictive.

PETITIONER'S EXHIBIT 1002
US PATENT NO. 6,581,565

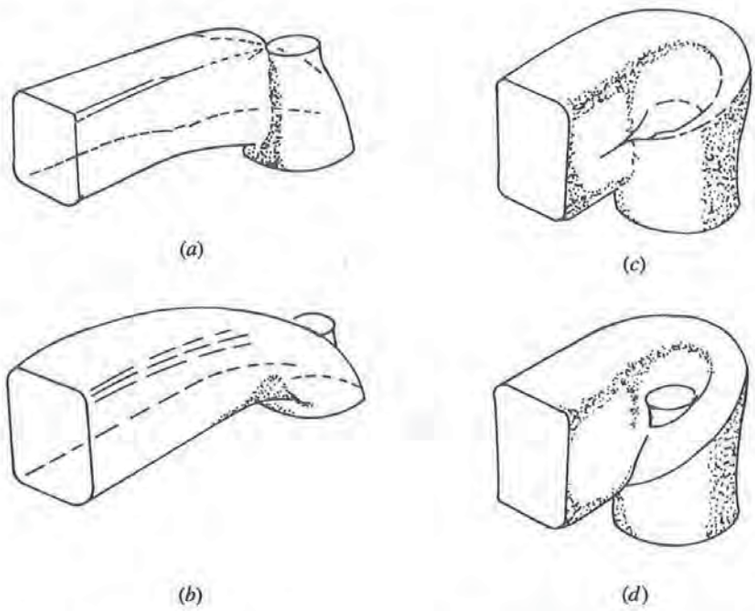


FIGURE 8-13
Different types of swirl-generating inlet ports: (*a*) deflector wall; (*b*) directed; (*c*) shallow ramp helical; (*d*) steep ramp helical.[24]

Flow rotation about the cylinder axis can also be generated by masking off or shrouding part of the peripheral inlet valve open area, as shown in Fig. 8-14. Use is often made of a mask or shroud on the valve in research engines because changes can readily be made. In production engines, the added cost and weight, problems of distortion, the need to prevent valve rotation, and reduced volumetric efficiency make masking the valve an unattractive approach. The more practical alternative of building a mask on the cylinder head around part of the inlet valve periphery is used in production spark-ignition engines to generate swirl. It can easily be incorporated in the cylinder head casting process.

The second broad approach is to generate swirl within the port, about the valve axis, prior to the flow entering the cylinder. Two examples of such *helical ports* are shown in Fig. 8-13. Usually, with helical ports, a higher flow discharge coefficient at equivalent levels of swirl is obtained, since the whole periphery of the valve open area can be fully utilized. A higher volumetric efficiency results. Also, helical ports are less sensitive to position displacements, such as can occur in casting, since the swirl generated depends mainly on the port geometry above the valve and not the position of the port relative to the cylinder axis.

Figure 8-15 compares steady-state swirl-rig measurements of examples of the ports in Fig. 8-13. The rig swirl number increases with increasing valve lift, reflecting the increasing impact of the port shape and decreasing impact of the flow restriction between the valve head and seat. Helical ports normally impart more angular momentum at medium lifts than do directed ports.[23, 25] The swirl

PETITIONER'S EXHIBIT 1002
US PATENT NO. 6,581,565

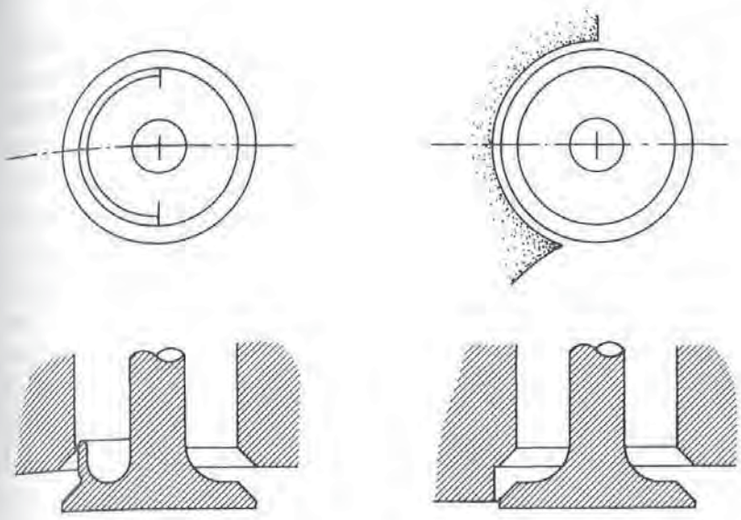


FIGURE 8-14
Shrouded inlet valve and masked cylinder head approaches for producing net in-cylinder angular momentum.

ratios for these ports calculated from this rig data using Eqs. (8.27) and (8.29) are: 2.5 for the directed port, 2.9 for the shallow ramp helical, and 2.6 for the steep ramp helical. Vane swirl-meter swirl ratios were about 30 percent less. These impulse-swirl-meter derived engine swirl ratios are within about 20 percent of the solid-body rotation rate which has equal angular momentum to that of the cylinder charge determined from tangential velocity measurements made within the cylinder of an operating engine with the same port, at the end of the induction process.[23]

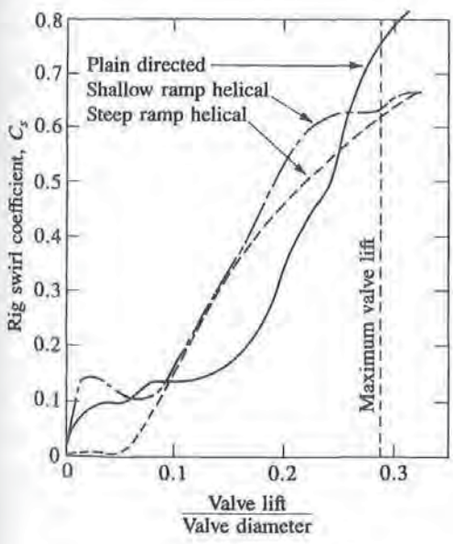


FIGURE 8-15
Steady-state torque meter swirl measurements of directed, shallow ramp, and steep ramp helical ports as a function of inlet valve lift/diameter ratio.[23]

PETITIONER'S EXHIBIT 1002
US PATENT NO. 6,581,565

Directed and deflector wall ports, and masked valve or head designs produce a tangential flow into the cylinder by increasing the flow resistance through that part of the valve open area where flow is not desired. A highly nonuniform flow through the valve periphery results and the flow into the cylinder has a substantial v_θ velocity component in the same direction about the cylinder axis. In contrast, helical ports produce the swirl in the port upstream of the valve, and the velocity components v_r, and v_z through the valve opening, and v_θ *about the valve axis* are approximately uniform around the valve open area. Figure 8-16 shows velocity data measured at the valve exit plane in steady-flow rig tests with examples of these two types of port. The valve and cylinder wall locations are shown. In Fig. 8-16*a*, the deflector wall of the tangentially oriented port effectively prevents any significant flow around half the valve periphery. In contrast, in Fig. 8-16*b* with the helical port, the air flows into the cylinder around

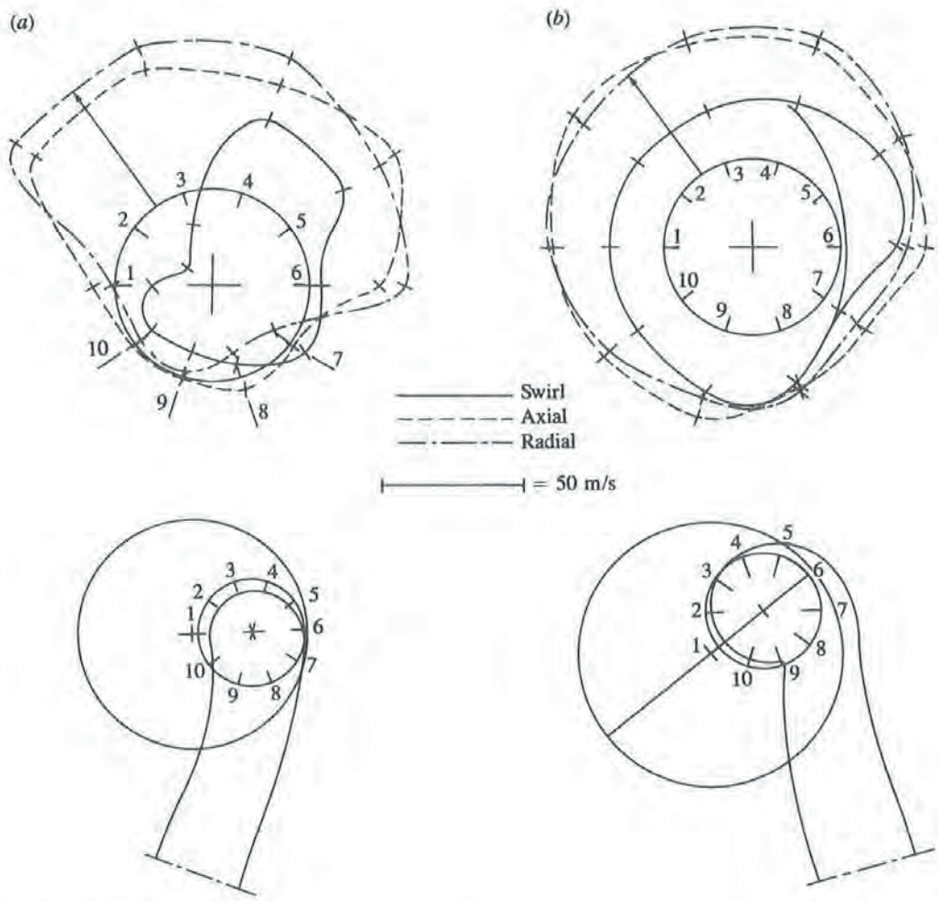


FIGURE 8-16
Swirl, axial, and radial velocities measured 2 mm from cylinder head around the valve circumference for (*a*) tangential deflector-wall port and (*b*) helical port; magnitude of velocity is given by the distance along a radial line (from valve axis), from valve outline to the respective curve scaled by the reference length (examples of radial velocity indicated by two arrows); valve lift = 12.8 mm.[26, 27]

PETITIONER'S EXHIBIT 1002
US PATENT NO. 6,581,565

the full valve open area. The radial and axial velocities are essentially uniform around the valve periphery. The swirl velocity about the valve axis (anticlockwise when viewed from above) for this helical port is relatively uniform and is about half the magnitude of the radial and axial velocities.

The swirling air flow within the cylinder of an operating engine is not uniform. The velocities generated at the valve at each point in the induction process depend on the valve open area and piston velocity. The velocities are highest during the first half of the intake process as indicated in Fig. 6-15. Thus, the swirl velocities generated during this portion of the induction stroke are higher than the swirl generated during the latter half of the stroke: there is swirl stratification. Also, the flow pattern close to the cylinder head during induction is comparatively disorganized, and not usually close to a solid-body rotation. It consists of a system of vortices, created by the high-velocity tangential or spiraling intake jet. Further down the cylinder, the flow pattern is closer to solid-body rotation with the swirl velocity increasing with increasing radius.[23, 24] This more ordered flow directly above the piston produces higher swirl velocities in that region of the cylinder. As the piston velocity decreases during intake, the swirl pattern redistributes, with swirl speeds close to the piston decreasing and swirl speeds in the center of the cylinder increasing.[27] Note that the axis of rotation of the in-cylinder gases may not exactly coincide with the cylinder axis.

8.3.3 Swirl Modification within the Cylinder

The angular momentum of the air which enters the cylinder at each crank angle during induction decays throughout the rest of the intake process and during the compression process due to friction at the walls and turbulent dissipation within the fluid. Typically one-quarter to one-third of the initial moment of momentum about the cylinder axis will be lost by top-center at the end of compression. However, swirl velocities in the charge can be substantially increased during compression by suitable design of the combustion chamber. In many designs of direct-injection diesel, air swirl is used to obtain much more rapid mixing between the fuel injected into the cylinder and the air than would occur in the absence of swirl. The tangential velocity of the swirling air flow set up inside the cylinder during induction is substantially increased by forcing most of the air into a compact bowl-in-piston combustion chamber, usually centered on the cylinder axis, as the piston approaches its top-center position. Neglecting the effects of friction, angular momentum is conserved, and as the moment of inertia of the air is decreased its angular velocity must increase.

However, the total angular momentum of the charge within the cylinder does decay due to friction at the chamber walls. The angular momentum of the cylinder charge Γ_c changes with time according to the moment of momentum conservation equation:

$$\frac{d\Gamma_c}{dt} = J_i - T_f \tag{8.30}$$

PETITIONER'S EXHIBIT 1002
US PATENT NO. 6,581,565

where J_i is the flux of angular momentum into the cylinder and T_f is the torque due to wall friction. At each point in the intake process J_i is given by

$$J_i = \int_{A_v} \rho r v_\theta \mathbf{v} \cdot d\mathbf{A}_v \tag{8.31}$$

where $d\mathbf{A}_v$ is an element of the valve open area, as defined in Fig. 8-17. While the angular momentum entering the cylinder during the intake process is

$$\Gamma_{c,i} = \int_{t_{ivo}}^{t_{ivc}} \int_{A_v} \rho r v_\theta \cdot d\mathbf{A}_v \, dt$$

the actual angular momentum within the cylinder at the end of induction will be less, due to wall friction during the intake process. Friction continues through the compression process so the total charge angular momentum at the end of compression is further reduced.

There is friction on the cylinder wall, cylinder head, and piston crown (including any combustion chamber within the crown). This friction can be estimated with sufficient accuracy using friction formulas developed for flow over a flat plate, with suitable definition of characteristic length and velocity scales. Friction on the cylinder wall can be estimated from the wall shear stress:

$$\tau = \tfrac{1}{2}\rho\left(\frac{\omega_s B}{2}\right)^2 C_F \tag{8.32}$$

where ω_s is the equivalent solid-body swirl. The friction factor C_F is given by the flat plate formula:

$$C_F = 0.037\lambda(\mathrm{Re}_B)^{-0.2} \tag{8.33}$$

where λ is an empirical constant introduced to allow for differences between the flat plate and cylinder wall ($\lambda \approx 1.5$)[28] and Re_B is the equivalent of the flat plate Reynolds number [$\mathrm{Re}_B = \rho(B\omega_s/2)(\pi B)/\mu$]. Friction on the cylindrical walls of a piston cup or bowl can be obtained from the above expressions with D_B, the bowl diameter, replacing the bore.

Friction on the cylinder head, piston crown, and piston bowl floor can be estimated from expressions similar to Eqs. (8.32) and (8.33). However, since the

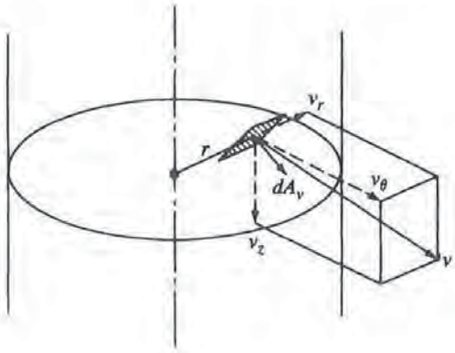


FIGURE 8-17
Definition of symbols in equation for angular momentum flux into the cylinder [Eq. (8.31)].

PETITIONER'S EXHIBIT 1002
US PATENT NO. 6,581,565

tangential velocity v_θ at the wall varies with radius, the shear stress should be evaluated at each radius and integrated over the surface: e.g.,[29]

$$\tau(r) = C_1 \tfrac{1}{2}\rho[v_\theta(r)]^2 \, \mathrm{Re}^{-0.2} \tag{8.34}$$

with

$$\mathrm{Re} = \frac{\rho v_\theta(r) r}{\mu}$$

where C_1 is an empirical constant (≈ 0.055). An alternative approximate approach is to evaluate these components of the wall shear stress at the mean radius.[28]

Next, consider the effects on swirl of radially inward displacement of the air charge during compression. The most common example of this phenomenon occurs with the bowl-in-piston combustion chamber design of medium- and high-speed direct-injection diesels (see Sec. 10.2.1). However, in spark-ignition engines where swirl is used to increase the burning rate, the shape of the combustion chamber close to top-center can also force radially inward motion of the charge. For a given swirling in-cylinder flow at the end of induction and neglecting the effects of friction, as the moment of inertia of the air about the cylinder axis is decreased the air's angular velocity must increase to conserve angular momentum. For example, for solid-body rotation of the cylinder air charge of mass m_c, the initial angular momentum $\Gamma_{c,i}$ and solid-body rotation $\omega_{s,i}$ are related at bottom-center by

$$\Gamma_{c,i} = I_c \, \omega_{s,i}$$

where I_c is the moment of inertia of the charge about the cylinder axis. For a disc-shaped combustion chamber, $I_c = m_c B^2/8$ and is constant. For a bowl-in-piston combustion chamber,

$$I_c = \frac{m_c B^2}{8} \frac{[(z/h_B) + (D_B/B)^4]}{[(z/h_B) + (D_B/B)^2]} \tag{8.35}$$

where D_B and h_B are the diameter and depth of the bowl, respectively, and z is the distance of the piston crown from the cylinder head. At TC crank position, $z \approx 0$ and $I_c \approx m_c D_B^2/8$. At the end of induction, $I_c \approx m_c B^2/8$. Thus, in the absence of friction ω_s would increase by $(B/D_B)^2$, usually a factor of about 4.

In an operating engine with this bowl-in-piston chamber design, the observed increase in swirl in the bowl is less; it is usually about a factor of 2 to 3.[23, 25] This is because of wall friction, dissipation in the fluid due to turbulence and velocity gradients, and the fact that a fraction of the fluid remains in the clearance height above the piston crown. The loss in angular momentum due to these effects will vary with geometric details, initial swirl flow pattern, and engine speed.

Swirl velocity distributions in the cylinder at the end of induction show the tangential velocity increasing with radius, except close to the cylinder wall where friction causes the velocity to decrease. While the velocity distribution is not that of a solid-body rotation, depending on port design and operating conditions it is

PETITIONER'S EXHIBIT 1002
US PATENT NO. 6,581,565

often close to solid-body rotation.[23, 25] Departures from the solid-body velocity distribution are greater at higher engine speeds, suggesting that the flow pattern in the cylinder at this point in the cycle is still developing with time.[23, 30] In the absence of radially inward gas displacement during compression, the flow pattern continues to develop toward a solid-body distribution throughout the compression stroke.[25] Swirl ratios of 3 to 5 at top-center can be achieved with the ports shown in Fig. 8-13, with flat-topped pistons (i.e., in the absence of any swirl amplification during compression).[23, 25]

With combustion chambers where the chamber radius is less than the cylinder bore, such as the bowl in piston, the tangential velocity distribution with radius will change during compression. Even if the solid-body rotation assumption is reasonable at the end of induction, the profile will distort as gas moves into the piston bowl. Neglecting the effects of friction, the angular momentum of each fluid element will remain constant as it moves radially inward. Thus the increase in tangential velocity of each fluid element as it moves radially inward is proportional to the change in the reciprocal of its radius. Measurements of the swirl velocity distribution within the cylinder of bowl-in-piston engine designs support this description. The rate of displacement of gas into the bowl depends on the bowl volume V_B, cylinder volume V, and piston speed S_p, at that particular piston position:

$$\frac{dm_B}{dt} = \frac{m_c}{L}\left(\frac{V_B}{V}\right)\left(\frac{V_d}{V}\right)S_p$$

The gas velocity into the bowl will therefore increase rapidly toward the end of the compression stroke and reach a maximum just before TC (see Sec. 8.4 where this radial "squish" motion is discussed more fully). Thus, there is a rapid increase in v_θ in the bowl as the crank angle approaches TC. The lower layers of the bowl rotate slower than the upper layers because that gas entered the bowl earlier in the compression process.[23, 25]

Velocity measurements illustrating the development of this radial distribution in tangential velocity are shown in Fig. 8-18. These measurements were made by analysing the motion of burning carbon particles in the cylinder of an operating diesel engine from movies of the combustion process. The figure shows the engine geometry and the data compared with a model based on gas displacement and conservation of angular momentum in each element of the charge as it is displaced inward. Different swirl velocity profiles exist within and outside the bowl as the piston approaches TC. Swirl velocities within the bowl increase as TC is approached, roughly as predicted by the ideal model. Outside the bowl, the swirl velocity decreases with increasing radius due to the combined effects of friction and inward gas displacement as the clearance height decreases.

Swirl ratios in bowl-in-piston engine designs of up to about 15 can be achieved with $D_B \approx 0.5B$, at top-center. Amplification factors relative to flat-topped piston swirl are typically about 2.5 to 3, some 30 percent lower than the ideal factor of $(B/D_B)^2$ given by Eq. (8.35) as $z \to 0$. This difference is due to the mass remaining within the clearance height which does not enter the bowl, and

PETITIONER'S EXHIBIT 1002
US PATENT NO. 6,581,565

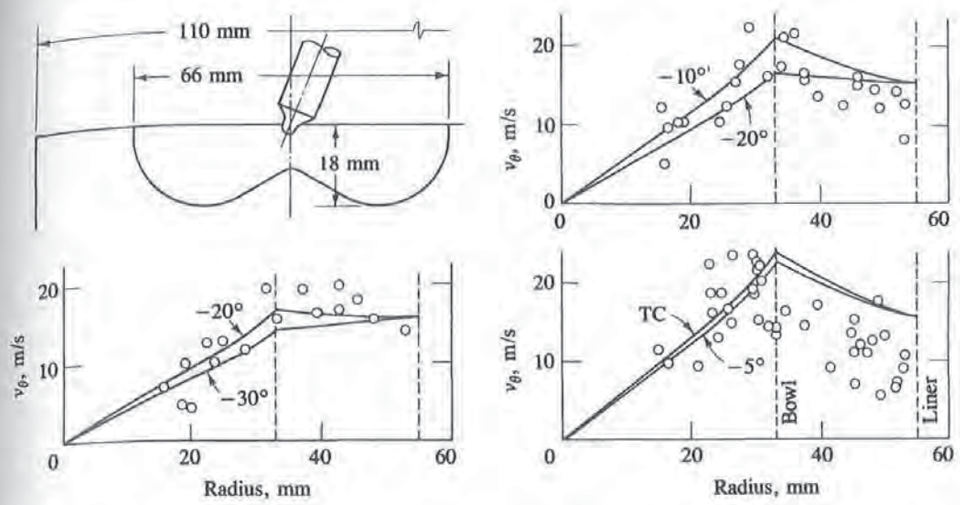


FIGURE 8-18
Velocity measurements as a function of radius across the combustion chamber of a firing, bowl-in-piston, direct-injection diesel engine. Schematic shows the chamber geometry. Solid lines are calculations based on the assumption of constant angular momentum for fluid elements as they move radially inward.[31]

the effects of wall friction (enhanced by the higher gas velocities in the bowl). Sometimes the bowl axis is offset from the cylinder axis and some additional loss in swirl amplification results.[25]

The effect of swirl generation during induction on velocity fluctuations in the combustion chamber at the end of compression has been examined.[32] The turbulence intensity with swirl was higher than without swirl (with the same chamber geometry). Integral scales of the turbulence were smaller with swirl than without. Cyclic fluctuations in the mean velocity are, apparently, reduced by swirl. Also, some studies show that the ensemble-averaged fluctuation intensity goes down when swirl is introduced.[18] There is evidence that swirl makes the turbulence intensity more homogeneous.[30]

8.4 SQUISH

Squish is the name given to the radially inward or transverse gas motion that occurs toward the end of the compression stroke when a portion of the piston face and cylinder head approach each other closely. Figure 8-19 shows how gas is thereby displaced into the combustion chamber. Figure 8-19*a* shows a typical wedge-shaped SI engine combustion chamber and Fig. 8-19*b* shows a bowl-in-piston diesel combustion chamber. The amount of squish is often defined by the *percentage squish area:* i.e., the percentage of the piston area, $\pi B^2/4$, which closely approaches the cylinder head (the shaded areas in Fig. 8-19). Squish-generated gas motion results from using a compact combustion chamber geometry.

A theoretical squish velocity can be calculated from the instantaneous dis-

PETITIONER'S EXHIBIT 1002
US PATENT NO. 6,581,565

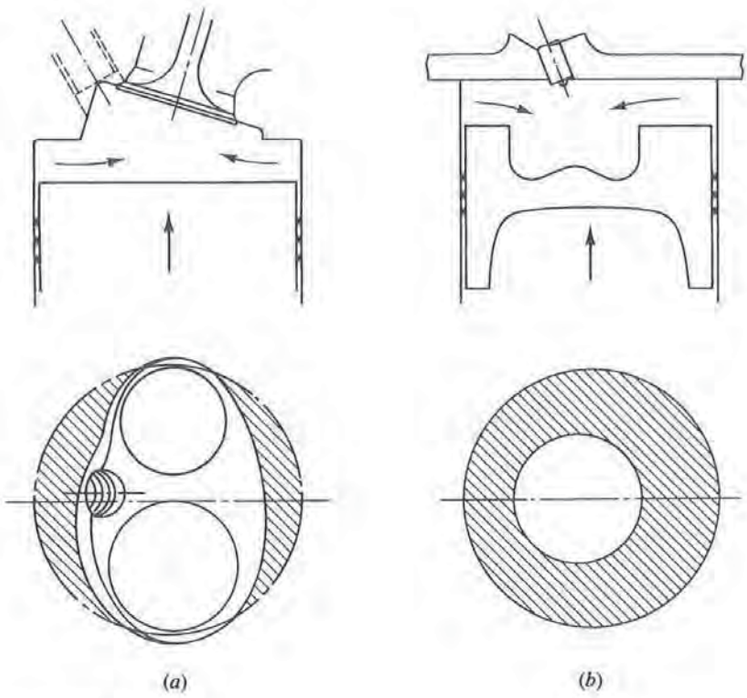


FIGURE 8-19
Schematics of how piston motion generates squish: (*a*) wedge-shaped SI engine combustion chamber; (*b*) bowl-in-piston direct-injection diesel combustion chamber.

placement of gas across the inner edge of the squish region (across the dashed lines in the drawings in Fig. 8-20*a* and *b*), required to satisfy mass conservation. Ignoring the effects of gas dynamics (nonuniform pressure), friction, leakage past the piston rings, and heat transfer, expressions for the squish velocity are:

1. *Bowl-in-piston chamber* (Fig. 8-20*a*):[33]

$$\frac{v_{sq}}{S_p} = \frac{D_B}{4z}\left[\left(\frac{B}{D_B}\right)^2 - 1\right]\frac{V_B}{A_c z + V_B} \tag{8.36}$$

   where V_B is the volume of the piston bowl, A_c is the cross-sectional area of the cylinder ($\pi B^2/4$), S_p is the instantaneous piston speed [Eq. (2.11)], and z is the distance between the piston crown top and the cylinder head ($z = c + Z$, where $Z = l + a - s$; see Fig. 2-1).

2. *Simple wedge chamber* (Fig. 8-20*b*):[34]

$$\frac{v_{sq}}{S_p} = \frac{A_s}{b(Z + c)}\left(1 - \frac{Z + c}{C + Z}\right) \tag{8.37}$$

   where A_s is the squish area, b is the width of the squish region, and C is $Z/(r_c - 1)$ evaluated at the end of induction.

PETITIONER'S EXHIBIT 1002
US PATENT NO. 6,581,565

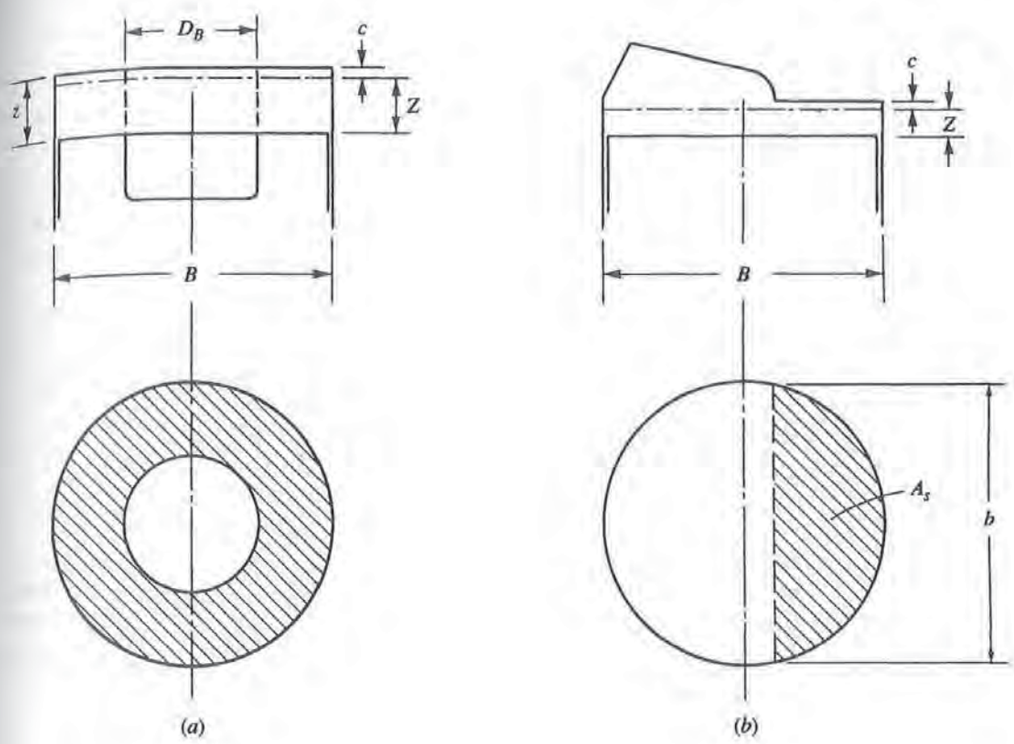


FIGURE 8-20
(*a*) Schematic of axisymmetric bowl-in-piston chamber for Eq. (8.36). (*b*) Schematic of wedge chamber with transverse squish for Eq. (8.37).

The theoretical squish velocity for a bowl-in-piston engine normalized by the mean piston speed $\bar{S}_p$ is shown in Fig. 8-21 for different ratios of D_B/B and clearance heights c. The maximum squish velocity occurs at about 10° before TC. After TC, v_{sq} is negative; a reverse squish motion occurs as gas flows out of the bowl into the clearance height region. Under motored conditions this is equal to the forward motion.

These models omit the effects of gas inertia, friction, gas leakage past the piston rings, and heat transfer. Gas inertia and friction effects have been shown to be small. The effects of gas leakage past the piston rings and of heat transfer are more significant. The squish velocity decrement Δv_L due to leakage is proportional to the mean piston speed and a dimensionless leakage number:

$$N_L = A_{E,L} \frac{\sqrt{\gamma R T_{IVC}}}{N V_d} \tag{8.38}$$

where $A_{E,L}$ is the effective leakage area and T_{IVC} is the temperature of the cylinder gases at inlet valve closing. Leakage was modeled as a choked flow through the effective leakage area. Values of $\Delta v_L/v_{sq}$ are shown in Fig. 8-22. The effect of leakage on v_{sq} is small for normal gas leakage rates. A decrement on squish

PETITIONER'S EXHIBIT 1002
US PATENT NO. 6,581,565

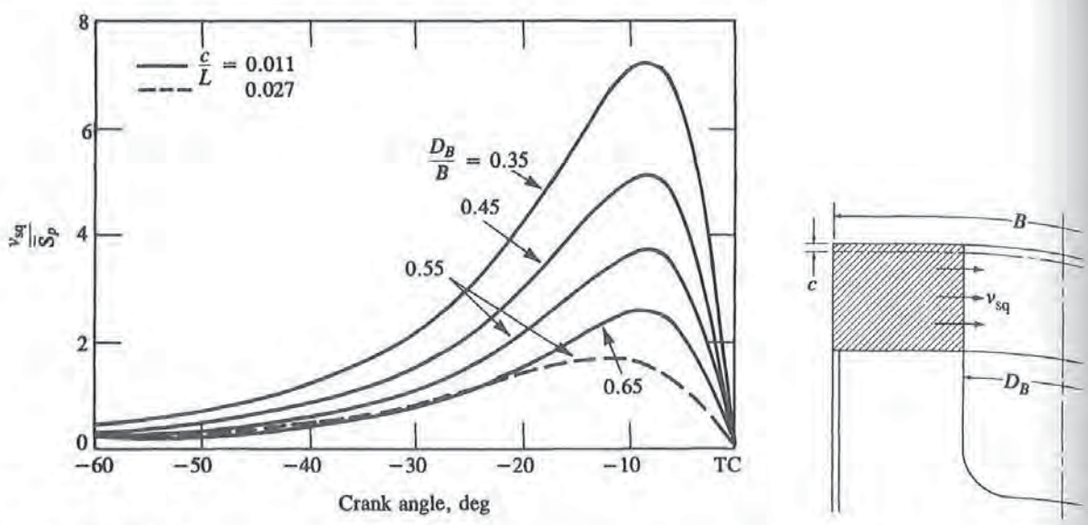


FIGURE 8-21
Theoretical squish velocity divided by mean piston speed for bowl-in-piston chambers, for different D_B/B and c/L (clearance height/stroke). $B/L = 0.914$, $V_B/V_d = 0.056$, connecting rod length/crank radius = 3.76.[35]

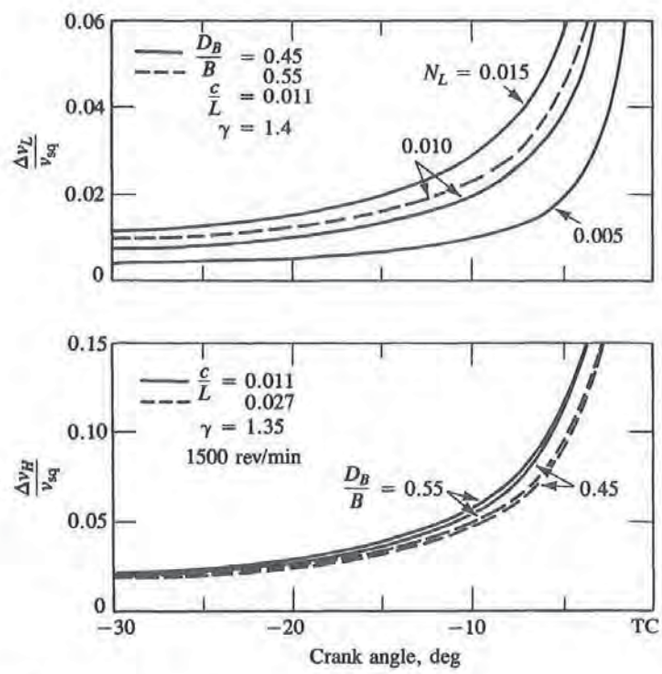


FIGURE 8-22
Values of squish velocity decrement due to leakage Δv_L and heat transfer Δv_H, normalized by the ideal squish velocity, as a function of crank angle.[35]

PETITIONER'S EXHIBIT 1002
US PATENT NO. 6,581,565

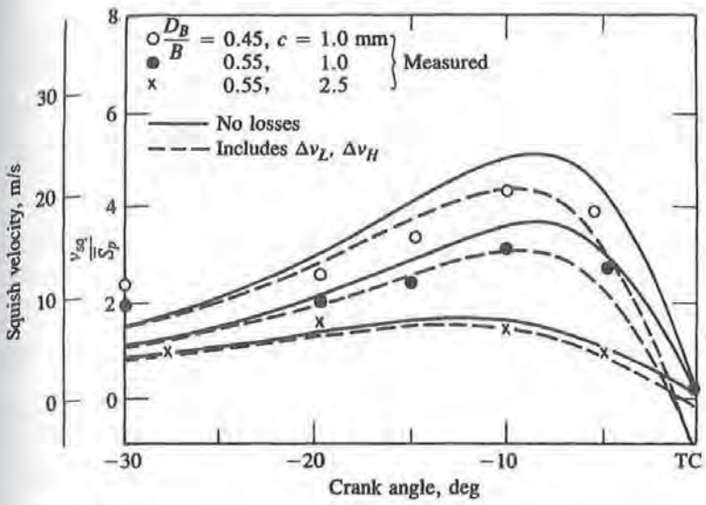


FIGURE 8-23
Comparison of measured squish velocities in bowl-in-piston combustion chambers, with different bowl diameter/bore ratios and clearance heights, to calculated ideal squish velocity (solid lines) and calculations corrected for leakage and heat transfer (dashed lines). Bore = 85 mm, stroke = 93 mm, 1500 rev/min.[35]

velocity due to heat transfer, Δv_H, has also been derived, using standard engine heat-transfer correlations (see Sec. 12.4). Values of $\Delta v_H/v_{sq}$ are also shown in Fig. 8-22. Again the effects are small in the region of maximum squish, though they become more important as the squish velocity decreases from its maximum value as the piston approaches TC.

Velocity measurements in engines provide good support for the above theory. The ideal theory adequately predicts the dependence on engine speed.[36] With appropriate corrections for leakage and heat-transfer effects, the above theory predicts the effects of the bowl diameter/bore ratio and clearance height on squish velocity (see Fig. 8-23). The change in direction of the radial motion as the piston moves through TC has been demonstrated under motored engine conditions. Under firing conditions, the combustion generated gas expansion in the open portion of the combustion chamber substantially increases the magnitude of the reverse squish motion after TC.[37]

8.5 PRECHAMBER ENGINE FLOWS

Small high-speed diesel engines use an auxiliary combustion chamber, or prechamber, to achieve adequate fuel-air mixing rates. The prechamber is connected to the main combustion chamber above the piston via a nozzle, passageway, or one or more orifices. Flow of air through this restriction into the prechamber during the compression process sets up high velocities in the prechamber at the time the fuel-injection process commences. This results in the required high fuel-air mixing rates. Figures 1-21 and 10-2 show examples of these prechamber or

PETITIONER'S EXHIBIT 1002
US PATENT NO. 6,581,565

indirect-injection diesels. The two most common designs of auxiliary chamber are: the swirl chamber (Fig. 10-2*a*), where the flow through the passageway enters the chamber tangentially producing rapid rotation within the chamber, and the prechamber (Fig. 10-2*b*) with one or more connecting orifices designed to produce a highly turbulent flow but no ordered motion within the chamber. Auxiliary chambers are sometimes used in spark-ignition engines. The torch-ignition three-valve stratified-charge engine (Fig. 1-27) is one such concept. The prechamber is used to create a rich mixture in the vicinity of the spark plug to promote rapid flame development. An alternative concept uses the prechamber around the spark plug to generate turbulence to enhance the early stages of combustion, but has no mixture stratification.

The most critical phase of flow into the prechamber occurs towards the end of compression. While this flow is driven by a pressure difference between the main chamber above the piston and the auxiliary chamber, this pressure difference is small, and the mass flow rate and velocity at the nozzle, orifice, or passageway can be estimated using a simple gas displacement model. Assuming that the gas density throughout the cylinder is uniform (an adequate assumption toward the end of compression—the most critical period), the mass in the prechamber m_P is given by $m_c(V_P/V)$, where m_c is the cylinder mass, V the cylinder volume, and V_P the prechamber volume. The mass flow rate through the throat of the restriction is, therefore,

$$\dot{m} = \frac{dm_P}{dt} = -\frac{m_c V_P}{V^2}\frac{dV}{dt} \tag{8.39}$$

Using the relations $dV/dt = -(\pi B^2/4)S_p$ where S_p is the instantaneous piston speed, $V_d = \pi B^2 L/4$, and $\bar{S}_p = 2NL$, Eq. (8.39) can be written as

$$\frac{\dot{m}}{m_c N} = 2(r_c - 1)\left(\frac{V_P}{V_c}\right)\left(\frac{S_p}{\bar{S}_p}\right)\left(\frac{V_c}{V}\right)^2 \tag{8.40}$$

where V_c is the clearance volume, $S_p/\bar{S}_p$ is given by Eq. (2.11), and V/V_c is given by Eq. (2.6). The gas velocity at the throat v_T can be obtained from $\dot{m}$ via the relation $\rho v_T A_T = \dot{m}$, the density $\rho = m_c/V$, and Eq. (8.40):

$$\frac{v_T}{\bar{S}_p} = \left(\frac{V_P}{V_c}\right)\left(\frac{\pi B^2/4}{A_T}\right)\left(\frac{S_p}{\bar{S}_p}\right)\left(\frac{V_c}{V}\right) \tag{8.41}$$

where A_T is the effective cross-sectional area of the throat. The variation of $\dot{m}/(m_c N)$ and $v_T/\bar{S}_p$ with crank angle during the compression process for values of r_c, V_P/V_c, and $A_T/(\pi B^2/4)$ typical of a swirl prechamber diesel are shown in Fig. 8-24. The velocity reaches its peak value about 20° before TC: very high gas velocities, an order of magnitude or more larger than the mean piston speed, can be achieved depending on the relative effective throat area. Note that as the piston approaches TC, first the nozzle velocity and then the mass flow rate decrease to zero. After TC, in the absence of combustion, an equivalent flow in the reverse direction out of prechamber would occur. Combustion in the pre-

PETITIONER'S EXHIBIT 1002
US PATENT NO. 6,581,565

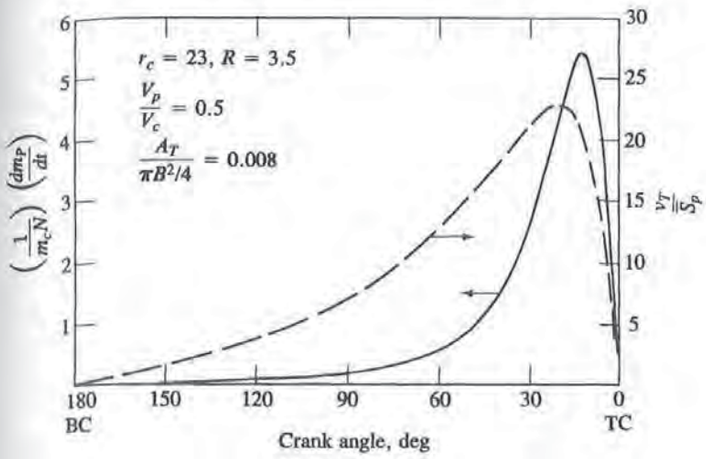


FIGURE 8-24
Velocity and mass flow rate at the prechamber nozzle throat, during compression, for a typical small swirl-prechamber automotive diesel.

chamber diesel usually starts just before TC, and the pressure in the prechamber then rises significantly above the main chamber pressure. The outflow from the prechamber is then governed by the development of the combustion process, and the above simple gas displacement model no longer describes the flow. This combustion generated prechamber gas motion is discussed in Sec. 14.4.4.

In prechamber stratified-charge engines, the flow of gas into the prechamber during compression is critical to the creation of an appropriate mixture in the prechamber at the crank angle when the mixture is ignited. In the concept shown in Fig. 1-27, a very rich fuel-air mixture is fed directly to the prechamber during intake via the prechamber intake valve, while a lean mixture is fed to the main chamber via the main intake valve. During compression, the flow into the prechamber reduces the prechamber equivalence ratio to a close-to-stoichiometric value at the time of ignition. Figure 8-25 shows a gas displacement calculation of this process and relevant data; the prechamber equivalence ratio, initially greater

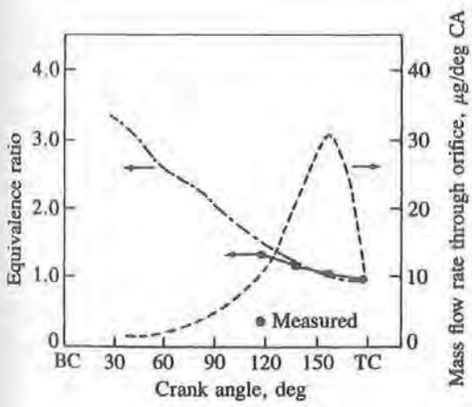


FIGURE 8-25
Effect of gas flow into the prechamber during compression on the prechamber equivalence ratio in a three-valve prechamber stratified-charge engine. Calculations based on gas displacement model.[38]

PETITIONER'S EXHIBIT 1002
US PATENT NO. 6,581,565

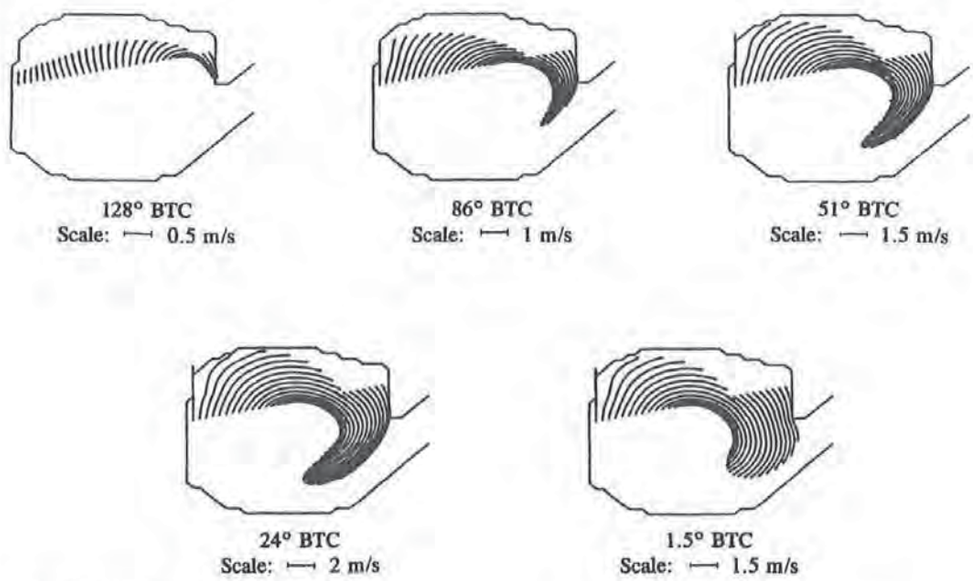


FIGURE 8-26
Calculations of developing flow field in (two-dimensional) swirl prechamber during compression process. Lines are instantaneous flow streamlines, analogous to streak photographs of flow field.[41]

than 3, is leaned out to unity as mass flows through the orifice into the prechamber (whose volume is 8.75 percent of the clearance volume).[38] Charts for estimating the final equivalence ratio, based on gas displacement, for this prechamber concept are available.[39]

The velocity field set up inside the prechamber during compression is strongly dependent on the details of the nozzle and prechamber geometry. Velocities vary linearly with mean piston speed.[40] In swirl prechambers, the nozzle flow sets up a vortex within the chamber. Figure 8-26 shows calculations of this developing flow field; instantaneous flow streamlines have been drawn in, with the length of the streamlines indicating how the particles of fluid move relative to each other.[41] The velocities increase with increasing crank angle as the compression process proceeds, and reach a maximum at about 20° before TC. Then, as the piston approaches TC and the flow through the passageway decreases to zero, the vortex in the swirl chamber expands to fill the entire chamber and mean velocities decay. Very high swirl rates can be achieved just before TC: local swirl ratios of up to 60 at intermediate radii and up to 20 at the outer radius have been measured. These high swirl rates produce large centrifugal accelerations.

8.6 CREVICE FLOWS AND BLOWBY

The engine combustion chamber is connected to several small volumes usually called *crevices* because of their narrow entrances. Gas flows into and out of these volumes during the engine operating cycle as the cylinder pressure changes.

PETITIONER'S EXHIBIT 1002
US PATENT NO. 6,581,565

The largest crevices are the volumes between the piston, piston rings, and cylinder wall. Some gas flows out of these regions into the crankcase; it is called *blowby*. Other crevice volumes in production engines are the threads around the spark plug, the space around the plug center electrode, the gap around the fuel injector, crevices between the intake and exhaust valve heads and cylinder head, and the head gasket cutout. Table 8.1 shows the size and relative importance of these crevice regions in one cylinder of a production V-6 spark-ignition engine determined from measurements of cold-engine components. Total crevice volume is a few percent of the clearance volume, and the piston and ring crevices are the dominant contributors. When the engine is warmed up, dimensions and crevice volumes will change.

The important crevice processes occurring during the engine cycle are the following. As the cylinder pressure rises during compression, unburned mixture or air is forced into each crevice region. Since these volumes are thin they have a large surface/volume ratio; the gas flowing into the crevice cools by heat transfer to close to the wall temperature. During combustion while the pressure continues to rise, unburned mixture or air, depending on engine type, continues to flow into these crevice volumes. After flame arrival at the crevice entrance, burned gases will flow into each crevice until the cylinder pressure starts to decrease. Once the crevice gas pressure is higher than the cylinder pressure, gas flows back from each crevice into the cylinder.

The volumes between the piston, piston rings, and cylinder wall are shown schematically in Fig. 8-27. These crevices consist of a series of volumes (numbered 1 to 5) connected by flow restrictions such as the ring side clearance and ring gap. The geometry changes as each ring moves up and down in its ring groove, sealing either at the top or bottom ring surface. The gas flow, pressure distribution, and ring motion are therefore coupled. Figure 8-28 illustrates this behavior: pressure distributions, ring motion, and mass flow of gas into and out

TABLE 8.1
V-6 engine crevice data†[42]

	cm^3	%
Displaced volume per cylinder	632	
Clearance volume per cylinder	89	100
Volume above first ring	0.93	1.05
Volume behind first ring	0.47	0.52
Volume between rings	0.68	0.77
Volume behind second ring	0.47	0.52
Total ring crevice volume	2.55	2.9
Spark plug thread crevice	0.25	0.28
Head gasket crevice	0.3	0.34
Total crevice volume	3.1	3.5

† Determined for cold engine.

PETITIONER'S EXHIBIT 1002
US PATENT NO. 6,581,565

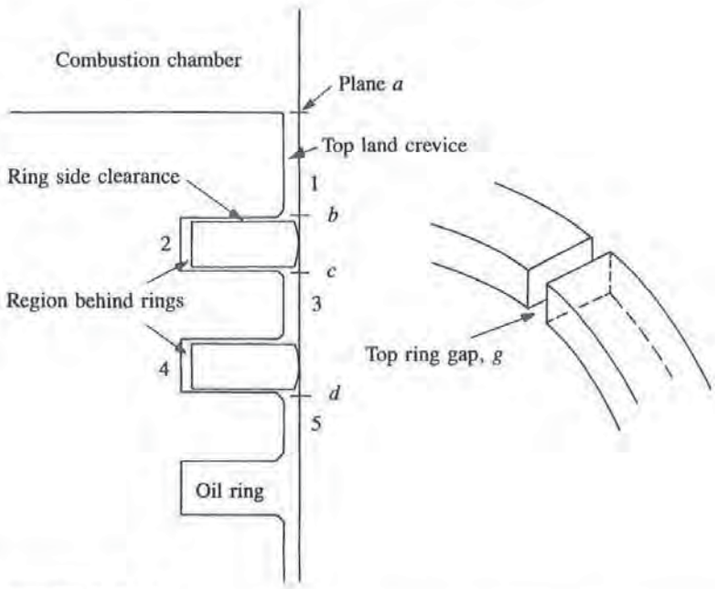


FIGURE 8-27
Schematic of piston and ring assembly in automotive spark-ignition engine.

of the regions defined by planes *a*, *b*, *c*, *d*, and through the ring gap *g* are plotted versus crank angle through compression and expansion. These results come from an analysis of these regions as volumes connected by passageways, with a prescribed cylinder pressure versus crank angle profile coupled with a dynamic model for ring motion, and assuming that the gas temperature equals the wall temperature.[42] During compression and combustion, the rings are forced to the groove lower surfaces and mass flows *into* all the volumes in this total crevice region. The pressure above and behind the first ring is essentially the same as the cylinder pressure; there is a substantial pressure drop across each ring, however. Once the cylinder pressure starts to decrease (after 15° ATC) gas flows out of regions 1 and 2 in Fig. 8-27 into the cylinder, but continues to flow *into* regions 3, 4, and 5 until the pressure in the cylinder falls below the pressure beneath the top ring. The top ring then shifts to seal with the upper grove surface and gas flows out of regions 2, 3, and 4 (which now have the same pressure), both into the cylinder and as blowby into the crackcase. Some 5 to 10 percent of the total cylinder charge is trapped in these regions at the time of peak cylinder pressure. Most of this gas returns to the cylinder; about 1 percent goes to the crankcase as blowby. The gas flow back into the cylinder continues throughout the expansion process. In spark-ignition engines this phenomenon is a major contributor to unburned hydrocarbon emissions (see Sec. 11.4.3). In all engines it results in a loss of power and efficiency.

There is substantial experimental evidence to support the above description of flow in the piston ring crevice region. In a special square-cross-section flow visualization engine, both the low-velocity gas expansion out of the volume above the first ring after the time of peak pressure and the jet-like flows through

PETITIONER'S EXHIBIT 1002
US PATENT NO. 6,581,565

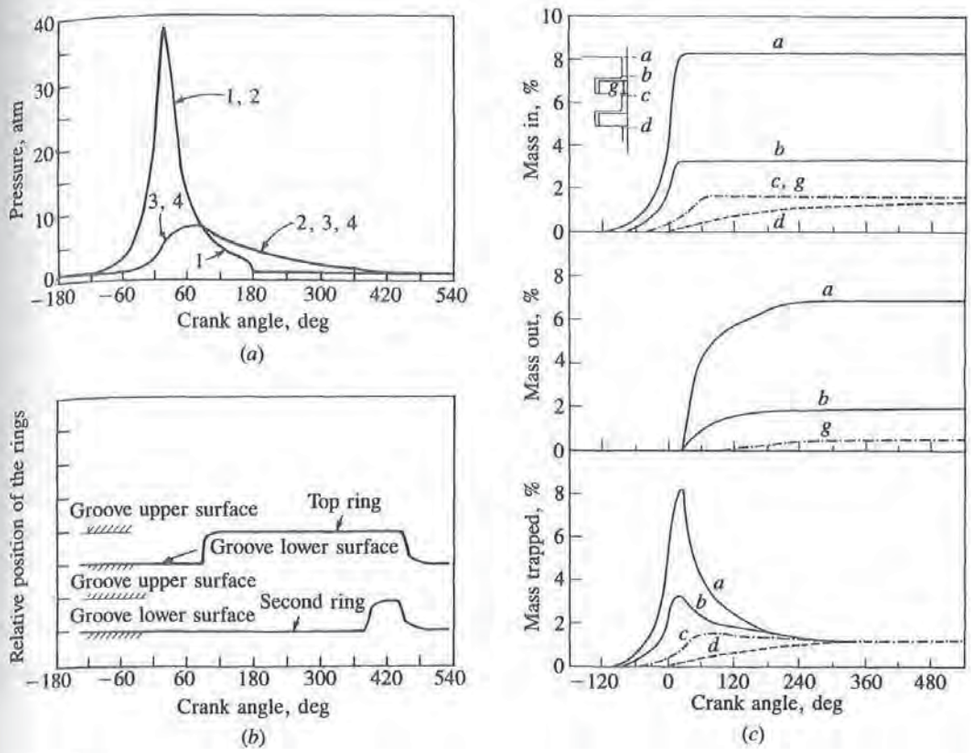


FIGURE 8-28
(*a*) Pressures in the combustion chamber (1), in region behind top ring (2), in region between rings (3), and behind second ring (4); (*b*) relative position of top and second rings; (*c*) percentage of total cylinder mass that flows into and out of the different crevice regions across planes *a*, *b*, *c*, and *d* and through the ring gap *g* in Fig. 8-27, and the percentage of mass trapped beneath these planes, as a function of crank angle. Automotive spark-ignition engine at wide-open throttle and 2000 rev/min.[42]

the top ring gap later in the expansion process when the pressure difference across the ring changes sign have been observed. Figure 8-29 shows these flows with explanatory schematics.

Blowby is defined as the gas that flows from the combustion chamber past the piston rings and into the crankcase. It is forced through any leakage paths afforded by the piston-bore-ring assembly in response to combustion chamber pressure. If there is good contact between the compression rings and the bore, and the rings and the bottom of the grooves, then the only leakage path of consequence is the ring gap. Blowby of gases from the cylinder to the crankcase removes gas from these crevice regions and thereby prevents some of the crevice gases from returning to the cylinder. Crankcase blowby gases used to be vented directly to the atmosphere and constituted a significant source of HC emissions. The crankcase is now vented to the engine intake system and the blowby gases are recycled. Blowby at a given speed and load is controlled primarily by the greatest flow resistance in the flow path between the cylinder and the crankcase. This is the smallest of the compression ring ring-gap areas. Figure 8-30 shows how measured blowby flow rates increase linearly with the smallest gap area.[43]

PETITIONER'S EXHIBIT 1002
US PATENT NO. 6,581,565

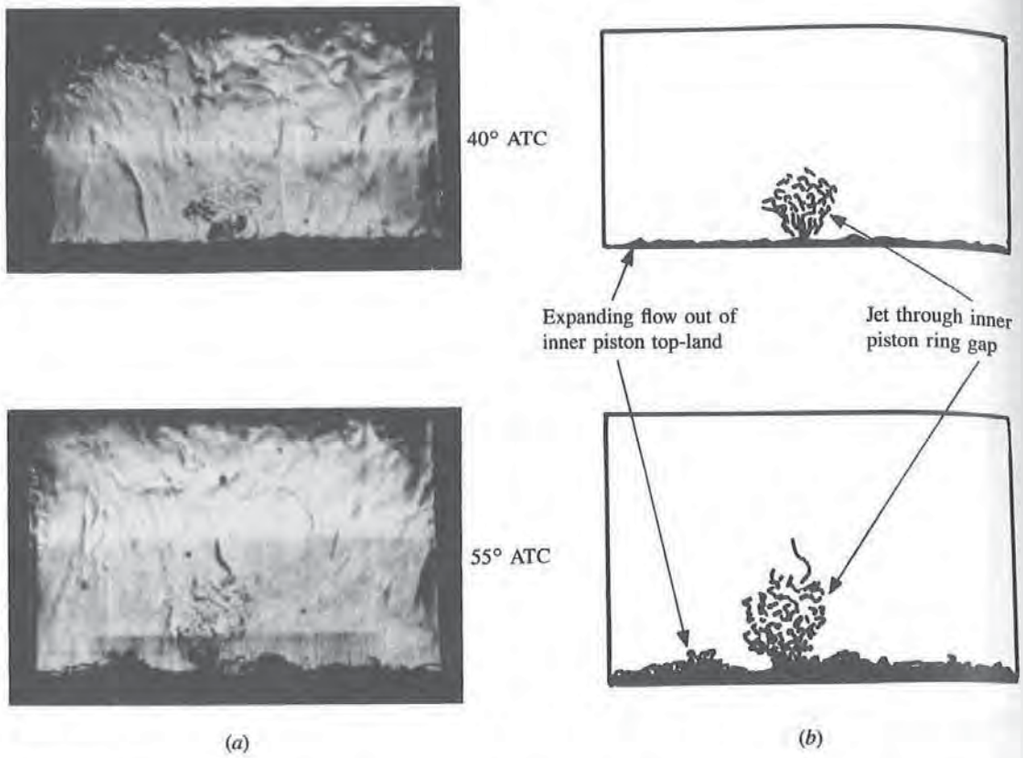


FIGURE 8-29
Schlieren photographs of the flow out of the piston–cylinder wall crevices during the expansion stroke. A production piston was inserted into the square cross-section piston of the visualization engine. Gas flows at low velocity out of the crevice entrance all around the production piston circumference once the cylinder pressure starts decreasing early in the expansion stroke. Gas flows out of the ring gap as a jet once the pressure above the ring falls below the pressure beneath the ring.[42]

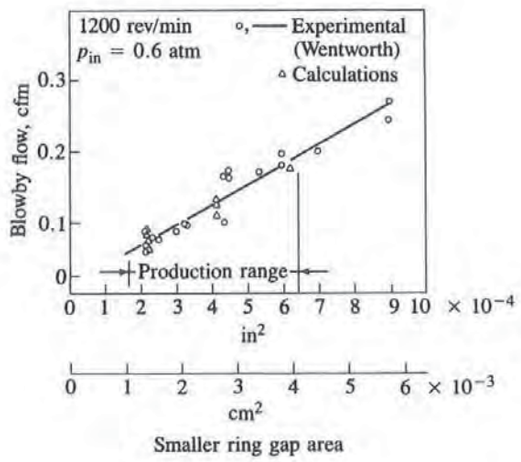


FIGURE 8-30
Measured blowby for one cylinder of an automobile spark-ignition engine as a function of the smallest ring gap area, compared with blowby calculations based on flow model described in text.[42, 43]

PETITIONER'S EXHIBIT 1002
US PATENT NO. 6,581,565

Calculations of blowby based on the model described earlier are in good agreement.[42] Extrapolation back to the zero gap area gives nearly zero blowby. Note, however, that if the bore finish is rough, or if the rings do not contact the bore all around, or if the compression rings lift off the bottom of the groove, this linear relationship may no longer hold.

8.7 FLOWS GENERATED BY PISTON–CYLINDER WALL INTERACTION

Because a boundary layer exists on the cylinder wall, the motion of the piston generates unusual flow patterns in the corner formed by the cylinder wall and the piston face. When the piston is moving away from top-center a sink-type flow occurs. When the piston moves toward top-center a vortex flow is generated. Figure 8-31 shows schematics of these flows (in a coordinate frame with the piston face at rest). The vortex flow has been studied because of its effect on gas motion at the time of ignition and because it has been suggested as a mechanism for removing hydrocarbons off the cylinder wall during the exhaust stroke (see Sec. 11.4.3).

The vortex flow has been studied in cylinders with water as the fluid over the range of Reynolds numbers typical of engine operation.[44, 45] Laminar, transition, and turbulent flow regimes have been identified. It has been shown that a quasi-steady flow assumption is valid and that

$$\frac{A_V}{L^2} = f\left(\frac{v_w L}{\nu}\right)$$

where A_V is the vortex area (area inside the dashed line in Fig. 8-31), L is the stroke, v_w is the wall velocity in piston stationary coordinates ($v_w = S_p$ in the engine), ν is the kinematic viscosity, and $(v_w L/\nu)$ is a Reynolds number.

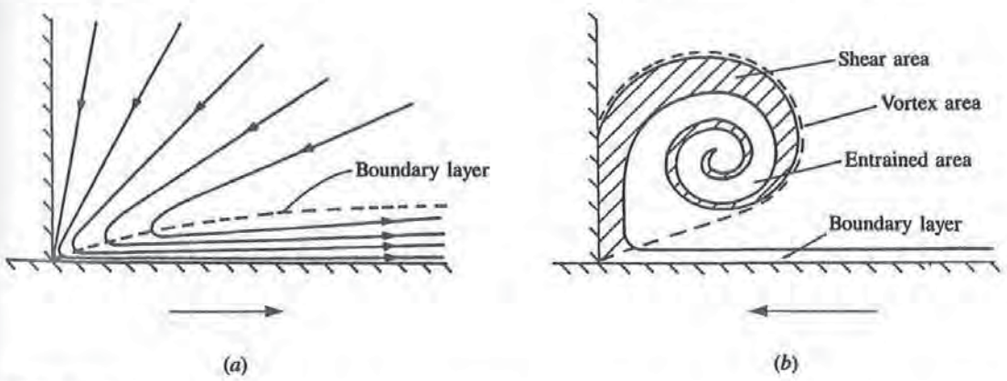


FIGURE 8-31
Schematics of the flow pattern set up in the piston face–cylinder wall corner, in piston-stationary coordinates, due to the boundary layer on the cylinder wall. Piston crown on left; cylinder wall at bottom. (*a*) Sink flow set up during intake and expansion; (*b*) vortex flow set up during compression and exhaust.[44] Arrow shows cylinder wall velocity relative to piston.

PETITIONER'S EXHIBIT 1002
US PATENT NO. 6,581,565

For the laminar flow regime, a good assumption is that A_V is proportional to the shear area in the vortex (shown cross-hatched), which equals the boundary-layer area; this can be estimated from boundary-layer theory. In the turbulent flow regime, an entrainment theory was used, which assumed that the rate of change of vortex area was proportional to the product of the exposed perimeter of the vortex and the velocity difference between the vortex and the stationary fluid ($\approx v_w$). The relevant relationships are:

$$\text{For } (v_w L/\nu) \leq 2 \times 10^4: \qquad \frac{A_V}{L^2} = \left(\frac{v_w L}{\nu}\right)^{-1/2} \tag{8.42a}$$

$$\text{For } (v_w L/\nu) \geq 2 \times 10^4: \qquad \frac{A_V}{L^2} = 0.006 \tag{8.42b}$$

Figure 8-32 shows these two theories correlated against hydraulic analog data.

These theories are for constant values of ν. During compression, ν decreases substantially as the gas temperature and pressure increase (ν decreases by a factor of 4 for a compression ratio of 8). This will decrease the size of the vortex until the turbulent regime is reached. During the exhaust stroke following blowdown, ν will remain approximately constant as the pressure and temperature do not change significantly. Typical parameter values at 1500 rev/min are: $\bar{S}_p = 5$ m/s, $L = 0.1$ m; average values of ν are 1.2×10^{-5} and 1.4×10^{-4} m^2/s for compression and exhaust stroke, respectively. Hence a Reynolds number for the compression stroke is 4×10^4, $A_V/L^2 \approx 0.006$, and the vortex diameter $d_V \approx 0.09L$. For the exhaust stroke, the Reynolds number is 4×10^3, $A_V/L^2 \approx 0.015$, and $d_V \approx 0.14L$. Thus the vortex dimensions at the end of the upward stroke of the piston are comparable to the engine clearance height.

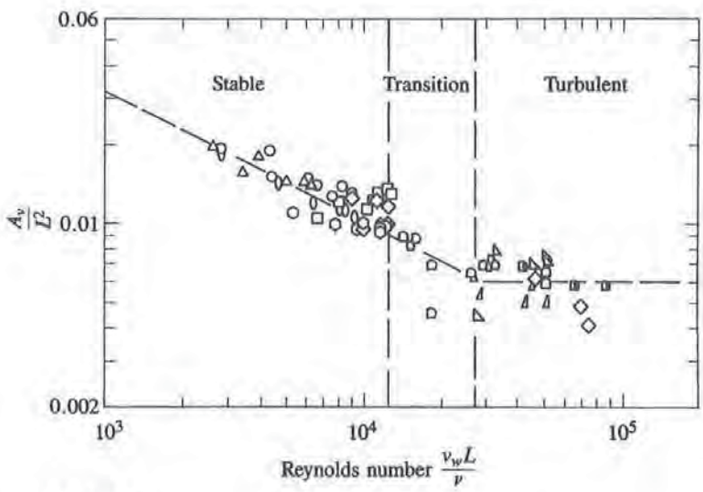


FIGURE 8-32
Ratio of area of vortex in piston face–cylinder wall corner to square of stroke, as a function of Reynolds number based on piston velocity, for piston moving toward the cylinder head.[44]

PETITIONER'S EXHIBIT 1002
US PATENT NO. 6,581,565

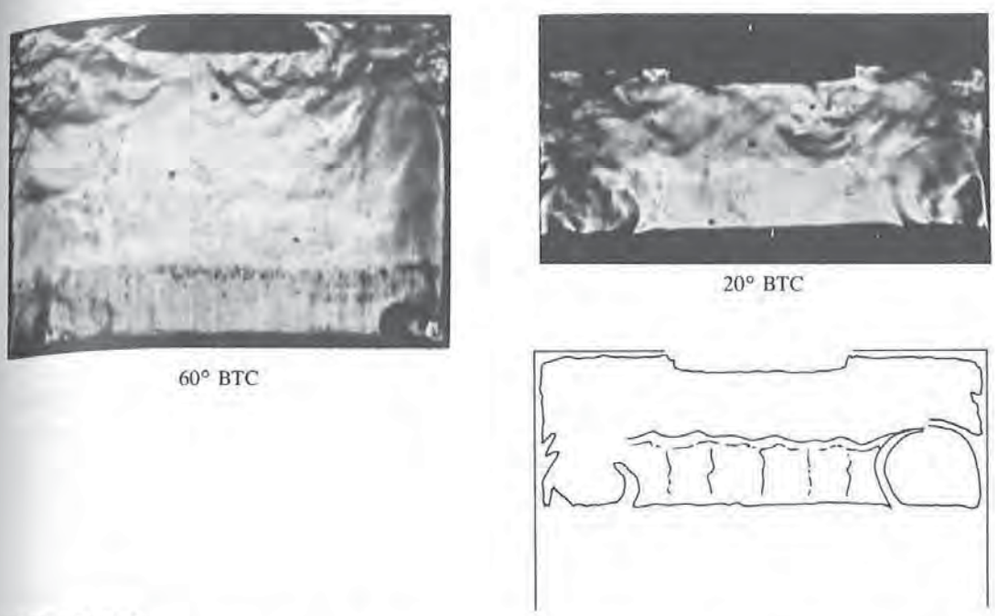


FIGURE 8-33
Schlieren photographs of in-cylinder flow during later stages of exhaust stroke. Growing vortex in the piston face–cylinder wall corner and turbulent outflow toward the valve are apparent at 60° BTC. At 20° BTC, the vortex has grown to of order $0.2B$ diameter.[42]

This vortex flow has been observed in an operating engine. Figure 8-33 shows schlieren photographs taken during the exhaust stroke in a special square-cross-section flow visualization spark-ignition engine. The accompanying schematic identifies the vortex structure which is visible in the photo because the cool boundary-layer gas is being scraped off the cylinder wall by the upward-moving piston and "rolled up." The vortex diameter as the piston approaches TC is about 20 percent of the bore.

PROBLEMS

8.1. (*a*) Estimate the ratio of the maximum gas velocity in the center of the hollow cone inlet jet to the mean piston speed from the data in Fig. 8-1.
(*b*) Compare this ratio with the ratio of inlet valve pseudo flow velocity determined from Fig. 6-15 to the mean piston speed at the same crank angle. The engine is that of Fig. 1-4.
(*c*) Are the engine velocity data in (*a*) consistent with the velocity calculated from the simple piston displacement model of (*b*)? Explain.

8.2. Given the relationship between turbulence intensity and mean piston speed [Eq. (8.23)] and that the turbulence integral scale is $\approx 0.2 \times$ clearance height, use Eqs. (8.14) and (8.15) to estimate the following quantities for a spark-ignition engine with bore = stroke = 86 mm, $r_c = 9$, at 1000 and 5000 rev/min and wide-open throttle:
(*a*) Mean and maximum piston speed, maximum gas velocity through the inlet valve (see Prob. 8.1)
(*b*) Turbulence intensity, integral length scale, micro length scale, and Kolmogorov length scale, all at TC

PETITIONER'S EXHIBIT 1002
US PATENT NO. 6,581,565

8.3. The swirl ratio at the end of induction at 2000 rev/min in a direct-injection diesel engine of bore = stroke = 100 mm is 4.0. What is the average tangential velocity (evaluated at the inlet valve–axis radial location) required to give this swirl ratio? What is the ratio of this velocity to the mean piston speed and to the mean flow velocity through the inlet valve estimated from the average valve open area and open time?

8.4. (*a*) Derive a relationship for the depth (or height) h_B of a disc-shaped bowl-in-piston direct-injection diesel engine combustion chamber in terms of compression ratio r_c, bore B, stroke L, bowl diameter D_B, and top-center cylinder-head to piston-crown clearance c. For $B = L = 100$ mm, $r_c = 16$, $D_B = 0.5B$, $c = 1$ mm find the fraction of the air charge within the bowl at TC.

(*b*) If the swirl ratio at the end of induction at 2500 rev/min is 3 find the swirl ratio and average angular velocity in the bowl-in-piston chamber of dimensions given above. Assume the swirling flow is always a solid-body rotation. Compare the tangential velocity at the bowl edge with the mean piston speed. Neglect any friction effects.

(*c*) What would the swirl ratio be if the top-center clearance height was zero?

8.5. Using Eq. (8.37) and Fig. 8-20*b* plot the squish velocity divided by the mean piston speed at 10° BTC (the approximate location of the maximum) as a function of squish area expressed as a percentage of the cylinder cross section, $A_s/(\pi B^2/4) \times 100$, from 50 to 0 percent. $r_c = 10$, $c/B = 0.01$, $B/L = 1$, $R = l/a = 3.5$.

8.6. Figure 8-24 shows the velocity at the prechamber nozzle throat during compression for dimensions typical of a small swirl chamber indirect-injection diesel. Assuming that the swirl chamber shape is a disc of height equal to the diameter, that the nozzle throat is at 0.8 × prechamber radius, and that the flow enters the prechamber tangentially, estimate the swirl ratio based on the total angular momentum about the swirl chamber axis in the prechamber at top-center. Assume $B = L$; neglect friction.

8.7. The total crevice volume in an automobile spark-ignition engine is about 3 percent of the clearance volume. If the gas in these crevice regions is close to the wall temperature (450 K) and at the cylinder pressure, estimate the fraction of the cylinder mass within these crevice regions at these crank angles: inlet valve closing (50° ABC), spark discharge (30° BTC), maximum cylinder pressure (15° ATC), exhaust valve opening (60° BBC), TC of the exhaust stroke. Use the information in Fig. 1-8 for your input data, and assume the inlet pressure is 0.67 atm.

REFERENCES

1. Bicen, A. F., Vafidis, C., and Whitelaw, J. H.: "Steady and Unsteady Airflow through the Intake Valve of a Reciprocating Engine," *ASME Trans., J. Fluids Engng*, vol. 107, pp. 413–420, 1985.
2. Namazian, M., Hansen, S. P., Lyford-Pike, E. J., Sanchez-Barsse, J., Heywood, J. B., and Rife, J.: "Schlieren Visualization of the Flow and Density Fields in the Cylinder of a Spark-Ignition Engine," SAE paper 800044, *SAE Trans.*, vol. 89, 1980.
3. Ekchian, A., and Hoult, D. P.: "Flow Visualization Study of the Intake Process of an Internal Combustion Engine," SAE paper 790095, *SAE Trans.*, vol. 88, 1979.
4. Hirotomi, T., Nagayama, I., Kobayashi, S., and Yamamasu, M.: "Study of Induction Swirl in a Spark Ignition Engine," SAE paper 810496, *SAE Trans.*, vol. 90, 1981.
5. Reynolds, W. C.: "Modeling of Fluid Motions in Engines—An Introductory Overview," in J. N. Mattavi and C. A. Amann (eds.), *Combustion Modelling in Reciprocating Engines*, pp. 69–124, Plenum Press, 1980.
6. Tennekes, H., and Lumley, J. L.: *A First Course in Turbulence*, MIT Press, 1972.

PETITIONER'S EXHIBIT 1002
US PATENT NO. 6,581,565

7. Rask, R. B.: "Laser Doppler Anemometer Measurements of Mean Velocity and Turbulence in Internal Combustion Engines," ICALEO '84 Conference Proceedings, vols. 45 and 47, *Inspection, Measurement and Control and Laser Diagnostics and Photochemistry*, Laser Institute of America, Boston, November 1984.
8. Tabaczynski, R. J.: "Turbulence and Turbulent Combustion in Spark-Ignition Engines," *Prog. Energy Combust. Sci.*, vol. 2, pp. 143–165, 1976.
9. Witze, P. O.: "A Critical Comparison of Hot-Wire Anemometry and Laser Doppler Velocimetry for I.C. Engine Applications," SAE paper 800132, *SAE Trans.*, vol. 89, 1980.
10. Witze, P. O., Martin, J. K., and Borgnakke, C.: "Conditionally-Sampled Velocity and Turbulence Measurements in a Spark Ignition Engine," *Combust. Sci. Technol.*, vol. 36, pp. 301–317, 1984.
11. Rask, R. B.: "Comparison of Window, Smoothed-Ensemble, and Cycle-by-Cycle Data Reduction Techniques for Laser Doppler Anemometer Measurements of In-Cylinder Velocity," in T. Morel, R. P. Lohmann, and J. M. Rackley (eds.), *Fluid Mechanics of Combustion Systems*, pp. 11–20, ASME, New York, 1981.
12. Liou, T-M., and Santavicca, D. A.: "Cycle Resolved LDV Measurements in a Motored IC Engine," *ASME Trans., J. Fluids Engng*, vol. 107, pp. 232–240, 1985.
13. Amann, C. A.: "Classical Combustion Diagnostics for Engine Research," SAE paper 850395, in *Engine Combustion Analysis: New Approaches*, P-156, SAE, 1985.
14. Dyer, T. M.: "New Experimental Techniques for In-Cylinder Engine Studies," SAE paper 850396, in *Engine Combustion Analysis: New Approaches*, P-156, SAE, 1985.
15. Rask, R. B.: "Laser Doppler Anemometer Measurements in an Internal Combustion Engine," SAE paper 790094, *SAE Trans.*, vol. 88, 1979.
16. Liou, T.-M., Hall, M., Santavicca, D. A., and Bracco, F. V.: "Laser Dopper Velocimetry Measurements in Valved and Ported Engines," SAE paper 840375, *SAE Trans.*, vol. 93, 1984.
17. Arcoumanis, C., and Whitelaw, J. H.: "Fluid Mechanics of Internal Combustion Engines: A Review," *Proc. Instn Mech. Engrs.*, vol. 201, pp. 57–74, 1987.
18. Bopp, S., Vafidis, C., and Whitelaw, J. H.: "The Effect of Engine Speed on the TDC Flowfield in a Motored Reciprocating Engine," SAE paper 860023, 1986.
19. Wong, V. W., and Hoult, D. P.: "Rapid Distortion Theory Applied to Turbulent Combustion," SAE paper 790357, *SAE Trans.*, vol. 88, 1979.
20. Fraser, R. A., Felton, P. G., and Bracco, F. V.: "Preliminary Turbulence Length Scale Measurements in a Motored IC Engine," SAE paper 860021, 1986.
21. Ikegami, M., Shioji, M., and Nishimoto, K.: "Turbulence Intensity and Spatial Integral Scale during Compression and Expansion Strokes in a Four-cycle Reciprocating Engine," SAE paper 870372, 1987.
22. Uzkan, T., Borgnakke, C., and Morel, T.: "Characterization of Flow Produced by a High-Swirl Inlet Port," SAE paper 830266, 1983.
23. Monaghan, M. L., and Pettifer, H. F.: "Air Motion and Its Effects on Diesel Performance and Emissions," SAE paper 810255, in *Diesel Combustion and Emissions*, pt. 2, SP-484, *SAE Trans.*, vol. 90, 1981.
24. Tindal, M. J., Williams, T. J., and Aldoory, M.: "The Effect of Inlet Port Design on Cylinder Gas Motion in Direct Injection Diesel Engines," in *Flows in Internal Combustion Engines*, pp. 101–111, ASME, New York, 1982.
25. Brandl, F., Reverencic, I., Cartellieri, W., and Dent, J. C.: "Turbulent Air Flow in the Combustion Bowl of a D.I. Diesel Engine and Its Effect on Engine Performance," SAE paper 790040, *SAE Trans.*, vol. 88, 1979.
26. Brandstätter, W., Johns, R. J. R., and Wigley, G.: "Calculation of Flow Produced by a Tangential Inlet Port," in *International Symposium on Flows in Internal Combustion Engines—III*, FED vol. 28, pp. 135–148, ASME, New York, 1985.
27. Brandstätter, W., Johns, R. J. R., and Wigley, G.: "The Effect of Inlet Port Geometry on In-Cylinder Flow Structure," SAE paper 850499, 1985.
28. Davis, G. C., and Kent, J. C.: "Comparison of Model Calculations and Experimental Measurements of the Bulk Cylinder Flow Processes in a Motored PROCO Engine," SAE paper 790290, 1979.

PETITIONER'S EXHIBIT 1002
US PATENT NO. 6,581,565

29. Borgnakke, C., Davis, G. C., and Tabaczynski, R. J.: "Predictions of In-Cylinder Swirl Velocity and Turbulence Intensity for an Open Chamber Cup in Piston Engine," SAE paper 810224, *SAE Trans.*, vol. 90, 1981.
30. Arcoumanis, C., Bicen, A. F., and Whitelaw, J. H.: "Squish and Swirl-Squish Interaction in Motored Model Engines," *Trans. ASME, J. Fluids Engng*, vol. 105, pp. 105–112, 1983.
31. Ikegami, M., Mitsuda, T., Kawatchi, K., and Fujikawa, T.: "Air Motion and Combustion in Direct Injection Diesel Engines," JARI technical memorandum no. 2, pp. 231–245, 1971.
32. Liou, T.-M., and Santavicca, D. A.: "Cycle Resolved Turbulence Measurements in a Ported Engine With and Without Swirl," SAE paper 830419, *SAE Trans.*, vol. 92, 1983.
33. Fitzgeorge, D., and Allison, J. L.: "Air Swirl in a Road-Vehicle Diesel Engine," *Proc. Instn Mech. Engrs* (A.D.), no. 4, pp. 151–168, 1962–1963.
34. Lichty, L. C.: *Combustion Engine Processes*, McGraw-Hill, 1967.
35. Shimamoto, Y., and Akiyama, K.: "A Study of Squish in Open Combustion Chambers of a Diesel Engine," *Bull. JSME*, vol. 13, no. 63, pp. 1096–1103, 1970.
36. Dent, J. C., and Derham, J. A.: "Air Motion in a Four-Stroke Direct Injection Diesel Engine," *Proc. Instn Mech. Engrs*, vol. 188, 21/74, pp. 269–280, 1974.
37. Asanuma, T., and Obokata, T.: "Gas Velocity Measurements of a Motored and Firing Engine by Laser Anemometry," SAE paper 790096, *SAE Trans.*, vol. 88, 1979.
38. Asanuma, T., Babu, M. K. G., and Yagi, S.: "Simulation of Thermodynamic Cycle of Three-Valve Stratified Charge Engine," SAE paper 780319, *SAE Trans.*, vol. 87, 1978.
39. Hires, S. D., Ekchian, A., Heywood, J. B., Tabaczynski, R. J., and Wall, J. C.: "Performance and NO_x Emissions Modelling of a Jet Ignition Prechamber Stratified Charge Engine," SAE paper 760161, *SAE Trans.*, vol. 85, 1976.
40. Zimmerman, D. R.: "Laser Anemometer Measurements of the Air Motion in the Prechamber of an Automotive Diesel Engine," SAE paper 830452, 1983.
41. Meintjes, K., and Alkidas, A. C.: "An Experimental and Computational Investigation of the Flow in Diesel Prechambers," SAE paper 820275, *SAE Trans.*, vol. 91, in *Diesel Engine Combustion, Emissions, and Particulates*, P-107, SAE, 1982.
42. Namazian, M., and Heywood, J. B.: "Flow in the Piston-Cylinder-Ring Crevices of a Spark-Ignition Engine: Effect on Hydrocarbon Emissions, Efficiency and Power," SAE paper 820088, *SAE Trans.*, vol. 91, 1982.
43. Wentworth, J. T.: "Piston and Ring Variables Affect Exhaust Hydrocarbon Emissions," SAE paper 680109, *SAE Trans.*, vol. 77, 1968.
44. Tabaczynski, R. J., Hoult, D. P., and Keck, J. C.: "High Reynolds Number Flow in a Moving Corner," *J. Fluid Mech.*, vol. 42, pp. 249–255, 1970.
45. Daneshyar, H. F., Fuller, D. E., and Deckker, B. E. L.: "Vortex Motion Induced by the Piston of an Internal Combustion Engine," *Int. J. Mech. Sci.*, vol. 15, pp. 381–390, 1973.

PETITIONER'S EXHIBIT 1002
US PATENT NO. 6,581,565

CHAPTER 9

COMBUSTION IN SPARK-IGNITION ENGINES

9.1 ESSENTIAL FEATURES OF PROCESS

In a conventional spark-ignition engine the fuel and air are mixed together in the intake system, inducted through the intake valve into the cylinder, where mixing with residual gas takes place, and then compressed. Under normal operating conditions, combustion is initiated towards the end of the compression stroke at the spark plug by an electric discharge. Following inflammation, a turbulent flame develops, propagates through this essentially premixed fuel, air, burned gas mixture until it reaches the combustion chamber walls, and then extinguishes. Photographs of this process taken in operating engines illustrate its essential features. Figure 9-1 (color plate) shows a sequence of frames from a high-speed color movie of the combustion process in a special single-cylinder engine with a glass piston crown.[1] The spark discharge is at $-30°$. The flame first becomes visible in the photos at about $-24°$. The flame, approximately circular in outline in this

FIGURE 9-1 (On color plate opposite p. 498)
Color photographs from high-speed movie of spark-ignition engine combustion process, taken through glass piston crown. Ignition timing 30° BTC, light load, 1430 rev/min, $(A/F) = 19$.[1]

PETITIONER'S EXHIBIT 1002
US PATENT NO. 6,581,565

view through the piston, then propagates outward from the spark plug location. The blue light from the flame is emitted most strongly from the front. The irregular shape of the turbulent flame front is apparent. At TC the flame diameter is about two-thirds of the cylinder bore. The flame reaches the cylinder wall farthest from the spark plug about 15° ATC, but combustion continues around parts of the chamber periphery for another 10°. At about 10° ATC, additional radiation—initially white, turning to pinky-orange—centered at the spark plug location is evident. This afterglow comes from the gases behind the flame which burned earlier in the combustion process, as these are compressed to the highest temperatures attained within the cylinder (at about 15° ATC) while the rest of the charge burns.[2, 3]

Additional features of the combustion process are evident from the data in Fig. 9-2, taken from several consecutive cycles of an operating spark-ignition engine. The cylinder pressure, fraction of the charge mass which has burned (determined from the pressure data, see Sec. 9.2), and fraction of the cylinder volume enflamed by the front (determined from photographs like Fig. 9-1) are shown, all as a function of crank angle.[4] Following spark discharge, there is a period during which the energy release from the developing flame is too small for the pressure rise due to combustion to be discerned. As the flame continues to grow and propagate across the combustion chamber, the pressure then steadily rises above the value it would have in the absence of combustion. The pressure reaches a maximum after TC but before the cylinder charge is fully burned, and then decreases as the cylinder volume continues to increase during the remainder of the expansion stroke.

The flame development and subsequent propagation obviously vary, cycle-by-cycle, since the shape of the pressure, volume fraction enflamed, and mass fraction burned curves for each cycle differ significantly. This is because flame growth depends on local mixture motion and composition. These quantities vary in successive cycles in any given cylinder and may vary cylinder-to-cylinder. Especially significant are mixture motion and composition in the vicinity of the spark plug at the time of spark discharge since these govern the early stages of flame development. Cycle-by-cycle and cylinder-to-cylinder variations in combustion are important because the extreme cycles limit the operating regime of the engine (see Sec. 9.4.1).

Note that the volume fraction enflamed curves rise more steeply than the mass fraction burned curves. In large part, this is because the density of the unburned mixture ahead of the flame is about four times the density of the burned gases behind the flame. Also, there is some unburned mixture behind the visible front to the flame: even when the entire combustion chamber is fully enflamed, some 25 percent of the mass has still to burn. From this description it is plausible to divide the combustion process into four distinct phases: (1) spark ignition; (2) early flame development; (3) flame propagation; and (4) flame termination. Our understanding of each of these phases will be developed in the remainder of this chapter.

The combustion event must be properly located relative to top-center to

PETITIONER'S EXHIBIT 1002
US PATENT NO. 6,581,565

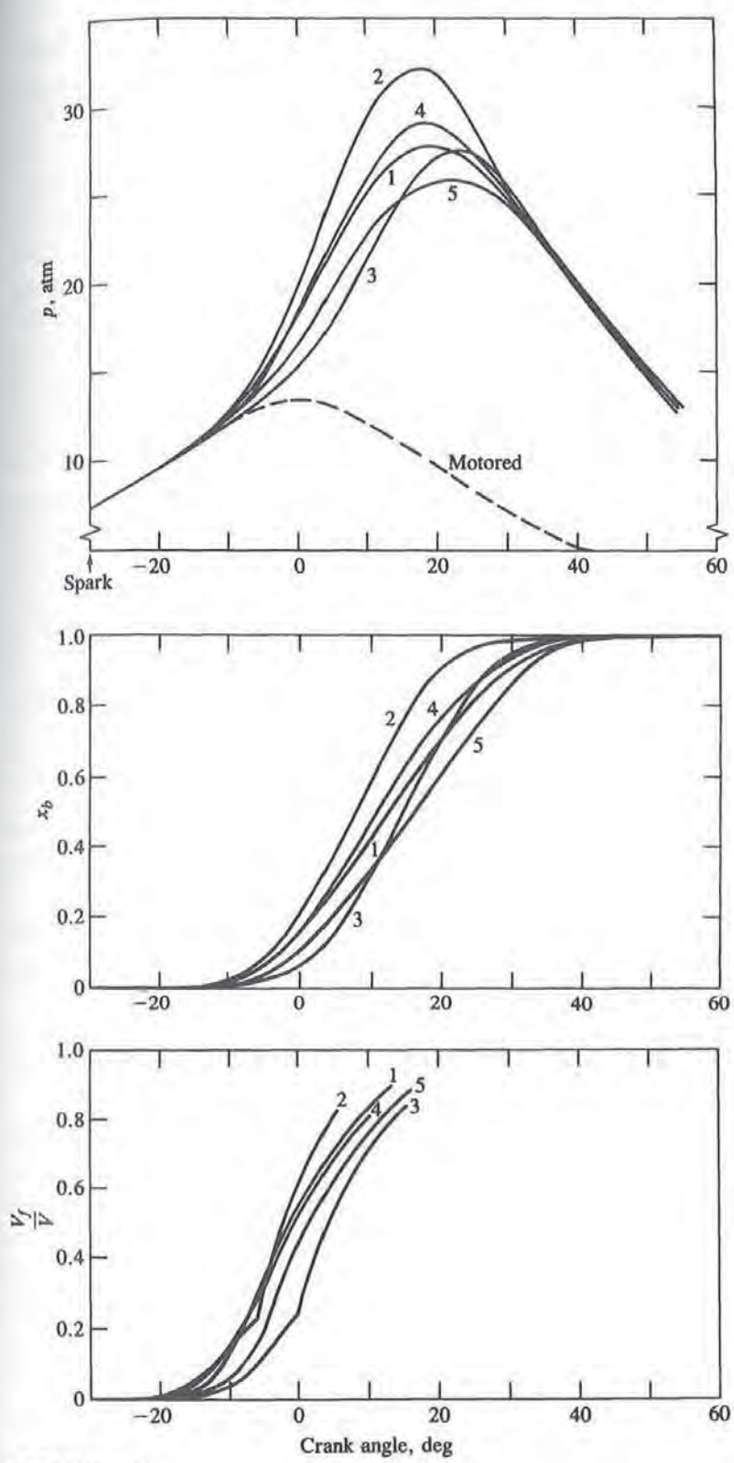


FIGURE 9-2
Cylinder pressure, mass fraction burned, and volume fraction enflamed for five consecutive cycles in a spark-ignition engine as a function of crank angle. Ignition timing 30° BTC, wide-open throttle, 1044 rev/min, $\phi = 0.98$.[4]

PETITIONER'S EXHIBIT 1002
US PATENT NO. 6,581,565

obtain the maximum power or torque. The combined duration of the flame development and propagation process is typically between 30 and 90 crank angle degrees. Combustion starts before the end of the compression stroke, continues through the early part of the expansion stroke, and ends after the point in the cycle at which the peak cylinder pressure occurs. The pressure versus crank angle curves shown in Fig. 9-3*a* allow us to understand why engine torque (at given engine speed and intake manifold conditions) varies as spark timing is varied relative to TC. If the start of the combustion process is progressively advanced before TC, the compression stroke work transfer (which is *from* the piston *to* the cylinder gases) increases. If the end of the combustion process is progressively delayed by retarding the spark timing, the peak cylinder pressure occurs later in the expansion stroke and is reduced in magnitude. These changes reduce the expansion stroke work transfer *from* the cylinder gases *to* the piston. The optimum timing which gives the maximum brake torque—called *maximum brake torque, or MBT, timing*—occurs when the magnitudes of these two opposing trends just offset each other. Timing which is advanced or retarded from this optimum gives lower torque. The optimum spark setting will depend on the rate of flame development and propagation, the length of the flame travel path across the combustion chamber, and the details of the flame termination process after it reaches the wall. These depend on engine design and operating conditions, and the properties of the fuel, air, burned gas mixture. Figure 9-3*b* shows the effect of variations in spark timing on brake torque for a typical spark-ignition engine. The maximum is quite flat.

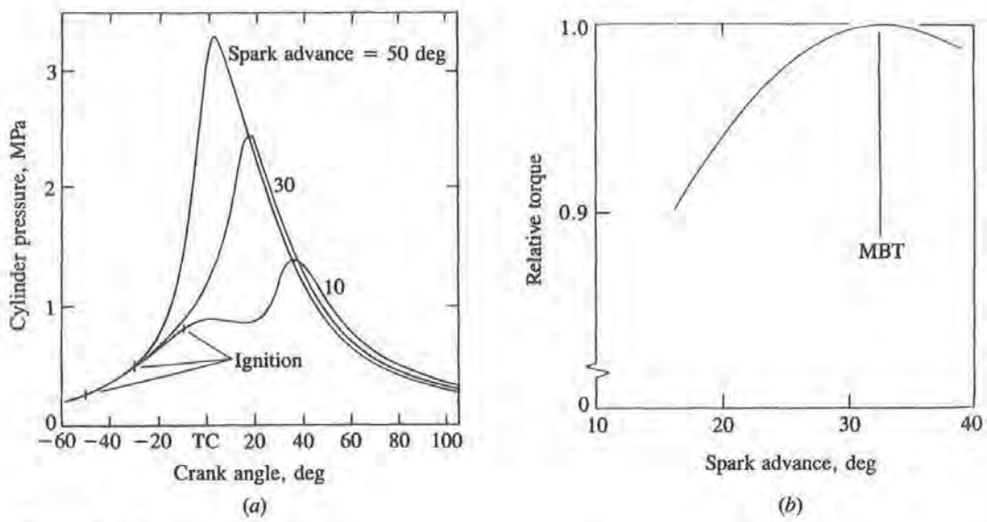


FIGURE 9-3
(*a*) Cylinder pressure versus crank angle for overadvanced spark timing (50°), MBT timing (30°), and retarded timing (10°). (*b*) Effect of spark advance on brake torque at constant speed and (*A*/*F*), at wide-open throttle. MBT is maximum brake torque timing.[5]

PETITIONER'S EXHIBIT 1002
US PATENT NO. 6,581,565

Empirical rules for relating the mass burning profile and maximum cylinder pressure to crank angle at MBT timing are often used. For example, with optimum spark timing: (1) the maximum pressure occurs at about 16° after TC; (2) half the charge is burned at about 10° after TC. In practice, the spark is often retarded to give a 1 or 2 percent reduction in brake torque from the maximum value, to permit a more precise definition of timing relative to the optimum.

So far we have described normal combustion in which the spark-ignited flame moves *steadily* across the combustion chamber until the charge is fully consumed. However, several factors—e.g., fuel composition, certain engine design and operating parameters, and combustion chamber deposits—may prevent this normal combustion process from occurring. Two types of abnormal combustion have been identified: knock and surface ignition.

Knock is the most important abnormal combustion phenomenon. Its name comes from the noise that results from the autoignition of a portion of the fuel, air, residual gas mixture ahead of the advancing flame. As the flame propagates across the combustion chamber, the unburned mixture ahead of the flame—called the *end gas*—is compressed, causing its pressure, temperature, and density to increase. Some of the end-gas fuel-air mixture may undergo chemical reactions prior to normal combustion. The products of these reactions may then autoignite: i.e., spontaneously and rapidly release a large part or all of their chemical energy. When this happens, the end gas burns very rapidly, releasing its energy at a rate 5 to 25 times that characteristic of normal combustion. This causes high-frequency pressure oscillations inside the cylinder that produce the sharp metallic noise called knock.

The presence or absence of knock reflects the outcome of a race between the advancing flame front and the precombustion reactions in the unburned end gas. Knock will not occur if the flame front consumes the end gas before these reactions have time to cause the fuel-air mixture to autoignite. Knock will occur if the precombustion reactions produce autoignition before the flame front arrives.

The other important abnormal combustion phenomenon is *surface ignition.* Surface ignition is ignition of the fuel-air charge by overheated valves or spark plugs, by glowing combustion-chamber deposits, or by any other hot spot in the engine combustion chamber: it is ignition by any source other than normal spark ignition. It may occur before the spark plug ignites the charge (preignition) or after normal ignition (postignition). It may produce a single flame or many flames. Uncontrolled combustion is most evident and its effects most severe when it results from preignition. However, even when surface ignition occurs after the spark plug fires (postignition), the spark discharge no longer has complete control of the combustion process.

Surface ignition may result in knock. Knock which occurs following normal spark ignition is called *spark knock* to distinguish it from knock which has been preceded by surface ignition. Abnormal combustion phenomena are reviewed in more detail in Sec. 9.6.

PETITIONER'S EXHIBIT 1002
US PATENT NO. 6,581,565

9.2 THERMODYNAMIC ANALYSIS OF SI ENGINE COMBUSTION

9.2.1 Burned and Unburned Mixture States

Because combustion occurs through a flame propagation process, the changes in state and the motion of the unburned and burned gas are much more complex than the ideal cycle analysis in Chapter 5 suggests. The gas pressure, temperature, and density change as a result of changes in volume due to piston motion. During combustion, the cylinder pressure increases due to the release of the fuel's chemical energy. As each element of fuel-air mixture burns, its density decreases by about a factor of four. This combustion-produced gas expansion compresses the unburned mixture ahead of the flame and displaces it toward the combustion chamber walls. The combustion-produced gas expansion also compresses those parts of the charge which have already burned, and displaces them back toward the spark plug. During the combustion process, the unburned gas elements move away from the spark plug; following combustion, individual gas elements move back toward the spark plug. Further, elements of the unburned mixture which burn at different times have different pressures and temperatures just prior to combustion, and therefore end up at different states after combustion. The thermodynamic state and composition of the burned gas is, therefore, non-uniform. A first law analysis of the spark-ignition engine combustion process enables us to quantify these gas states.

Consider the schematic of the engine cylinder while combustion is in progress, shown in Fig. 9-4. Work transfer occurs between the cylinder gases and the piston (*to the gas* before TC; *to the piston* after TC). Heat transfer occurs to the chamber walls, primarily from the burned gases. At the temperatures and pressures typical of spark-ignition engines it is a reasonable approximation to assume that the volume of the reaction zone *where combustion is actually occurring* is a negligible fraction of the chamber volume even though the thickness of the turbulent flame may not be negligible compared with the chamber dimensions (see Sec. 9.3.2). With normal engine operation, at any point in time or crank angle, the pressure throughout the cylinder is close to uniform. The condi-

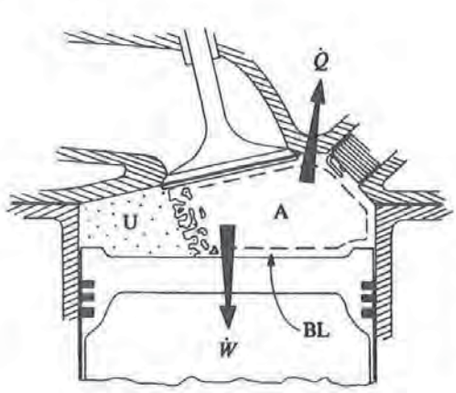


FIGURE 9-4
Schematic of flame in the engine cylinder during combustion: unburned gas (U) to left of flame, burned gas to right. A denotes adiabatic burned-gas core, BL denotes thermal boundary layer in burned gas, $\dot{W}$ is work-transfer rate to piston, $\dot{Q}$ is heat-transfer rate to chamber walls.

PETITIONER'S EXHIBIT 1002
US PATENT NO. 6,581,565

tions in the burned and unburned gas are then determined by conservation of mass:

$$\frac{V}{m} = \int_0^{x_b} v_b \, dx + \int_{x_b}^1 v_u \, dx \tag{9.1}$$

and conservation of energy:

$$\frac{U_0 - W - Q}{m} = \int_0^{x_b} u_b \, dx + \int_{x_b}^1 u_u \, dx \tag{9.2}$$

where V is the cylinder volume, m is the mass of the cylinder contents, v is the specific volume, x_b is the mass fraction burned, U_0 is the internal energy of the cylinder contents at some reference point θ_0, u is the specific internal energy, W is the work done on the piston, and Q is the heat transfer to the walls. The subscripts u and b denote unburned and burned gas properties, respectively. The work and heat transfers are

$$W = \int_{V_0}^{V} p \, dV' \qquad Q = \int_{\theta_0}^{\theta} \left(\frac{\dot{Q}}{360N}\right) d\theta \tag{9.3}$$

where $\dot{Q}$ is the instantaneous heat-transfer rate to the chamber walls.

To proceed further, models for the thermodynamic properties of the burned and unburned gases are required. Several categories of models are described in Chap. 4. Accurate calculations of the state of the cylinder gases require an equilibrium model (or good approximation to it) for the burned gas and an ideal gas mixture model (of frozen composition) for the unburned gas (see Table 4.2). However, useful illustrative results can be obtained by assuming that the burned and unburned gases are different ideal gases, each with constant specific heats;[6] i.e.,

$$pv_b = R_b T_b \qquad u_b = c_{v,b} T_b + h_{f,b} \tag{9.4}$$

$$pv_u = R_u T_u \qquad u_u = c_{v,u} T_u + h_{f,u} \tag{9.5}$$

Combining Eqs. (9.1) to (9.5) gives

$$\frac{pV}{m} = x_b R_b \bar{T}_b + (1 - x_b) R_u \bar{T}_u \tag{9.6}$$

and

$$\frac{U_0 - W - Q}{m} = x_b(c_{v,b} \bar{T}_b + h_{f,b}) + (1 - x_b)(c_{v,u} \bar{T}_u + h_{f,u}) \tag{9.7}$$

where

$$\bar{T}_b = \frac{1}{x_b} \int_0^{x_b} T_b \, dx \qquad \bar{T}_u = \frac{1}{1 - x_b} \int_{x_b}^1 T_u \, dx$$

PETITIONER'S EXHIBIT 1002
US PATENT NO. 6,581,565

are the mean temperatures of the burned and unburned gases. Equations (9.6) and (9.7) may now be solved to obtain

$$x_b = \frac{pV - p_0 V_0 + (\gamma_b - 1)(W + Q) + (\gamma_b - \gamma_u)mc_{v,u}(\bar{T}_u - T_0)}{m[(\gamma_b - 1)(h_{f,u} - h_{f,b}) + (\gamma_b - \gamma_u)c_{v,u}\bar{T}_u]} \tag{9.8}$$

and

$$\bar{T}_b = \frac{R_u}{R_b}\bar{T}_u + \frac{pV - mR_u\bar{T}_u}{mR_b x_b} \tag{9.9}$$

If we now assume the unburned gas is initially uniform and undergoes isentropic compression, then

$$\frac{\bar{T}_u}{T_0} = \left(\frac{p}{p_0}\right)^{(\gamma_u - 1)/\gamma_u} \tag{9.10}$$

This equation, with Eqs. (9.8) and (9.9) enables determination of both x_b and $\bar{T}_b$ from the thermodynamic properties of the burned and unburned gases, and known values of p, V, m, and $\dot{Q}$. Alternatively, if x_b is known then p can be determined. Mass fraction burned and cylinder gas pressure are uniquely related.

While Eq. (9.9) defines a mean burned gas temperature, the burned gas is not uniform. Mixture which burns early in the combustion process is further compressed after combustion as the remainder of the charge is burned. Mixture which burns late in the combustion process is compressed prior to combustion and, therefore, ends up at a different final state. A temperature gradient exists across the burned gas with the earlier burning portions at the higher temperature.[7,8] Two limiting models bracket what occurs in practice: (1) a *fully mixed* model, where it is assumed that each element of mixture which burns mixes instantaneously with the already burned gases (which therefore have a uniform temperature), and (2) an *unmixed* model, where it is assumed that no mixing occurs between gas elements which burn at different times.

In the fully mixed model the burned gas is uniform, $T_b = \bar{T}_b$, and the equations given above fully define the state of the cylinder contents. In the unmixed model, the assumption is made that no mixing occurs between gas elements that burn at different times, and each burned gas element is therefore isentropically compressed (and eventually expanded) after combustion.† Thus:

$$\frac{T_b(x_b', x_b)}{T_b(x_b')} = \left[\frac{p(x_b)}{p(x_b')}\right]^{(\gamma_b - 1)/\gamma_b} \tag{9.11}$$

† This model applies to burned gas regions of the chamber *away* from the walls. Heat transfer to the walls results in a thermal boundary layer on the walls which grows with time. The gas in the boundary layer is not isentropically compressed and expanded.

PETITIONER'S EXHIBIT 1002
US PATENT NO. 6,581,565

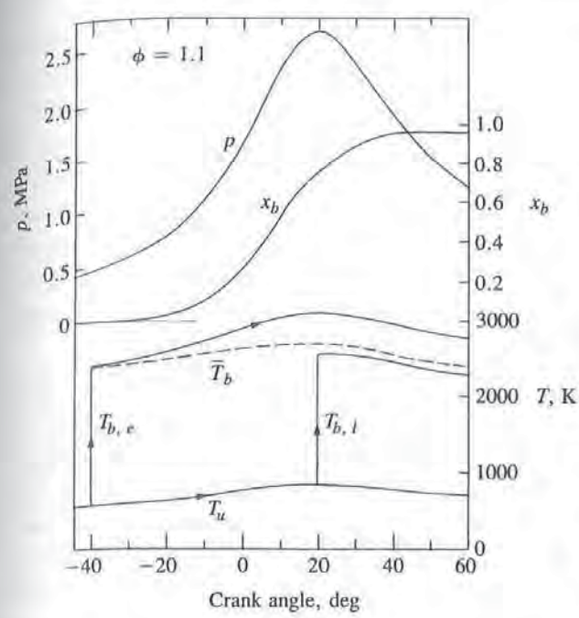


FIGURE 9-5
Cylinder pressure, mass fraction burned, and gas temperatures as functions of crank angle during combustion. T_u is unburned gas temperature, T_b is burned gas temperature, the subscripts e and l denote early and late burning gas elements, and $\bar{T}_b$ is the mean burned gas temperature.[9] (*Reprinted with permission. Copyright 1973, American Chemical Society.*)

where $T_b(x_b', x_b)$ is the temperature of the element which burned at the pressure $p(x_b')$ when the pressure is $p(x_b)$, and

$$T_b(x_b') = \frac{h_{f,u} - h_{f,b} + c_{p,u}\, T_u(x_b')}{c_{p,b}} \tag{9.12}$$

is the temperature resulting from isenthalpic combustion of the unburned gas at $T_u(x_b')$, $p(x_b')$. An example of the temperature distribution computed with this model is shown in Fig. 9-5. A mixture element that burns right at the start of the combustion process reaches, in the absence of mixing, a peak temperature after combustion about 400 K higher than an element that burns toward the end of the combustion process. The mean burned gas temperature is closer to the lower of these temperatures. These two models approximate respectively to situations where the time scale that characterizes the turbulent mixing process in the burned gases is (1) much less than the overall burning time (for the fully mixed model) or (2) much longer than the overall burning time (for the unmixed model). The real situation lies in between.

Measurements of burned gas temperatures have been made in engines using spectroscopic techniques through quartz windows in the cylinder head. Examples of measured temperatures are shown in Fig. 9-6. The solid lines marked A, B, and C are the burned gas temperatures measured by Rassweiler and Withrow[7] using the sodium line reversal technique in an L-head engine, for the spark plug end (A), the middle (B), and the opposite end (C) of the chamber, respectively. Curves labeled W_2 and W_3 were measured by Lavoie[8] through two different windows, W_2 and W_3 (with W_2 closer to the spark), again in an L-head engine. Each set of experimental temperatures shows a temperature gradient across the burned gas comparable to that predicted, and the two sets have similar shapes.

PETITIONER'S EXHIBIT 1002
US PATENT NO. 6,581,565

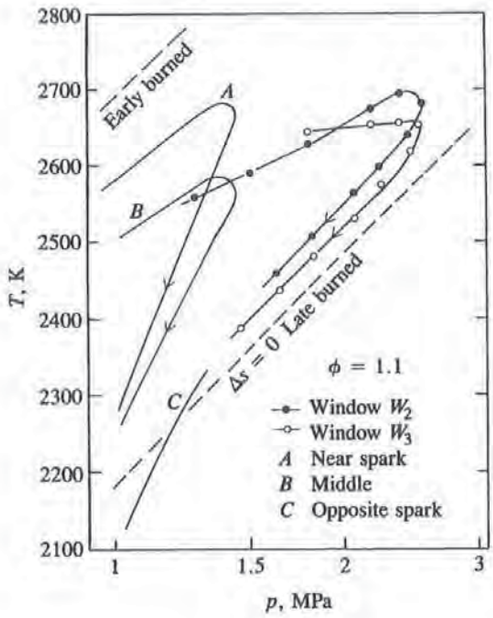


FIGURE 9-6
Burned gas temperatures measured using spectroscopic techniques through windows in the cylinder head, as a function of cylinder pressure. Temperatures measured closer to spark plug have higher values. Dashed lines show isentropic behavior.[7, 8]

In the unmixed model, the temperature of each burned gas element follows a different isentropic line as it is first compressed as p increases to p_{max} and then expanded as the pressure falls after p_{max}. The measured temperature curves in Fig. 9-6 do not follow the calculated isentropes because of gas motion past the observation ports. As has already been mentioned, the expansion of a gas element which occurs during combustion compresses the gas ahead of the flame and moves it away from the spark plug. At the same time, previously burned gas is compressed and moved back toward the spark plug. Defining this motion in an engine requires sophisticated flow models, because the combustion chamber shape is rarely symmetrical, the spark plug is not usually centrally located, and often there is a bulk gas motion at the time combustion is initiated. However, the gas motion in a spherical or cylindrical combustion bomb with central ignition which can readily be computed illustrates the features of the combustion-induced motion in an engine. Figure 9-7 shows calculated particle trajectories for a stoichiometric methane-air mixture, initially at ambient conditions, as a laminar

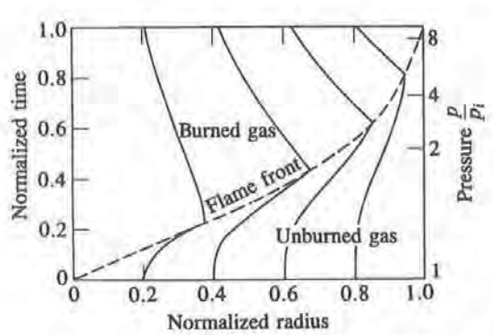


FIGURE 9-7
Particle trajectories in unburned and burned gas as flame propagates outward at constant velocity from the center of a spherical combustion bomb. Stoichiometric methane-air mixture initially at 1 atm and 300 K.

PETITIONER'S EXHIBIT 1002
US PATENT NO. 6,581,565

flame with a constant burning velocity propagates outward from the center of a spherical container. Applying this gas motion model to an engine, it can be concluded that a window in the cylinder head initially views earlier burned gas (of higher temperature and entropy) and that as more of the charge burns, the window views later burned gas of progressively lower entropy. The experimental curves fit this description: they cross the constant entropy lines toward lower entropy. Note that the gradient in temperature persists well into the expansion stroke, indicating that the "unmixed" model is closer to reality than the "fully mixed" model.

More accurate calculations relating the mass fraction burned, gas pressure, and gas temperature distribution are often required. Note that the accuracy of such calculations depends on the accuracy with which the time-varying heat loss to the chamber walls can be estimated (see Sec. 12.4.3) and whether flows into and out of crevice regions are significant (see Sec. 8.6), as well as the accuracy of the models used to describe the thermodynamic properties of the gases. Appropriate more accurate models for the thermodynamic properties are: an equilibrium model for the burned gas, and specific heat models which vary with temperature for each of the components of the unburned mixture (see Secs. 4.1 and 4.7). In the absence of significant crevice effects, Eqs. (9.1) and (9.2) can be written as

$$\frac{V}{m} = \bar{v}_b x_b + \bar{v}_u(1 - x_b) \tag{9.13}$$

$$\frac{U_0 - W - Q}{m} = \bar{u}_b x_b + \bar{u}_u(1 - x_b) \tag{9.14}$$

where

$$\bar{v}_b = \frac{1}{x_b}\int_0^{x_b} v_b \, dx \qquad \text{and} \qquad \bar{v}_u = \frac{1}{1 - x_b}\int_{x_b}^{1} v_u \, dx$$

and similar definitions hold for $\bar{u}_b$ and $\bar{u}_u$. For a given equivalence ratio, fuel and burned gas fraction:

$$h_u = h_u(T_u) \qquad h_b = h_b(T_b, p) \tag{9.15a, b}$$

$$pv_u = \left(\frac{\tilde{R}}{M_u}\right)T_u \qquad pv_b = \left(\frac{\tilde{R}}{M_b}\right)T_b \tag{9.16a, b}$$

and

$$\bar{u}_u = \bar{h}_u - p\bar{v}_u \qquad \bar{u}_b = \bar{h}_b - p\bar{v}_b \tag{9.17a, b}$$

To simplify the calculations, it is convenient to assume that, for the burned gas, $\bar{u}_b = u_b(\bar{T}_b, p)$ and $\bar{v}_b = v_b(\bar{T}_b, p)$. This corresponds to the fully mixed assumption described above. The effect of neglecting the temperature distribution in the calculation of mass fraction burned is small. In addition, the heat losses from the unburned gas can usually be neglected; the unburned gas is then compressed isentropically. $\bar{T}_u$ is specified for some initial state of the unburned gas (where

PETITIONER'S EXHIBIT 1002
US PATENT NO. 6,581,565

$x_b = 0$) by p_0, V_0, M_u, and the mass of charge m. Then, since for any isentropic process

$$\left(\frac{\partial T}{\partial p}\right)_s = \frac{v - (\partial h/\partial p)_T}{(\partial h/\partial T)_p} \tag{9.18}$$

$\bar{T}_u$ can be determined.

Equations (9.13) to (9.18) constitute a set of nine equations for the nine unknowns $\bar{v}_u$, $\bar{v}_b$, $\bar{u}_u$, $\bar{u}_b$, $\bar{h}_u$, $\bar{h}_b$, $\bar{T}_u$, $\bar{T}_b$, and x_b or p. One convenient solution method is to eliminate x_b from Eqs. (9.13) and (9.14) to obtain

$$\frac{(V/m) - \bar{v}_u}{\bar{v}_b - \bar{v}_u} - \frac{(U/m) - \bar{u}_u}{\bar{u}_b - \bar{u}_u} = f(\bar{T}_b, \bar{T}_u) = 0 \tag{9.19}$$

where $U = U_0 - W - Q$. $\bar{T}_u$ can be determined from Eq. (9.18). Equation (9.19) can then be solved using an appropriate iterative technique for $\bar{T}_b$, and x_b can be obtained from Eq. (9.13). An alternative formulation based on the rate of change of pressure $dp/d\theta$ and equations for $d\bar{T}_u/d\theta$, $d\bar{T}_b/d\theta$, $dm_b/d\theta$, and $dV_b/d\theta$ can be found in Ref. 10. Some examples of mass fraction burned curves obtained from measured pressure data, with gasoline and methanol fuels, are shown in Fig. 9-8. With accurate pressure versus crank angle records, values of final mass fraction burned should be close to but lower than unity, usually in the range 0.93 to 0.98; the difference from unity is the combustion inefficiency for lean mixtures (see Fig. 3-9) and incomplete oxygen utilization for rich mixtures (see Fig. 4-20).

More accurate burned gas temperature calculations need to account for the presence of a thermal boundary layer (of order 1 mm thick) around the combustion chamber walls (see Sec. 12.6.5). The burned gas region in Fig. 9-4 can be

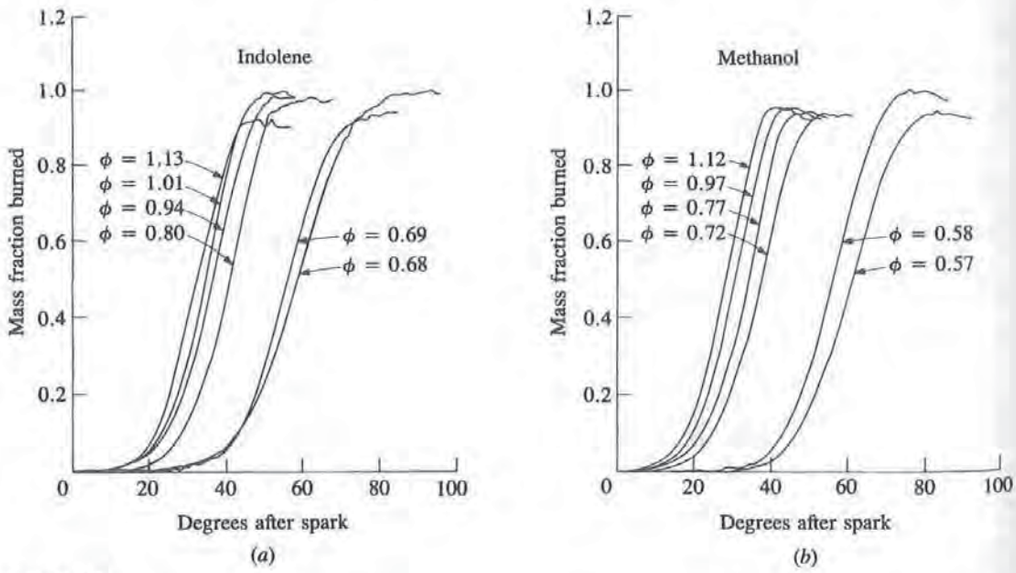


FIGURE 9-8
Mass fraction burned curves determined from measured cylinder pressure data using two-zone combustion model: (*a*) gasoline; (*b*) methanol. ϕ = fuel/air equivalence ratio.[11]

PETITIONER'S EXHIBIT 1002
US PATENT NO. 6,581,565

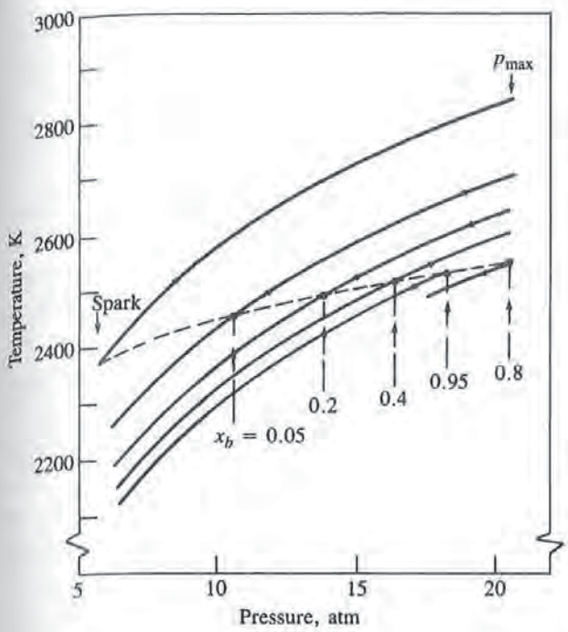


FIGURE 9-9
Calculated temperature distribution in the adiabatic core of the burned gas zone for the unmixed model assuming thermodynamic equilibrium. $\phi = 1.0$. Dashed line is temperature of each element just after it burns.

divided into an adiabatic core and a boundary layer that grows in thickness with time. In the adiabatic core, in the absence of mixing between gas elements that burn at different times, burned gas is compressed and then expanded isentropically. The burned gas temperature distribution can be calculated as follows. Given the pressure versus crank angle data, the unburned mixture state can be determined using Eq. (9.18) above. Each small element of unburned mixture burns in a constant-enthalpy constant-pressure process. So the burned state of an element of unburned charge, which burns at $p = p_i$, can be obtained from the relation

$$h_b(T_{b,i}, p_i) = h_u(T_{u,i}, p_i)$$

After combustion, this element which burned at $p = p_i$ is compressed and expanded along the isentropic:

$$s_b(T_b, p) = s_b(T_{b,i}, p_i)$$

An example of the temperature distribution computed in this manner for this unmixed model in the burned gas adiabatic core is shown in Fig. 9-9. The element ignited by the spark is compressed to the highest peak temperature at p_{max}. The temperature difference across the bulk of the charge ($0.05 < x_b < 0.95$) is about 200 K.

9.2.2 Analysis of Cylinder Pressure Data

Cylinder pressure changes with crank angle as a result of cylinder volume change, combustion, heat transfer to the chamber walls, flow into and out of crevice regions, and leakage. The first two of these effects are the largest. The effect of

PETITIONER'S EXHIBIT 1002
US PATENT NO. 6,581,565

volume change on the pressure can readily be accounted for; thus, combustion rate information can be obtained from accurate pressure data provided models for the remaining phenomena can be developed at an appropriate level of approximation. The previous section has developed the fundamental basis for such calculations.

Cylinder pressure is usually measured with piezoelectric pressure transducers. This type of transducer contains a quartz crystal. One end of the crystal is exposed through a diaphragm to the cylinder pressure; as the cylinder pressure increases, the crystal is compressed and generates an electric charge which is proportional to the pressure. A charge amplifier is then used to produce an output voltage proportional to this charge. Accurate cylinder pressure versus crank angle data can be obtained with these systems provided the following steps are carried out: (1) the correct reference pressure is used to convert the measured pressure signals to absolute pressures; (2) the pressure versus crank angle (or volume) phasing is accurate to within about 0.2°; (3) the clearance volume is estimated with sufficient accuracy; (4) transducer temperature variations (which can change the transducer calibration factor) due to the variation in wall heat flux during the engine cycle are held to a minimum. Log p versus log V plots can be used to check the quality of cylinder pressure data. The first three of the above requirements can be validated using log p–log V diagrams for a motored engine. If the effects of thermal cycling are significant, the expansion stroke on the log p–log V plot for a firing engine shows excessive curvature.[12]

Figure 9-10 shows pressure-volume data from a firing spark-ignition engine on both a linear p–V and a log p–log V diagram. On the log p–log V diagram the compression process is a straight line of slope 1.3. The start of combustion can be identified by the departure of the curve from the straight line. The end of com-

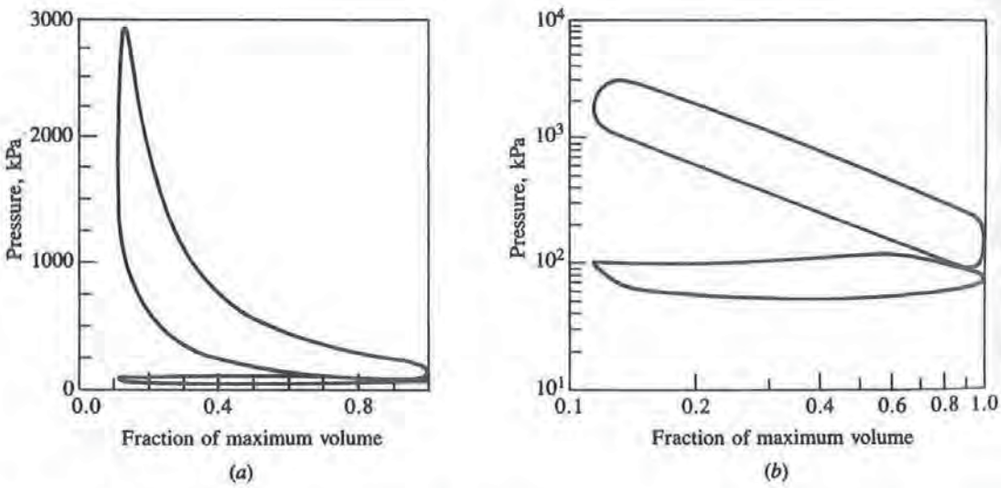


FIGURE 9-10
(*a*) Pressure-volume diagram; (*b*) log p–log (V/V_{max}) plot. 1500 rev/min, MBT timing, imep = 513 kPa, $\phi = 0.8$, $r_c = 8.72$, propane fuel.[12]

PETITIONER'S EXHIBIT 1002
US PATENT NO. 6,581,565

bustion can be located approximately in similar fashion; the expansion stroke following combustion is essentially linear with slope 1.33. Since both the compression of the unburned mixture prior to combustion and the expansion of the burned gases following the end of combustion are close to adiabatic isentropic processes (for which $pV^\gamma = \text{constant}$; $\gamma = c_p/c_v$), the observed behavior is as expected. More extensive studies[12, 13] show that the compression and expansion processes are well fitted by a polytropic relation:

$$pV^n = \text{constant} \tag{9.20}$$

The exponent n for the compression and expansion processes is 1.3 (± 0.05) for conventional fuels. It is comparable to the average value of γ_u for the unburned mixture over the compression process, but is larger than γ_b for the burned gas mixture during expansion due to heat loss to the combustion chamber walls (see Figs. 4-13 and 4-16).

Log p–log V plots such as Fig. 9-10 approximately define the start and end of combustion, but do not provide a mass fraction burned profile. One well-established technique for estimating the mass fraction burned profile from the pressure and volume data is that developed by Rassweiler and Withrow.[2] They correlated cylinder pressure data with flame photographs, and showed how Eq. (9.20) could be used to account for the effect of cylinder volume change on the pressure during combustion. Assuming that the unburned gas filling the volume V_u ahead of the flame at any crank angle during combustion has been compressed polytropically by the advancing flame front, then the volume $V_{u,0}$ it occupied at time of spark is

$$V_{u,0} = V_u\left(\frac{p}{p_0}\right)^{1/n} \tag{9.21}$$

Similarly, the burned gas behind the flame filling the volume V_b would, at the end of combustion, fill a volume $V_{b,f}$ given by

$$V_{b,f} = V_b\left(\frac{p}{p_f}\right)^{1/n} \tag{9.22}$$

The mass fraction burned x_b is equal to $1 - (V_{u,0}/V_0)$ and to $V_{b,f}/V_f$, where V_0 amd V_f are the total cylinder volumes at time of spark and at the end of combustion, respectively. Since $V = V_u + V_b$, Eqs. (9.21) and (9.22) then give:

$$x_b = \frac{p^{1/n}V - p_0^{1/n}V_0}{p_f^{1/n}V_f - p_0^{1/n}V_0} \tag{9.23}$$

This method is widely used, though it contains several approximations. Heat-transfer effects are included only to the extent that the polytropic exponent n in Eq. (9.22) differs appropriately from γ. The pressure rise due to combustion is proportional to the amount of fuel chemical energy released rather than the mass of mixture burned. Also, the polytropic exponent n is not constant during combustion. Selecting an appropriate value for n (whether n is assumed to be con-

PETITIONER'S EXHIBIT 1002
US PATENT NO. 6,581,565

stant or to vary through the combustion process) is the major difficulty in applying this pressure data analysis procedure.

The effects of heat transfer, crevices, and leakage can be explicitly incorporated into cylinder pressure data analysis by using a "heat release" approach based on the first law of thermodynamics. A major advantage of such an approach is that the pressure changes can be related directly to the amount of fuel chemical energy released by combustion, while retaining the simplicity of treating the combustion chamber contents as a single zone. Figure 9-11 shows the appropriate open-system boundary for the combustion chamber.[14] The first law for this open system is

$$\delta Q_{\text{ch}} = dU_s + \delta Q_{\text{ht}} + \delta W + \sum h_i \, dm_i \tag{9.24}$$

The change in sensible energy of the charge dU_s is separated from that due to change in composition: the term δQ_{ch} represents the "chemical energy" released by combustion. The work is piston work and equal to $p\,dV$. δQ_{ht} is heat transfer to the chamber walls. The mass flux term represents flow across the system boundary. In the absence of fuel injection, it represents flow into and out of crevice regions (see Sec. 8.6).

The accuracy with which this energy balance can be made depends on how adequately each term in the above equation can be quantified. Assuming that U_s is given by $mu(T)$, where T is the mean charge temperature and m is the mass within the system boundary, then

$$dU_s = mc_v(T)\,dT + u(T)\,dm$$

Note that this mean temperature determined from the ideal gas law is close to the mass-averaged cylinder temperature during combustion since the molecular weights of the burned and unburned gases are essentially identical. Crevice effects can usually be modeled adequately by flow into and out of a single volume at the cylinder pressure, with the gas in the crevice at a substantially lower temperature. Leakage to the crankcase can usually be neglected. Then Eq. (9.24), on substituting for dU_s and dm_i ($=dm_{\text{cr}} = -dm$), becomes

$$\delta Q_{\text{ch}} = mc_v\,dT + (h' - u)dm_{\text{cr}} + p\,dV + \delta Q_{\text{ht}} \tag{9.25}$$

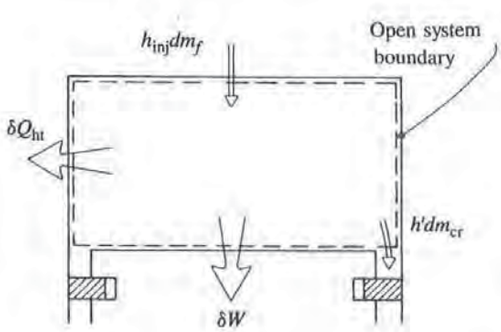


FIGURE 9-11
Open system boundary for combustion chamber for heat-release analysis.

PETITIONER'S EXHIBIT 1002
US PATENT NO. 6,581,565

where

$dm_{cr} > 0$ when flow is out of the cylinder into the crevice
$dm_{cr} < 0$ when flow is from the crevice to the cylinder
h' is evaluated at cylinder conditions when $dm_{cr} > 0$ and
at crevice conditions when $dm_{cr} < 0$

Use of the ideal gas law (neglecting the change in gas constant R) with Eq. (9.25) then gives

$$\delta Q_{ch} = \left(\frac{c_v}{R}\right) V\, dp + \left(\frac{c_v}{R} + 1\right) p\, dV + (h' - u + c_v T)\, dm_{cr} + \delta Q_{ht} \qquad (9.26)$$

This equation can be used in several ways. When the heat or energy release term, δQ_{ch}, is combined with the heat-transfer and crevice terms, the combination is termed *net heat release*—the combustion energy release less heat lost to the walls. It is equal to the first two terms on the right-hand side of Eq. (9.26) which, together, represent the sensible energy change and work transfer to the piston. While heat losses during combustion are a small fraction of the fuel energy (10 to 15 percent), the distributions of heat release and heat transfer with crank angle are different; heat transfer becomes more important as the combustion process ends and average gas temperatures peak. The net heat-release profile obtained from integrating the first two terms on the right-hand side of Eq. (9.26), normalized to give unity at its maximum value, is often interpreted as the burned mass fraction (or, more correctly, the energy-release fraction) versus crank angle profile.

Use of Eq. (9.26) requires a value for c_v/R $[= 1/(\gamma - 1)]$. The ratio of specific heats γ for both unburned and burned gases decreases with increasing temperature and varies with composition (see Figs. 4-13, 4-16, and 4-18). As the mean charge temperature increases during compression and combustion and then decreases during expansion, γ should vary. An approximate approach, modeling $\gamma(T)$ with a linear function of temperature fitted to the appropriate curves in Figs. 4-13, 4-16, and 4-18 and with γ constant during combustion, has been shown to give adequate results.[15]

The convective heat-transfer rate to the combustion chamber walls can be calculated from the relation

$$\frac{dQ_{ht}}{dt} = A h_c (T - T_w)$$

where A is the chamber surface area, T is the mean gas temperature, T_w is the mean wall temperature, and h_c is the heat-transfer coefficient (averaged over the chamber surface area). h_c can be estimated from engine heat-transfer correlations (see Sec. 12.4.3). Since crevice effects are usually small, a sufficiently accurate model for their overall effect is to consider a single aggregate crevice volume where the gas is at the same pressure as the combustion chamber, but at a different temperature. Since these crevice regions are narrow, an appropriate assumption is that the crevice gas is at the wall temperature. Inserting this crevice model

PETITIONER'S EXHIBIT 1002
US PATENT NO. 6,581,565

into Eq. (9.26), with $\gamma(T) = a + bT$, gives the *chemical energy-* or *gross heat-release rate*:

$$\frac{dQ_{ch}}{d\theta} = \frac{\gamma}{\gamma - 1} p \frac{dV}{d\theta} + \frac{1}{\gamma - 1} V \frac{dp}{d\theta} + V_{cr}\left[\frac{T'}{T_w} + \frac{T}{T_w(\gamma - 1)} + \frac{1}{bT_w} \ln\left(\frac{\gamma - 1}{\gamma' - 1}\right)\right] \frac{dp}{d\theta} + \frac{dQ_{ht}}{d\theta} \quad (9.27)$$

An example of the use of Eq. (9.27) to analyze an experimental pressure versus crank angle curve for a conventional spark-ignition engine is shown in Fig. 9-12. The integrated heat release is plotted against crank angle. The lowest curve shown is the net heat release. The addition of heat transfer and crevice models gives the chemical energy release. The curve at the top of the figure is the mass of fuel within the combustion chamber times its lower heating value. It decreases slightly as p_{max} is approached due to flow into crevices. The difference between the final value of Q_{ch} and $(m_f Q_{LHV})$ should equal the combustion inefficiency (which is a few percent of $m_f Q_{LHV}$). The combustion inefficiency can be determined from the exhaust gas composition (see Sec. 4.9.4). Inaccuracies in the cylinder pressure data and the heat-release calculation will also contribute to this difference. An important advantage of a heat-release analysis that relates the pressure changes to the amount of fuel chemical energy within the cylinder is that this error can be determined. In the example in Fig. 9-12, the measured combustion inefficiency was close to the amount shown.

Two-zone models (one zone representing the unburned mixture ahead of the flame and one the burned mixture behind the flame) are used to calculate the mass fraction burned profile from measured cylinder pressure data.[10] Figure 9-8 shows results from such an analysis, using the methodology described in Sec. 9.2.1. The advantage of a two-zone analysis is that the thermodynamic properties of the cylinder contents can be quantified more accurately. The disadvantages are that the unburned and the burned zone heat-transfer areas must both now be estimated, and a model for the composition of the gas flowing into the crevice

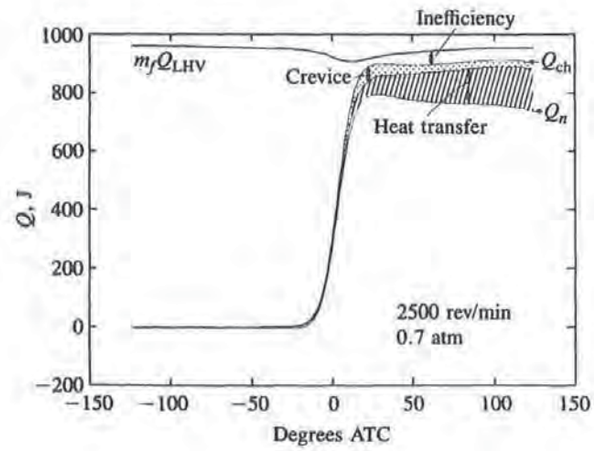


FIGURE 9-12
Results of heat-release analysis showing the effects of heat transfer, crevices, and combustion inefficiency.[14]

PETITIONER'S EXHIBIT 1002
US PATENT NO. 6,581,565

region must be developed. Due to this complexity, crevice models are usually omitted despite the fact that their impact can be significant.

9.2.3 Combustion Process Characterization

The mass fraction burned profiles as a function of crank angle in each individual cycle shown in Fig. 9-2 and the chemical energy- or gross heat-release curve in Fig. 9-12 have a characteristic S-shape. The rate at which fuel-air mixture burns increases from a low value immediately following the spark discharge to a maximum about halfway through the burning process and then decreases to close to zero as the combustion process ends. It proves convenient to use these mass fraction burned or energy-release fraction curves to characterize different stages of the spark-ignition engine combustion process by their duration in crank angles, thereby defining the fraction of the engine cycle that they occupy. The flame development process, from the spark discharge which initiates the combustion process to the point where a small but measurable fraction of the charge has burned, is one such stage. It is influenced primarily by the mixture state, composition, and motion in the vicinity of the spark plug (see Sec. 9.3). The stage during which the major portion of the charge burns as the flame propagates to the chamber walls is next. This stage is obviously influenced by conditions throughout the combustion chamber. The final stage, where the remainder of the charge burns to completion, cannot as easily be quantified because energy-release rates are comparable to other energy-transfer processes that are occurring.

The following definitions are most commonly used to characterize the energy-release aspects of combustion:

Flame-development angle $\Delta\theta_d$. The crank angle interval between the spark discharge and the time when a small but significant fraction of the cylinder mass has burned or fuel chemical energy has been released. Usually this fraction is 10 percent, though other fractions such as 1 and 5 percent have been used.†

Rapid-burning angle $\Delta\theta_b$. The crank angle interval required to burn the bulk of the charge. It is defined as the interval between the end of the flame-development stage (usually mass fraction burned or energy-release fraction of 10 percent) and the end of the flame-propagation process (usually mass fraction burned or energy-release fraction of 90 percent).‡

Overall burning angle $\Delta\theta_o$. The duration of the overall burning process. It is the sum of $\Delta\theta_d$ and $\Delta\theta_b$.

---

† This angle is sometimes called the *ignition delay*. Since the flame starts to propagate outward immediately following the spark discharge there is no delay, and the terminology used here is preferred (see Sec. 9.3).

‡ An alternative definition for $\Delta\theta_b$ uses the maximum burning rate to define an angle or time characteristic of the bulk charge burning process[4] (see Fig. 9-13). $\Delta\theta_b$ and $\Delta\theta_b^*$ are usually closely comparable.

PETITIONER'S EXHIBIT 1002
US PATENT NO. 6,581,565

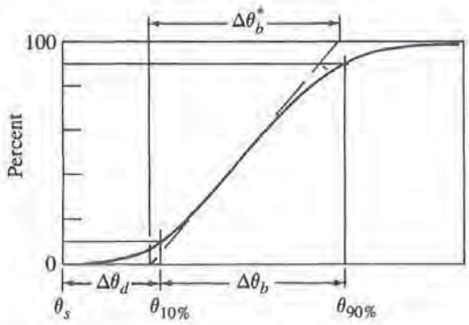


FIGURE 9-13
Definition of flame-development angle, $\Delta\theta_d$, and rapid-burning angle, $\Delta\theta_b$, on mass fraction burned versus crank angle curve.

Figure 9-13 illustrates these definitions on a mass fraction burned, or fraction of fuel energy released, versus crank angle plot. While the selection of the 10 and 90 percent points is arbitrary, such a choice avoids the difficulties involved in determining accurately the shape of the curve at the start and end of combustion. These angles can be converted to times (in seconds) by dividing by $6N$ (with N in revolutions per minute).

A functional form often used to represent the mass fraction burned versus crank angle curve is the Wiebe function:

$$x_b = 1 - \exp\left[-a\left(\frac{\theta - \theta_0}{\Delta\theta}\right)^{m+1}\right] \tag{9.28}$$

where θ is the crank angle, θ_0 is the start of combustion, $\Delta\theta$ is the total combustion duration ($x_b = 0$ to $x_b = 1$), and a and m are adjustable parameters. Varying a and m changes the shape of the curve significantly. Actual mass fraction burned curves have been fitted with $a = 5$ and $m = 2$.[16]

9.3 FLAME STRUCTURE AND SPEED

9.3.1 Experimental Observations

The combustion process in the spark-ignition engine takes place in a turbulent flow field. This flow field is produced by the high shear flows set up during the intake process and modified during compression, as described in Chap. 8. The importance of the turbulence to the engine combustion process was recognized long ago through experiments where the intake event, and the turbulence it generates, was eliminated and the rate of flame propagation decreased substantially. Understanding the structure of this engine flame as it develops from the spark discharge and the speed at which it propagates across the combustion chamber, and how that structure and speed depend on charge motion, charge composition, and chamber geometry, are critical to engine optimization. This section reviews experimental evidence that describes the essential features of the flame development and propagation processes.

Direct flame photographs such as those in Fig. 9-1 indicate the location and shape of the actual reaction zone which radiates in the blue region of the visible spectrum. An irregular front is apparent. Further insight into the structure of the

PETITIONER'S EXHIBIT 1002
US PATENT NO. 6,581,565

flame can be obtained from photographs taken with techniques that are sensitive to density changes in the flow field, such as schlieren and shadowgraph. With these techniques, a parallel light beam is passed through the combustion chamber. Portions of the beam which pass through regions where density gradients normal to the beam exist are deflected, due to the refractive index gradients that result from the density gradients. In the schlieren technique, the beam is focused on a knife edge; the deflected parts of the beam are displaced relative to the knife edge and produce lighter or darker regions when subsequently refocused onto film. With the shadowgraph technique, the parallel beam emerging from the combustion chamber is photographed directly; deflected parts of the beam produce lighter and darker regions on the film. With these techniques, details of flame structure can be discerned.

Figure 9-14 shows a set of photographs from one engine cycle, from a high-speed schlieren movie taken in a special visualization spark-ignition engine operating at 1400 rev/min and 0.5 atm inlet pressure. Also shown are the cylinder pressure versus crank angle data, and the mass fraction burned profile calculated from the pressure data using the method of Rassweiler and Withrow[2] (see Sec. 9.2.2). This engine had a square-cross-section cylinder with two quartz walls to permit easy optical access, but otherwise operated normally.[17] Visualization of

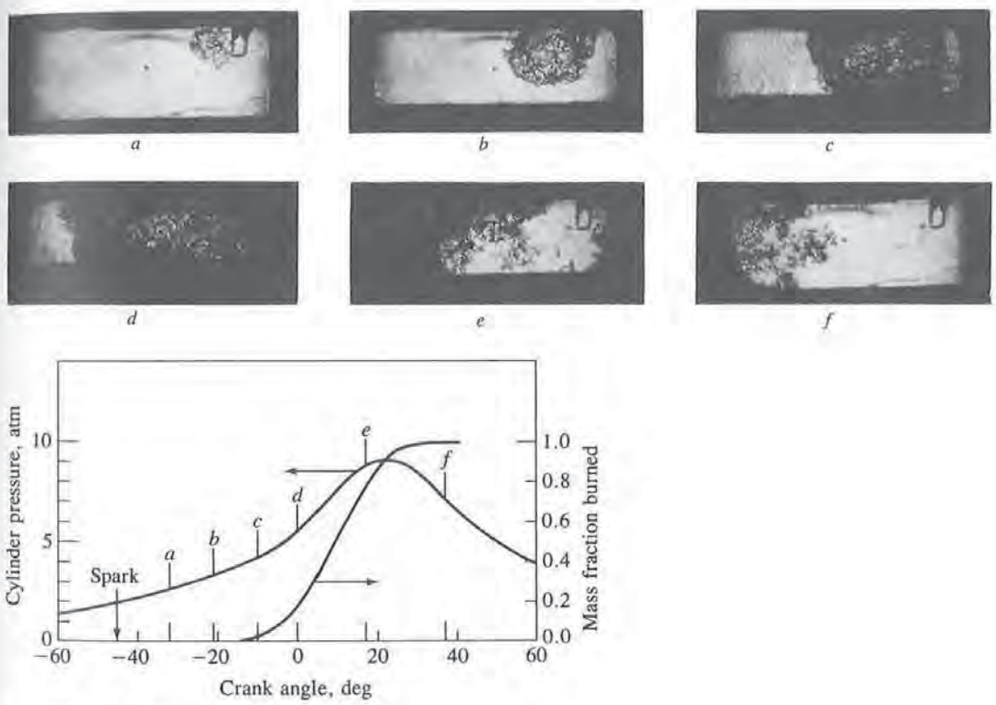


FIGURE 9-14
Sequence of movie frames from one engine cycle in a square-cross-section cylinder, single-cylinder, engine with two glass walls, and corresponding pressure and mass fraction burned curves. 1400 rev/min, 0.5 atm inlet pressure.

PETITIONER'S EXHIBIT 1002
US PATENT NO. 6,581,565

the flame is especially important during the early stages of flame development when the pressure rise due to combustion is too small to be detected.

These photographs show how the flame "ball," roughly spherical in shape, grows steadily from the time of spark discharge. The effect of turbulence is already visible in the convoluted flame surface in Fig. 9-14*a*. The volume enflamed behind the front continues to grow in a roughly spherical manner, except where intersected by the chamber walls, as seen in Fig. 9-14*b* and *c*. The mass fraction burned and the associated pressure rise due to combustion become significant by the time the flame front has traversed two-thirds to three-quarters of the field of view. Note that the fraction of the cylinder filled with enflamed charge is less than is suggested by the photos because the front of the flame is approximately spherical and the cylinder has a square cross section. Maximum cylinder pressure occurs close to the time the flame makes contact with the far wall, as seen in Fig. 9-14*e*. Finally, the unburned mixture ahead of and within the front burns out and the density gradients associated with the flame reaction zone disappear, clearing the field of view as shown in Fig. 9-14*e* and *f*.

A useful relationship between the mass fraction burned, $x_b(=m_b/m)$, and the volume fraction occupied by the burned gas, $y_b(=V_b/V)$, can be obtained from the identities

$$m = m_u + m_b \qquad V = V_u + V_b$$

and the ideal gas law:

$$x_b = \left[1 + \frac{\rho_u}{\rho_b}\left(\frac{1}{y_b} - 1\right)\right]^{-1} \tag{9.29}$$

While the density ratio (ρ_u/ρ_b) does depend on the equivalence ratio, burned gas fraction in the unburned mixture, gas temperature, and pressure, its value is close to 4 for most spark-ignition engine operating conditions. Thus, the plot of x_b against y_b has a universal form,[10] as shown in Fig. 9-15. This curve is an important aid in interpreting flame geometry information.

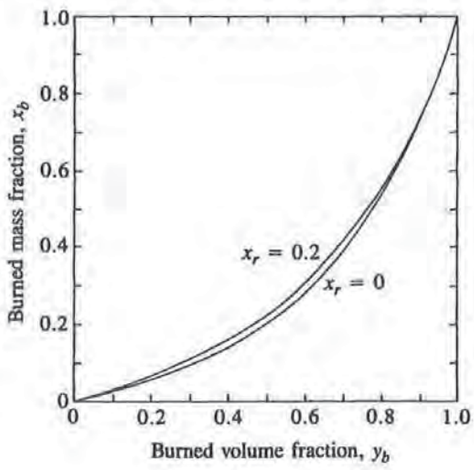


FIGURE 9-15
Relation between mass fraction burned x_b and volume fraction burned y_b. x_r is residual mass fraction.[4]

PETITIONER'S EXHIBIT 1002
US PATENT NO. 6,581,565

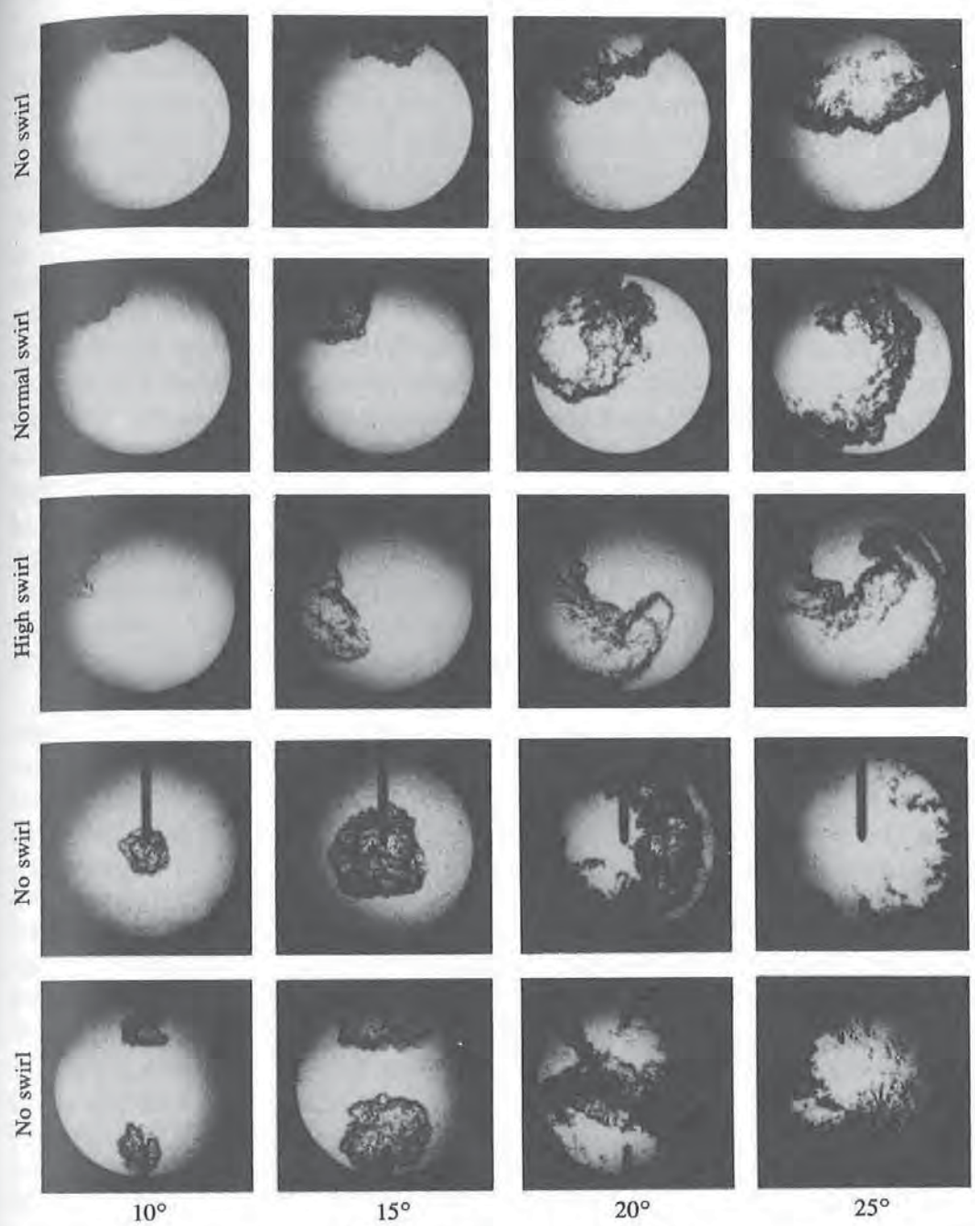


FIGURE 9-16
Laser shadowgraph photographs of engine combustion process taken in single-cylinder engine with transparent cylinder head. From top to bottom: side plug without swirl; side plug with normal swirl; side plug with high swirl; central plug without swirl; two plugs without swirl.[18]

The above-described features of the developing and propagating flame are common to almost all engine geometries and operating conditions. Figure 9-16 shows shadowgraph photographs of the flame at fixed crank angle intervals after ignition, taken through a transparent cylinder head with different geometric and flow configurations.[18] The approximately spherical development of the flame

PETITIONER'S EXHIBIT 1002
US PATENT NO. 6,581,565

from the vicinity of the spark plug, except where it intercepts the chamber walls, is evident for side and center ignition with one plug, and for ignition with two plugs in the absence of any intake generated swirl. With normal levels of swirl, the flame center is convected with the swirling flow, but the flame front as it grows is still approximately spherical in shape. Only with unusually high levels of swirl and aerodynamic stabilization of the flame at the spark plug location does the flame become stretched out and distorted by the flow in a major way.[18]

At any given flame radius, the geometry of the combustion chamber and the spark plug location govern the flame front surface area—the area of the approximately spherical surface corresponding to the leading edge of the flame contained by the piston, cylinder head, and cylinder wall. The larger this surface area, the greater the mass of fresh charge that can cross this surface and enter the flame zone. The photos in Fig. 9-16 illustrate the importance of flame area. The center plug location gives approximately twice the flame area of the side plug geometry at a given flame radius, and burns about twice as fast (the fraction of the cylinder volume enflamed is about twice the size, at a fixed crank angle interval after spark). The arrangement with two spark plugs at opposite sides of the chamber is not significantly different in enflamed volume from the single center plug because, once the flame fronts are intersected by the cylinder wall, the flame front areas are comparable.

Mixture burning rate is strongly influenced by engine speed. It is well established that the duration of combustion in crank angle degrees only increases slowly with increasing engine speed.[19] Figure 9-17 shows how the interval between the spark discharge and 10 percent mass fraction burned, the flame development angle $\Delta\theta_d$, and the interval between the spark and 90 percent mass fraction burned, the overall burning angle $\Delta\theta_d + \Delta\theta_b$ (see Sec. 9.2.3), vary with engine speed.[20] Both intervals increase by a factor of about 1.6 for a factor of 4 increase in engine speed; i.e., the burning rate throughout the combustion process increases almost, though not quite, as rapidly as engine speed. Additionally, at a given engine speed, increasing in-cylinder gas velocities (e.g., with intake generated swirl) increases the burning rate: the flame size for the swirling flows in Fig. 9-16 is larger than for the quiescent case with the same plug location at the crank angle intervals after spark shown. Increasing engine speed and introducing swirl both increase the levels of turbulence in the engine cylinder at the time of combustion (see Sec. 8.2.2). Increased turbulence increases the rate of development and propagation of the turbulent premixed engine flame.

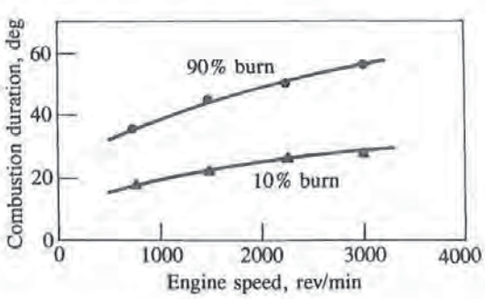


FIGURE 9-17
Effect of engine speed on flame-development angle (0 to 10 percent burned) and overall burning angle (0 to 90 percent burned). $\phi = 1.0$, intake pressure 0.54 atm, spark 30° BTC.[20]

PETITIONER'S EXHIBIT 1002
US PATENT NO. 6,581,565

It is also well established that unburned mixture composition and state affect the burning rate. Reducing the inlet pressure (and maintaining the ratio of exhaust to inlet pressure fixed to hold the residual gas fraction constant) increases both the flame development and rapid burning angles.[19] The fuel/air equivalence ratio affects the burning rate. Both flame development and burning angles show a minimum for slightly rich mixtures ($\phi \approx 1.2$) and increase significantly as the mixture becomes substantially leaner than stoichiometric.[19, 20] The burned gas fraction in the unburned mixture, due to the residual gas fraction *and* any recycled exhaust gases, affects the burning rate: increasing the burned gas fraction slows down both flame development and propagation.[20] Fuel composition changes can be significant also. While mixtures of isooctane or conventional gasolines with air and burned gases (at identical conditions) have closely comparable burning rates, propane, methane, methanol, and ethanol mixtures exhibit modest differences in burning rate and hydrogen-air mixtures substantial differences. The basic combustion chemistry of the fuel, air, burned gas mixture influences the combustion process. However, the relative importance of combustion chemistry effects depends on combustion chamber design and burn rate. Faster burning engines (which have higher turbulence) are less sensitive to changes in mixture composition, pressure, and temperature than are slower burning engines (which have lower turbulence). The effects of chamber geometry, gas motion, and gas composition and state are interrelated.[21]

9.3.2 Flame Structure

Laminar flames in premixed fuel, air, residual gas mixtures are characterized by a laminar flame speed S_L and a laminar flame thickness δ_L (see Sec. 9.3.3). The laminar flame speed is the velocity at which the flame propagates into quiescent premixed unburned mixture ahead of the flame. There are several ways to define the thickness of a laminar flame.[22] Given the molecular diffusivity D_L (see Sec. 4.8), dimensional arguments give the most commonly used definition: $\delta_L = D_L/S_L$. Turbulent flames are also characterized by the root mean square velocity fluctuation, the turbulence intensity u' [Eq. (8.3)], and the various length scales of the turbulent flow ahead of the flame. The integral length scale l_I [Eq. (8.8)] is a measure of the size of the large energy-containing structures of the flow. The Kolmogorov scale l_K [Eq. (8.11)] defines the smallest structures of the flow where small-scale kinetic energy is dissipated via molecular viscosity.

Several dimensionless parameters are used to characterize turbulent premixed flames. The dimensionless parameter used to define the turbulence is the turbulent Reynolds number, $\mathrm{Re}_T = u' l_I/\nu$. For homogeneous and isotropic (no preferred direction) turbulence, the integral and Kolmogorov scales are related by Eq. (8.14): $l_K/l_I = \mathrm{Re}_T^{-3/4}$. A characteristic turbulent eddy turnover time τ_T can be defined as

$$\tau_T = \frac{l_I}{u'}$$

PETITIONER'S EXHIBIT 1002
US PATENT NO. 6,581,565

A characteristic chemical reaction time is the residence time in a laminar flame:

$$\tau_L = \frac{\delta_L}{S_L}$$

The ratio of the characteristic eddy turnover time to the laminar burning time is called the *Damköhler number*:

$$\mathrm{Da} = \frac{\tau_T}{\tau_L} = \left(\frac{l_I}{\delta_L}\right)\left(\frac{S_L}{u'}\right) \tag{9.30}$$

It is an inverse measure of the influence of the turbulent flow on the chemical processes occurring in the flame. Other ratios are of interest. The ratio δ_L/l_K is a measure of the stretch or local distortion to which a laminar flame is subjected by the turbulent flow. Unless $l_I/\delta_L \gg 1$ the concept of a localized flame region has little significance. The ratio u'/S_L is a measure of the relative strength of the turbulence.[22]

Different regimes of turbulent flames are apparent in the plot of Damköhler number versus turbulent Reynolds number in Fig. 9-18.[22] It has been assumed that $D_L \approx \nu$ and that the relationships for homogeneous isotropic turbulence are valid. Two regimes—distributed reactions and reaction sheets—are normally identified. In the distributed reaction regime, chemical reactions proceed in distributed reaction zones and thin-sheet flames do not occur. A sufficient condition for this regime is $l_I \ll \delta_L$. In the reaction sheet regime, propagating reaction fronts are wrinkled and convoluted by the turbulence. A sufficient condition for the existence of reaction sheets is $l_K \gg \delta_L$. For $\mathrm{Re}_T > 1$, there is a region in Fig. 9-18 where $l_I > \delta_L > l_K$: the characteristics of flames in this regime are unclear.

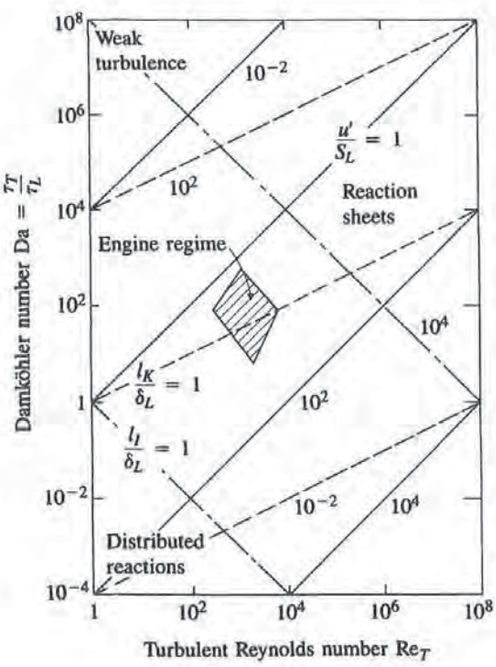


FIGURE 9-18
Different turbulent flame regimes on plot of Damköhler number versus turbulence Reynolds number, u' is turbulence intensity; S_L is laminar flame speed; l_I, l_K, and δ_L are integral scale, Kolmogorov scale, and laminar flame thickness. (*From Abraham* et al.[22])

PETITIONER'S EXHIBIT 1002
US PATENT NO. 6,581,565

Values of Da and Re_T for a typical spark-ignition engine (the cross-hatched region in Fig. 9-18) lie predominantly in the reaction sheet flame regime. Engine operation at high speed (the lower right boundary) and low load (the lower left boundary) gives values of Da and Re_T which fall below the $l_K/\delta_L = 1$ line. This is largely due to the low values of laminar flame speed that result from the high amounts of residual gas and EGR under these conditions (see Sec. 9.3.4 and Fig. 6-19). Whether the flame structure under these conditions is significantly different is not known. Observations of engine flames to date, described below, lie above the $l_K/\delta_L = 1$ line, within the reaction sheet regime. One would expect, then, the structure of the flame in a spark-ignition engine, once developed, to be that of a thin reaction sheet wrinkled and convoluted by the turbulent flow.

Detailed observations have been made of flame structure from ignition to flame extinguishing at the far cylinder wall. A flame develops from the spark discharge which causes ignition as follows. In the initial breakdown phase of ignition, a cylindrical discharge between the spark plug electrodes is established.[23] As electrical energy is fed into the discharge, the arc expands and exothermic chemical reactions capable of sustaining a propagating flame develop. Figure 9-19 shows how this development of a flame kernel occurs, with a set of shadowgraph photographs taken at 40-μs intervals of the spark plug electrode gap in one cylinder of a 2-liter conventional engine. The first photograph is between 20 and 50 μs after the spark breakdown occurred. The complete sequence ($\sim$200 μs) corresponds to 1.3 crank angle degrees. The outer boundary of this developing flame kernel is approximately spherical and is smooth with modest irregularities, corresponding to a thin reaction zone with high-temperature gases inside. As this developing sheetlike flame grows it interacts with the turbulent flow field in the vicinity of the spark plug: the flame outer surface becomes increasingly convoluted and the flame center can be convected away from the plug in a direction and with a velocity that can vary substantially cycle-by-cycle, as seen in Fig. 9-20.[4, 17]

The structure of the flame continues to develop as it propagates across the chamber. Evidence, largely from schlieren photographs and studies of flame structure with laser diagnostics, shows that early in the burning process the flame

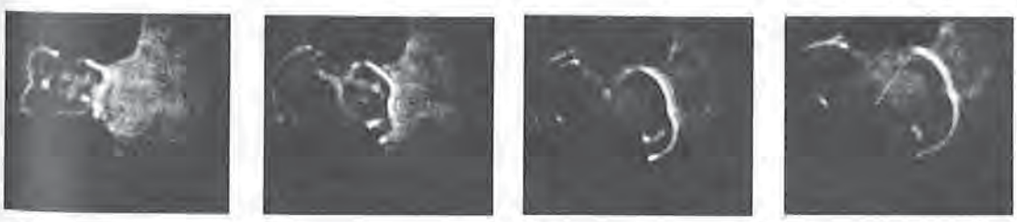


FIGURE 9-19
Shadowgraph photographs of spark-generated kernel between the spark plug electrodes. First photograph on left, 20 to 50 μs after breakdown; 40 μs between photos. Stoichiometric mixture, 1100 rev/min. (*Courtesy A. Douad, Institut Francais du Petrole.*)

PETITIONER'S EXHIBIT 1002
US PATENT NO. 6,581,565

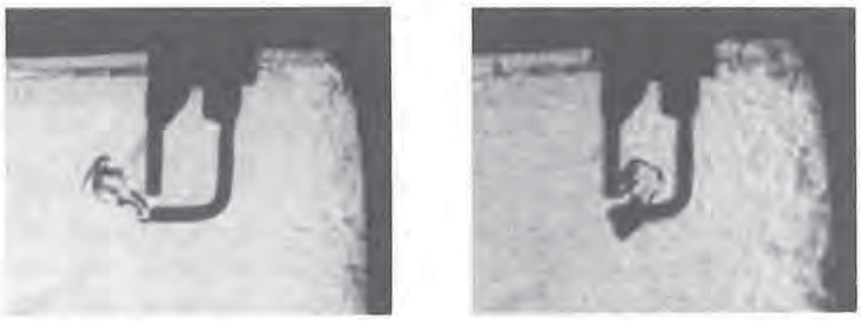


FIGURE 9-20
Schlieren photographs of developing flame, 5° after spark discharge, showing different convection processes in two different cycles. Spark plug wires 0.8 mm diameter. 1400 rev/min; 0.5 atm inlet pressure; propane fuel; $\phi = 0.9$; spark advance 45° BTC.[17]

is a thin, moderately wrinkled but simply connected, front or reaction sheet between unburned and burned gas. The thickness of the front is about 0.1 mm which is comparable to the thickness of a laminar flame under the prevailing conditions. The scale of the wrinkles is typically about 2 mm at engine speeds of 1000 to 2000 rev/min. As the flame propagates across the chamber, the thickness of the reaction sheet front remains roughly constant, the flame front becomes more convoluted, and the scale of the wrinkles tends to decrease with time.[24]

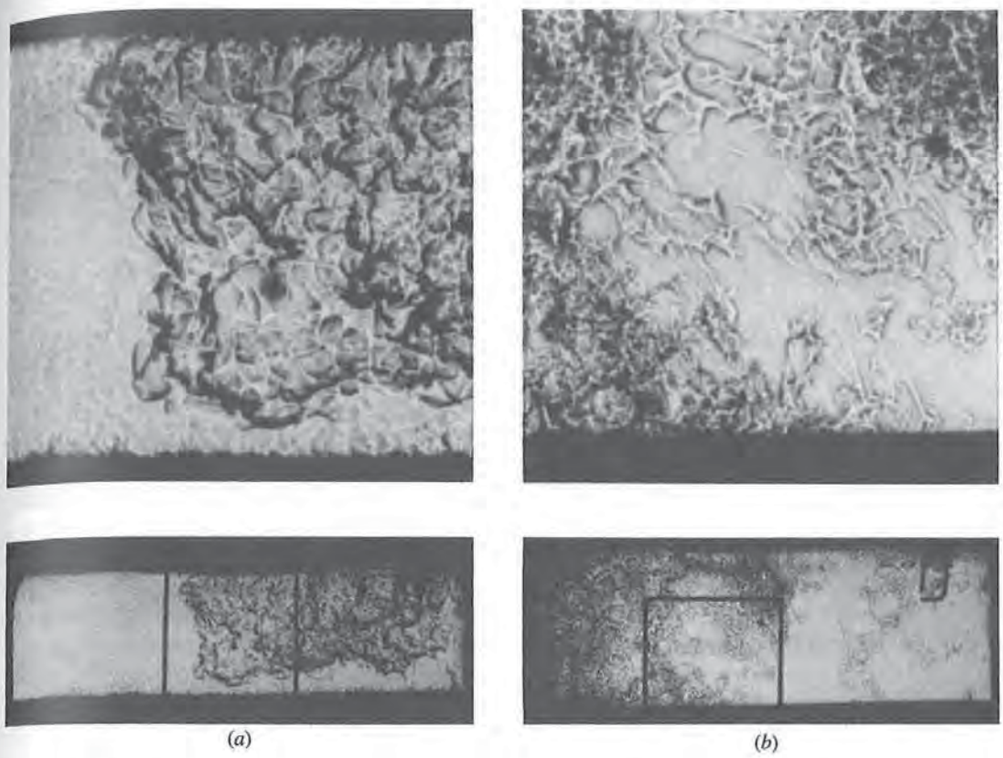
Further evidence that the thin reaction sheet front becomes highly wrinkled and convoluted by the turbulent flow field into a thick turbulent flame "brush" is provided by the schlieren photographs in Fig. 9-21. These show a flame propagating across the combustion chamber of a square-cross-section single-cylinder engine with a special transparent piston crown containing a 13-mm wide channel to isolate a small section of the flame.[25] The flame on the left is for a propane-air mixture; that on the right is hydrogen-air. The energy density per unit volume of mixture and the flow field are comparable for each fuel. The effective thickness of this turbulent flame—the average distance between the region ahead of the flame, where only unburned mixture exists, and the region behind the flame, where only



(*a*) (*b*)

FIGURE 9-21
Schlieren photographs of flame in square-cross-section cylinder engine, with narrow channel in piston crown (at bottom of pictures) which permits observation of 13-mm wide section of flame. (*a*) Propane fuel, spark timing 36° BTC, photograph at 14° ATC, flame thickness ≈ 4.6 mm. (*b*) Hydrogen fuel, spark timing 3° BTC, photograph at 10° ATC, flame thickness ≈ 1.5 mm. Stoichiometric mixtures, 1380 rev/min, 0.5 atm inlet pressure.[25]

PETITIONER'S EXHIBIT 1002
US PATENT NO. 6,581,565



(*a*) (*b*)

FIGURE 9-22
Enlarged schlieren photographs of (*a*) flame front and (*b*) flame back in square-cross-section cylinder engine with two glass side walls. 1400 rev/min, 0.5 atm inlet pressure, propane fuel, $\phi = 0.9$.[17]

burned mixture exists—is apparent.† It was 4 to 5 mm for propane and 1.5 mm for hydrogen. The difference is due to the substantially higher laminar flame speed for the hydrogen, air, burned gas mixture (see Sec. 9.3.4) which increases the Damköhler number and shifts the flame toward the weak-turbulence (i.e., less wrinkled) flame regime in Fig. 9-18.

Additional insight into the structure of the developed engine flame can be obtained by enlarging photographs of the leading and trailing edges of the flame, obtained with the schlieren or shadowgraph technique. Figure 9-22*a* shows the front of the flame 40° after the spark, when it has propagated about halfway across the chamber. It shows the irregular but smoothly curved surfaces which comprise the leading edge of the flame. Figure 9-22*b* shows the back of the flame 70° after the spark, when the front of the flame has just reached the wall of the combustion chamber farthest from the spark plug. It shows large clear regions of burned gas behind the flame and smaller clear regions connected by a lacelike

† These photographs were selected from a large number to give the minimum flame thickness corresponding to the flame front perpendicular to the channel length.

PETITIONER'S EXHIBIT 1002
US PATENT NO. 6,581,565

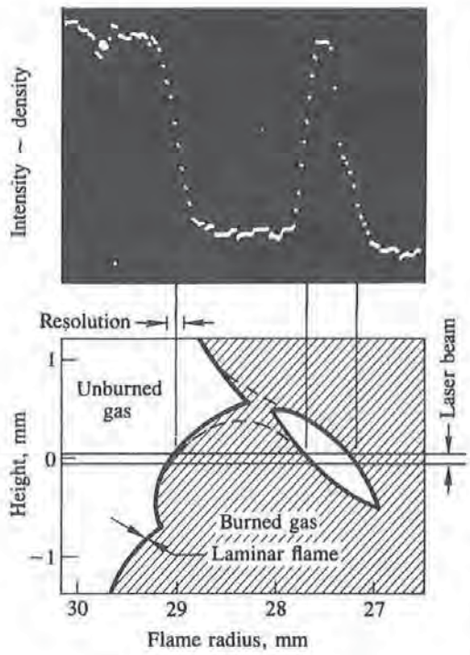


FIGURE 9-23
Upper picture: oscillogram of output of optical multichannel analyzer showing the intensity of light scattered from a narrow laser beam as a function of distance through the flame. Intensity is a measure of gas density. Lower picture: schematic of flame structure corresponding to this signal. 600 rev/min, 1 atm inlet pressure, propane fuel, $\phi = 1.0$.[24]

structure within which the remaining regions of unburned mixture are being consumed.[17] The analogy with a crumpled sheet of paper is appropriate.

Laser scattering experiments, where "snapshots" of the density profile along a laser beam passed through the flame were obtained using Rayleigh scattered light from the gas molecules, provide explicit evidence of this structure.[26] Figure 9-23 shows an oscillogram of the output of the optical analyzer. Each dot represents the intensity of the scattered light which is a measure of the gas density. The signal on the left corresponds to unburned gas. The flame is propagating from right to left. The oscillogram shows a thin transition zone of width 0.25 mm between unburned and burned gas, followed at a distance of 1.5 mm by an "island" of unburned gas. The fraction of oscillograms showing such "islands" varied from 0 at 300 rev/min to 20 percent at 1800 rev/min. An interpretation of this signal consistent with the available photographic evidence is shown underneath.[24]

The above results suggest that increasing engine speed, which increases turbulence levels in the unburned charge, increasingly convolutes and probably multiply-connects the thin reaction sheet flame front. Enlarged schlieren photographs of a 9-mm diameter section of the developed engine flame, viewed normal to the flame surface, indicate that increasing turbulence intensity and decreasing turbulence scales result in increasingly finely wrinkled flame structures. Figure 9-24 shows a set of such photographs, arranged in order of increasing turbulent Reynolds number. Increases in turbulence intensity, which was measured, were achieved by increases in engine speed and by modifying the inlet valve. Relevant parameters for each photograph are given in Table 9.1.

The above theoretical discussion and experimental evidence indicates that

PETITIONER'S EXHIBIT 1002
US PATENT NO. 6,581,565

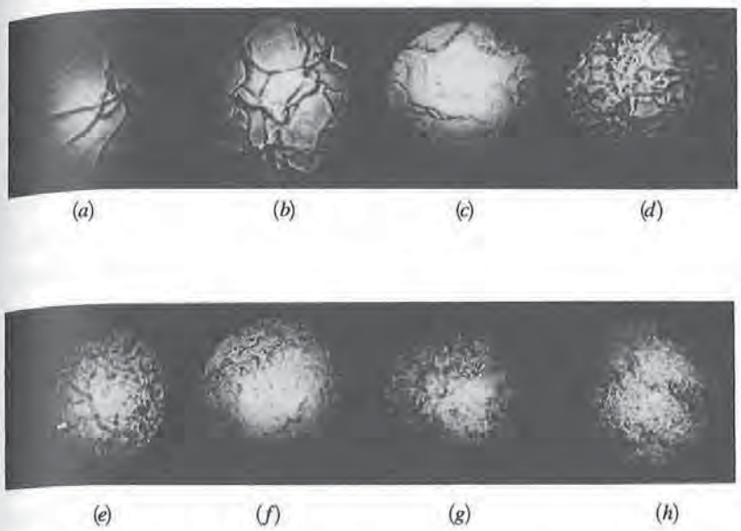


FIGURE 9-24
Shadowgraph photographs, with light beam normal to flame front, of 10-mm diameter section of flame. Photographs, arranged in order of increasing turbulent Reynolds number, suggest this is an appropriate scaling parameter (see Table 9.1).[27]

developed turbulent flames in spark-ignition engines, under normal operating conditions, are highly wrinkled and probably multiply-connected thin reaction sheets. The overall thickness of the turbulent flame "brush," front to back, is of order 1 cm. The thickness of the thin reaction sheet is comparable to estimates of the laminar flame thickness under the prevailing unburned mixture conditions which are of order 0.1 mm. The scale of the wrinkles is of order 1 mm.[24] Direct evidence to date is limited to the low to mid engine speed and low to high engine

TABLE 9.1
Parameters for shadowgraph photographs in Fig. 9-24

Photograph	Engine speed, rev/min	Turbulence intensity, m/s	Valve	Re_M	Re_T
a	300	0.44	S	106	229
b	600	0.88	S	157	503
c	300	1.07	US	173	611
d	900	1.33	S	193	760
e	1200	1.80	S	224	1024
f	600	1.95	US	234	1117
g	900	2.90	US	285	1658
h	1200	4.0	US	333	2263

Note: Valve: S, shrouded; US, unshrouded (produced higher turbulence due to less ordered flow). $Re_M = l_M u'/\nu$; $Re_T = l_I u'/\nu$ (see Sec. 8.2.1).[27]

PETITIONER'S EXHIBIT 1002
US PATENT NO. 6,581,565

load ranges. Whether the structure becomes significantly different at high engine speed is not known. Models of this turbulent flame development and propagation process are reviewed in Chap. 14.

9.3.3 Laminar Burning Speeds

An important intrinsic property of a combustible fuel, air, burned gas mixture is its laminar burning velocity. This burning velocity is defined as the velocity, relative to and normal to the flame front, with which unburned gas moves into the front and is transformed to products under laminar flow conditions. Some details of flame structure help explain the significance of this quantity. A flame is the result of a self-sustaining chemical reaction occurring within a region of space called the flame front where unburned mixture is heated and converted into products. The flame front consists of two regions: a preheat zone and a reaction zone. In the preheat zone, the temperature of the unburned mixture is raised mainly by heat conduction from the reaction zone: no significant reaction or energy release occurs and the temperature gradient is concave upward ($\partial^2 T/\partial x^2 > 0$). Upon reaching a critical temperature, exothermic chemical reaction begins. The release of chemical energy as heat results in a zone where the temperature gradient is concave downward ($\partial^2 T/\partial x^2 < 0$). The region between the temperature where exothermic chemical reaction begins and the hot boundary at the downstream equilibrium burned gas temperature is called the reaction zone. The thicknesses of the preheat and reaction zones can be calculated for one-dimensional flames from conservation equations of mass and energy. The thickness of the preheat zone $\delta_{L,\,\mathrm{ph}}$ is

$$\delta_{L,\,\mathrm{ph}} = \frac{4.6\bar{k}}{\bar{c}_p \rho_u S_L} \tag{9.31}$$

where $\bar{k}$ and $\bar{c}_p$ are the mean thermal conductivity and specific heat at constant pressure in the preheat zone and S_L is the laminar burning velocity.[28] Thus, the factors which govern the laminar burning velocity of a specific unburned mixture—the velocity at which this flame structure propagates relative to the unburned gas ahead of it—are the temperature and species concentration gradients within the flame and the mixture transport and thermodynamic properties.

Laminar burning velocities at pressures and temperatures typical of unburned mixture in engines are usually measured in spherical closed vessels by propagating a laminar flame radially outward from the vessel center. The laminar burning velocity is then given by

$$S_L = \frac{dm_b/dt}{A_f \rho_u} \tag{9.32}$$

where the mass burning rate is determined from the rate of pressure rise in the vessel and A_f is the flame area. Because the laminar flame thickness [e.g., given by Eq. (9.31)] under engine conditions is of order 0.2 mm[26] and is therefore much less than characteristic vessel dimensions, in applying Eq. (9.32) the flame can be

PETITIONER'S EXHIBIT 1002
US PATENT NO. 6,581,565

treated as negligibly thin. Laminar burning velocities for methane, propane, isooctane, methanol, gasoline, and hydrogen—premixed with air—at pressures, temperatures, and equivalence ratios which occur in engines have been measured using this technique.[29–33] Also, the effect of a burned gas diluent on laminar burning velocity with gasoline-air mixtures has been determined.[32] Correlations derived from these data are the most accurate means available for estimating laminar burning velocities for mixtures and conditions relevant to spark-ignition engines.

The effect of the mixture fuel/air equivalence ratio on laminar burning velocity for several hydrocarbon fuels and methanol is shown in Fig. 9-25. The burning velocity peaks slightly rich of stoichiometric for all the fuels shown. The values for isooctane and gasoline are closely comparable. Data at higher pressures and temperatures have been fitted to a power law of the form:

$$S_L = S_{L,0}\left(\frac{T_u}{T_0}\right)^{\alpha}\left(\frac{p}{p_0}\right)^{\beta} \tag{9.33}$$

where $T_0 = 298$ K and $p_0 = 1$ atm are the reference temperature and pressure, and $S_{L,0}$, α, and β are constants for a given fuel, equivalence ratio, and burned gas diluent fraction. For propane, isooctane, and methanol, these constants can be represented by

$$\alpha = 2.18 - 0.8(\phi - 1) \tag{9.34a}$$

$$\beta = -0.16 + 0.22(\phi - 1) \tag{9.34b}$$

and

$$S_{L,0} = B_m + B_\phi(\phi - \phi_m)^2 \tag{9.35}$$

where ϕ_m is the equivalence ratio at which $S_{L,0}$ is a maximum with value B_m.

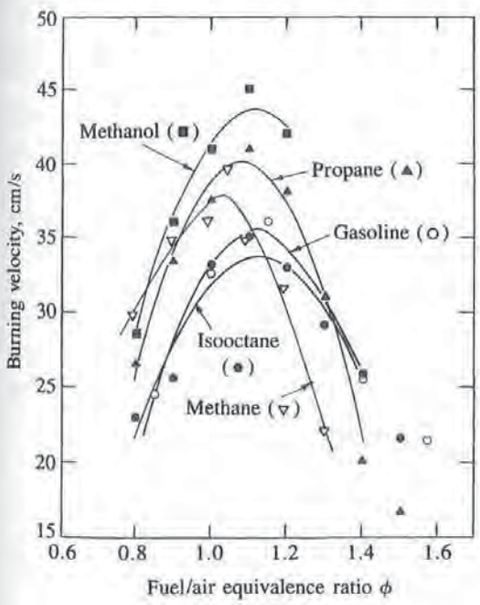


FIGURE 9-25
Laminar burning velocity for several fuels as function of equivalence ratio, at 1 atm and 300 K. Lines are least-squares polynomial fits to data.[29, 30]

PETITIONER'S EXHIBIT 1002
US PATENT NO. 6,581,565

TABLE 9.2
Parameters ϕ_m, B_m, and B_ϕ for Eq. (9.35)

Fuel	ϕ_m	B_m, cm/s	B_ϕ, cm/s	Ref.
Methanol	1.11	36.9	−140.5	30
Propane	1.08	34.2	−138.7	30
Isooctane	1.13	26.3	−84.7	30
Gasoline	1.21	30.5	−54.9	32

Note: Values of $S_{L,0}$ given by Eq. (9.35) are obtained from least-squares fits of Eq. (9.33) to data over the range $p = 1$–8 atm, $T_u = 300$–700 K. They do not correspond exactly to the laminar flame speed data at 1 atm and 298 K in Fig. 9-25.

Values of ϕ_m, B_m, and B_ϕ are given in Table 9.2.[30] For gasoline (a reference gasoline with average molecular weight of 107 and an H/C ratio of 1.69) additional data were available and were correlated by[32]

$$\alpha_g = 2.4 - 0.271\phi^{3.51} \tag{9.36a}$$

$$\beta_g = -0.357 + 0.14\phi^{2.77} \tag{9.36b}$$

For methane, simple equations such as (9.34*a*, *b*) do not adequately correlate the data over the range of p and T_u relevant to engines. However, laminar burning velocity data from a spherical constant-volume bomb experiment have been obtained along an unburned gas isentropic path, as the pressure in the bomb rises during combustion. Variation in laminar burning velocity along such unburned gas isentropes does correlate with a power law:

$$S_{L,s} = S_{L,0}\left(\frac{\rho_u}{\rho_{u0}}\right)_s^{\varepsilon} \tag{9.37}$$

Values for $S_{L,0}$ and ε from the literature are summarized in Table 9.3.

TABLE 9.3
Parameters for methane-air laminar burning velocity correlation [Eq. (9.37)]

ϕ	p_i, atm	$S_{L,0}$,† cm/s	ε	Ref.
1.0	0.5	49	0.51	31
1.0	1.0	35	0.2	31
0.8–1.2	1–8	‡	0.17–0.19	33

† At 298 K initial temperature.
‡ See Fig. 9-25.

PETITIONER'S EXHIBIT 1002
US PATENT NO. 6,581,565

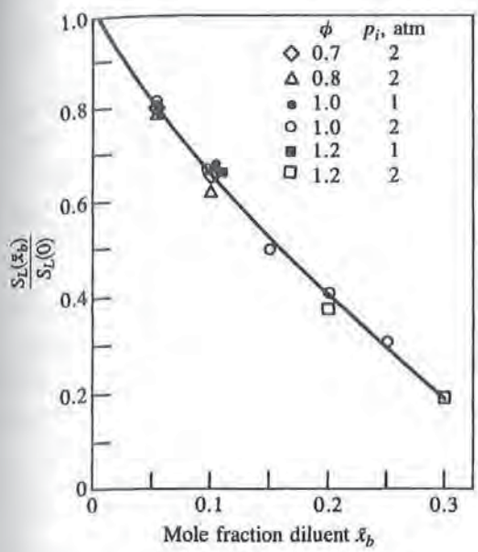


FIGURE 9-26
Effect of burned gas mole fraction $\tilde{x}_b$ in unburned mixture on laminar burning velocity. Fuel: gasoline.[32]

The presence of burned gas in the unburned cylinder charge due to residual gases and any recycled exhaust gases causes a substantial reduction in the laminar burning velocity. Any burned gas in the unburned mixture reduces the heating value per unit mass of mixture and, thus, reduces the adiabatic flame temperature. It acts as a diluent. The effect of increasing burned gas or diluent fraction on laminar flame speed is shown in Fig. 9-26. The diluent used was a mixture of CO_2 and N_2, chosen to match the heat capacity of actual gasoline-air combustion products.† The proportional reduction in laminar burning velocity is essentially independent of the unburned mixture equivalence ratio, pressure, and temperature over the range of interest in engines. The data in Fig. 9-26 are correlated by the relation:

$$S_L(\tilde{x}_b) = S_L(\tilde{x}_b = 0)(1 - 2.06\tilde{x}_b^{0.77}) \tag{9.38}$$

where $\tilde{x}_b$ is the mole fraction of burned gas diluent. Other studies corroborate the magnitude of this burned gas effect.[32]

Note that for equal heat capacity added to the unburned mixture, burned gases have a much larger effect on laminar burning velocity than does excess air. For example, the laminar burning velocity of a stoichiometric mixture as it is leaned to $\phi = 0.8$ is reduced by 23 percent. The excess air required has a heat capacity of about 0.2 times that of the combustion products of the undiluted mixture. Adding the same heat capacity by adding stoichiometric burned gases (which requires a burned gas mole fraction of 0.175) reduces the laminar burning

† The water in actual residual and exhaust gas was omitted. A mixture of 80 percent N_2 and 20 percent CO_2, by volume, was used.

PETITIONER'S EXHIBIT 1002
US PATENT NO. 6,581,565

velocity by 55 percent.[32] Proper allowance for the burned gas fraction in estimating laminar burning velocities for spark-ignition engines is most important.

The above correlations define the laminar burning velocity as a function of unburned mixture thermodynamic properties and composition, only. It has been assumed that flame thickness and curvature effects are negligible.[28] Our interest in laminar burning velocity is twofold: first, it is used to define the characteristic chemical reaction time of the mixture in Eq. (9.30); second, a presumed consequence of the wrinkled thin-reaction-sheet turbulent-flame structure is that, locally, the sheet propagates at the laminar burning velocity. The above correlations adequately characterize a quiescent burning process. However, laminar flame propagation can be influenced by the local flow field in the unburned gas. If the flame thickness is less than the Kolmogorov scale, the primary effect is one of straining which affects both the flame area (usually referred to as flame stretching for an area increase) and the local (laminar) burning velocity. While this problem is not yet well understood, it is known that straining can affect the laminar burning velocity and can cause flame extinction. The laminar burning velocity decreases with increasing strain rate, and the Lewis number of the unburned mixture has a significant influence on this rate of decrease. The Lewis number is the ratio of diffusivities of heat and mass. For stoichiometric mixtures it is close to one; it increases above about unity as the unburned fuel-air mixture is leaned out. Thus the local flow field may have a discernable effect on the local burning velocity of the thin laminarlike reaction-sheet flame, especially for lean or dilute mixtures.[34]

9.3.4 Flame Propagation Relations

If the heat-release or mass burning rate analysis of Sec. 9.2.2 is coupled with an analysis of flame geometry data, substantial additional insight into the behavior of spark-ignition engine flames is obtained. Flame photographs (such as those in Figs. 9-1, 9-14, and 9-16 and Refs. 4 and 35) effectively define the position of the front or leading edge of the turbulent engine flame. The "shadow" of the enflamed zone, under normal engine conditions, is close to circle: only in the presence of very high swirl does substantial distortion of the flame shape occur.[18] Thus, to a good approximation, the surface which defines the leading edge of the turbulent flame (ahead of which only unburned mixture exists) is a portion of the surface of a sphere. Figure 9-27 indicates the geometrical parameters which define this flame surface: r_c, α_c, z_c, the coordinates of the flame center; r_f, the radius of the best-fit circle to the flame front silhouette; and the geometry of the combustion chamber walls. The flame is initiated at the spark plug; however, it may move away from the plug during the early stages of its development as shown. We define the *flame front area* A_f as the spherical surface of radius r_f coinciding with the leading edge of the flame contained within the combustion chamber, and the *enflamed volume* V_f as the volume within the chamber behind this flame front.

The thermodynamic analysis of cylinder pressure data allows us to define additional geometrical parameters. The *burned gas radius* r_b is the radius of the

PETITIONER'S EXHIBIT 1002
US PATENT NO. 6,581,565

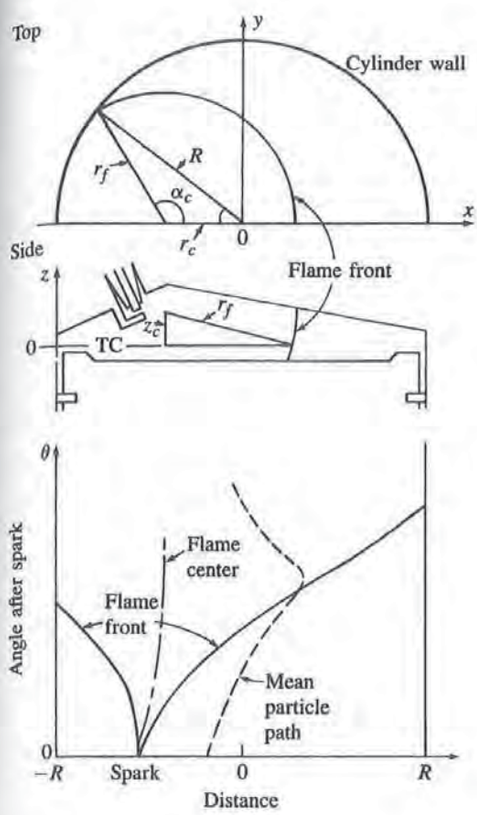


FIGURE 9-27
Schematic of spherical flame front in engine combustion chamber identifying parameters which define flame geometry. (*From Beretta* et al.[4])

spherical surface within the combustion chamber which would contain all the burned gas behind it; i.e.,

$$V_b(r_b, r_c, \alpha_c, z_c) = V_b(p, \theta) \tag{9.39}$$

The *spherical burning area* A_b is the area of this spherical surface; i.e.,

$$A_b = \frac{\partial V_b(r_b, r_c, \alpha_c, z_c)}{\partial r_b} \tag{9.40}$$

The *laminar burning area* A_L is the surface area the flame would have if it burned at the laminar flame speed, i.e.,

$$A_L = \frac{dm_b/dt}{\rho_u S_L} \tag{9.41}$$

where S_L is the laminar flame speed in the unburned mixture ahead of the flame (see Sec. 9.3.3).

Several velocities can be defined. The *mean expansion speed* of the front u_f is given by

$$u_f = \frac{dA_S/dt}{L_S} \tag{9.42}$$

PETITIONER'S EXHIBIT 1002
US PATENT NO. 6,581,565

where A_S is the "shadow" area enclosed by the "best-fit" circle through the leading edge of the flame and

$$L_S = \frac{\partial A_S}{\partial r_f}$$

is the arc length within the chamber of this "best-fit" circle. The *mean expansion speed* of the *burned gas* u_b is

$$u_b = \frac{\partial V_b/\partial t}{A_b} \tag{9.43}$$

This derivative is taken with the piston position fixed since only burned volume changes due to combustion are of interest. The *burning speed* S_b is defined by

$$S_b = \frac{dm_b/dt}{\rho_u A_b} \tag{9.44}$$

The *mean gas speed* just ahead of the flame front u_g is

$$u_g = u_b - S_b \tag{9.45}$$

Note that combining Eqs. (9.41) and (9.44) gives the relation

$$S_b A_b = S_L A_L \tag{9.46}$$

Also, it follows from Eqs. (9.29), (9.43), and (9.44) that

$$\frac{u_b}{S_b} = \frac{\rho_u}{\rho_b}(1 - y_b) + y_b = \frac{\rho_u/\rho_b}{[(\rho_u/\rho_b) - 1]x_b + 1} \tag{9.47}$$

As x_b and $y_b \to 0$, u_b/S_b approaches the expansion ratio ρ_u/ρ_b. As x_b and $y_b \to 1$, u_b/S_b approaches unity.

The variation of the above quantities during the engine combustion process, coupled with the photographs and discussion in Sec. 9.3.2, provide substantial insight into the flame development and propagation process. Figure 9-28 shows results from an analysis of cylinder pressure data and the corresponding flame front location information (determined from high-speed movies through a window in the piston) of several individual engine operating cycles. The combustion chamber was a typical wedge design with a bore of 102 mm and a compression ratio of 7.86. The flame radius initially grows at a rate that increases with time and exhibits substantial cycle-by-cycle variation in its early development (Fig. 9-28*a*). Later ($r_f \gtrsim 30$ mm) the growth rate, which approximates the expansion speed u_b, reaches an essentially constant value. The flame radius r_f is initially equal to the burned gas radius r_b; it increases above r_b as the flame grows and becomes increasingly distorted by the turbulent flow field (Fig. 9-28*b*). Eventually $r_f - r_b$ goes to an essentially constant value of about 6 mm for $r_b \gtrsim 30$ mm. This difference, $r_f - r_b$, is approximately half the thickness of the turbulent flame brush.

PETITIONER'S EXHIBIT 1002
US PATENT NO. 6,581,565

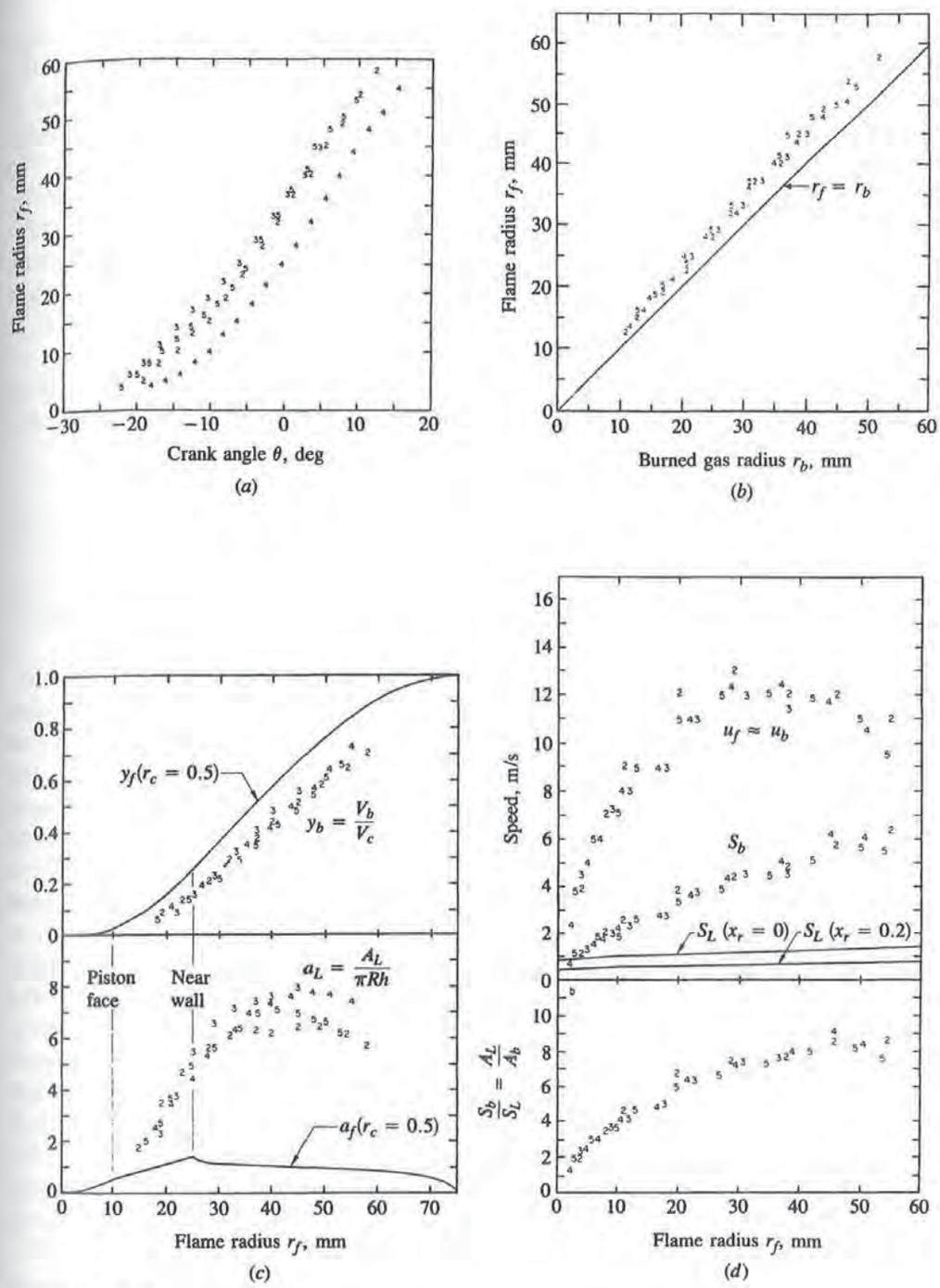


FIGURE 9-28
Variation of flame geometry and velocity parameters during four individual combustion cycles at 1044 rev/min, $\phi = 0.98$, 1 atm inlet pressure: (*a*) flame radius r_f versus crank angle; (*b*) flame radius r_f versus burned gas radius r_b; (*c*) normalized enflamed volume y_f, burned volume y_b, normalized flame front area a_f, and laminar area a_L versus flame radius; (*d*) front expansion speed u_b, burning speed S_b, and laminar flame speed S_L versus flame radius. (*From Beretta* et al.[4])

PETITIONER'S EXHIBIT 1002
US PATENT NO. 6,581,565

Normalized enflamed and burned volumes, and flame front area and laminar burning area, are shown in Fig. 9-28*c*. Volumes are normalized by the cylinder volume, and areas by πRh, where h is the average clearance height and R the cylinder radius. Discontinuities occur in the flame area a_f at the points where the flame front contacts first the piston face and then the near cylinder wall. The laminar area A_L is initially close to the flame area A_f and then increases rapidly as the flame grows beyond 10 mm in radius. During the rapid burning combustion phase ($y_f \gtrsim 0.2$) the value of y_f is significantly greater than y_b. During this phase, the laminar area exceeds the flame area by almost an order of magnitude. These observations indicate the existence of substantial pockets of unburned mixture behind the leading edge of the flame.[4]

The ratio of the volume of the unburned mixture within the turbulent flame zone ($V_f - V_b$) to the reaction-sheet area within the flame zone ($A_L - A_f$) defines a characteristic length

$$l_T = \frac{V_f - V_b}{A_L - A_f} \tag{9.48}$$

which can be thought of as the scale of the pockets of unburned mixture within the flame. For the data set of Fig. 9-28, l_T is approximately constant and of order 1 mm.[24]

These flame geometry results would be expected from the previous photographic observations of how the flame grows from a small approximately spherical smooth-surfaced kernal shortly after ignition to a highly wrinkled reaction-sheet turbulent flame of substantial overall thickness. Initially, the amount of unburned gas within the enflamed volume is small. During the rapid burning phase of the combustion process, however, a significant fraction (some 25 percent; see Fig. 9-2) of the gas entrained into the flame zone is unburned.

The front expansion speed u_f, burning speed S_b, and laminar flame speed S_L are shown in Fig. 9-28*d*. The expansion speed increases as the flame develops to a maximum value that is several times the mean piston speed of 3.1 m/s and is comparable to the mean flow velocity through the inlet valve of 18 m/s.[24] The burning speed increases steadily from a value close to the laminar flame speed at early times to almost an order of magnitude greater than S_L during the rapid burning phase. During this rapid burning phase, since $(r_f - r_b)$ is approximately constant, the flame front expansion speed and the mean burned gas expansion speed are essentially equal. The difference between $u_b \approx u_f$ and S_b is the unburned gas speed u_g just ahead of the flame front. Note that the ratio u_f/S_b ($\approx u_b/S_b$) decreases monotonically from a value equal to the expansion ratio (ρ_u/ρ_b) at spark to unity as the flame approaches the far wall, as required by Eq. (9.47).

The effect of flame propagation on the flow field in the unburned mixture ahead of the flame is important because it is the turbulence just ahead of the flame that determines the local burning velocity. Measurements of mean velocities, rms fluctuation velocities, and turbulence intensities have been made using laser doppler anemometry (see Sec. 8.2.2) at different locations within engine combustion chambers (e.g., Refs. 36 and 37). Such data are difficult to interpret

PETITIONER'S EXHIBIT 1002
US PATENT NO. 6,581,565

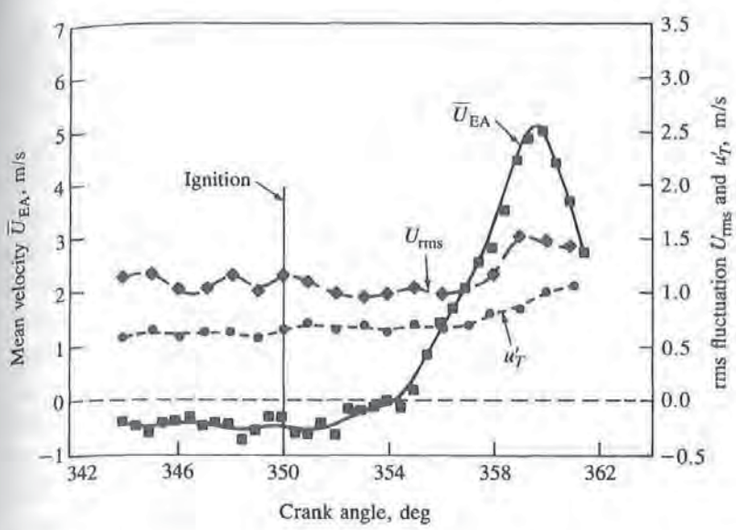


FIGURE 9-29
Laser doppler anemometer measurements of ensemble-averaged mean velocity $\bar{U}_{EA}$ [Eq. (8.20)], rms fluctuation in individual-cycle mean velocity U_{rms} [Eq. (8.21)] and turbulence intensity u'_T [Eq. (8.22)], close to the cylinder axis, from before ignition to after flame arrival. Disc-shaped chamber, spark plug in cylinder wall, measurement at $x/B = 0.57$, $B = 76$ mm, 300 rev/min. $\bar{S}_p = 0.83$ m/s.[36]

because the mean flow varies cycle-by-cycle, the turbulence is not homogeneous, and the flame motion and shape show substantial cyclic variations. The results in Fig. 9-29 were taken in a special single-cylinder engine with a disc-shaped combustion chamber where the spark plug was located in the cylinder liner. Shown are the ensemble-averaged mean velocity, cyclic variation in mean velocity, and the turbulence intensity, normal to the front, during the major portion of the combustion process, close to the chamber center.

The mean velocity normal to the front increases steadily from shortly after ignition, as the combustion-produced gas expansion displaces unburned mixture toward the wall. It peaks as the flame arrives at the measurement location. The cyclic variation in mean velocity and the turbulence intensity normal to the front remain essentially constant until a few degrees before the flame arrival. These two quantities are comparable in magnitude; thus the turbulence intensity is lower than the rms fluctuation velocity (in this case by about a factor of 2) (see Sec. 8.2.2). Whether the increase in turbulence as the flame approaches is due to rapid distortion resulting from the compression of the unburned mixture which occurs during combustion or is the result of inadequate resolution of cycle-to-cycle flow variations is unclear. Rapidly imposed distortions of a turbulent flow field, such as those imposed by combustion-produced gas expansion, would lead to an increase in vorticity and turbulence intensity. Other studies, e.g., Ref. 37, indicate there is little or no increase in turbulence intensity ahead of the flame.

The variation of burning speed with engine speed has also been carefully examined in a study where flame position was determined from high-speed movies, mass burning rates from cylinder pressure, and turbulence information

PETITIONER'S EXHIBIT 1002
US PATENT NO. 6,581,565

from experiments at equivalent motored conditions.[35] The turbulence quantity obtained during motoring experiments was the ensemble-averaged root mean square velocity fluctuation defined by Eq. (8.18). Values of S_b/S_L and u'_F/S_L were determined at two points in the combustion process: at a flame radius of 30 mm (the end of the flame development process) and at mass fraction burned equal to 0.5 (halfway through the rapid burning phase). To correct the motored turbulence data for the higher pressure levels corresponding to engine firing conditions, a simple rapid distortion model (see Sec. 14.4.2) based on conservation of angular momentum in turbulent eddies was used. A linear correlation between S_b and u'_F results, as shown in Fig. 9-30, for the rapid burning combustion phase. Note that as u'_F/S_L goes to zero, S_b/S_L approaches a value close to unity.

Once the flame front reaches the far cylinder wall (see Fig. 9-27) the front can no longer propagate: however, combustion continues behind the front until all the unburned mixture entrained into the enflamed region is consumed. This final burning or termination phase of the combustion process can be approximated by an exponential decay in the mass burning rate with a characteristic time constant τ_b of order 1 ms. Since these "islands" or "pockets" of unburned mixture behind the leading edge of the flame have a characteristic scale l_T based on the laminar flame area [Eqs. (9.41) and (9.48)], it follows that

$$l_T = \tau_b S_L \tag{9.49}$$

In summary, the above flame data analysis procedures show that the relationships between r_f and r_b, V_f and V_b, A_f and A_L, u_f, S_b and S_L are distinctly different in the three phases of combustion: (1) the development phase, where a highly wrinkled reaction-sheet "thick"-overall turbulent flame evolves from the essentially spherical flame kernal established by the spark discharge; (2) the rapid-burning phase, where this thick "developed" turbulent flame propagates across the combustion chamber to the far wall, during which most of the mass is burned; and (3) the termination phase after the flame front has reached the far wall and propagation of the front is no longer possible, when the remaining unburned mixture within the flame burns up. The burning velocity, in the rapid-burning phase of the combustion process, scales with turbulence intensity, which in turn scales with engine speed.

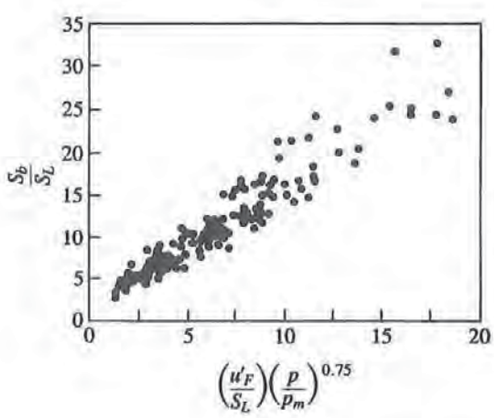


FIGURE 9-30
Variation of burning speed with turbulence intensity. The ensemble-averaged rms velocity fluctuation was measured during motoring engine operation. The ratio p/p_m (firing pressure/motoring pressure) corrects for the effect of additional compression on the turbulence intensity. Range of engine speeds and spark timings.[35]

PETITIONER'S EXHIBIT 1002
US PATENT NO. 6,581,565

9.4 CYCLIC VARIATIONS IN COMBUSTION, PARTIAL BURNING, AND MISFIRE

9.4.1 Observations and Definitions

Observation of cylinder pressure versus time measurements from a spark-ignition engine, for successive operating cycles, shows that substantial variations on a cycle-by-cycle basis exist. Since the pressure development is uniquely related to the combustion process, substantial variations in the combustion process on a cycle-by-cycle basis are occurring. In addition to these variations in each individual cylinder, there can be significant differences in the combustion process and pressure development between the cylinders in a multicylinder engine. Cyclic variations in the combustion process are caused by variations in mixture motion within the cylinder at the time of spark cycle-by-cycle, variations in the amounts of air and fuel fed to the cylinder each cycle, and variations in the mixing of fresh mixture and residual gases within the cylinder each cycle, especially in the vicinity of the spark plug. Variations between cylinders are caused by differences in these same phenomena, cylinder-to-cylinder.

Cycle-by-cycle variations in the combustion process are important for two reasons. First, since the optimum spark timing is set for the "average" cycle, faster-than-average cycles have effectively overadvanced spark-timing and slower-than-average cycles have retarded timing, so losses in power and efficiency result. Second, it is the extremes of the cyclic variations that limit engine operation. The fastest burning cycles with their overadvanced spark timing are most likely to knock. Thus, the fastest burning cycles determine the engine's fuel octane requirement and limit its compression ratio (see Sec. 9.6.3). The slowest burning cycles, which are retarded relative to optimum timing, are most likely to burn incompletely. Thus these cycles set the practical lean operating limit of the engine or limit the amount of exhaust gas recycle (used for NO emissions control) which the engine will tolerate. Due to cycle-by-cycle variations, the spark timing and average air/fuel ratio must always be compromises, which are not necessarily the optimum for the average cylinder combustion process. Variations in cylinder pressure have been shown to correlate with variations in brake torque which directly relate to vehicle driveability.

An example of the cycle-by-cycle variations in cylinder pressure and the variations in mixture burning rate that cause them are shown in Fig. 9-31. Pressure and gross heat-release rate [calculated from the cylinder pressure using Eq. (9.27)] for several successive cycles at a mid-load, mid-speed point are shown as a function of crank angle. The maximum heat-release rate and the duration of the heat release or burning process vary by a factor of two from the slowest to the fastest burning cycle shown. The peak cylinder pressure varies accordingly. The faster burning cycles have substantially higher values of maximum pressure than do the slower burning cycles; with the faster burning cycles peak pressure occurs closer to TC.

The heat-release rate data in Fig. 9-31 show that there are cycle-by-cycle variations in the early stages of flame development (from zero to a few percent of

PETITIONER'S EXHIBIT 1002
US PATENT NO. 6,581,565

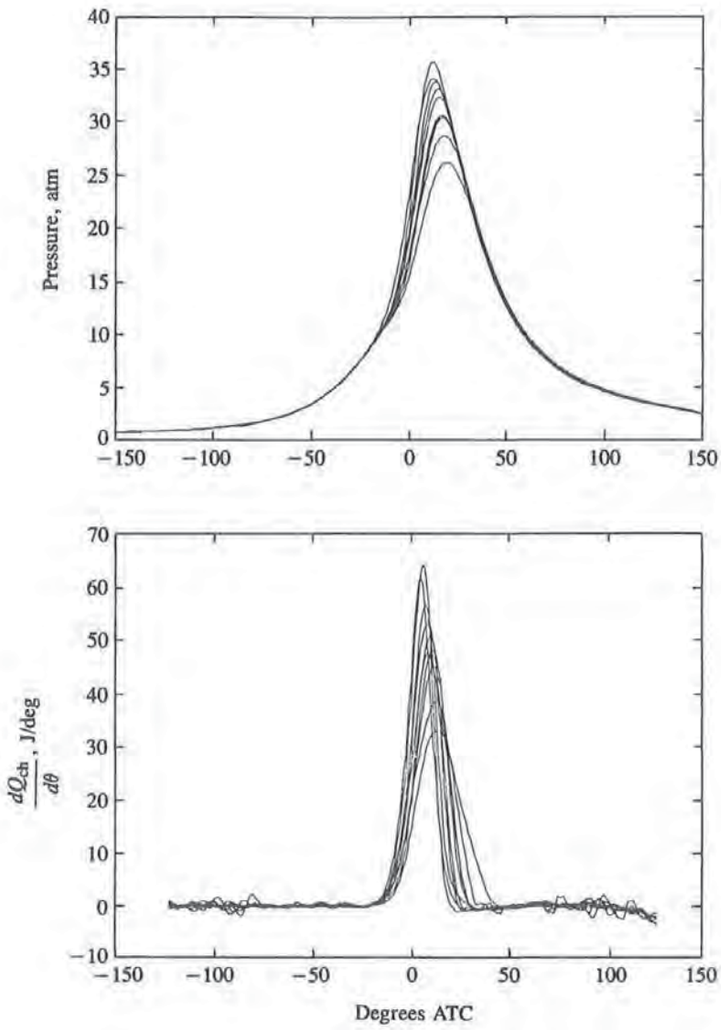


FIGURE 9-31
Measured cylinder pressure and calculated gross heat-release rate for ten cycles in single-cylinder spark-ignition engine operating at 1500 rev/min, $\phi = 1.0$, $p_{inlet} = 0.7$ atm, MBT timing 25° BTC.[14]

the total heat release) and in the major portion of the combustion process—the rapid-burning phase—indicated by the variations in the maximum burning rate.

As the mixture becomes leaner with excess air or more dilute with a higher burned gas fraction from residual gases or exhaust gas recycle, the magnitude of cycle-by-cycle combustion variations increases. Eventually, some cycles become sufficiently slow burning that combustion is not completed by the time the exhaust opens: a regime where *partial burning* occurs in a fraction of the cycles is encountered. For even leaner or more dilute mixtures, the *misfire* limit is reached. At this point, the mixture in a fraction of the cycles fails to ignite. While spark-ignition engines will continue to operate with a small percentage of the cycles in the partial-burn or misfire regimes, such operation is obviously undesirable from

PETITIONER'S EXHIBIT 1002
US PATENT NO. 6,581,565

the point of efficiency, hydrocarbon emissions, torque variations, and roughness. The partial-burn and misfire regimes are discussed in Sec. 9.4.3.

Various measures of cycle-by-cycle combustion variability are used. It can be defined in terms of variations in the cylinder pressure between different cycles, or in terms of variations in the details of the burning process which cause the differences in pressure. The following quantities have been used:

1. *Pressure-related parameters.* The maximum cylinder pressure p_{max}; the crank angle at which this maximum pressure occurs θ_{pmax}; the maximum rate of pressure rise $(dp/d\theta)_{max}$; the crank angle at which $(dp/d\theta)_{max}$ occurs; the indicated mean effective pressure [which equals $\int p\, dV/V_d$, see Eqs. (2.14), (2.15), and (2.19)].
2. *Burn-rate-related parameters.* The maximum heat-release rate (net or gross, see Sec. 9.2.2); the maximum mass burning rate; the flame development angle $\Delta\theta_d$ and the rapid burning angle, $\Delta\theta_b$ (see Sec. 9.2.3).
3. *Flame front position parameters.* Flame radius, flame front area, enflamed or burned volume, all at given times; flame arrival time at given locations.

Pressure-related quantities are easiest to determine; however, the relation between variations in combustion rate and variations in cylinder pressure is complex.[38] Equation (9.26) defines the factors that govern this relationship. Because the rate of change of pressure is substantially affected by the rate of change of cylinder volume as well as rate of burning, changes in the phasing of the combustion process relative to TC (e.g., which result from changes in flame development angle) as well as changes in the shape and magnitude of the heat-release rate profile affect the pressure. Figure 9-32 illustrates how the magnitude of the maximum cylinder pressure p_{max} and the crank angle at which it occurs θ_{pmax} vary as the crank angle at which combustion effectively starts (e.g., θ at which 1 percent of the cylinder mass has burned) and the burning rate are varied. Curve $CABE$ shows how p_{max} and θ_{pmax} vary for a fixed fast-burning heat-release profile (the duration of the heat-release process and its maximum value are held

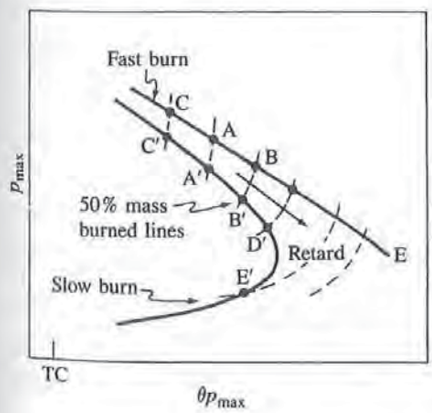


FIGURE 9-32
Schematic of variation in maximum cylinder pressure and crank angle at which it occurs, in individual cycles. $CABE$ typical of fast heat-release process; $C'A'B'D'E'$ typical of slow heat-release process. (*From Matekunas.*[38])

PETITIONER'S EXHIBIT 1002
US PATENT NO. 6,581,565

constant), as the phasing of this combustion process relative to TC is varied. A corresponds to MBT timing where the start of combustion is phased to give maximum brake torque, B corresponds to retarded timing, and C to over-advanced timing. $C'A'B'D'E'$ is a similar curve for a slow-burning heat-release profile. A' corresponds to MBT timing, and B' and D' to increasingly retarded timing. Note that with a sufficiently slow-burning heat-release profile, beyond D', $\theta_{p\max}$ decreases as the burn process is increasingly retarded. This occurs when the rate of increase of pressure due to combustion becomes so low that it is more than offset by the pressure decrease due to volume increase: eventually for extremely slow and late burning, the maximum pressure approaches the motored pressure at TC. The dashed lines show the constant start-of-combustion timing *relative* to MBT for each burn rate curve. Note that $\theta_{p\max}$ for constant relative timing varies little as the heat-release profile or burn rate varies.[38]

We can now explain the effects of variations in the heat-release profile (both in the development stage of the burning process, which effectively changes the location of the start of combustion, and in the rate of burning throughout the process) on $p_{\max}$ and $\theta_{p\max}$, when the spark timing occurs at a fixed crank angle. For a fixed burning rate profile (duration of burn and maximum burning rate) as the start of combustion is delayed to be closer to TC, $p_{\max}$ decreases and $\theta_{p\max}$ initially increases (A to B or A' to B'). This is the effect of a change in relative timing or phase of the burning process due to a slower initial rate of flame development with fixed spark timing. If, in addition to the flame development being slower, the heat-release rate throughout the burning process is lower, then that combustion process is even more retarded from the optimum and $p_{\max}$ decreases and $\theta_{p\max}$ increases further, to their values at D'. The effect of a faster initial flame development and faster burning rate, with fixed spark time, is the opposite. The magnitudes of the changes in $p_{\max}$ and $\theta_{p\max}$ depend, obviously, on the extent of the cyclic variations; they also depend on whether the average burn process is fast or slow. For fast-burning engines, a larger fraction of the heat release occurs near TC when the chamber volume is changing relatively slowly. Thus pressure variations are mainly due to combustion variations. With slow-burning engines, where a significant fraction of the energy release occurs well after TC, the effect of volume change also becomes significant and augments the effect of combustion variations. For large variations and a slow average burning process, $p_{\max}$ can fall below E', and $\theta_{p\max}$ then decreases. A fast-burning combustion process significantly reduces the impact of cyclic combustion variations on engine performance.[39]

We can now evaluate the various measures of combustion variability. The maximum pressure variation has been shown to depend on both changes in phasing and burning rate. The magnitude of this variation depends on whether the combustion chamber is faster or slower burning, on average. It also depends on whether the burning process is substantially retarded relative to MBT. It depends, too, on cyclic cylinder fuel and air charging variations. Thus the interpretation of variations in $p_{\max}$ [or in the maximum rate of pressure rise $(dp/d\theta)_{\max}$] in terms of variations in the rate and phasing of the burning process

PETITIONER'S EXHIBIT 1002
US PATENT NO. 6,581,565

must be done with care. The location of maximum pressure $\theta_{p\max}$ also depends on relative phasing of combustion and on the burn rate profile. In addition, for slow-burning chambers and retarded timing (around E') variations produce little change in $\theta_{p\max}$. However, for fast-burning chambers, with MBT or only slightly retarded timing, the location of peak pressure depends essentially on the phasing of each combustion process relative to its MBT phasing, and is independent of charging variations. For these reasons, $\theta_{p\max}$ is a useful measure of variability in combustion event phasing.[38]

One important measure of cyclic variability, derived from pressure data, is the *coefficient of variation* in *indicated mean effective pressure*. It is the standard deviation in imep divided by the mean imep, and is usually expressed in percent:

$$\mathrm{COV}_{\mathrm{imep}} = \frac{\sigma_{\mathrm{imep}}}{\mathrm{imep}} \times 100 \tag{9.50}$$

It defines the cyclic variability in indicated work per cycle, and it has been found that vehicle driveability problems usually result when $\mathrm{COV}_{\mathrm{imep}}$ exceeds about 10 percent.

Figure 9-33 illustrates the relationships between $p_{\max}$, $\theta_{p\max}$, and imep for 120 cycles of an engine cylinder at fixed operating conditions and three different spark timings.[38] The MBT timing data show a spread in imep at a fixed value of $\theta_{p\max}$. This imep data band is relatively flat and is centered around $\theta_{p\max} \approx 16°$; only at later values of $\theta_{p\max}$ does imep fall off significantly. The vertical spread in imep around $\theta_{p\max} = 16°$ is due to variations in the amount of fuel entering the cylinder each cycle; normal variations in the burn profile under these conditions, which effectively change the phasing of the combustion process, produce only modest reductions in imep. For early $\theta_{p\max}$ (the extreme upper left of Fig. 9-33*a*), the variations in $p_{\max}$ are also due mainly to these fuel-charging variations, cycle-by-cycle; these are the fastest burning cycles with the most advanced phasing. As

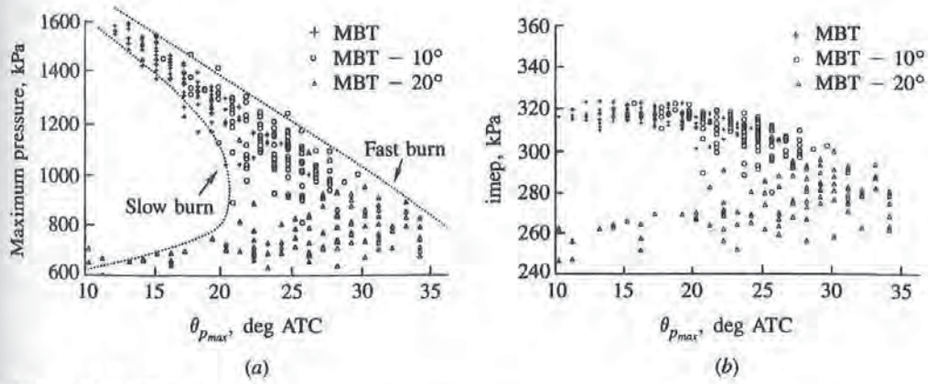


FIGURE 9-33
(*a*) Individual-cycle maximum pressure versus crank angle at which $p_{\max}$ occurs. (*b*) Individual-cycle indicated mean effective pressure versus $\theta_{p\max}$.[38]

PETITIONER'S EXHIBIT 1002
US PATENT NO. 6,581,565

$\theta_{p\max}$ increases, the dispersion increases as cyclic variations in phasing and burning rate have increasing impact.

An important issue is whether variations in the early stages of flame development and variations in subsequent portions of the burning process are independent of each other or are correlated. Plots of early flame development angle (spark to 1 percent mass burned) against the burning angle (1 to 90 percent burned) from individual cycles for several different combustion chambers indicate the following. There is a trend with increasing flame development angle for the burning angle to increase (or the burning rate to decrease); however, there is much scatter about this trend (for a given value of flame development angle different cycles show a substantial range in burning angle), and the quantitative aspects of the trend depend on operating conditions and on combustion chamber design. In addition, as the mean rapid burning angle increases (due to changing operating conditions or a slower-burning chamber design) the mean flame development angle, the cyclic variation in the flame development angle, and the cyclic variation in the rapid burning angle all increase.[40] This topic is discussed more fully in the following section.

The shapes of the frequency distributions in individual-cycle pressure data (e.g., in $p_{\max}$, $(dp/d\theta)_{\max}$, $\theta_{p\max}$) and in burn rate data such as $\Delta\theta_d$, $\Delta\theta_b$, $(dQ/d\theta)_{\max}$ depend on whether the combustion process is fast and "robust" (e.g., with close-to-stoichiometric mixtures at higher loads at optimum timing—well away from the lean operating limit of the engine) or slower and less repeatable, closer to the lean or dilute-mixture operating limit. Under robust combustion conditions these distributions are close to normal distributions.[41–43] When the combustion process is much slower, the cyclic variability becomes large and the distribution becomes skewed toward the slower burning cycles which have low imep (due to the substantial retard of these slower cycles). When partial burning and then misfire occur, the low-pressure tail of the distribution approaches the motored pressure value at TC.[44] Examples of the frequency distributions of imep in these two combustion variability regimes are shown later in Fig. 9-36.

Cylinder pressure data are often averaged over many cycles to obtain the mean cylinder pressure at each crank angle. The primary use of this average pressure versus crank angle data is in calculating the average indicated mean effective pressure (which is a linear function of p). Since combustion parameters are not linearly related to the cylinder pressure [see Eq. (9-27)], analysis of the *average* pressure data will not necessarily yield accurate values of average combustion parameters. The error will be most significant when the combustion variability is largest. It is best to determine mean combustion parameters by averaging their values obtained from a substantial number of individual cycle analysis results. The number of cycles which must be averaged to obtain the desired accuracy depends on the extent of the combustion variability. For example, while 40 to 100 cycles may define imep to within a few percent when combustion is highly repeatable, several hundred cycles of data may be required when cyclic combustion variations are large.[12]

PETITIONER'S EXHIBIT 1002
US PATENT NO. 6,581,565

9.4.2 Causes of Cycle-by-Cycle and Cylinder-to-Cylinder Variations

Cycle-by-cycle combustion variations are evident from the beginning of the combustion process. Analysis of flame photographs from many engine cycles taken in special research engines with windows in the combustion chamber has shown that dispersion in the fraction of the combustion chamber volume inflamed is present from the start of combustion (e.g., see Refs. 3 and 23). Dispersion in burning rate is also evident throughout the combustion process (see Figs. 9-2 and 9-31). Three factors have been found to influence this dispersion:[45]

1. The variation in gas motion in the cylinder during combustion, cycle-by-cycle
2. The variation in the amounts of fuel, air, and recycled exhaust gas supplied to a given cylinder each cycle
3. Variations in mixture composition within the cylinder each cycle—especially near the spark plug—due to variations in mixing between air, fuel, recycled exhaust gas, and residual gas

The relative importance of these factors is not yet fully defined, and depends on engine design and operating variables. The variation in the velocity field within the engine cylinder throughout the cycle, and from one cycle to the next, has been reviewed in Sec. 8.2.2. Toward the end of the compression stroke, the ensemble-averaged rms velocity fluctuation is of comparable magnitude to the mean piston speed, and may be larger than the mean flow velocity if there is no strongly directed local mean flow pattern (see Figs. 8-8 and 8-9). This ensemble-averaged velocity fluctuation combines both cycle-by-cycle variation in the mean flow and the turbulent velocity fluctuations. During compression, these two components are of comparable magnitude (see Figs. 8-9 and 9-29). While this data base is limited, it indicates that substantial variations in the mean flow exist, cycle-by-cycle, both in the vicinity of the spark plug *and* throughout the combustion chamber. Velocity variations contribute in a major way to variations in the initial motion of the flame center as it grows from the kernel established by the spark, and in the initial rate of growth of the flame; they can also affect the burning rate once the flame has developed to fill a substantial fraction of the combustion chamber. Variations in gas motion near the spark plug convect the flame in its early stages in different directions and at different velocities, cycle-by-cycle. This affects the flame's interaction with the cylinder walls, changing the flame area development with time. Variations in the turbulent velocity fluctuations near the spark plug will result in variations in the rate at which the small initially laminarlike flame kernel develops into a turbulent flame. Variations in the mean flow throughout the chamber will produce differences in flame front shape; also, they may produce differences in turbulence which affect the propagation velocity of the front (see Fig. 9-30 for the relation between mean burning speed and turbulence intensity).

PETITIONER'S EXHIBIT 1002
US PATENT NO. 6,581,565

It is well known that, on a time-averaged basis, the fuel, air, and recycled exhaust gas flows into each cylinder of a multicylinder engine are not identical. These flow rate differences are typically a few percent (see Secs. 7.6.2 and 7.6.3). It is also known that the flow patterns within the different cylinders are not necessarily identical due to differences between the individual intake manifold runner and port geometries in many production engines. All these factors contribute to cylinder-to-cylinder variations in the combustion process: there can be significant differences in the mean burn rate parameters as well as in the cyclic variations in these parameters.[41] Also, the limited data available on the variation in mixture composition within each cylinder for each cycle indicates that cyclic charging variations in individual cylinders are comparable in magnitude to cylinder-to-cylinder differences (i.e., of order ± 5 percent[46]). Whether the amount of residual gas left in the cylinder varies significantly, cycle-by-cycle, is not known. At higher loads, where the combustion process is more repeatable (and always completed relatively early in the expansion stroke) and the residual gas fraction smaller (see Sec. 6.4), variations in the total amount of residual are not expected to be significant. At light loads (particularly at idle), where combustion variability is much higher and partial-burning cycles may occur, and especially with high valve overlap engine designs, variations in the residual gas mass and its composition may become important.

In addition, mixing of fuel, air, recycled exhaust, and residual is not complete: nonuniformities in composition exist within the cylinder at the start of combustion. Composition variations, cycle-by-cycle, in the vicinity of the spark plug electrode gap will affect the early stages of flame development, especially as the flame grows through the laminarlike burning phase following the creation of a small flame kernel by the spark discharge (see Sec. 9.5.1). Figure 9-34 indicates the extent of these composition nonuniformities. The available data comes from experiments where a small rapid-acting sampling valve located in the spark plug center electrode was used to extract gas from the vicinity of the electrode gap, close to the start of combustion, for individual cycle composition analysis. Figure 9-34*a* shows the cycle-by-cycle air/fuel ratio fluctuations in the burned gases sampled from one cylinder of a four-cylinder gasoline-fueled carbureted engine just after combustion has started. The standard deviation was typically 2 to 6 percent of the mean (A/F).[46–48] Figure 9-34*b* shows the relationship between total hydrocarbon and CO_2 concentrations in unburned mixture, sampled just before spark discharge. The CO_2 concentration is a measure of the burned gas fraction in the sampled unburned mixture; hence on average it correlates inversely with the total hydrocarbon concentration. However, there is substantial fluctuation in CO_2 concentration about the mean value, at a given fuel fraction, indicating significant fluctuations, cycle-by-cycle, in the mixing of fresh mixture with residual gas. Nonuniformities in EGR distribution between cylinders and EGR mixing within the cylinder would also increase the variations in burned gas fraction locally at the spark gap, cycle-by-cycle.[48]

Experiments in a multicylinder production SI engine, where the fuel/air ratio nonuniformities and the nonuniform mixing of fresh mixture with residual

PETITIONER'S EXHIBIT 1002
US PATENT NO. 6,581,565

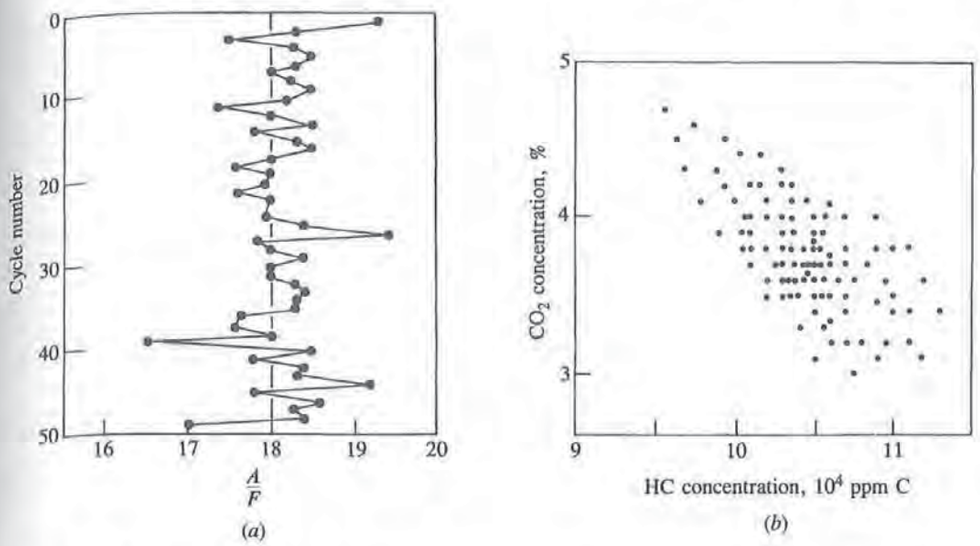


FIGURE 9-34
(*a*) Air/fuel ratio in 50 consecutive cycles, in vicinity of spark plug, measured just after ignition with a rapid-acting sampling valve located in the plug center electrode. Engine operated at 1400 rev/min, MBT timing, imep = 314 kPa.[47] (*b*) CO_2 and unburned HC concentrations in gas sampled in individual cycles from the vicinity of the spark plug just prior to ignition. Engine operated at 1200 rev/min, $\phi = 0.98$, $p_{inlet} = 0.5$ atm, gasoline fuel.[48]

gas were removed in turn as contributors to cycle-by-cycle variations (by comparing premixed propane operation with conventional carbureted operation with gasoline, and by removing residual gas by purging with nonfiring cycles), showed that the three contributing factors to cyclic combustion variations—velocity variations, fuel/air ratio variations, and residual gas mixing variations—are of comparable importance at road-load conditions.[45]

An explanation for cycle-by-cycle variations can be developed from the description of the turbulent flame propagation process in Sec. 9.3. Conditions in the *vicinity* of the spark plug will influence the initial stages of the flame propagation process—establishing a stable kernel and its development into a turbulent flame. During the developed flame propagation phase, the *average* conditions in the bulk gas within the combustion chamber will be the determining factors since the flame front spans the chamber, effectively averaging out local nonuniformities. By conditions are meant the turbulent velocity fluctuations and length scales in the flow, proportions of fuel, air, and burned gas in the mixture, and the mixture state.

Using the turbulent combustion model described in Sec. 14.4.2 (which is based on the description of the flame development and propagation process in Sec. 9.3), the flame development angle $\Delta\theta_d$ (the time to burn a few large eddies and establish a developed turbulent flame) can be expressed as[20]

$$\Delta\theta_d = C\left(\frac{l_I}{u'}\right)^{1/3}\left(\frac{l_M}{S_L}\right)^{2/3} \tag{9.51}$$

PETITIONER'S EXHIBIT 1002
US PATENT NO. 6,581,565

The turbulent flow field influences $\Delta\theta_d$ through l_I, u', and l_M, the integral scale, the turbulence intensity, and the microscale, respectively. The mixture composition influences $\Delta\theta_d$ through the laminar flame speed S_L. There is therefore a variability in the flame development period, since all of these quantities can vary in the vicinity of the spark plug on a cycle-by-cycle basis.

The pressure development during the rapid-burning developed turbulent flame propagation phase, when the flame spans the combustion chamber, depends on the average rate of burning in the flame. Thus, variations in the turbulent flow field and mixture composition across the gas entering the flame front are averaged out and are not important. However, variation in chamber-average quantities are significant. The combustion model in Sec. 14.4.2 leads to the following expression for the maximum burning rate:

$$\left(\frac{dm_b}{dt}\right)_{\max} = \frac{Cm_f(h^*/B)(\rho_u^*/\rho_i)^{10/9}[(\bar{u}'^* S_L^*)/h_i]^{2/3}}{\nu^{*1/3}} \tag{9.52}$$

Here, m_f is the mass of fuel in the chamber, h is the instantaneous (mean) clearance height, B is the bore, ρ the density, $\bar{u}'$ the average turbulence intensity across the flame front, and ν the kinematic viscosity; the * denotes the value at the time of the maximum burning rate and the subscript i the value at spark; C is a constant depending on engine design. It can be seen from Eq. (9.52) that cycle-by-cycle variations in the maximum burning rate can result from variations in the overall flow pattern within the combustion chamber (which vary $\bar{u}'^*$) and from variations in the amount of fuel (m_f) that enters the cylinder each cycle.† Also, it can be seen that variations in the flame development process will result in variations in the maximum burning rate because the crank angle at which the maximum burning rate occurs is shifted, and all the starred parameters in Eq. (9.52) will have different values.

From the discussion of flame development and structure in Sec. 9.3, and Eqs. (9.51) and (9.52) above, we would expect that mixture conditions and motion leading to slower flame development rates (longer flame development angles, $\Delta\theta_d$)—lower turbulence intensities and more dilute mixtures—would also give lower burning rates (longer rapid burning angles, $\Delta\theta_b$). Data from many different engines and a wide range of operating cases show that this is the case, on average, though there is substantial variation about the mean trend. Figure 9-35 shows these trends; it also shows that the standard deviation of $\Delta\theta_d$ and the standard deviation of $\Delta\theta_b$ for a given chamber and operating condition generally increase as the average burning process becomes slower.[40]

One final factor of importance is how variations in flame development and burning rate affect engine torque. With fixed spark timing, such variations in the combustion process cycle-by-cycle result in slower developing and/or burning

† Variations in the total amount of air, recycled exhaust gas, and residual in the chamber could also, for some operating regimes, be significant.

PETITIONER'S EXHIBIT 1002
US PATENT NO. 6,581,565

cycles being retarded and faster developing and/or burning cycles being overadvanced. The curve of torque versus combustion timing (relative to optimum timing), Fig. 9-3*b*, is almost independent of the burning rate; i.e., a given magnitude retard (of say 10°) relative to optimum timing gives almost the same reduction in torque for a very fast burn as it does for a very slow burn. This is because the burning process, for optimum timing, is centered at about 10° ATC independent of the burn rate, and retard or advance shifts this "center" by equal amounts for all burn rates.[16] One of the major advantages of fast-burn engines is now apparent. The magnitude of the variations in the flame development process and subsequent flame propagation rate are decreased as the burning rate is increased (see Fig. 9-35): the ratio of standard deviation in $\Delta\theta_d$ and $\Delta\theta_b$ to the mean values remains approximately constant. Thus, these smaller combustion variations in fast-burn engines, which correspond to modest retard and overadvance in nonaverage burn rate cycles, have little effect on torque. In contrast, the larger combustion variations of slow-burning engines result in significant cyclic torque variations.

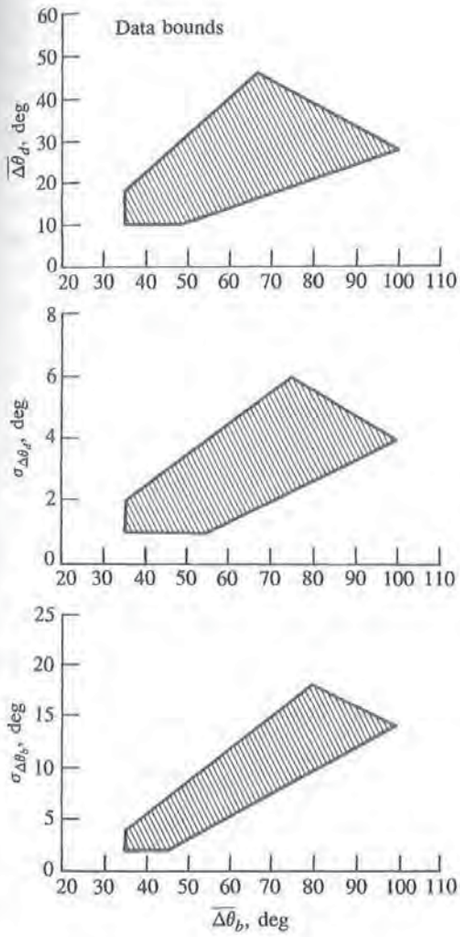


FIGURE 9-35
Variation in mean value of flame development angle $\overline{\Delta\theta_d}$ (spark to 1 percent mass burned) and standard deviations of flame development angle and rapid burning angle $\Delta\theta_b$ (1 to 90 percent mass burned) with mean rapid burning angle $\overline{\Delta\theta_b}$. Range of combustion chamber geometries and engine operating conditions.[40]

PETITIONER'S EXHIBIT 1002
US PATENT NO. 6,581,565

9.4.3 Partial Burning, Misfire, and Engine Stability

As the unburned mixture in a spark-ignition engine is leaned out with excess air or is diluted with increasing amounts of burned residual gas and exhaust gas recycle, the flame development period, the duration of the rapid burning phase, and the cycle-by-cycle fluctuations in the combustion process all increase. Eventually a point is reached where engine operation becomes rough and unstable, and hydrocarbon emissions increase rapidly. The point at which these phenomena occur effectively defines the engine's *stable operating limit.*† These phenomena result from the lengthening of all stages of the combustion process as the unburned mixture is diluted. With increasing dilution, first a fraction of the cycles burns so slowly that combustion is only just completed prior to exhaust valve opening. Then as burning lengthens further, in some cycles there is insufficient time to complete combustion within the cylinder; also, flame extinguishment before the exhaust valve opens and before the flame has propagated across the chamber may start to occur in some cycles. Finally, misfiring cycles where the mixture never ignites may start to occur. The proportion of partial burning or nonburning cycles increases rapidly if the mixture is made even more lean or dilute, and the point is soon reached where the engine will not run at all.

The impact on engine stability of increasing combustion variability, due to increased exhaust gas recycle at part-load, is shown in Fig. 9-36. Figure 9-36*a* shows the distributions of individual-cycle indicated mean effective pressure values for 0, 20, and 28 percent EGR. Without EGR at these conditions, the spread in imep is narrow. Increasing EGR widens the distribution significantly and cycles with low imep, and eventually zero imep, occur. Figure 9-36*b* shows how the coefficient of variation of imep and hydrocarbon emissions increase as EGR is increased. Slow burn, then partial burn, and then misfire cycles occur with increasing frequency. In the slow-burn cycles, combustion is complete but ends after 80° ATC and the indicated mean effective pressure is low (between 85 and 46 percent of the mean value). Imep in partial-burn cycles was less than 46 percent of the mean. In misfiring cycles, imep < 0. Empirically, it has been found that COV_{imep} [see Eq. (9.50)] is about 10 percent at the engine's stable operating limit, which here occurs just before the onset of partial-burning cycles[49].

An explanation of combustion phenomenon at the engine stable operating limit has been developed by Quader.[50] It involves the following terms:

> **Ignition-limited spark timing** or the **ignition limit.** The spark timing [advanced from maximum brake torque (MBT) timing] at which *misfire* (i.e., failure of flame initiation) first occurs at a given mixture composition, in a given small but arbitrary fraction of cycles (e.g., 0.5 to 1 percent).

† This limit has often been called the *lean operating limit.* Since what limits engine operation in practice is excessive torque fluctuations, cycle-by-cycle, and high hydrocarbon emissions, resulting from the use of mixtures made overly dilute with either air or burned gases (or with both), *stable operating limit* is a more appropriate term.

PETITIONER'S EXHIBIT 1002
US PATENT NO. 6,581,565

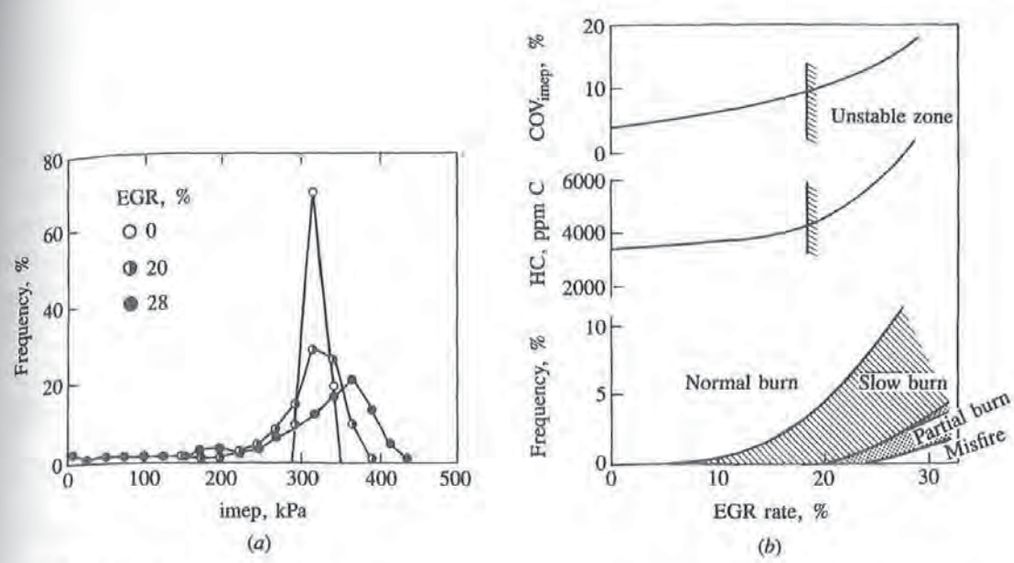


FIGURE 9-36
(*a*) Frequency distributions in indicated mean effective pressure at different EGR rates; 0 percent gave excellent engine stability, 20 percent acceptable stability, and 28 percent poor stability. (*b*) Coefficient of variation in imep, HC emissions, and percentage of normal, slow, partial-burn, and misfire cycles. Engine conditions: 1400 rev/min, $\phi = 1.0$, MBT timing, imep = 324 kPa.[49]

Partial-burn-limited spark timing or the **partial-burn limit.** The spark timing (retarded from MBT) at which incomplete flame propagation occurs at a given mixture composition in a given small percent of the cycles (again, this frequency is selected arbitrarily for experimental convenience).

Lean misfire limit at MBT spark. The leanest mixture stoichiometry at which the engine could be stabilized to operate at MBT spark timing with a misfire frequency below a specified value (again, this frequency, usually a percent or less of the cycles, is selected arbitrarily for convenience). A *dilute misfire limit*, the maximum amount of exhaust gas recycle that can be absorbed at a given stoichiometry for stable engine operation, can be similarly defined.

Engine experiments have defined the locations of the ignition limit line and the partial-burn limit line; they are shown qualitatively in Fig. 9-37. At a given spark timing, on this spark timing versus equivalence ratio plot, progressive leaning of the mixture fed to the engine will lead to the onset of misfire or to the onset of partial burning, depending on the location of the lines and the spark timing selected. The individual figures show the possible interactions of the maximum brake torque (MBT) timing line—leaner mixtures require greater advance—with the ignition limit and partial-burn limit lines. At MBT timing, the partial-burn limit may or may not be reached prior to misfire or the ignition limit. It will depend on the engine and ignition system design and operating conditions. For spark timings retarded relative to MBT, partial burning and not failure of flame initiation is the primary cause of unstable engine operation.

PETITIONER'S EXHIBIT 1002
US PATENT NO. 6,581,565

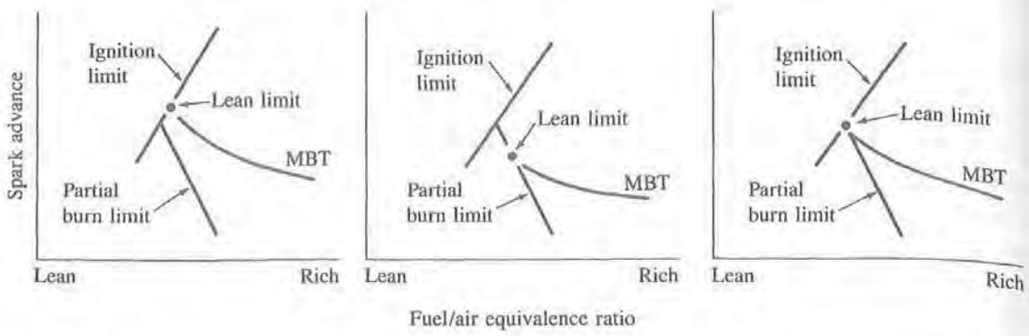


FIGURE 9-37
Schematics of three possible combinations of ignition limit, partial-burn limit, and MBT timing curves as function of fuel/air equivalence ratio. (*From Quader.*[50])

An example of these limiting combustion regimes for lean engine operation is shown in Fig. 9-38. With MBT timing, as the mixture is leaned out (at constant air flow rate), complete combustion in all cycles changes to partial burning in some cycles which changes to no ignition in some cycles at the ignition limit. In the partial-burning regime, the most common type of incomplete-combustion cycle was a slow-burning cycle which required more time to complete burning than was available: flame extinguishment during expansion was much less common. Engine performance measurements showed that the engine stability limit—evidenced by minimum fuel consumption and onset of rapid increase in HC emissions—occurred at $\phi = 0.65$, just before the partial-burn limit line where some slow-burning cycles occur but combustion is still complete in all cycles.[44]

From the above it is clear that flame initiation is a necessary but not sufficient condition for complete combustion. Too-slow flame development and prop-

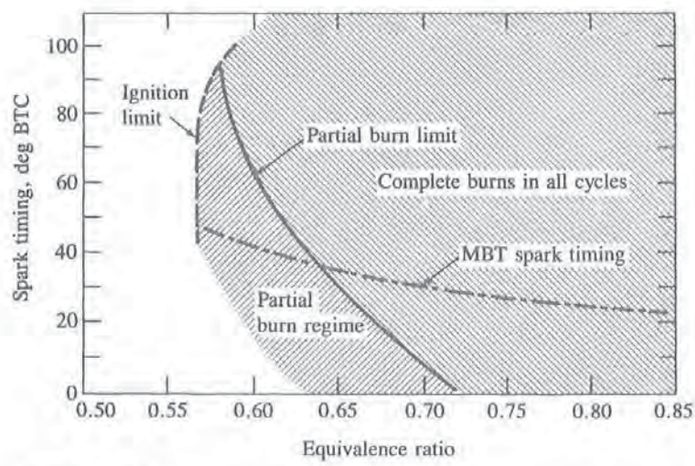


FIGURE 9-38
Actual limiting combustion regimes for lean-operating engine. 1200 rev/min, volumetric efficiency ≈ 60 percent, methane fuel, 40 mJ spark energy, 2.5 ms spark duration.[44]

PETITIONER'S EXHIBIT 1002
US PATENT NO. 6,581,565

agation following successful ignition is usually the factor which limits engine operation with dilute mixtures. Experiments have shown that a limited interval, of order 80 crank angle degrees (depending on engine geometry and spark plug location), is available during the engine cycle when conditions are favorable for complete flame propagation.[49, 51] Outside of this interval, the mixture pressure and temperature are too low, and the turbulence intensity is too low to sustain a sufficiently rapid rate of combustion. Thus, it is factors which increase the flame development and propagation rates which primarily extend the partial-burn limit.

9.5 SPARK IGNITION

In spark-ignition engines, the electrical discharge produced between the spark plug electrodes by the ignition system starts the combustion process close to the end of the compression stroke. The high-temperature plasma kernel created by the spark develops into a self-sustaining and propagating flame front—a thin reaction sheet where the exothermic combustion chemical reactions occur. The function of the ignition system is to initiate this flame propagation process, in a repeatable manner cycle-by-cycle, over the full load and speed range of the engine at the appropriate point in the engine cycle. Shadowgraph and schlieren photographs of the kernel created by the discharge between the plug electrodes, the growth of that kernal, and its transition to a propagating flame have already been presented in Figs. 9-19 and 9-20, and described in the accompanying text. A spark can arc from one electrode to another when a sufficiently high voltage is applied. Ignition systems commonly used to provide this spark are: battery ignition systems where the high voltage is obtained with an ignition coil (coil ignition systems); battery systems where the spark energy is stored in a capacitor and transferred as a high-voltage pulse to the spark plug by means of a special transformer (capacitive-discharge ignition systems); and magneto ignition systems where the magneto—a rotating magnet or armature—generates the current used to produce a high-voltage pulse.

This section reviews our basic understanding of electrical discharges in inflammable gas mixtures relevant to engine ignition (Sec. 9.5.1), the major design and operating characteristics of conventional engine ignition systems (Sec. 9.5.2), and, briefly, some alternative approaches to generating a propagating flame (Sec. 9.5.3).

9.5.1 Ignition Fundamentals

A spark can arc from one plug electrode to the other only if a sufficiently high voltage is applied. In a typical spark discharge, the electrical potential across the electrode gap is increased until breakdown of the intervening mixture occurs. Ionizing streamers then propagate from one electrode to the other. The impedance of the gap decreases drastically when a streamer reaches the opposite electrode, and the current through the gap increases rapidly. This stage of the

PETITIONER'S EXHIBIT 1002
US PATENT NO. 6,581,565

discharge is called the *breakdown phase.* It is followed by the *arc phase*, where the thin cylindrical plasma expands largely due to heat conduction and diffusion and, with inflammable mixtures, the exothermic reactions which lead to a propagating flame develop. This may be followed by a *glow discharge phase* where, depending on the details of the ignition system, the energy storage device (e.g., the ignition coil) will dump its energy into the discharge circuit.[52, 53]

Figure 9-39 shows the behavior of the discharge voltage and current as a function of time for a conventional coil ignition system. Typical values are shown; actual values depend on the details of the electrical components. The breakdown phase is characterized by a high-voltage (~10 kV), high-peak current (~200 A), and an extremely short duration (~10 ns). A narrow (~40 μm diameter) cylindrical ionized gas channel is established very early. The energy supplied is transferred almost without loss to this plasma column. The temperature and pressure in the column rise very rapidly to values up to about 60,000 K and a few hundred atmospheres, respectively. A strong shock or blast wave propagates outward, the channel expands, and, as a result, the plasma temperature and pressure fall. Some 30 percent of the plasma energy is carried away by the shock wave; however, most of this is regained since spherical blast waves transfer most of their energy to the gas within a small (~2 mm diameter) sphere into which the breakdown plasma soon expands.[52, 53]

A breakdown phase always precedes arc and glow discharges: it creates the electrically conductive path between the electrodes. The arc phase voltage is low

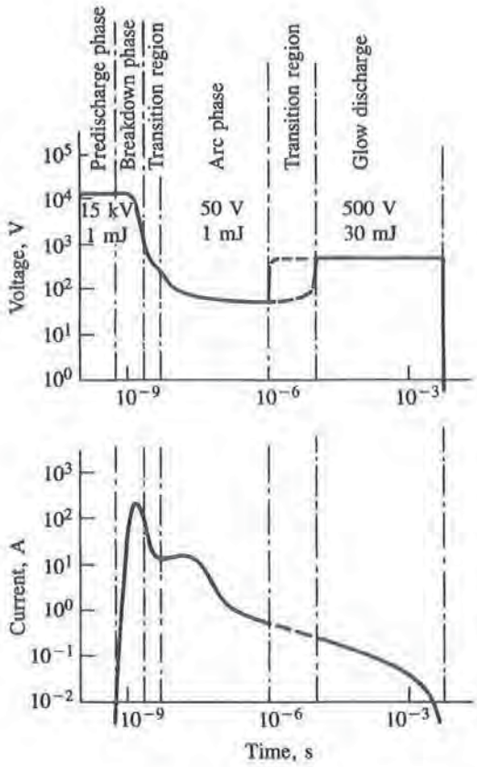


FIGURE 9-39
Schematic of voltage and current variation with time for conventional coil spark-ignition system. Typical values for energy and voltage in the three phases—breakdown, arc, and glow discharge—are given.[52]

PETITIONER'S EXHIBIT 1002
US PATENT NO. 6,581,565

(<100 V), though the current can be as high as the external circuit permits. In contrast to the breakdown phase where the gas in the channel is fully dissociated and ionized, in the arc phase the degree of dissociation may still be high at the center of the discharge, but the degree of ionization is much lower (about 1 percent). Voltage drops at the cathode and anode electrodes are a significant fraction of the arc voltage, and the energy deposited in these electrode sheath regions, which is conducted away by the metal electrodes, is a substantial fraction of the total arc energy (see Table 9.4 below). The arc requires a hot cathode spot, so evaporation of the cathode material occurs. The arc increases in size due primarily to heat conduction and mass diffusion. Due to these energy transfers the gas temperature in the arc is limited to about 6000 K: the temperature and degree of dissociation decrease rapidly with increasing distance from the arc axis. Currents less than 200 mA, a large electrode voltage drop at the cathode (300 to 500 V), a cold cathode, and less than 0.01 percent ionization are typical for the glow discharge. Energy losses are higher than in the arc phase, and peak equilibrium gas temperatures are about 3000 K.[52]

About 0.2 mJ of energy is required to ignite a quiescent stoichiometric fuel-air mixture at normal engine conditions by means of a spark. For substantially leaner and richer mixtures, and where the mixture flows past the electrodes, an order of magnitude greater energy (~ 3 mJ) may be required.[54] Conventional ignition systems deliver 30 to 50 mJ of electrical energy to the spark. Due to the physical characteristics of the discharge modes discussed above, only a fraction of the energy supplied to the spark gap is transmitted to the gas mixture. The energy balance for the breakdown, arc, and glow phases of the discharge is given in Table 9.4. Radiation losses are small throughout. The end of the breakdown phase occurs when a hot cathode spot develops, turning the discharge into an arc; heat losses to the electrodes then become substantial. The breakdown phase reaches the highest power level (~ 1 MW), but the energy supplied is small (0.3 to 1 mJ). The glow discharge has the lowest power level (~ 10 W) but the highest energy (30 to 100 mJ), due to its long discharge time. The arc phase lies between.

The proportions of the electrical energy supplied, which can be transferred to the plasma in these three phases of the discharge, are shown in Fig. 9-40.[53, 55] The different transfer capabilities for breakdown arc and glow discharges arise

TABLE 9.4
Energy distribution for breakdown, arc, and glow discharges†

	Breakdown, %	Arc, %	Glow, %
Radiation loss	<1	5	<1
Heat loss to electrodes	5	45	70
Total losses	6	50	70
Plasma energy	94	50	30

† Typical values, under idealized conditions with small electrodes.
Source: Maly and Vogel.[52]

PETITIONER'S EXHIBIT 1002
US PATENT NO. 6,581,565

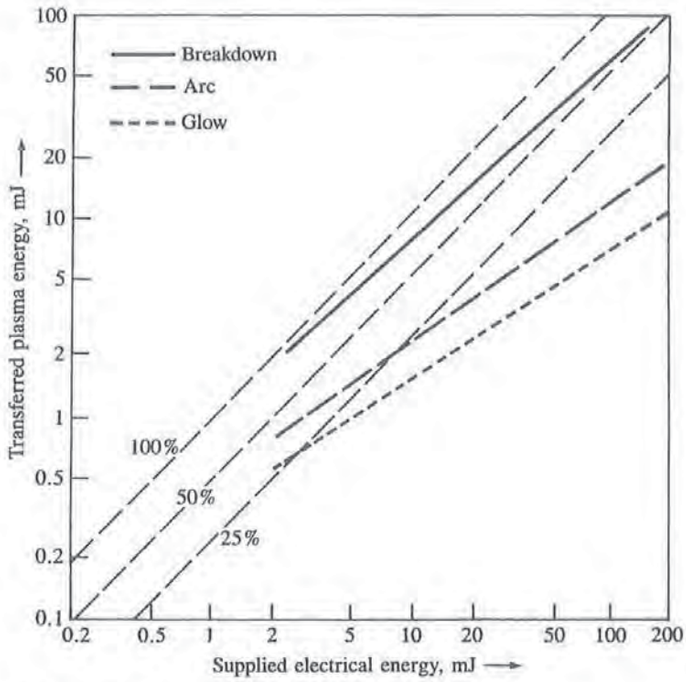


FIGURE 9-40
Energy transferred to the spark kernal as a function of supplied electrical energy for breakdown, arc, and glow discharges.[55]

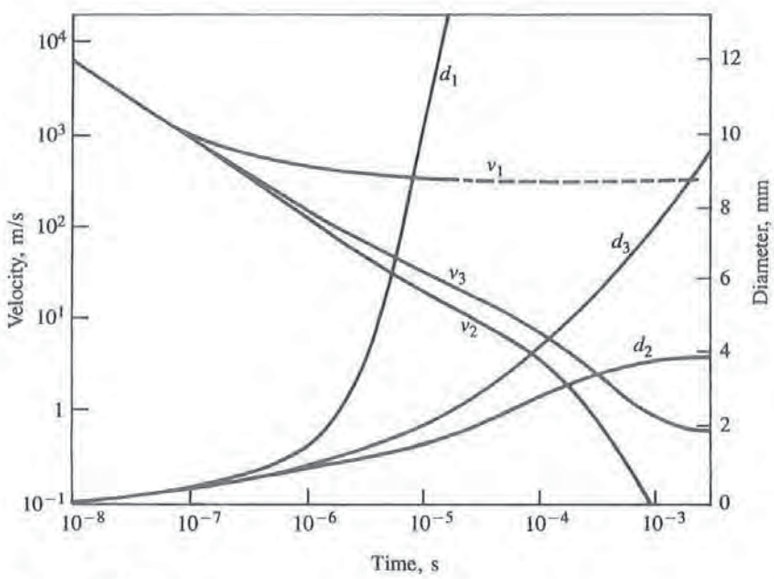


FIGURE 9-41
Diameters (d) and expansion velocities (v) of volumes activated by a capacitive-discharge ignition system: 3 mJ electrical energy, 100 μs duration. Subscripts denote: 1, shock in air at 1 atm; 2, plasma in air at 1 atm; 3, electrical and chemical plasma in stoichiometric methane-air mixture at 1 atm.[52]

PETITIONER'S EXHIBIT 1002
US PATENT NO. 6,581,565

primarily from the differences in heat losses to the electrodes, as explained above. These losses increase with increasing supplied energy. In arc and glow discharges, increases in either discharge time or discharge current (or in both) always lead to substantial decreases in energy-transfer efficiency. If the glow discharge current is increased above about 100 mA, the discharge changes to the arc mode and heavy electrode erosion will result. Thus there are practical limits to the arc and glow discharge currents; also, the time available for ignition in the engine limits increases in discharge time.

The initial expansion velocities in the discharge are much higher than those in self-propagating flames. Figure 9-41 shows the expansion velocities and diameters of the volumes activated by a 3-mJ, 100-μs discharge from a capacitor-discharge ignition system as a function of time after spark onset.[52] The curves shown are (1) for the shock wave following a discharge in air at 1 atm; (2) the plasma in air at 1 atm; (3) the electrical and chemical plasma following a discharge in a stoichiometric methane-air mixture at 1 atm. The initially strong shock wave attenuates rapidly to the local sound speed. Up to times of order microseconds, the effects of fuel combustion chemistry are small. The change in slope of the velocity curves for the plasmas at about 100 μs indicates the transition from an expansion caused by the initial high pressure in the breakdown discharge to expansion resulting from heat conduction and diffusion.

The temperature distributions within the three different types of discharge provide additional insight. During the breakdown discharge, on a time scale of nanoseconds, the temperature rises to 60,000 K. Increasing the breakdown energy does not produce *higher* kernel temperatures; instead the channel diameter increases, producing a larger plasma volume. The kernel temperatures then decrease to the order of 10,000 K on a microsecond time scale as the plasma expands behind the shock wave. Arc and glow discharges, because their power inputs are much lower, do not increase the kernel temperatures; rather, they extend the cooling period on a microsecond and millisecond time scale, respectively.[52]

The characters of the temperature profiles that each of these three types of discharge create in air, with essentially the same total electrical energy input (30 to 33 mJ), are indicated in Fig. 9-42. The radial profiles in the undisturbed midplane of the arc are shown. The expansion-wave-induced expansion of the plasma behind the shock with the breakdown discharge produces a larger plasma, earlier, with a steep temperature front. Thus it creates favorable conditions for transferring heat and radicals to the surrounding unburned mixture. In addition cold gas flows into the central region of the plasma, due to the boundary layers which the rapidly expanding flow sets up on the electrodes, effectively insulating the hottest plasma region from the cold electrode surfaces.[53] The arc and glow discharges, each preceded by a much lower energy initial breakdown process, show a much slower expansion rate and the more gradual temperature profile produced by heat conduction and diffusion.

Chemical reactions can be observed spectroscopically a few nanoseconds after spark onset. They are initiated by the very high radical density in the break-

PETITIONER'S EXHIBIT 1002
US PATENT NO. 6,581,565

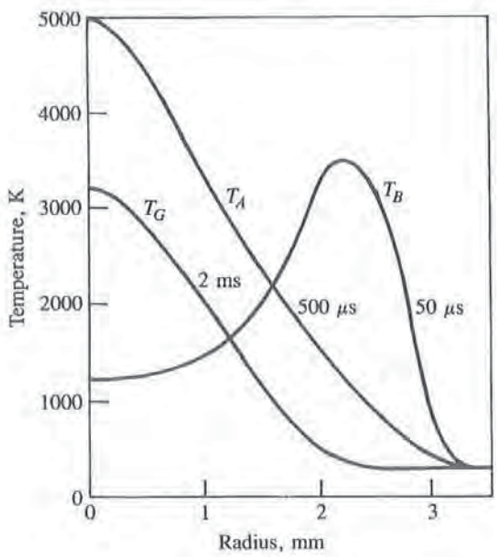


FIGURE 9-42
Radial temperature profiles at selected times after spark onset for ignition systems with different electrical energies and discharge times in air at 1 atm. T_B, breakdown discharge, 30 mJ energy, 60 ns duration; T_A, capacitive discharge, 3 mJ energy, 100 μs duration with superimposed current arc of 2 A, 30 mJ energy, for 230 μs; T_G, capacitive-discharge system, 3 mJ energy, 100 μs duration with superimposed constant-current glow discharge of 60 mA, 30 mJ energy, 770 μs duration.[52]

down plasma where all the heavy particles are present as highly excited atoms and ions. Since the kernel temperatures are much too high to allow the species present in normal combustion products to exist, combustion reactions take place at the outer plasma surface where the conditions are ideal for rapid chemical activity (temperatures of one thousand to a few thousand kelvins). The chemical energy released is added to the plasma energy and becomes evident when the plasma velocity falls below about 100 m/s (see Fig. 9-41). At this point, the inte-

TABLE 9.5
Equilibrium composition of stoichiometric isooctane-air combustion products

	Temperature, K†			
Species	**2000**	**3000**	**4000**	**5000**
CO	2.4(−3)	6.1(−2)	9.4(−2)	9.0(−2)
CO_2	1.2(−1)	5.7(−2)	5.0(−3)	3.5(−4)
H	2(−5)	9.7(−3)	1.2(−1)	1.9(−1)
H_2	6.1(−4)	1.5(−2)	2.4(−2)	3.5(−3)
H_2O	1.4(−1)	1.0(−1)	1.1(−2)	1.2(−4)
N	*n*	1(−5)	6.6(−4)	1.2(−2)
NH	*n*	*n*	2(−5)	6(−5)
NO	5.7(−4)	1.5(−2)	2.9(−2)	1.7(−2)
N_2	7.3(−1)	6.9(−1)	5.7(−1)	5.1(−1)
O	1(−5)	8.6(−3)	9.8(−2)	1.6(−1)
OH	4.5(−4)	2.2(−2)	3.3(−2)	5.6(−3)
O_2	1.1(−3)	2.3(−2)	1.7(−2)	2.2(−3)

† At 4 atm pressure: mole fractions, $9.0(-2) = 9.0 \times 10^{-2}$.
$n = < 5 \times 10^{-6}$

PETITIONER'S EXHIBIT 1002
US PATENT NO. 6,581,565

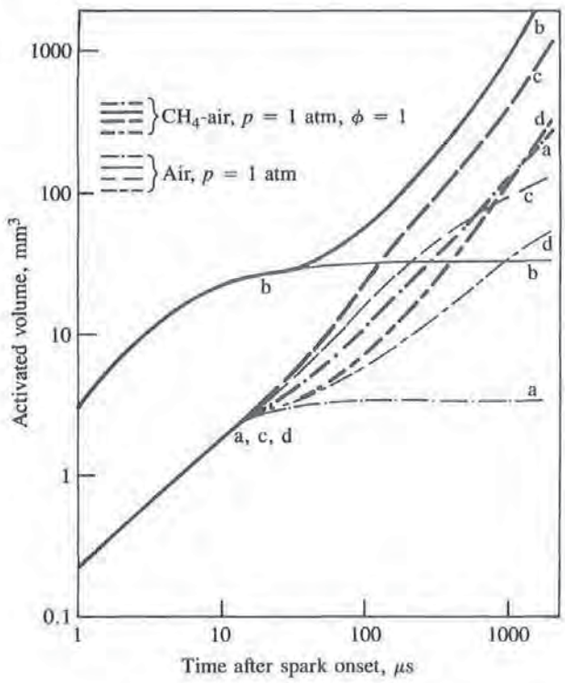
rior of the plasma still consists of a fully dissociated reacted gas mixture with most of its energy stored in radicals. An indication of the gas composition across the steep temperature profile at the plasma interface can be obtained from Table 9.5, which shows the equilibrium composition of C_8H_{18}-air combustion products over the relevant temperature range. Note, however, that the gas will not be in equilibrium. The different radicals have different diffusivities, with the hydrogen atom some five times that of other species. Thus the H radical will diffuse furthest into the as-yet unreacted mixture. On the high-temperature side of the inflammation zone, the large number of radical particles transfer their energy to the mixture molecules within a few collisions. On the low-temperature side of the zone, above-equilibrium concentrations of combustion-initiating radicals (O and H) build up. In addition, a high heat flux into the region occurs, from the plasma core, by conduction down the steep temperature gradient. As a consequence of these conditions, reactions will occur and energy will be released more rapidly than in a normal flame.[53]

Figure 9-43*a* shows the size of the activated volume as a function of time for several types of discharge, both in a stoichiometric mixture and in air. It can be seen from the air curves for the capacitive discharge (CDI) and breakdown discharge that, after about 10 μs, the plasma ceases to be the energy source for continued growth of the activated volume. At this time, the plasma temperature at the interface has fallen to a value comparable to flame temperatures. With combustible mixtures, molecules such as OH, CH, C_2, CO, etc., appear, indicating that combustion reactions are now occurring. Figure 9-43*a* shows that for $t \geq 20$ μs, the volume activated by the discharge with the combustible mixture grows much faster than the volume activated in air. Continuing the supply of electrical energy in the arc and glow discharge does produce a higher expansion rate in both the combustible mixture and in air, due to additional heat conduction and diffusion to the interface, but the onset of inflammation is not significantly affected. The radial temperature profiles across the discharge at selected times, shown in Fig. 9-43*b*, illustrate these points. This, therefore, is the critical point in the inflammation process: at some 20 μs after onset of the discharge the flame reactions must be proceeding sufficiently rapidly to be self-sustaining; i.e., chemical energy release must more than offset heat losses across the front to the surrounding unburned mixture via diffusion and conduction.[53]

Thus the characteristics of the breakdown phase of the discharge have the greatest impact on inflammation. The size of the activated volume a given time interval after spark initiation, the temperature difference across the kernel interface, and the velocity of the interface are all substantially increased by increasing the breakdown phase energy (see Fig. 9-43). Additional energy input during the arc and glow discharge phases has a more modest effect on these critical kernel properties. This is graphically illustrated by Fig. 9-44 where the same energy input into breakdown, arc, and glow discharge modes produces substantially different ignition limits.

Several models of the plasma–unburned mixture interface have been developed in attempts to quantify the complex phenomena described above (e.g., Refs.

PETITIONER'S EXHIBIT 1002
US PATENT NO. 6,581,565



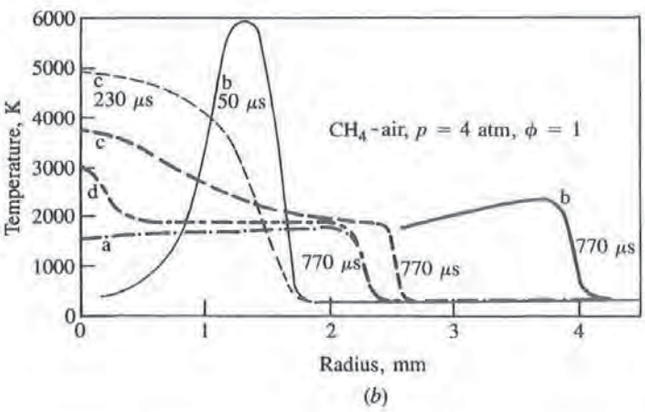


FIGURE 9-43
(*a*) Size of discharge-activated volume as function of time for several types of discharge in air and in stoichiometric methane-air mixture at 1 atm. a: CDI, 3 mJ energy, 100 μs duration; b: breakdown discharge, 30 mJ energy, 20 ns duration; c: CDI plus arc discharge, 1.5 A, 40 V, 500 μs duration; d: CDI + glow discharge, 30 mA, 500 V, 2 ms duration. (*b*) Temperature profiles for different discharge modes at different times in stoichiometric methane-air mixture at 300 K, 4 atm. a: CDI, 3 mJ energy, 100 μs duration; b: breakdown discharge, 20 mJ energy, 80 ns duration; c: CDI, 3 mJ energy, 100 μs duration, plus 2 A, 30 mJ energy, 230 μs duration arc; d: CDI, 3 mJ energy, 100 μs duration, plus 60 mA, 30 mJ energy, 770 μs duration glow discharge.[53]

56 and 57). They are based on the requirement that the energy release due to chemical reaction in the plasma front (and production of radical species) exceed the losses due to conduction and diffusion to the unburned gas ahead of the front. While these models are incomplete, they do provide a theoretical basis for the well-known fact that the minimum energy required to ignite a premixed fuel-air mixture depends strongly on mixture composition. Figure 9-45 shows a typical set of results on the minimum ignition energy as a function of the equivalence ratio under quiescent conditions.[58] The curve shows a minimum for slightly rich-of-stoichiometric mixtures; the minimum energy required for successful ignition increases rapidly as the mixture is leaned out. While the initial plasma kernel

PETITIONER'S EXHIBIT 1002
US PATENT NO. 6,581,565

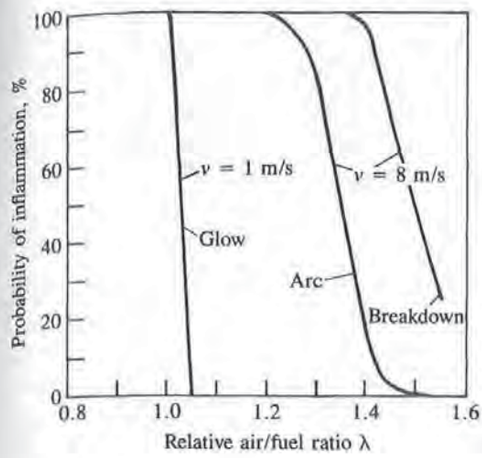


FIGURE 9-44
Probability of inflammation of stoichiometric methane-air mixture, at 300 K, 4 atm, as function of relative air/fuel ratio λ ($=1/\phi$) for different ignition discharges with equal total electrical energy (30–33 mJ). Breakdown: 30 mJ, 60 ns duration. Arc: CDI, 3 mJ, 100 μs duration; plus 2 A, 30 mJ, 230 μs duration arc. Glow: CDI, 3 mJ, 100 μs duration; plus 60 mA, 30 mJ, 770 μs duration glow discharge. v = mixture velocity.[52]

growth (up to 10 to 100 μs) is not greatly affected by the mixture equivalence ratio, the inflammation process and the thickness and rate of propagation of the resulting flame are strongly affected. The lean side of the minimum is of more practical interest than the rich side. Because the chemical energy density of the mixture and flame temperature decrease as the mixture is leaned out, the flame speed decreases and the flame becomes thicker. Thus more time is available for heat losses from the inflammation zone, less energy is available to offset these losses, and the rate of energy transfer into the zone decreases. The consequence is that, as the mixture is leaned out, the approximately spherical discharge-created plasma must grow to a larger size before inflammation will occur. Substantially, more energy must therefore be supplied to the discharge.[53]

In engines, the mixture is not quiescent: mean and fluctuating velocities in the range 1 to 10 m/s exist in the clearance volume at TC (see Sec. 8.2.2). On the time scale of the breakdown discharge phase (10 ns), this fluid motion is not important. In the arc and glow discharge phases, however, the arc is convected

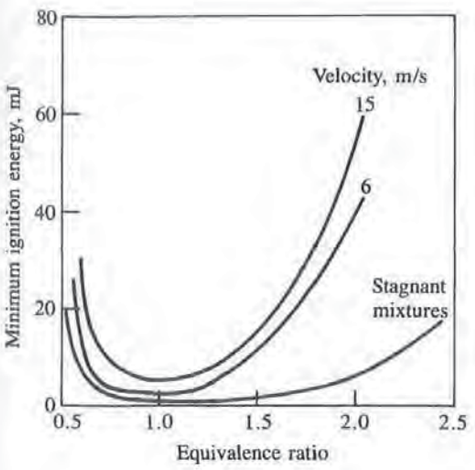


FIGURE 9-45
Effect of mixture equivalence ratio and flow velocity on minimum ignition energy for propane-air mixtures at 0.17 atm.[58]

PETITIONER'S EXHIBIT 1002
US PATENT NO. 6,581,565



FIGURE 9-46
Photographs of single glow discharge (30 mJ, 0.77–1.5 ms) in air at 2 atm flowing perpendicular to axis of electrodes. Below 25 m/s almost no multiple discharges; above 25 m/s only multiple discharges. 1.2 mm electrode gap.[56]

by the flow and lengthened accordingly, as illustrated in Fig. 9-46. For velocities below 15 m/s a steady increase in discharge channel length occurs. For higher velocities, an increasing number of reignitions occur, so the discharge energy is distributed into many separate channels. As the channel lengthens, the ratio of total discharge voltage to anode plus cathode voltage drop increases substantially, and the relative importance of heat losses to the electrodes decreases. Thus more energy is transferred to the gas—the energy-transfer efficiency increases. However, as the channel is lengthened, the energy transferred is spread over a larger volume. Depending on flow velocity, and mixture and discharge conditions, increasing velocity may increase or decrease the minimum ignition energy or the lean ignition limit for a specific ignition system. Both the mean flow velocity and turbulence levels are important.[53–58] With a conventional coil ignition system, increasing mean flow velocity up to the point where reignitions start to occur extends the lean limit. With breakdown discharge systems, the lean ignition limit decreases as flow velocity increases.[53] With capacitive-discharge systems at low flow velocities, the flow has little impact: at high flow velocities the minimum ignition energy increases.[59]

Maly[53] has summarized these fundamental aspects of spark-discharge ignited flames as follows:

1. Of the total electrical energy supplied to the spark, only that fraction contained within the outer surface layer of the plasma (of thickness of the order of the inflammation zone) is available for initiating the flame propagation process. The energy density and the temperature gradient in this layer depend on the discharge mode. Highest energy densities and temperature gradients are achieved if the ignition energy is supplied in the shortest time interval.
2. A minimum radius of the spark plasma is required for inflammation of the fuel-air mixture to occur. This radius increases rapidly as the mixture is leaned out (or diluted); it decreases with increasing pressure and increasing plasma expansion velocity.
3. After inflammation, burning rates are proportional to flame surface area. Thus discharges and plasma geometries that produce the largest inflammation zone surface area, most rapidly, are advantageous.

PETITIONER'S EXHIBIT 1002
US PATENT NO. 6,581,565

4. The time over which the ignition energy can be used effectively for inflammation decreases as the initial flame velocity increases. Ignition energy supplied after inflammation has occurred will have only a modest impact on flame propagation.

9.5.2 Conventional Ignition Systems

The ignition system must provide sufficient voltage across the spark plug electrodes to set up the discharge and supply sufficient energy to the discharge to ignite the combustible mixture adjacent to the plug electrodes under all operating conditions. It must create this spark at the appropriate time during the compression stroke. Usually spark timing is set to give maximum brake torque for the specific operating condition, though this maximum torque may be constrained by emission control or knock control requirements. For a given engine design, this optimum spark timing varies as engine speed, inlet manifold pressure, and mixture composition vary. Thus, in most applications, and especially the automotive applications, the system must have means for automatically changing the spark timing as engine speed and load vary.

With an equivalence ratio best suited for ignition and with homogeneous mixture distribution, spark energies of order 1 mJ and durations of a few microseconds would suffice to initiate the combustion process. In practice, circumstances are less ideal. The air, fuel, and recycled exhaust are not uniformly distributed between cylinders; the mixture of air, fuel, recycled exhaust gas, and residual gas within each cylinder is not homogeneous. Also, the pressure, temperature, and density of the mixture between the spark plug electrodes at the time the spark is needed affect the voltage required to produce a spark. These vary significantly over the load and speed range of an engine. The spark energy and duration, therefore, has to be sufficient to initiate combustion under the most unfavorable conditions expected in the vicinity of the spark plug over the complete engine operating range. Usually if the spark energy exceeds 50 mJ and the duration is longer than 0.5 ms reliable ignition is obtained.

In addition to the spark requirements determined by mixture quality, pressure, temperature, and density, there are others determined by the state of the plugs. The erosion of the plug electrodes over extended mileage increases the gap width and requires a higher breakdown voltage. Also, spark plug fouling due to deposit buildup on the spark plug insulator can result in side-tracking of the spark. When compounds formed by the burning of fuel, lubricating oil, and their additives are deposited on the spark plug insulator, these deposits provide an alternative path for the spark current. If the resistance of the spark plug deposits is sufficiently low, the loss of electrical energy through the deposits may prevent the voltage from rising to that required to break down the gas. The influence of side-tracking on spark generation decreases with lower source impedance of the high-voltage supply, and therefore with a higher available energy.

The fundamental requirements of the high-voltage ignition source can be summarized as: (1) a high ignition voltage to break down the gap between the

PETITIONER'S EXHIBIT 1002
US PATENT NO. 6,581,565

plug electrodes; (2) a low source impedance or steep voltage rise; (3) a high energy storage capacity to create a spark kernel of sufficient size; (4) sufficient duration of the voltage pulse to ensure ignition. There are several commonly used concepts that partly or fully satisfy these requirements.[54, 60]

COIL IGNITION SYSTEMS. Breaker-operated inductive ignition systems have been used in automotive engines for many years. While they are being replaced with more sophisticated systems (such as transistorized coil ignition systems), they provide a useful introduction to ignition system design and operation. Figure 9-47 shows the circuit of a typical breaker ignition system. The system includes a battery, switch, resistor, coil, distributor, spark plugs, and the necessary wiring. The circuit functions as follows. If the breaker point is closed when the ignition is switched on, current flows from the battery, through the resistor, primary winding of the ignition coil, contacts, and back to the battery through ground. This current sets up a magnetic field within the iron core of the coil. When ignition is required, the breaker points are opened by the action of the distributor cam, interrupting the primary current flow. The resulting decay of magnetic flux in the coil induces a voltage in both the primary and secondary windings. The voltage induced in the secondary winding is routed by the distributor to the correct spark plug to produce the ignition spark.

The current and voltage waveforms are shown in Fig. 9-48. The primary current for any given time of contact closure t is given by

$$I_p = \frac{V_0}{R}(1 - e^{-Rt/L_p}) \tag{9.53}$$

where I_p is the primary current, V_0 is the supply voltage, R is the total primary circuit resistance, and L_p is the primary circuit inductance. The primary current requires time to build up. At low speeds the time of contact closure is sufficient for the primary current to reach the maximum permitted by the circuit resistance; at high speeds the primary current may not reach its maximum. Thus, only at higher engine speeds does the term e^{-Rt/L_p} become significant. When the points open the primary current falls to zero and a voltage of order 15 kV is induced in the secondary winding. If the coil is not connected to a spark plug,

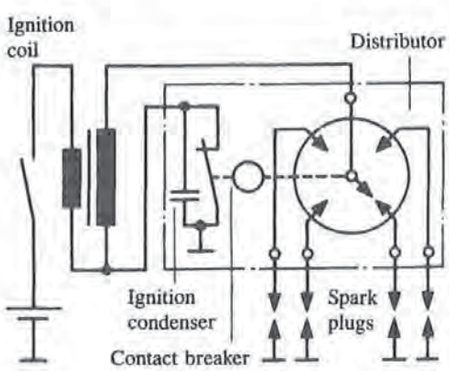


FIGURE 9-47
Schematic of conventional coil ignition system. (*Courtesy Robert Bosch GmbH and SAE.*[54])

PETITIONER'S EXHIBIT 1002
US PATENT NO. 6,581,565

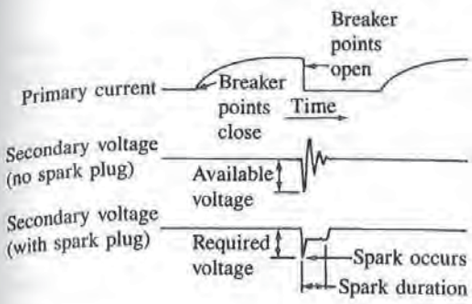


FIGURE 9-48
Current and voltage waveforms for breaker ignition system.[61]

this induced voltage will have a damped sinusoidal waveform, as shown in the center trace. The peak value of this voltage is the maximum voltage that can be produced by the system and is called the *available voltage* V_a of the system. The maximum energy transferred to the secondary system is given by

$$E_{s,\,\max} = \frac{1}{2} C_s V_a^2$$

where C_s is the total capacitance of the secondary circuit. Hence, the available voltage of the system is given by

$$V_a = \left(\frac{2E_{s,\,\max}}{C_s} \right)^{1/2} \tag{9.54}$$

If all the energy stored in the primary circuit of the coil, $\frac{1}{2} L_p I_p^2$, is transferred to the secondary,

$$V_a = I_p \left(\frac{L_p}{C_s} \right)^{1/2} \tag{9.55}$$

When the coil is connected to a spark plug, the secondary voltage will rise to the breakdown potential of the spark plug, and a discharge between the plug electrodes will occur. This alters the waveform as shown in the bottom trace of Fig. 9-48. After the spark occurs, the voltage is reduced to a lower value until all the energy is dissipated and the arc goes out. The value of this voltage which caused breakdown to occur is called the *required voltage* of the spark plug. The interval during which the spark occurs is called the *spark duration*. The available voltage of the ignition system must always exceed the required voltage of the spark plug to ensure breakdown. The spark must then possess sufficient energy and duration to initiate combustion under all conditions of operation.

The major limitations of the breaker-operated induction-coil system are the decrease in available voltage as engine speed increases due to limitations in the current switching capability of the breaker system, and the decreasing time available to build up the primary coil stored energy. Also, because of the high source impedance (about 500 kΩ) the system is sensitive to side-tracking across the spark plug insulator. A further disadvantage is that due to their high current

PETITIONER'S EXHIBIT 1002
US PATENT NO. 6,581,565

load, the breaker points are subject to electrical wear in addition to mechanical wear, which results in short maintenance intervals. The life of the breaker points is dependent on the current they are required to switch. Acceptable life is obtained with $I_p \approx 4$ A; increased currents cause a rapid reduction in breaker point life and system reliability.

TRANSISTORIZED COIL IGNITION (TCI) SYSTEMS. In automotive applications, the need for much reduced ignition system maintenance, extended spark plug life, improved ignition of lean and dilute mixtures, and increased reliability and life has led to the use of coil ignition systems which provide a higher output voltage and which use electronic triggering to maintain the required timing without wear or adjustment (see Refs. 54 and 61). These are called transistorized coil ignition (TCI) or high-energy electronic-ignition systems. The higher output voltage is required because spark plugs are now set to wider gaps (e.g., about 1 mm) to extend the ability to ignite the fuel mixture over a wider range of engine operation, and because during the extended mileage between spark plug replacement electrode erosion further increases the gap. In automotive applications an available ignition voltage of 35 kV is now usually provided. In addition to higher voltage, longer spark duration (about 2 ms) has been found to extend the engine operating conditions over which satisfactory ignition is achieved.

Most of the solid-state ignition systems now in use operate on the same basic principle. Figure 9-49 shows the block circuit diagram of a transistorized coil ignition system. The distributor points and cam assembly of the conventional ignition system are replaced by a magnetic pulse generating system which detects the distributor shaft position and sends electrical pulses to an electronic control module. The module switches off the flow of current to the coil primary windings, inducing the high voltage in the secondary windings which is distributed to the

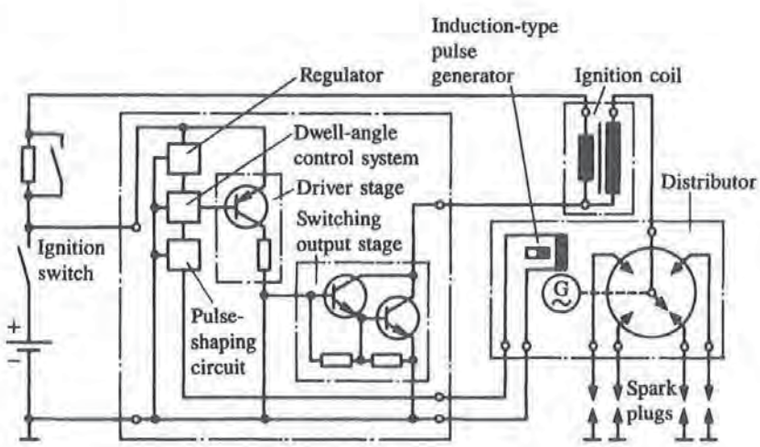


FIGURE 9-49
Schematic of transistorized coil ignition system with induction pulse generator. (*Courtesy Robert Bosch GmbH and SAE.*[54])

PETITIONER'S EXHIBIT 1002
US PATENT NO. 6,581,565

spark plugs as in the conventional breaker system. The control module contains timing circuits which then close the primary circuit so that buildup of primary circuit current can occur. There are many types of pulse generators that could trigger the electronic circuit of the ignition system.[60] A magnetic pulse generator, where a gear-shaped iron rotor driven by the distributor shaft rotates past the stationary pole piece of the pickup, is usually used. The number of teeth on the rotor is the same as the number of cylinders. A magnetic field is provided by a permanent magnet. As each rotor tooth passes the pole piece it first increases and then decreases the magnetic field strength ψ linked with the pickup coil, producing a voltage signal proportional to $d\psi/dt$. The electronic module switches off the coil current to produce the spark as the rotor tooth passes through alignment and the pickup coil voltage abruptly reverses and passes through zero. The increasing portion of the voltage waveform, after this voltage reversal, is used by the electronic module to establish the point at which the primary coil current is switched on for the next ignition pulse.

CAPACITIVE-DISCHARGE IGNITION (CDI) SYSTEMS. With this type of system (shown schematically in Fig. 9-50) a capacitor, rather than an induction coil, is used to store the ignition energy. The capacitance and charging voltage of the capacitor determine the amount of stored energy. The ignition transformer steps up the primary voltage, generated at the time of spark by the discharge of the capacitor through the thyristor, to the high voltage required at the spark plug. The CDI trigger box contains the capacitor, thyristor power switch, charging device (to convert battery voltage to the charging voltage of 300 to 500 V by means of pulses via a voltage transformer), pulse shaping unit, and control unit.

The principal advantage of CDI is its insensitivity to electrical shunts in the high-voltage ignition circuit that result from spark plug fouling. Because of the fast capacitive discharge, the spark is strong but short (0.1 to 0.3 ms). This can lead to ignition failure at operating conditions where the mixture is very lean or dilute.[54]

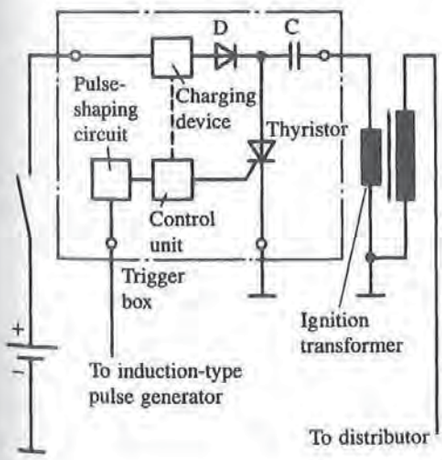


FIGURE 9-50
Schematic of capacitive-discharge system. (*Courtesy Robert Bosch GmbH and SAE.*[54])

PETITIONER'S EXHIBIT 1002
US PATENT NO. 6,581,565

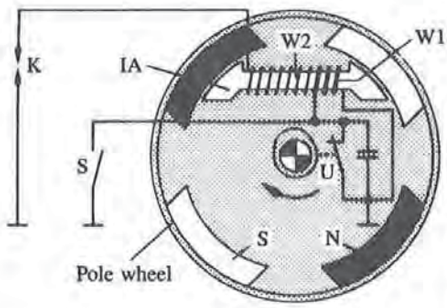


FIGURE 9-51
Schematic of breaker-triggered magneto system with ignition armature. (*Courtesy Robert Bosch GmbH and SAE.*[54])

MAGNETO IGNITION. With this type of ignition system, a magneto supplies the ignition voltage for the spark discharge independent of a battery or generator. Magneto ignition is commonly used in small four-stroke and two-stroke engines. Figure 9-51 illustrates the system and its operation. A time-varying magnetic flux Φ_0 is set up in the ignition armature (IA) as the rotating permanent magnets on the pole wheel generate a current in the closed primary winding W1. This primary current generates an additional flux Φ_I, giving a resultant flux $\Phi_R = \Phi_0 + \Phi_I$. To generate the ignition voltage, the primary current flow is interrupted and the flux collapses rapidly from Φ_R to Φ_0, producing a high-voltage pulse in the winding which is connected to the spark plug electrode. The current can be interrupted with contact breakers (breaker-triggered magneto) or with a transistor (semiconductor magneto). Since the flux generated by the rotating pole wheel depends on engine speed, the magnitude of the ignition voltage varies with speed.[54]

SPARK PLUG DESIGN. The function of the spark plug is to provide an electrode gap across which the high-voltage discharge occurs which ignites the compressed mixture of fuel vapor and air in the combustion chamber. In addition, it must provide a gas-tight conducting path from the high-voltage wire to the electrode gap. Figure 9-52 shows a typical spark plug design. There are three principal

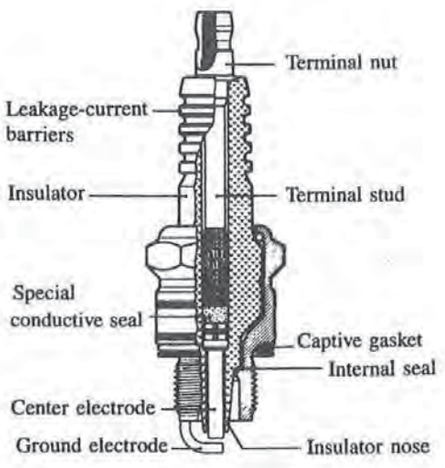


FIGURE 9-52
Cutaway drawing of conventional spark plug. (*Courtesy Robert Bosch GmbH and SAE.*[54])

PETITIONER'S EXHIBIT 1002
US PATENT NO. 6,581,565

components: an insulator, electrodes, and a shell. The insulated material must have adequate thermal shock resistance, tensile and compressive strength, and impact strength. It must also have low porosity to limit absorption of combustion gases and high resistivity to prevent leakage of high-voltage charge at both ambient temperatures and normal operating temperatures. Alumina is usually used as the insulator material.

The electrodes are normally made of high-nickel alloys to withstand the high ignition voltage, high temperatures, and corrosive gases with minimum erosion. The center-electrode surface temperatures can average 650–700°C under normal operating conditions. A wide range of electrode geometries are available.

The location of the special conductive seal within the shell affects the *heat rating* of the spark plug. For a "hot" plug, an insulator with a long conical nose is used; for a "cold" plug a short-nosed insulator is used. The length of the heat conduction path from the insulator nose to the shell is changed in this way to vary and control the temperature of the exposed part of the insulator. The spark plug insulator tip temperature increases with increasing speed. It is desirable to have the tip hotter than about 350°C to prevent fouling at low speed. High-speed high-load tip temperatures must be kept below about 950°C to prevent preignition. Normally, the gap between the center and ground electrodes is 0.7 to 0.9 mm. For extremely dilute mixtures this is usually increased to 1.2 mm. Magneto ignition systems use smaller gaps ($\sim$0.5 mm). High-compression-ratio racing engines use smaller gaps (0.3 to 0.4 mm).[54]

9.5.3 Alternative Ignition Approaches

A large number of methods for initiating combustion in spark-ignition engines with electrical discharges, in addition to those described in the previous section, have been proposed and examined. These include different designs of spark plug, use of more than one plug, use of higher power, higher energy, or longer-duration discharges, and ignition systems that initiate the main combustion process with a high-temperature reacting jet—plasma-jet and flame-jet ignition systems.[62] Conventional ignition systems normally ignite the unburned fuel, air, burned gas mixture within the cylinder and perform satisfactorily under conditions away from the lean or dilute engine stable operating limit. Thus, these alternative ignition approaches have the goal of extending the engine stability limit (and/or of reducing the cyclic combustion variability near the stability limit), usually by achieving a faster initial burning rate than can be obtained with conventional systems. This section describes the more interesting of these alternative ignition approaches.

ALTERNATIVE SPARK-DISCHARGE APPROACHES. There are many different designs of spark plugs. These use different geometry electrodes, gap widths, and gap arrangements. The effects of the major plug electrode design features on the engine's stable lean operating limit are illustrated in Fig. 9-53.[63] Ignition system effects are important when misfire due to the quenching effect of the spark plug

PETITIONER'S EXHIBIT 1002
US PATENT NO. 6,581,565

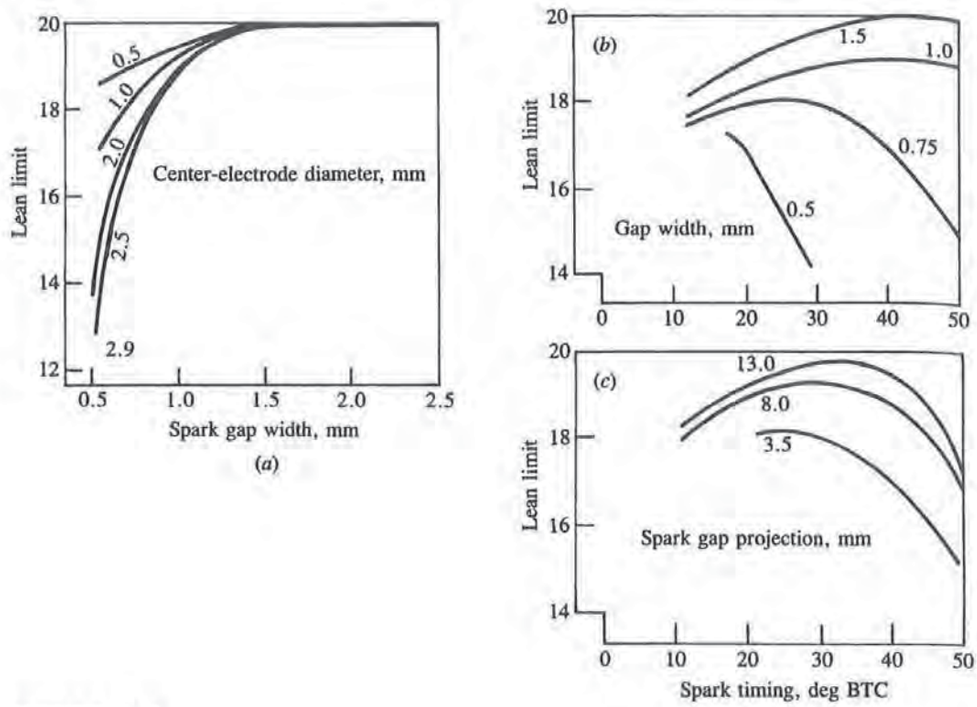


FIGURE 9-53
Effect of spark plug electrode diameter, plug gap width, and projection of gap into chamber on air/fuel ratio at engine's lean stable operating limit. Baseline conditions: 30 mJ spark energy, 3.5 mm projection, center electrode diameter 2.5 mm, gap width 0.75 mm, 40° BTC spark timing. 1600 rev/min, intake pressure 300 mmHg.[63]

electrodes determines the stable operating limit.† Thus, smaller spark plug center-electrode diameters (Fig. 9-53*a*), larger electrode gap widths (Fig. 9-53*b*), and higher electrode temperatures (obtained by projecting the gap further into the combustion chamber; Fig. 9-53*c*), all extend the lean stability limit to leaner (or more dilute) mixtures for the more advanced spark timings and smaller gap widths. For spark timing closer to TC and for larger gap widths, these data show the lean stability limit to be much less sensitive (or not sensitive at all) to plug geometry or spark energy. Multigap plugs, designed to produce a series of discharges which together form a long arc, have also been used to generate a larger initial flame kernel and thereby extend the lean limit.

Use of more than one plug, at separate locations in the combustion chamber and fired simultaneously, is also common.[49] The advantages are twofold. First, the effective flame area in the early stages of flame development is increased substantially (e.g., by almost a factor of two for two widely spaced plugs). Second, the variations in flow velocity and mixture composition in the vicinity of the (multiple) plugs produce less variability in the initial mixture burning rate than occurs with a single plug. Studies of heat-release rates, flame

† See Sec. 9.4.3 for a detailed discussion of the stable operating limit.

PETITIONER'S EXHIBIT 1002
US PATENT NO. 6,581,565

development angle, and rapid-burning angle, and imep and torque fluctuations have defined the effects of both increasing the number of ignition sites from 1 to 12 and of changing their geometric location.[64] These results confirm that increasing the number of simultaneously developing flame kernels increases the initial mixture burning rate, as anticipated. It also extends the lean stable operating limit and reduces cyclic combustion variability under conditions where slow and occasional partial-burning cycles would occur with fewer spark plug gaps.

Many studies have examined the effects of higher-energy discharges on engine operation near the lean operating limit. It is useful to differentiate between higher current discharges and longer duration discharges: most high-energy (conventional-type) ignition systems have both these features. The results of these studies show that away from the lean or dilute stable operating limit, increasing the discharge current or duration has no significant effect on engine operating characteristics. The higher current does, as would be expected, result in a larger flame kernel during the inflammation process and thereby modestly reduces the spark advance required for maximum brake torque with a given combustion chamber and set of operating conditions. Figure 9-54 shows these trends for rich, stoichiometric, and slightly lean mixtures. The figure also shows that both higher

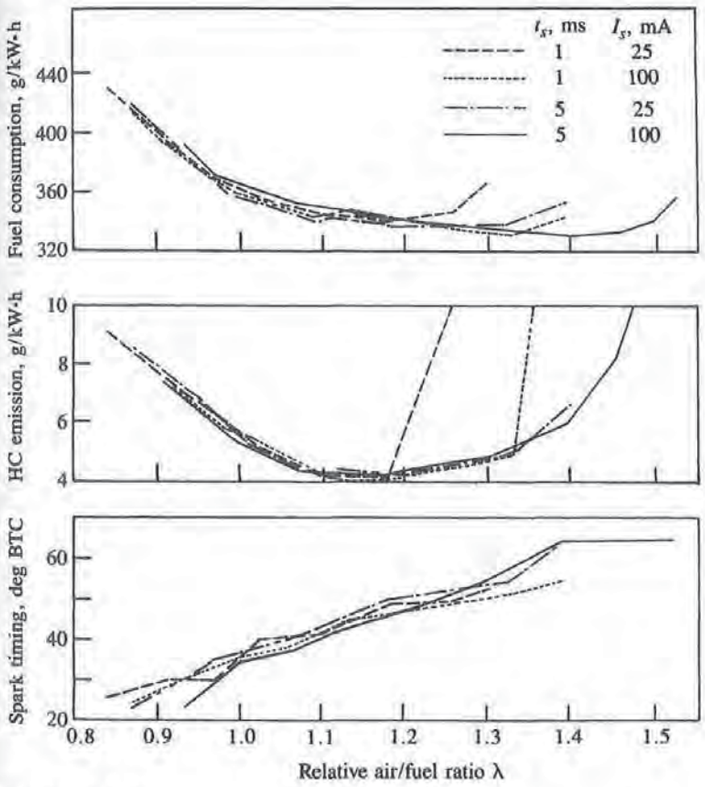


FIGURE 9-54
Effect of higher spark currents I_s and longer spark durations t_s on fuel consumption, HC emissions, and MBT spark timing, as a function of relative air/fuel ratio λ ($=1/\phi$). 2000 rev/min, bmep = 3 atm, 2.8-dm^3 six-cylinder engine.[65]

PETITIONER'S EXHIBIT 1002
US PATENT NO. 6,581,565

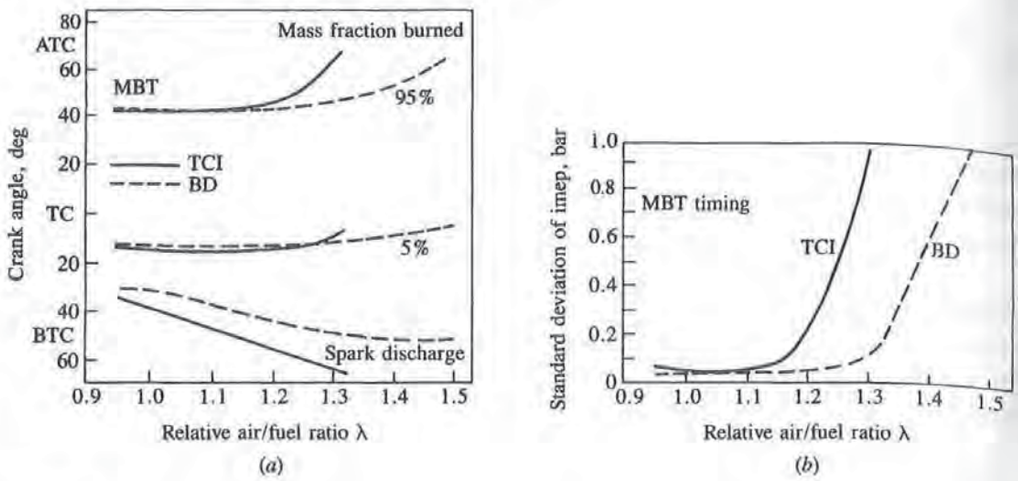


FIGURE 9-55
(*a*) MBT spark timing and location of 5 and 95 percent mass fraction burned points for conventional transistorized coil ignition (TCI) system (43 mJ energy, 2 ms duration) and breakdown system (BD) (43 mJ energy, ~10 ns duration) as function of relative air/fuel ratio λ ($=1/\phi$). (*b*) Standard deviation in indicated mean effective pressure as a function of relative air/fuel ratio λ for TCI and BD systems.[66]

currents and longer duration discharges do extend the lean engine stability limit [and also the dilute (with EGR) stability limit]. Note the HC emissions data, which indicate that longer discharges have a greater impact than higher currents on extending the *misfire* limit. The increase in fuel consumption as the lean operating limit is approached is due to the rapidly increasing cycle-by-cycle combustion variability.

The discussion of discharge fundamentals in Sec. 9.5.1 showed that depositing energy into the discharge during the initial short breakdown phase resulted in faster flame kernel growth than did depositing the same energy at slower rates. Ignition systems of this type have been used. In such systems, a capacitor is connected in parallel with the spark plug electrodes, and a low-impedance discharge path allows the energy stored in the capacitor to be discharged into the gap very rapidly. The anticipated effects on the engine's combustion process are observed. Away from the lean engine stability limit, the primary impact is a reduction in the flame development period due to the more rapid initial flame kernel growth. Thus MBT timing is less advanced with these breakdown systems than with conventional systems (see Fig. 9-55*a*). The lean limit can also be extended, and acceptable engine stability obtained (i.e., tolerable cycle-by-cycle combustion variations) for leaner or more dilute engine operation, as shown in Fig. 9-55*b*.[66, 67]

PLASMA-JET IGNITION. In a plasma-jet ignitor, the spark discharge is confined within a cavity that surrounds the plug electrodes, which connects with the combustion chamber via an orifice. The electrical energy supplied to the plug elec-

PETITIONER'S EXHIBIT 1002
US PATENT NO. 6,581,565

trodes is substantially increased above values used in normal ignition systems by allowing a capacitor to discharge at a relatively low voltage and high current through the spark generated in a conventional manner with a high-voltage low-current ignition system. Stored energies of about 1 J are typically used, and this energy is discharged in some 20 μs. This high-power discharge creates a high-temperature plasma so rapidly that the pressure in the cavity increases substantially, causing a supersonic jet of plasma to flow from the cavity into the main combustion chamber. The plasma enters the combustion chamber as a turbulent jet, preceded by a hemispherical blast wave. The gas dynamic effects of the blast wave are dissipated by the time combustion starts, which is typically of order 1 ms after the discharge commences. Ignition in the main combustion chamber takes place in the turbulent jet; the flame starts out as a turbulent flame in contrast to the flame with conventional ignition systems, which is initially laminarlike. The penetration of the jet depends on its initial momentum; it thus depends on the amount of energy deposited, cavity size, and orifice area. If the cavity is filled prior to ignition with a hydrocarbon (or a mixture of hydrocarbons) the ignition capabilities are enhanced due to the large increase in hydrogen atoms created in the plasma.[62]

The effects of plasma-jet ignitors on engine combustion are similar to those of breakdown ignition systems: the flame development period is significantly shortened, and the engine's lean stable operating limit is extended. In addition, the phenomenon of misfire, which is the failure to initiate combustion in a fraction of the engine's operating cycles, no longer occurs.[68] The lean operating limit of the engine is, however, normally controlled by flame extinguishment.

FLAME-JET IGNITION. With this type of system, ignition occurs in a prechamber cavity which is physically separated from the main chamber above the piston and is connected to it via one or more orifices or nozzles. As the flame develops in this cavity the pressure of the gases in the prechamber rises, forcing gas out into the main chamber through the orifice (or orifices) as one or more turbulent burning jets. The jet or jets penetrate into the main chamber, igniting the unburned mixture in the main chamber, thereby initiating the primary combustion process. Ignition within the cavity is usually achieved with a conventional spark discharge. The function of the prechamber or cavity is to transform the initial flame around the spark plug electrodes into one or more flame jets in the main chamber, which have a substantial surface area that can ignite extremely lean or dilute mixtures in a repeatable manner. Many different systems for achieving this goal have been developed; some of these have been used in production spark-ignition engines. Examples of the three major types of flame-jet ignition systems are shown in Fig. 9-56.

Figure 9-56*a* shows an example of the simplest type of flame-jet ignition concept (often called a *torch cell*). The cavity has no separate valve so is unscavenged; nor is there any prechamber fuel metering system. The function of the prechamber cavity is to increase the initial growth rate of the flame immediately following spark discharge by having this flame growth take place in a

PETITIONER'S EXHIBIT 1002
US PATENT NO. 6,581,565

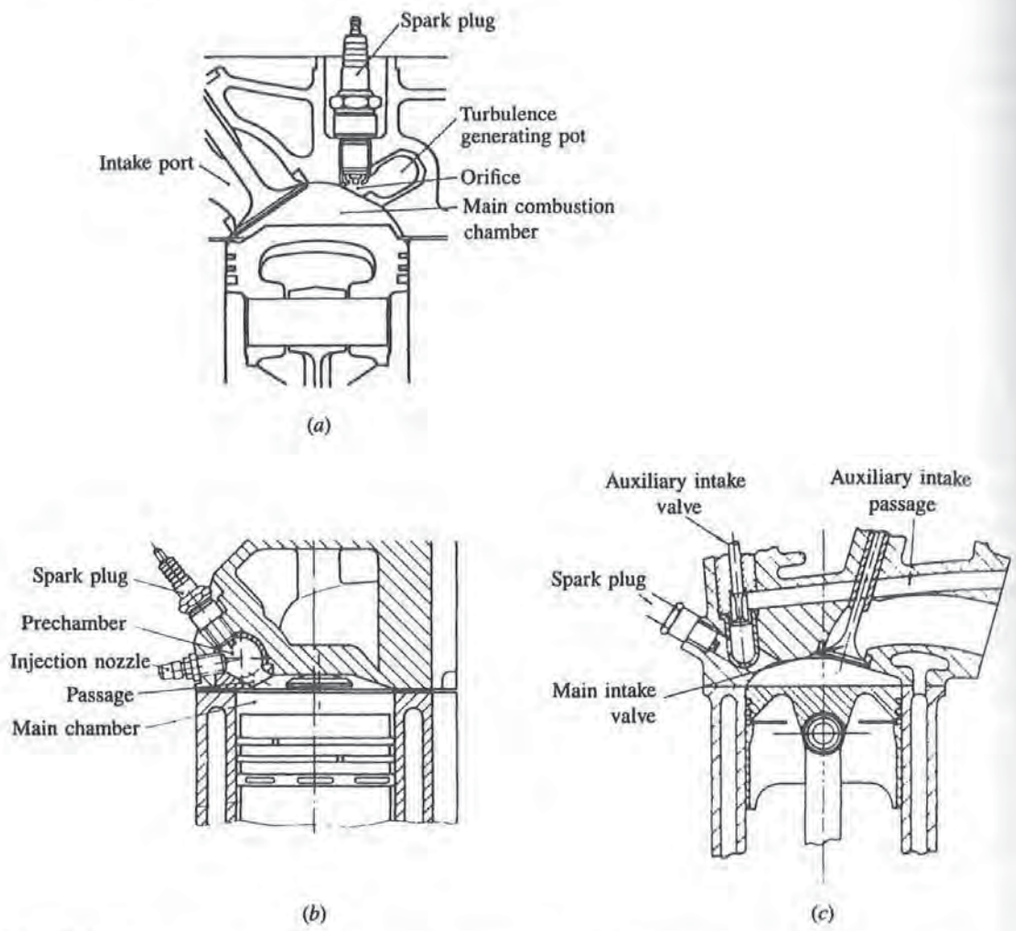


FIGURE 9-56
Flame-jet ignition concepts: (*a*) turbulence-generating torch cell;[69] (*b*) prechamber stratified-charge engine with auxiliary fuel injector with no prechamber scavenging;[70] (*c*) prechamber stratified-charge engine with prechamber inlet valve and auxiliary carburetor.[71]

more turbulent region than the main combustion chamber: the flame jet or jets which then emerge from the cavity produce a large initial flame surface area in the main chamber to start the bulk charge combustion process. The prechamber system shown was called a turbulent generating pot.[69] Another approach is to incorporate the cavity into the spark plug. Systems with prechamber volumes varying from 20 percent of the clearance volume to less than 1 percent have been developed. The flow pattern produced within the prechamber by the flow into the cavity during compression and the location of the spark plug electrodes within the cavity and of the nozzle or orifice are critical design issues. A major problem with these systems is that the prechamber is never completely scavenged by fresh mixture between cycles, so the burned gas fraction in the unburned mixture within the prechamber is always substantially higher than the burned gas fraction in the unburned main chamber mixture.[72]

PETITIONER'S EXHIBIT 1002
US PATENT NO. 6,581,565

Figure 9-56*b* and *c* shows two *prechamber stratified-charge* engine flame-jet ignition concepts. Here the mixture in the prechamber cavity is enriched by addition of fuel so that it ends up being slightly rich-of-stoichiometric at the time of spark discharge. The initial inflammation process in the cavity then occurs more rapidly and more repeatably. The operating principle of these stratified-charge systems is described briefly in Sec. 1.9. Figure 9-56*b* shows a system where the prechamber is unscavenged and fuel is injected directly into the prechamber cavity (in addition to the main fuel-injection process which occurs into the fresh charge in the intake system) to richen the mixture (which is lean overall) at the time of spark to an easily ignitable rich-of-stoichiometric composition. With this approach, the prechamber volume is usually 20 to 25 percent of the clearance volume. Figure 9-56*c* shows a prechamber stratified-charge flame-jet ignition system where the prechamber is scavenged between each combustion event. With this approach, a separate small intake valve feeds very rich mixture into the prechamber during the intake process, while the main fuel metering system feeds lean mixture to the main intake valve. During intake the prechamber is completely scavenged by the rich intake stream. During compression the lean mixture flowing from the main chamber to the prechamber brings the prechamber mixture equivalence ratio to slightly rich-of-stoichiometric at the time of spark discharge.[71]

The number and size of the orifices connecting the prechamber and the main chamber have a significant effect on the development of the main chamber burning process. Two different approaches are shown in the flame development stage in Fig. 9-57. Figure 9-57*a* shows the jets produced when the prechamber has more than one small nozzle which direct the burning prechamber mixture deep into the main chamber charge. A fast burning of the lean main-chamber charge results. With this approach, prechamber volumes of 2 to 3 percent of the clearance volume and nozzle area/prechamber volume ratios of 0.03 to 0.04 cm^{-1} are used. Figure 9-57*b* shows the approach used by Honda in their CVCC engine.

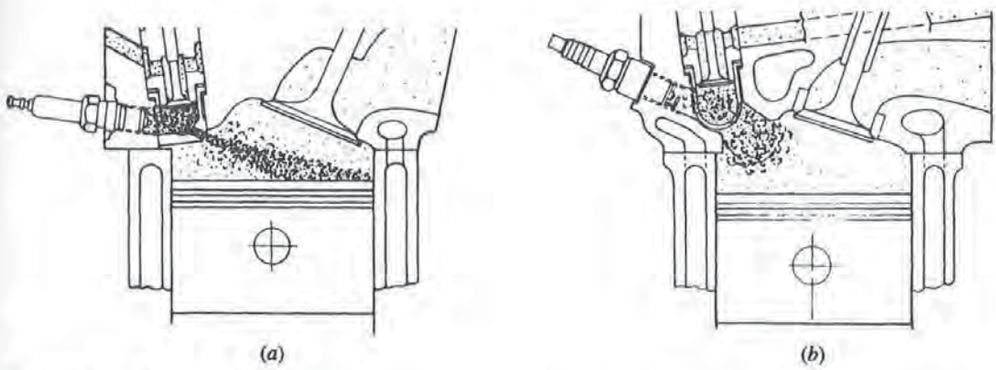


FIGURE 9-57
Two different approaches to prechamber orifice design with the prechamber stratified-charge carbureted and scavenged engine: (*a*) one or more small orifice(s) for deep jet penetration and faster burning process; (*b*) large orifice for lower-velocity jet and slower burn.[73]

PETITIONER'S EXHIBIT 1002
US PATENT NO. 6,581,565

A larger prechamber (5 to 12 percent) and larger orifice (orifice area/prechamber volume ratio of 0.04 to 0.2 cm^{-1}) gives a lower velocity jet which penetrates the main chamber charge more slowly, resulting in a slower burn.

All these concepts extend the engine's lean stable operating limit, relative to equivalent conventional engines, by several air/fuel ratios. For example, the unscavenged cavity without auxiliary fueling can operate satisfactorily at part-load with air/fuel ratios of 18 (equivalence ratio $\phi \approx 0.8$, relative air/fuel ratio $\lambda \approx 1.25$). The prechamber stratified-charge flame-jet ignition concepts can operate much leaner than this; however, the best combination of fuel consumption and emissions characteristics is obtained with $\phi \approx 0.9 - 0.75$, $\lambda \approx 1.1 - 1.3$.[70, 71] One performance penalty associated with all these flame-jet ignition concepts is the additional heat losses to the prechamber walls due to increased surface area and flow velocities. The stratified-charge prechamber concepts also suffer an efficiency penalty, relative to equivalent operation with uniform air/fuel ratios, due to the presence of fuel-rich regions during the combustion process.

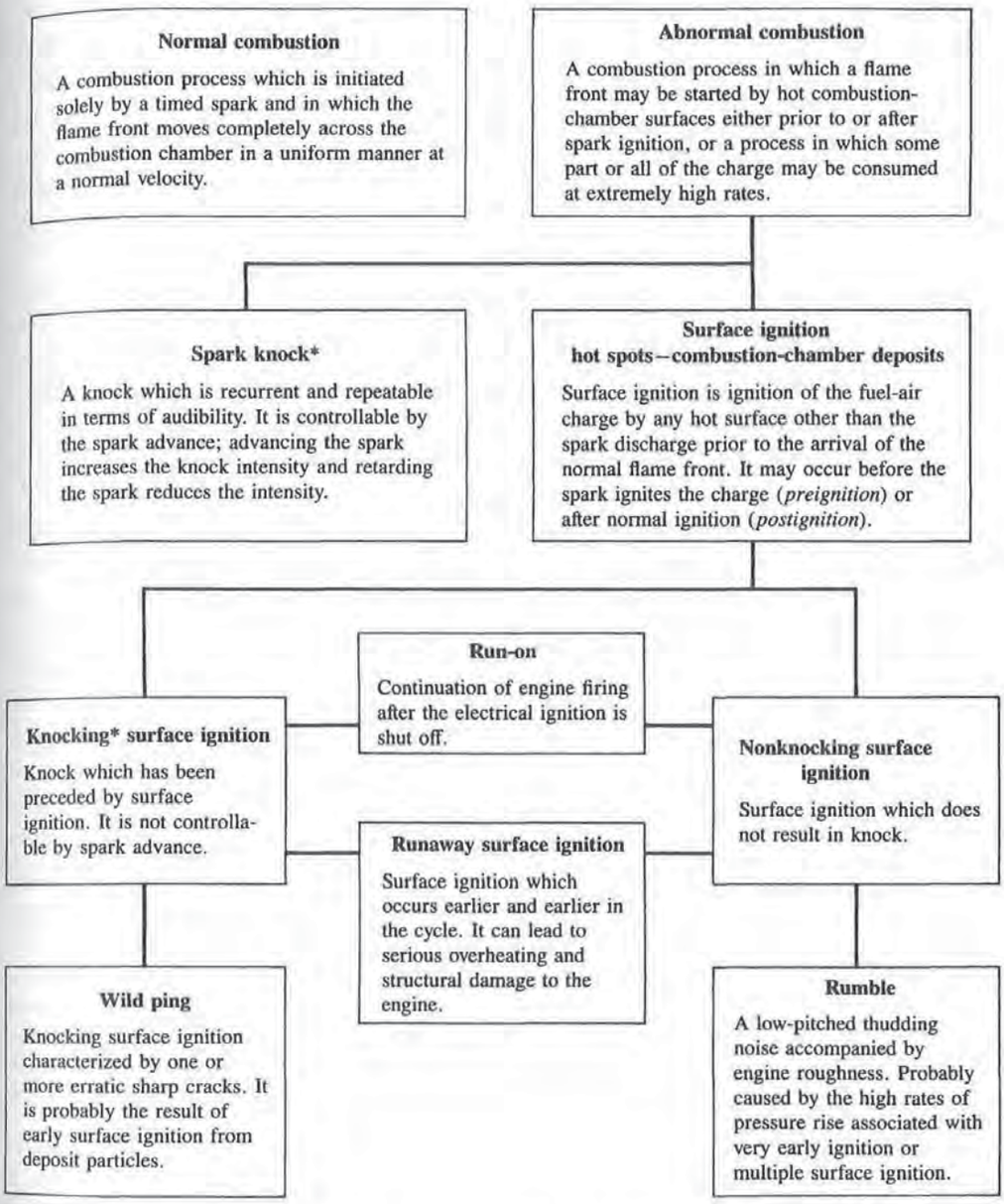
9.6 ABNORMAL COMBUSTION: KNOCK AND SURFACE IGNITION

9.6.1 Description of Phenomena

Abnormal combustion reveals itself it many ways. Of the various abnormal combustion processes which are important in practice, the two major phenomena are knock and surface ignition. These abnormal combustion phenomena are of concern because: (1) when severe, they can cause major engine damage; and (2) even if not severe, they are regarded as an objectionable source of noise by the engine or vehicle operator. *Knock* is the name given to the noise which is transmitted through the engine structure when essentially spontaneous ignition of a portion of the end-gas—the fuel, air, residual gas, mixture ahead of the propagating flame—occurs. When this abnormal combustion process takes place, there is an extremely rapid release of much of the chemical energy in the end-gas, causing very high local pressures and the propagation of pressure waves of substantial amplitude across the combustion chamber. *Surface ignition* is ignition of the fuel-air mixture by a hot spot on the combustion chamber walls such as an overheated valve or spark plug, or glowing combustion chamber deposit: i.e., by any means other than the normal spark discharge. It can occur before the occurrence of the spark (*preignition*) or after (*postignition*). Following surface ignition, a turbulent flame develops at each surface-ignition location and starts to propagate across the chamber in an analogous manner to what occurs with normal spark ignition.

Because the spontaneous ignition phenomenon that causes knock is governed by the temperature and pressure history of the end gas, and therefore by the phasing and rate of development of the flame, various combinations of these two phenomena—surface ignition and knock—can occur. These have been categorized as indicated in Fig. 9-58. When autoignition occurs repeatedly, during

PETITIONER'S EXHIBIT 1002
US PATENT NO. 6,581,565



**Knock*: The noise associated with autoignition of a portion of the fuel-air mixture ahead of the advancing flame front. Autoignition is the spontaneous ignition and the resulting very rapid reaction of a portion or all of the fuel-air mixture.

FIGURE 9-58
Definition of combustion phenomena—normal and abnormal (knock and surface ignition)—in a spark-ignition engine. (*Courtesy Coordinating Research Council.*)

PETITIONER'S EXHIBIT 1002
US PATENT NO. 6,581,565

otherwise normal combustion events, the phenomena is called *spark-knock*. Repeatedly here means occurring more than occasionally: the knock phenomenon varies substantially cycle-by-cycle, and between the cylinders of a multicylinder engine, and does not necessarily occur every cycle (see below). Spark-knock is controllable by the spark advance: advancing the spark increases the knock severity or intensity and retarding the spark decreases the knock. Since surface ignition usually causes a more rapid rise in end-gas pressure and temperature than occurs with normal spark ignition (because the flame either starts propagating sooner, or propagates from more than one source), knock is a likely outcome following the occurrence of surface ignition. To identify whether or not surface ignition causes knock, the terms knocking surface ignition and nonknocking surface ignition are used. Knocking surface ignition usually originates from preignition caused by glowing combustion chamber deposits: the severity of knock generally increases the earlier that preignition occurs. Knocking surface ignition cannot normally be controlled by retarding the spark timing, since the spark-ignited flame is not the cause of knock. Nonknocking surface ignition is usually associated with surface ignition that occurs late in the operating cycle.

The other abnormal combustion phenomena in Fig. 9-58, while less common, have the following identifying names. Wild ping is a variation of knocking surface ignition which produces sharp cracking sounds in bursts. It is thought to result from early ignition of the fuel-air mixture in the combustion chamber by glowing loose deposit particles. It disappears when the particles are exhausted and reappears when fresh particles break loose from the chamber surfaces. Rumble is a relatively stable low-frequency noise (600 to 1200 Hz) phenomenon associated with deposit-caused surface ignition in high-compression-ratio engines. This type of surface ignition produces very high rates of pressure rise following ignition. Rumble and knock can occur together. Run-on occurs when the fuel-air mixture within the cylinder continues to ignite after the ignition system has been switched off. During run-on, the engine usually emits knocklike noises. Run-on is probably caused by compression ignition of the fuel-air mixture, rather than surface ignition. Runaway surface ignition is surface ignition that occurs earlier and earlier in the cycle. It is usually caused by overheated spark plugs or valves or other combustion chamber surfaces. It is the most destructive type of surface ignition and can lead to serious overheating and structural damage to the engine.[74]

After some additional description of surface-ignition phenomena, the remainder of Sec. 9.6 will focus on knock. This is because surface ignition is a problem that can be solved by appropriate attention to engine design, and fuel and lubricant quality. In contrast, knock is an inherent constraint on engine performance and efficiency since it limits the maximum compression ratio that can be used with any given fuel.

Of all the engine surface-ignition phenomena in Fig. 9-58, preignition is potentially the most damaging. Any process that advances the start of combustion from the timing that gives maximum torque will cause higher heat rejection because of the increasing burned gas pressures and temperatures that result.

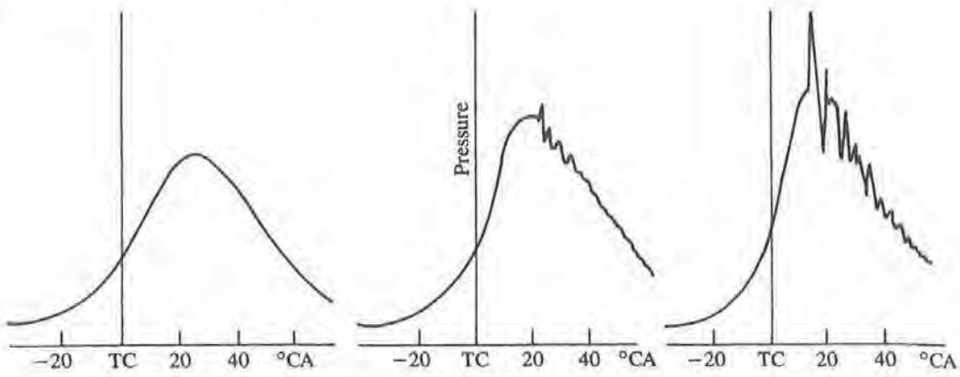
PETITIONER'S EXHIBIT 1002
US PATENT NO. 6,581,565

Higher heat rejection causes higher temperature components which, in turn, can advance the preignition point even further until critical components can fail. The parts which can cause preignition are those least well cooled and where deposits build up and provide additional thermal insulation: primary examples are spark plugs, exhaust valves, metal asperities such as edges of head cavities or piston bowls. Under normal conditions, using suitable heat-range spark plugs, preignition is usually initiated by an exhaust valve covered with deposits coming from the fuel and from the lubricant which penetrates into the combustion chamber. Colder running exhaust valves and reduced oil consumption usually alleviate this problem: locating the exhaust valve between the spark plug and the end-gas region avoids contact with both the hottest burned gas near the spark plug and the end-gas. Engine design features that minimize the likelihood of preignition are: appropriate heat-range spark plug, removal of asperities, radiused metal edges, well-cooled exhaust valves with sodium-cooled valves as an extreme option.[75, 76]

Knock primarily occurs under wide-open-throttle operating conditions. It is thus a direct constraint on engine performance. It also constrains engine efficiency, since by effectively limiting the temperature and pressure of the end-gas, it limits the engine compression ratio. The occurrence and severity of knock depend on the knock resistance of the fuel and on the antiknock characteristics of the engine. The ability of a fuel to resist knock is measured by its octane number: higher octane numbers indicate greater resistance to knock (see Sec. 9.6.3). Gasoline octane ratings can be improved by refining processes, such as catalytic cracking and reforming, which convert low-octane hydrocarbons to high-octane hydrocarbons. Also, antiknock additives such as alcohols, lead alkyls, or an organomanganese compound can be used. The octane-number requirement of an engine depends on how its design and the conditions under which it is operated affect the temperature and pressure of the end-gas ahead of the flame and the time required to burn the cylinder charge. An engine's tendency to knock, as defined by its *octane requirement*—the octane rating of the fuel required to avoid knock—is increased by factors that produce higher temperatures and pressures or lengthen the burning time. Thus knock is a constraint that depends on both the quality of available fuels and on the ability of the engine designer to achieve the desired normal combustion behavior while holding the engine's propensity to knock at a minimum.[74]

The pressure variation in the cylinder during knocking combustion indicates in more detail what actually occurs. Figure 9-59 shows the cylinder pressure variation in three individual engine cycles, for normal combustion, light knock, and heavy knock, respectively.[77] When knock occurs, high-frequency pressure fluctuations are observed whose amplitude decays with time. Figures 9-59*a* and *b* have the same operating conditions and spark advance. About one-third of the cycles in this engine at these conditions had no trace of knock and had normal, smoothly varying, cylinder pressure records as in Fig. 9-59*a*. Knock of varying severity occurred in the remaining cycles. With light or trace knock, knock occurs late in the burning process and the amplitude of the pressure fluctuations

PETITIONER'S EXHIBIT 1002
US PATENT NO. 6,581,565



(*a*) Normal combustion, spark 28°BTC

(*b*) Slight knock, spark 28°BTC

(*c*) Intense knock, spark 32°BTC

FIGURE 9-59
Cylinder pressure versus crank angle traces of cycles with (*a*) normal combustion, (*b*) light knock, and (*c*) heavy knock. 4000 rev/min, wide-open throttle, 381-cm^3 displacement single-cylinder engine.[77]

is small (Fig. 9-59*b*). With heavy knock, illustrated here with more advanced spark timing and by selecting an especially high intensity knocking cycle, knock occurs closer to top-center earlier in the combustion process and the initial amplitude of the pressure fluctuation is much larger. These pressure fluctuations produce the sharp metallic noise called "knock." They are the result of the essentially spontaneous release of much of the end-gas fuel's chemical energy. This produces a substantial *local* increase in gas pressure and temperature, thereby causing a shock wave to propagate away from the end-gas region across the combustion chamber. This shock wave, the expansion wave that accompanies it, and the reflection of these waves by the chamber walls create the oscillatory pressure versus time records shown in Fig. 9-59*b* and *c*. Note that once knock occurs, the pressure distribution across the combustion chamber is no longer uniform: transducers located at different points in the chamber will record different pressure levels at a given time until the wave propagation phenomena described above have been damped out.[78]

Many methods of knock detection and characterization have been used. The human ear is a surprisingly sensitive knock detector and is routinely used in determining the octane requirement of an engine—the required fuel quality the engine must have to avoid knock. Knock detectors used for knock control systems normally respond to the vibration-driven acceleration of parts of the engine block caused by knocking combustion pressure waves. A high-intensity flash is observed when knock occurs; this is accompanied by a sharp increase in ionization. Optical probes and ionization detectors have therefore been used. The spark plug can serve as an ionization detector. For more detailed studies of knock in engines, the piezoelectric pressure transducer is the most useful monitoring device. Often the transducer signal is filtered so that the pressure fluctuations caused by knock are isolated.[75]

The amplitude of the pressure fluctuation is a useful measure of the inten-

PETITIONER'S EXHIBIT 1002
US PATENT NO. 6,581,565

sity of knock because it depends on the amount of end-gas which ignites spontaneously and rapidly, and because engine damage due to knock results from the high gas pressures (and temperatures) in the end-gas region. Use of this measure of knock severity or intensity shows there is substantial variation in the extent of knock, cycle-by-cycle. Figure 9-60 shows the knock intensity in one hundred consecutive cycles in a given cylinder of a multicylinder engine operating at fixed conditions for knocking operation. The intensity varies randomly from essentially no knock to heavy knock.[79] Cylinder-to-cylinder variations are also substantial due to variations in compression ratio, mixture composition and conditions, burn rate, and combustion chamber cooling. One or more cylinders may not knock at all while others may be knocking heavily.[80]

Since the knock phenomenon produces a nonuniform state in the cylinder, and since the details of the knock process in each cycle and in each cylinder are different, a fundamental definition of knock intensity or severity is extremely difficult. The ASTM-CFR method for rating fuel octane quality (see Sec. 9.6.3) by the severity of knocking combustion uses the time derivative of pressure during the cycle. Cylinder pressure is determined with a pressure transducer. The low-frequency component of pressure change due to normal combustion is filtered out and the rate of pressure rise is averaged over many cycles during the pressure fluctuations following knock. This approach obviously provides only an average relative measure of knock intensity. The maximum rate of pressure rise has been used to quantify knock severity. An accelerometer mounted on the engine can give indications of relative knock severity provided that it is mounted in the same location for all tests. The most precise measure of knock severity is the maximum amplitude of the pressure oscillations that occur with knocking combustion. The cylinder pressure signal (from a high-frequency response pressure transducer) is filtered with a band-pass filter so that only the component of the pressure signal that corresponds to the fluctuations occurring after knock remains. The filter is set for the first transverse mode of gas vibration in the cylinder (in the 3 to 10 kHz range, depending on bore and chamber geometry). The maximum amplitude of pressure oscillation gives a good indication of the severity of knock.[81] The knock intensities in individual cycles shown in Fig. 9-60 were determined in

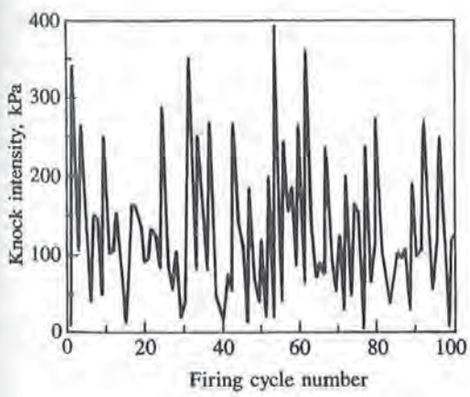


FIGURE 9-60
Knock intensity (maximum amplitude of band-pass-filtered pressure signal) in one hundred individual consecutive cycles. One cylinder of V-8 engine, 2400 rev/min, wide-open throttle.[79]

PETITIONER'S EXHIBIT 1002
US PATENT NO. 6,581,565

this manner.[79] Note that because the pressure fluctuations are the consequence of a wave propagation phenomenon, the location of the pressure transducer in relation to the location of the knocking end-gas and the shape of the combustion chamber will affect the magnitude of the maximum recorded pressure-fluctuation amplitude.

The impact of knock depends on its intensity and duration. Trace knock has no significant effect on engine performance or durability. Heavy knock can lead to extensive engine damage. In automobile applications, a distinction is usually made between "acceleration knock" and "constant-speed knock." Acceleration knock is primarily an annoyance, and due to its short duration is unlikely to cause damage. Constant-speed knock, however, can lead to two types of engine damage. It is especially a problem at high engine speeds where it is masked by other engine noises and is not easily detected. Heavy knock at constant speed can easily lead to:

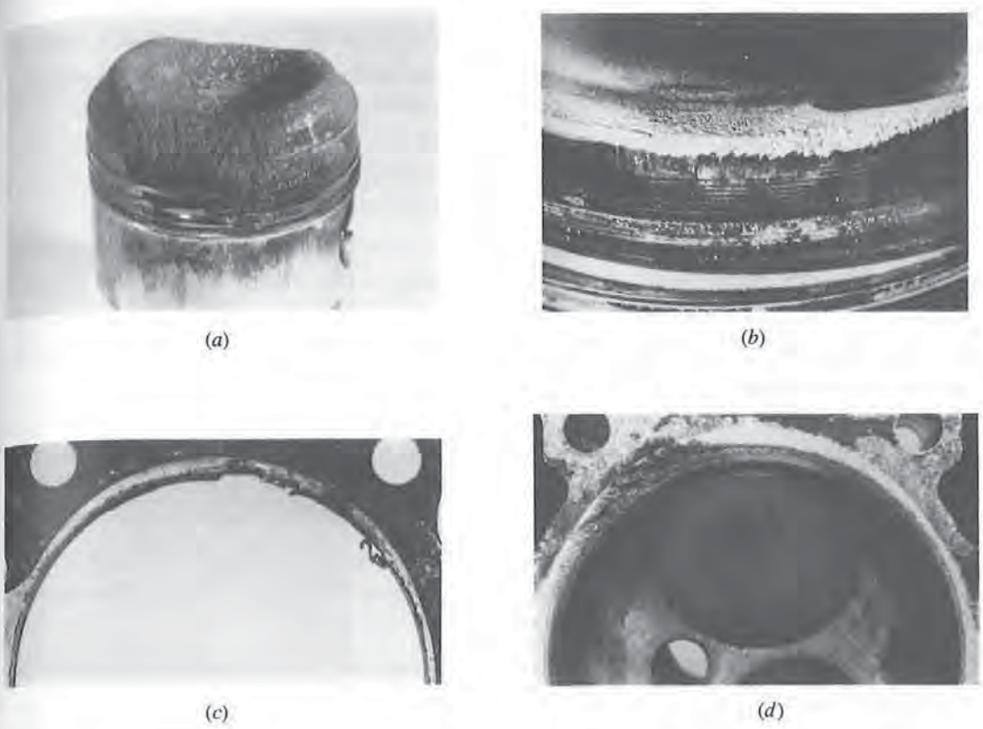
1. Preignition, if significant deposits are present on critical combustion chamber components. This could lead to runaway preignition.†
2. Runaway knock—spark-knock occurring earlier and earlier, and therefore more and more intensely. This soon leads to severe engine damage.
3. Gradual erosion of regions of the combustion chamber, even if runaway knock does not occur.

The engine can be damaged by knock in different ways: piston ring sticking; breakage of the piston rings and lands; failure of the cylinder head gasket; cylinder head erosion; piston crown and top land erosion; piston melting and holing. Examples of component damage due to preignition and knock are shown in Fig. 9-61.[82–84]

The mechanisms that cause this damage are thought to be the following. Preignition damage is largely thermal as evidenced by fusion of spark plugs or pistons. When knock is very heavy, substantial additional heat is transferred to the combustion chamber walls and rapid overheating of the cylinder head and piston results. Under these conditions, knock is not stable: the overheating increases the engine's octane requirement which in turn increases the intensity of knock. It becomes heavier and heavier, and the uncontrolled running away of this phenomena can lead to engine failure in minutes. This damage is due to overheating of the engine: the piston and rings seize in the bore. The damage due to heavy knock over extended periods—erosion of piston crowns and (aluminum) cylinder heads in the end-gas region—is due primarily to the high gas pressures in this region. Extremely high pressure pulses of up to 180 atm due to heavy knock can occur locally in the end-gas region, in the 5 to 10 kHz frequency

† Note that heavy knock can also remove deposits from the combustion chamber walls, thereby decreasing the octane requirement of the engine.

PETITIONER'S EXHIBIT 1002
US PATENT NO. 6,581,565



(*a*) (*b*)

(*c*) (*d*)

FIGURE 9-61
Examples of component damage from abnormal engine combustion. (*a*) Piston holing by preignition;[83] (*b*) piston crown erosion after 10 hours of high-speed knocking;[82] (*c*) cylinder head gasket splitting failure due to heavy knock;[83] (*d*) erosion of aluminum cylinder head along the top of the cylinder liner due to heavy knock.[83]

range. These high local pressures are combined with the higher-than-normal local surface temperatures which occur with the higher knocking heat fluxes and weaken the material. Pitting and erosion due to fatigue with these excessive mechanical stresses, and breakage of rings and lands, can then occur.[78, 82–84]

9.6.2 Knock Fundamentals

As yet, there is no complete fundamental explanation of the knock phenomenon over the full range of engine conditions at which it occurs. It is generally agreed that knock originates in the extremely rapid release of much of the energy contained in the end-gas ahead of the propagating turbulent flame, resulting in high local pressures. The nonuniform nature of this pressure distribution causes pressure waves or shock waves to propagate across the chamber, which may cause the chamber to resonate at its natural frequency. Two theories have been advanced to explain the origin of knock: the autoignition theory and the detonation theory. The former holds that when the fuel-air mixture in the end-gas region is compressed to sufficiently high pressures and temperatures, the fuel oxidation process—starting with the preflame chemistry and ending with rapid

PETITIONER'S EXHIBIT 1002
US PATENT NO. 6,581,565

energy release—can occur spontaneously in parts or all of the end-gas region. The latter theory postulates that, under knocking conditions, the advancing flame front accelerates to sonic velocity and consumes the end-gas at a rate much faster than would occur with normal flame speeds.[75] These theories attempt to describe what causes the rapid release of chemical energy in the end-gas which creates very high pressures, locally, in the end-gas region. The engine phenomenon "knock" includes also the propagation of strong pressure waves across the chamber, chamber resonance, and transmission of sound through the engine structure. The detonation theory has led many to call knock "detonation." However, the more general term "knock" is preferred, since this engine phenomenon includes more than the end-gas energy release, and there is much less evidence to support the detonation theory than the autoignition theory as the initiating process. Most recent evidence indicates that knock originates with the spontaneous or autoignition of one or more local regions within the end-gas. Additional regions (some adjacent to already ignited regions and some separated from these regions) then ignite until the end-gas is essentially fully reacted. This sequence of processes can occur extremely rapidly. Thus, the autoignition theory is most widely accepted.

Photographic studies of knocking combustion have been an important source of insight into the fundamentals of the phenomenon over the past fifty years.† Figure 9-62 shows two sets of schlieren photographs, one from a cycle with normal combustion and the other from a cycle with knock.[88] These photographs were taken in an overhead valve engine with a disc-shaped combustion chamber, with a window which permits observation of the chamber opposite to the spark plug. A reflecting mirror on the piston crown permits use of the schlieren technique which identifies regions where changes in gas density exist. Operating conditions, except for spark advance, were the same for both cycles. In the normal combustion sequence, the turbulent flame front moves steadily through the end-gas as combustion goes to completion. The cylinder pressure varies smoothly throughout this process. When the spark is advanced by 15°, the end-gas temperature and pressure are increased significantly and knock occurs. In this sequence of photographs (*b*), the initial flame propagation process (photographs 1 to 3) is like that of the normal combustion sequence: then almost

† See Refs. 85 to 87 for early high-speed photographic studies. See Refs. 88 to 91 for some recent studies.

FIGURE 9-62
Schlieren photographs from high-speed movies of (*a*) normal flame propagation through the end gas and (*b*) knocking combustion (autoignition occurs in photograph 4), with corresponding cylinder pressure versus crank angle traces. Disc-shaped combustion chamber with details of window shown in insert. 1200 rev/min, 80 percent volumetric efficiency, $(A/F) = 12.5$; spark timing: (*a*) 10° BTC, (*b*) 25° BTC.[88]

PETITIONER'S EXHIBIT 1002
US PATENT NO. 6,581,565

PETITIONER'S EXHIBIT 1002
US PATENT NO. 6,581,565

the entire region ahead of the flame appears dark (photograph 4). Between photographs 3 and 4 substantial changes in the density and temperature throughout most of the end-gas region have occurred. Examination of the cylinder pressure trace shows that this corresponds closely to the time when the pressure recorded by the pressure transducer rises rapidly. Immediately after this, pressure oscillations (at 6 to 8 kHz) are detected. In photograph 5 the flame is no longer visible: the end-gas expansion has pushed the flame back out of the field of view. Subsequent photographs are alternatively lighter and darker, indicative of changing local density fields as pressure waves propagate back and forth across the chamber.

More extensive studies of this type, which relate photographs from high-speed movies of the combustion process to the cylinder pressure development, indicate that the location or locations where ignition of one or more portions of the end-gas first occur and the subsequent rate with which the ignition process develops throughout the rest of the end-gas vary substantially cycle-by-cycle and with the intensity of the knocking process. Figure 9-63 shows five shadowgraph photographs from a knocking engine cycle in a research engine similar to that shown in Fig. 9-62.[89] The photographs are 33 μs apart; the total sequence shown lasts 1°. The first photograph shows the flame front prior to onset of knock. The second photograph shows the onset of autoignition with the appearance of dark regions near the wall (two identified by arrows) where substantial density gradients resulting from local energy release exist. The third, fourth, and fifth photographs show the spread of these ignited regions with time through the remaining end-gas. The exact location where autoignition occurred was identified with a photodigitizing system which ranked regions of the photograph by their brightness or darkness. The digitized version of the second photograph is also shown in Fig. 9-63. Additional smaller regions of autoignition are evident adjacent to the wall and in the vicinity of the flame front. While the location of autoig-

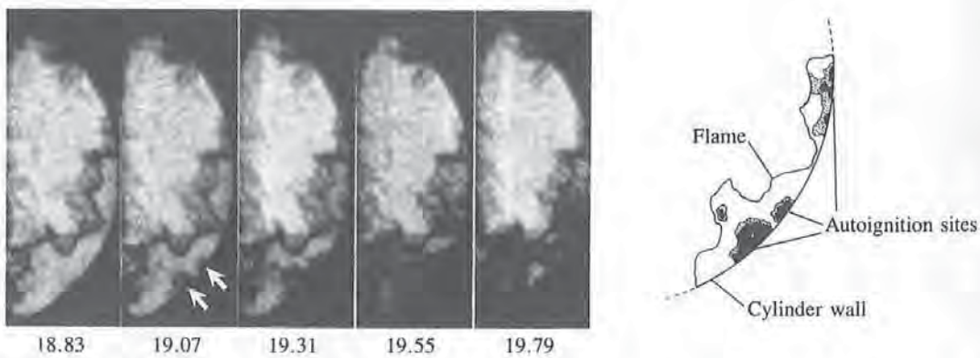


FIGURE 9-63
Five shadowgraph photographs of knocking combustion cycle identifying location of autoignition sites (arrows). Crank angle of each photo indicated: 33 μs between frames. Operating conditions and engine details as in Fig. 9-62. Photodigitized picture of second photograph showing additional details of the autoignition sites in the end-gas region on right.[89]

PETITIONER'S EXHIBIT 1002
US PATENT NO. 6,581,565

nition sites varied with engine operating conditions, the majority of occurrences in this study were in the vicinity of the cylinder wall. The rate of spread of the autoignited end-gas region also varied significantly. Under heavy knocking conditions the entire end-gas region became ignited very rapidly and high-amplitude pressure oscillations occurred. Under trace knock conditions, autoignition could occur; yet the spread of the autoignited region could be sufficiently slow for no pressure oscillations to be detected.

When the above-described end-gas ignition process occurs rapidly, the gas pressure in the end-gas region rises substantially due to the rapid release of the end-gas fuel's chemical energy. The erosion damage that knock can produce, due to stress-induced material fatigue as described in the previous section, indicates the location of this high-pressure region. With the chamber geometry typical of most engines where the flame propagates toward the cylinder wall, the damage is confined to the thin crescent-shaped region on the opposite side of the chamber to the spark plug, where one expects the end-gas to be located. A shock wave propagates from the outer edge of this high-pressure end-gas region across the chamber at supersonic velocity, and an expansion wave propagates into the high-pressure region toward the near wall. The presence of such a shock wave has been observed photographically.[90] The shock wave and expansion wave reflect off the walls of the chamber, eventually producing standing waves. Usually these standing waves are due to transverse gas vibration and are of substantial amplitude. The amplitude of the pressure oscillations builds up as the standing waves are established, and then decays as the gas motion is damped out. The frequency of the pressure oscillations (normally in the 5 to 10 kHz range) decreases with time as the initially finite-amplitude supersonic pressure waves decay to small-amplitude sound waves.[80] Thus the pressure signal detected with a transducer during a knocking combustion cycle will depend on the details of the end-gas ignition process, the combustion chamber geometry, and the location of the transducer in relation to the end-gas region.

The pressure variation across the cylinder bore, due to knock, can be illustrated by the following example. Consider the disc-shaped combustion chamber with the spark plug located in the cylinder wall shown in Fig. 9-64*a*. Figure 9-64*b* shows the pressure and temperature distribution across the combustion chamber due to the normal flame propagation process, at the time rapid ignition of the end-gas occurs. If the end-gas ignites completely and instantaneously, its pressure and temperature will suddenly rise, as shown. A shock wave will now propagate to the right and an expansion wave to the left, as shown in the distance-time diagram in Fig. 9-64*c*. These waves reflect off the walls and interact. The pressures at the cylinder wall, in the end-gas region and on the opposite side of the chamber at the spark plug, develop as shown in Fig. 9-64*d*. Figure 9-65 shows two simultaneously recorded pressure traces with heavy knock from two transducers at the top of the cylinder liner, one located near the spark plug and one in the end-gas region. In the end-gas region the pressure rises extremely rapidly when knock occurs, to a value considerably higher than that recorded on the opposite side of the chamber where the pressure rises more gradually. Standing

PETITIONER'S EXHIBIT 1002
US PATENT NO. 6,581,565

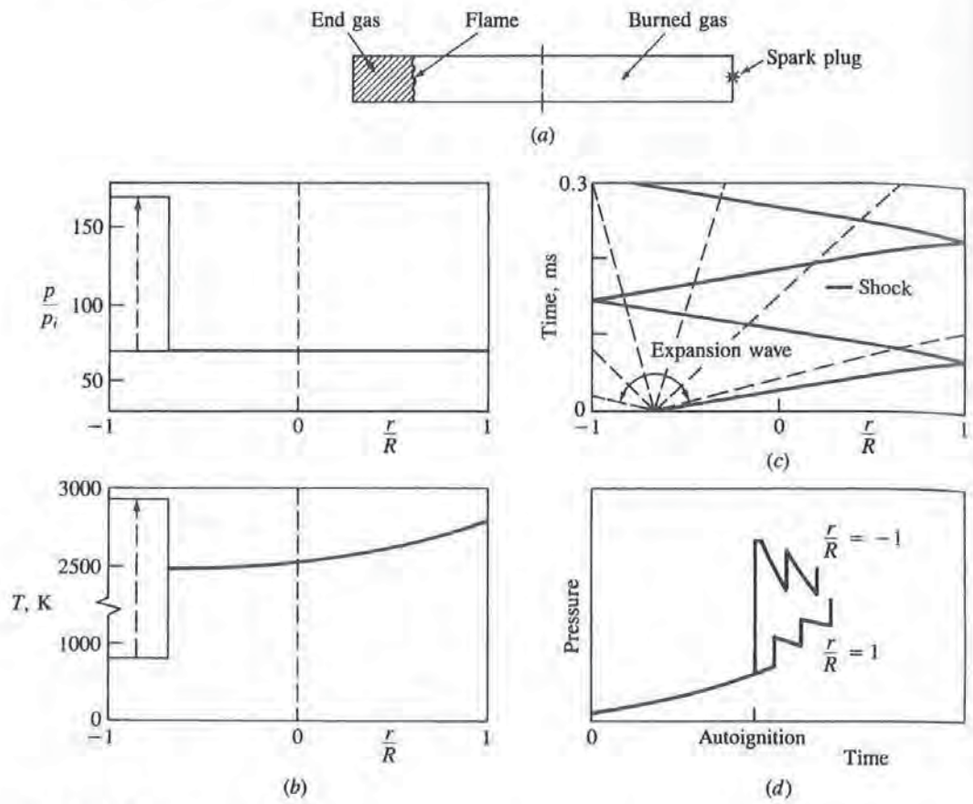


FIGURE 9-64
Illustration of how cylinder pressure distribution develops following knock. (*a*) Schematic of disc-shaped combustion chamber at time of knock. (*b*) Pressure and temperature across the diameter of a disc-shaped engine combustion chamber, before and after end-gas autoignition (assumed to occur very rapidly, at constant end-gas density). (*c*) Schematic of shock and expansion wave pattern following end-gas autoignition on distance-time plot. (*d*) Pressure variation with time at cylinder wall in the end-gas region, and at the opposite side of the cylinder.

waves are then set up and the amplitudes of the oscillations decay as the waves are damped out.[78]

The fundamental theories of knock are based on models for the autoignition of the fuel-air mixture in the end-gas. *Autoignition* is the term used for a rapid combustion reaction which is not initiated by any external ignition source. Often in the basic combustion literature this phenomenon is called an explosion. Before discussing the relevant theories of hydrocarbon oxidation, the necessary terminology will be defined and illustrated with the autoignition behavior of the much simpler hydrogen-oxygen system. For the hydrocarbons commonly found in practical fuels, the chemical reaction schemes by which the fuel molecules are broken down and react to form products are extremely complicated, and are as yet imperfectly understood.

The autoignition of a gaseous fuel-air mixture occurs when the energy re-

PETITIONER'S EXHIBIT 1002
US PATENT NO. 6,581,565

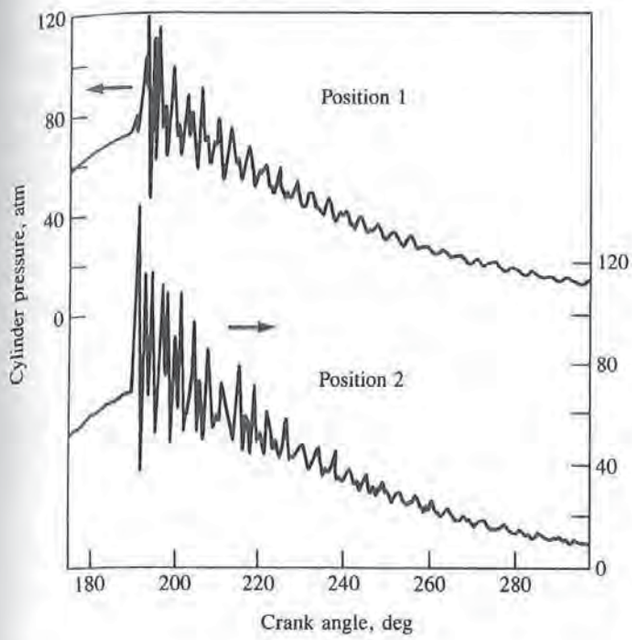


FIGURE 9-65
Simultaneously recorded pressure traces on opposite sides of spark-ignition engine combustion chamber in heavily knocking cycle. Position 1: at top of cylinder liner closest to spark plug. Position 2: at top of cylinder liner farthest from spark plug. 2000 rev/min, wide-open throttle, $(A/F) = 12.3$, spark advance 20° BTC.[78]

leased by the reaction as heat is larger than the heat lost to the surroundings; as a result the temperature of the mixture increases, thereby rapidly accelerating, due to their exponential temperature dependence, the rates of the reactions involved. The state at which such spontaneous ignition occurs is called the *self-ignition temperature* and the resulting self-accelerating event where the pressure and temperature increases rapidly is termed a *thermal explosion.*

In complex reacting systems such as exist in combustion, the "reaction" is not a single- or even a few-step process; the actual chemical mechanism consists of a large number of simultaneous, interdependent reactions or *chain reactions.* In such chains there is an *initiating* reaction where highly reactive intermediate species or *radicals* are produced from stable molecules (fuel and oxygen). This step is followed by *propagation* reactions where radicals react with the reactant molecules to form products and other radicals to continue the chain. The process ends with *termination* reactions where the chain propagating radicals are removed. Some propagating reactions produce two reactive radical molecules for each radical consumed. These are called *chain-branching* reactions. When, due to chain-branching, the number of radicals increases sufficiently rapidly, the reaction rate becomes extremely fast and a *chain-branching explosion* occurs. While the terms thermal and chain-branching explosions have been introduced separately, in many situations the self-accelerations in temperature and radicals occur simultaneously and the two phenomena must be combined.[92, 93]

The oxidation of hydrogen at high pressures and temperatures provides a good illustration of these phenomena. For stoichiometric hydrogen-oxygen mixtures, no reaction occurs below 400°C unless the mixture is ignited by an external

PETITIONER'S EXHIBIT 1002
US PATENT NO. 6,581,565